Indium Phosphide Nanowire Arrays for Gas Sensing Applications

Shiyu Wei

June 2024

A Thesis Submitted for the Degree of Doctor of Philosophy of the Australian National University

Research School of Physics

College of Science

The Australian National University

© Copyright by Shiyu Wei 2024

All Rights Reserved

Declaration

I certify that this thesis does not incorporate, without acknowledgement, any material previously submitted for a degree or diploma in any university and that to the best of my knowledge, it does not contain any material previously published or written by another person except where due reference is made in the text. The work in this dissertation is my own, except for the contributions made by others as described in the Acknowledgements.

Shiyu Wei

June 2024

Acknowledgments

I would like to extend my heartfelt gratitude to the following individuals and institutions who have given me support and guidance for my Ph.D. study and thesis:

Firstly, I would like to deeply thank our group leader, Distinguished Professor Chennupati Jagadish. It is a great honour and privilege for me to work with him. Owing to his great dedication and personal kindness to each member of our group, I am able to devote in research at an amazing learning and supportive environment with world-leading infrastructure. He always offers encouragements and insightful comments on my study. I truly appreciate his guidance and facilitation for my study.

I want to express my sincere appreciation to my primary supervisor, Professor Lan Fu for her invaluable guidance, unwavering support, and mentorship throughout my research process. Her expertise and insightful feedback have been instrumental in shaping the direction of my projects. Not only for academia research, but she has also guided me to improve my skills in speech, presentation and organisation, which hugely benefit my career development.

I would also like to express my deepest thanks to my supervisory panel, Professor Hoe Tan, Professor Antonio Tricoli, Professor Dragomir Neshev and Dr. Ziyuan Li whose constructive critiques and suggestions have significantly improved the quality and depth of this thesis.

I extend my thanks to Professor Christopher Nolan, Dr. Zhe Li, Dr. Buddini Karawdeniya and Dr. Krishnan Murugappan, whose collaboration and expertise have contributed to the successful execution of experiments, data analysis and paper writing. In particular, Dr. Zhe Li contributes to all the simulation study in this thesis. Their expertise and guidance have enriched my Ph.D. research and this thesis.

I want to thank my friends in our group Anha, Aswani, Fanlu, Josh, Mohmmed, Nikita, Sonachand, Vidur, Wei, Xiaoying, Yang, Yue, Zhicheng and Zahra, for their encouragement, company, and support in both work and life. Specifically, I thank Fanlu, Zhicheng, Vidur, Wei for helping me learn the experimental skills, equipment operation and fundamental theory, making my research work much easier. I wish them all the best in your career journey and hope we will be friends forever.

I acknowledge the Australian National University for providing the world-class resources, facilities and a conducive academic environment for the pursuit of knowledge and research. My collaborators at the Australian National University (Ms. Alishba John, Dr. Tuomas Haggren), Royal Melbourne Institute of Technology (Dr. Litty Thekkekara), University of Technology Sydney (Dr. Aiswarya Pradeepkumar), and the Australian National Fabrication Facility ACT Node (Dr. Kaushal Vora, Dr. Li Li, Dr. Mark Lockrey, Dr. Mykhaylo Lysevych, Dr. Gayatri Vaidya and Mrs. Sue Berkeley) have also greatly supported my research.

This research was made possible through the financial support of Ph.D. scholarships from the Australian National University and Chinese Scholarship Council. Their investment in this project has been instrumental in its successful completion.

I would like to extend my sincere thanks to our administrators at the Australian National University: Ms. Julie Arnold, Ms. Samara Thorn, Ms. Mary Gary, Ms. Karen Nulty, Ms. Siobhan Ryman and Ms. Liudmila Mangos. This journey has been a collective effort, and I am truly fortunate to have received such immense support which have make this whole journey a smooth one. Thank you for being an integral part of my academic endeavour.

Last but not least, it was of course impossible to finish this dissertation without the unconditional love and support from my family. I truly appreciate my family for their constant encouragements, understandings, and patience. I sincerely thank my parents, Wen and Hongying for their unwavering support and encouragement. I express my

sincere love and appreciation to my beloved husband, Chenrui. I acknowledge that this Ph.D. has culminated due to your unconditional love, accompany and support. Also, I cannot express how thankful I am for your support to make our wedding ceremony possible in the place I completed my Ph.D. study. I dedicate this Ph.D. thesis to you, Chenrui.

Abstract

Semiconductor chemiresistive gas sensor is one of the most promising technologies for the development of next-generation chemical sensing, with applications ranging from explosive detection and environmental monitoring to industrial safety, healthcare and the Internet of Things (IoTs). Recently, there have been growing efforts in developing room temperature chemiresistive gas sensors with high sensitivity, selectivity, long-term stability, and low power consumption. In this thesis, we develop indium phosphide (InP) nanowire (NW) array based chemiresistive gas sensors and demonstrate that they represent a new and promising platform for achieving high-performance gas sensing for real-world applications.

Firstly, by carefully engineering the NW geometry (i.e., diameter and pitch), we demonstrate a NO_2 sensor with superior sensitivity (limit of detection 3.1 ppb) at room temperature, with outstanding selectivity and long-term stability. Kinetic analysis and electrical simulation reveal the array geometry correlated sensing mechanism. To minimize the device power consumption, a novel axial p-i-n homojunction self-powered photovoltaic (PV) NO_2 NW sensor was further designed through numerical simulation and optimization. The fabricated InP NW array PV sensor achieved 84% sensing response to 1 ppm NO2 with a record limit of detection down to sub-ppb level even under <5% of 1 sun illumination. With such high atmospheric light fidelity, the sensor was integrated onto a commercial microchip interface for dynamic self-powered monitoring of on-field motor vehicle exhaust.

Not only for oxidizing gas such as NO_2, we have also shown that by applying surface-modification, the InP NW array can also be fabricated into highly sensitive sensors to

reducing gases such as acetone. This is critical for the development of breath ketone sensors for diabetes monitoring and diagnostics. This acetone sensor was then integrated into a breath testing apparatus, named Ketowhistle, and proven to be highly effective across an ultrabroad range of acetone concentrations from the simulated breath.

Finally, a wearable multipixel InP nanowire array sensor was fabricated on a flexible substrate. A signal decoupling strategy was designed and implemented through careful device fabrication control, surface-functionalisation and different contact metal selection. This approach has led to the demonstration of a multipixel sensor device consisting of four sensing elements with integrated functionality, including NO_2 and acetone sensing, as well as simultaneous pulse and body temperature measurements.

The thesis work indicates that III-V compound semiconductor nanowire array presents a promising chemical sensing platform for the development of high performance, miniaturized, low power consumption, multiplexing on-chip sensing system for future large-scale implementation of IoT technology.

List of Publications

First author:

1. **Wei, S. Y.,** Karawdeniya, B. I., Li, Z, Zhang, P., Lysevych, M., Vora, K., Tan, H. H., Jagadish, C., Antonio, T., and Fu, L. Wearable multiplex sensor platform based on nanowire array device. (To be submitted).

2. **Wei, S. Y.,** Haggren, T., Li, Z., Tan, H. H., Jagadish, C., Antonio, T., and Fu, L. Ultrasensitive indium phosphide nanomembrane wearable gas sensors. *Energy & Environmental Materials.* e12763 (**2024**).

3. **Wei, S. Y.,** Li, Z, Murugappan, K., Li, Z. Y., Lysevych, M., Vora, K., Tan, H. H., Jagadish, C., Karawdeniya, B. I., Nolan, C. J., Antonio, T., and Fu, L. Nanowire Array Breath Acetone Sensor for Diabetes Monitoring. *Advanced Science.* 2309481 (**2024**).

4. **Wei, S.Y.,** Li, Z, Murugappan, K., Li, Z. Y., Zhang, F. L., Saraswathyvilasam, A. G., Lysevych, M., Tan, H. H., Jagadish, C., Karawdeniya, B. I., Antonio, T., and Fu, L. A Self-Powered Portable Nanowire Array Gas Sensor for Dynamic NO_2 Monitoring at Room Temperature. *Advanced Materials*. **35**, 2207199 (**2023**).

5. **Wei, S.Y.,** Li, Z, Murugappan, K., Li, Z. Y., Zhang, F. L., Vora, K., Tan, H. H., Jagadish, C., Karawdeniya, B. I., Antonio, T., and Fu, L. Semiconductor Nanowire Arrays for High-Performance Miniaturized Chemical Sensing. *Advanced Functional Materials*. **32**, 2107596 (**2022**).

Co-author:

1. Alishba, T. J., **Wei, S. Y.,** Yuwono J. A., Kumar P., Nisbet, D. R., Karawdeniya, B. I., Fu, L., Murugappan, K., and Antonio, T. Nano-structuring metal organic frameworks on semiconductor nanowire arrays for highly sensitive and selective chemical sensing. *Applied Physics Review*. **10**, 031421 (**2023**).

2. Zhao, X., **Wei, S.Y.,** Wang, X.H. & Qiu, L.Z. A Novel Multilevel Non-volatile Solar-Blind Deep Ultraviolet Photoelectric Memory Based on an Organic Field Effect Transistor. *Advanced Optical Materials* **9**, 2002256 (**2021**).

3. Ge, F., **Wei, S.Y.,** Liu, Z., Wang, G. H, Wang, X. H, Zhan G. B., Lu, H. B, Cho, K., and Qiu, L.Z. Tailoring Structure and Field-Effect Characteristics of Ultrathin Conjugated Polymer Films via Phase Separation. *Acs Applied Materials & Interfaces* **10**, 9602-9611 (**2018**).

List of Presentations/Awards at Conferences

1. Australian Centre for Accelerating Diabetes Innovations (ACADI) Health Tech Innovation Challenge, 2023, granted by the seed funding.

2. IEEE Nanotechnology Materials and Devices Conference 2023. Awarded by "Young Investigator award". Oral presentation "Self-powered InP Nanowire Array Based Gas Sensors".

3. TMOS 2022 Meta Together Conference. Oral presentation "InP Nanowire Array Based Gas Sensors", awarded by the "Student of the Year".

4. The ANU Women in Physics First Annual Gala 2022. Poster presentation "InP Nanowire Array Based Gas Sensors", awarded by the Best poster.

5. Chemical Nanosensors Australia (CNA) 2022. Poster presentation "Semiconductor Nanowire Array for High-performance Miniaturised Chemical Sensing", awarded by the Best poster.

List of Abbreviations

Abbreviation	Description
ALD	atomic layer deposition
CL	cathodoluminescence
CVD	chemical vapour deposition
DEZn	diethylzinc
EBIC	electron beam-induced current
EBL	electron beam lithography
EDX	energy dispersive X-ray spectroscopy
EL	electroluminescence
FDTD	finite-difference time-domain
FIB	focused ion beam
I-V	current-voltage
LED	light emitting diode
MBE	molecular beam epitaxy
MOCVD	metal-organic chemical vapour deposition
MOVPE	metal-organic vapour phase epitaxy
SAE	selective area epitaxy
NW	nanowire
SEM	scanning electron microscopy
STEM	scanning transmission electron microscopy
SGS	Semiconductor gas sensor
TEM	transmission electron microscopy
TMAl	trimethylaluminium

TMGa	trimethylgallium
TMIn	trimethylindium
TMSb	trimethylantimony
VLS	vapour-liquid-solid
WZ	wurtzite
ZB	zinc blende
PL	photoluminescence
μ-PL	micro-photoluminescence

Table of Contents

List of Figures

List of Tables

Chapter 1. Introduction

This chapter begins with a general preview of gas sensors including their importance, categories and the corresponding sensing mechanisms. Subsequently, it provides a review of the current research progress of nanomaterial-based gas sensors and their advantages and disadvantages. The existing challenges of nanomaterial gas sensors for real-world applications are also discussed. Then, a promising III-V semiconductor nanomaterial, InP nanowires (NWs), is introduced to address those issues and the pathway to realise practical application as the next-generation high performance gas sensors is also discussed. Finally, the aim and scope for each of the chapters are presented.

1.1 Development of nanostructured gas sensors and their applications

Gas sensors are devices designed to identify and quantify the presence of various gases in the surrounding environment,[1] and find applications across various industries and sectors[2-3]. They serve vital functions in several key areas[4-5]:

1. Industrial safety - In industrial processes, gas sensors are utilised to monitor gas concentrations, regulate reactions and enhance production efficiency. They ensure the well-being of workers by identifying hazardous gases such as H_2S, CH_4, CO, NH_3 and volatile organic compounds (VOCs).[6]

2. Environmental monitoring - Gas sensors can detect pollutants such as ozone (O_3), NO_2, SO_2, etc., playing an important role in assessing and controlling air pollution levels.[7-8]

3. Indoor air quality - Gas sensors are employed in residential, commercial, and institutional buildings to monitor indoor air quality. They detect harmful gases arising from activities like cooking, heating systems, smoking and other indoor processes.[9]

4. Automotive applications - Gas sensors are integral to vehicle emission control systems, helping to monitor and regulate emissions of harmful gases from automobiles to comply with environmental regulations.[10]

5. Medical and healthcare - Gas sensors are utilised in medical settings to detect and measure gases like CO_2, O_2 and anaesthetic gases during surgeries, patient monitoring, and in respiratory equipment.[6] Analysing exhaled breath samples through gas sensors is a new research frontier in healthcare and medicine.[11] Within every breath lies more than 1700 of VOCs produced from metabolic processes and inflammation,[12] providing valuable physiological information of our well-being.[13]

6. Agriculture - Gas sensors monitor gases emitted by ripening fruits, spoilage of stored produce and in greenhouse environments to optimise crop growth conditions.[11]

7. Mining - Gas sensors are employed in mining to detect potentially dangerous gases like methane, ensuring worker safety and preventing potential explosions.

8. Food and beverage industry - Gas sensors monitor gases released during food processing and packaging, ensuring food safety and quality.[14]

9. Environmental research - Gas sensors collect data on gas concentrations in different environments, contributing to climate studies and research.[15]

There are a wide variety of gas sensors based on different principles to detect and measure different types of gases (Figure 1-1), including:

a. Electrochemical gas sensors: This type of sensor reacts with the target gas, producing an electrical signal proportional to the gas concentration.[16] It comprises two electrodes (a working electrode and a counter electrode) and operates by allowing charge molecules to pass through a thin electrolyte layer. The chemical reaction between the target gas and the electrode generates an electric current proportional to the gas concentration.[17]

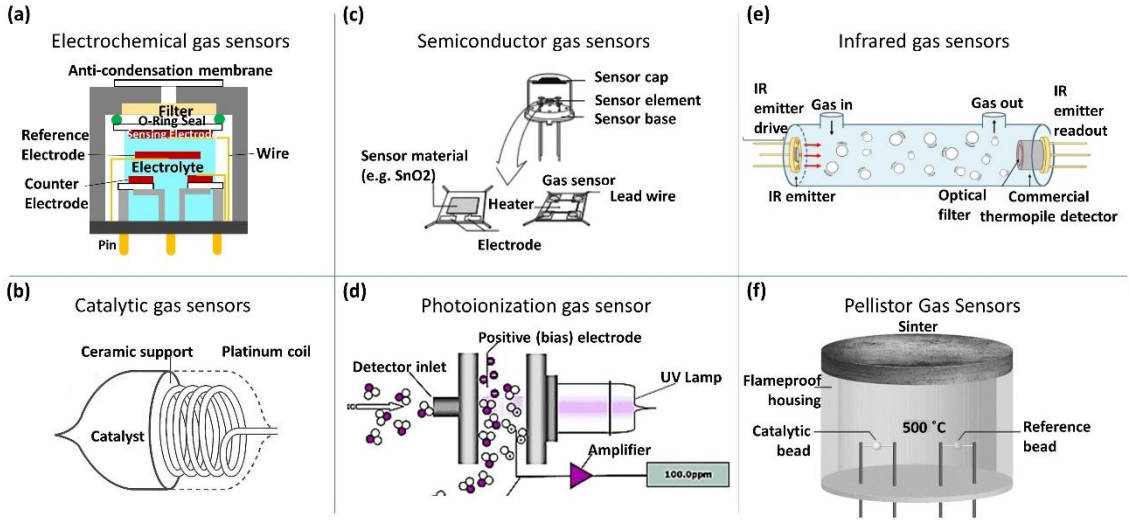

Figure 1-1. Schematic diagrams of different type of gas sensors: (a) electrochemical gas sensors, (b) catalytic gas sensors, (c) semiconductor gas sensors, (d) photoionization sensors, (e) infrared gas sensors, (f) pellistor gas sensors. (Adapted from [15-22])

b. Catalytic gas sensors: The sensor operates on the principle that oxidation of gas produces heat and converts the temperature change into a sensor signal proportional to the gas concentration.[18] Its components include a pair of heating coils, with the active element embedded in a catalyst. Combustible gases react exothermically with oxygen in the air on the catalyst surface, raising its temperature and resulting in a change of resistance. These sensors are designed to detect combustible gases like CH_4 and H_2.

c. Semiconductor gas sensors (SGSs): This type of sensor relies on the change in electrical resistance of a semiconductor material when exposed to specific gases.[19] The resistance change is proportional to the gas concentration, making them suitable for detecting various gases like hydrogen, methane, ammonia, carbon monoxide and various VOCs.[20]

d. Photoionization gas sensors: This type of device utilises high-energy photons, typically in the vacuum ultraviolet (VUV) range, to break molecules into positively charged ions.[21] As compounds enter the detector, they are bombarded by high-energy UV photons, resulting in ionisation. This process ejects electrons and forms positively

charged ions, producing an electric current, which serves as the signal output of the detector.[22] The concentration of the component correlates with the number of ions produced, amplifying the current displayed on an ammeter or digital concentration display. The ions can undergo various reactions, including reactions with oxygen or water vapour, rearrangement and fragmentation. While some ions may recapture an electron within the detector to reform their original molecules, only a small portion of the airborne analytes is typically ionised, making the practical impact negligible. These sensors are non-destructive, suitable for use before other sensors in multiple-detector configurations.

e. Infrared gas sensors: Infrared (IR) gas sensor operates based on the absorption of IR radiation at specific wavelengths as it passes through a volume of gas.[23] This type of sensor relies on the ability of certain gases to absorb IR radiation.[24] IR sensors detect gases based on their unique absorption spectra, allowing identification and measurement of the concentration of target gases.[23] They are commonly used for detecting gases such as CO_2, hydrocarbons and methane. Typically, two IR light sources and an IR light detector measure the intensity of two different wavelengths - one at the absorption wavelength and one outside the absorption wavelength. If a gas intervenes between the source and the detector, the radiation falling on the detector is reduced. Gas concentration is determined by comparing the relative values between the two wavelengths in this dual-beam IR detector. Another type of optical gas sensor employs the innovative metamaterial approach to detect and identify specific gases or analyse the gas adsorption.[25] Metamaterials are engineered materials with unique electromagnetic properties, differing from naturally occurring materials.[26] The two-dimensional arrangements of subwavelength structures in metamaterials manipulate electromagnetic waves, exhibiting resonant behaviour at specific frequencies within the electromagnetic spectrum. Depending on the target gases and sensor design, these resonant frequencies may be in the IR, terahertz or other relevant parts of the spectrum. The sensing properties arise from

changes in the optical properties (e.g., refractive index, absorption, scattering) due to adsorption of gas molecules and their interaction with the metasurface[27] which is related to the gas concentration and detectable through spectral analysis.[28]

f. Pellistor gas sensors: A pellistor is a solid-state device utilised for detecting gases that are either combustible or exhibit a significant difference in thermal conductivity compared to air.[29] The word "pellistor" is a combination of pellet and resistor.[30] The detecting element comprises small pellets of ceramic loaded with a catalyst, and its resistance changes in the presence of gas. Many pellistors require some heating during operation, making them four-terminal devices with two connections for a small heating element and two for the sensor itself. To mitigate the risk of explosion, the sensitive element is typically enclosed in a wire mesh housing. In more robust sensors designed for high-risk environments, a solid steel housing may be employed, featuring a gas port with sintered metal granules.

Each type of gas sensor presents its own set of advantages and limitations. The choice of an appropriate sensor depends on factors such as the target gas, sensitivity requirements, environmental conditions, cost and the intended applications. Many of these sensors have drawbacks, including relatively high costs, low sensitivity and selectivity, sophisticated design, and the need for additional equipment, sometimes lacking portability. However, SGSs stand out with several advantages compared to other types, making them a preferred choice for various gas sensing applications.[31] The most notable advantage of SGSs is their cost-effectiveness in manufacturing, surpassing other sensor types like electrochemical or solid-state sensors.[32] This affordability makes them accessible for a wide range of applications.[33] Also, they can be fabricated in small sizes and integrated into compact and portable devices, suitable for applications such as wearable technology, Internet of Things (IoT) devices and mobile gas detectors.[34] The fast response and

recovery times could also be achieved by SGSs, allowing for real-time gas monitoring and detection with continuously signal collection, which is crucial in safety monitoring related applications where immediate action is required.[35] Many SGSs operate at low power, making them suitable for battery-powered applications or energy-efficient systems. This property can be further leveraged to create self-powered devices by incorporating energy harvest devices or structures, facilitating implementation in remote and wireless sensor networks.[31] Semiconductor-based sensors often exhibit good long-term stability and durability due to their intrinsic chemical properties, ensuring reliable and consistent performance over time.[36] This stability allows them to operate over a wide temperature range, under various environmental conditions, from indoor settings to harsh industrial environments - vital for continuous monitoring and industrial applications. The highly tuneable nature of semiconductors, in terms of chemical composition, scale, heterojunction, etc., enables SGSs to be designed for detecting a wide range of gases, including toxic gases, combustible gases, and VOCs across different sensing applications.

While SGSs may not be as inherently selective as some sensors like electrochemical sensors, they can achieve selectivity by using specific sensing materials, surface-functionalisation, or by analysing sensor response patterns, ensuring targeted gas detection and minimising false alarms.[37] The electrode-based configuration of SGSs is relatively easy to integrate into electronic circuits and systems, allowing connection with microcontrollers, signal processing units and data communication devices.[38] In recent decades, there has been a rapid increase in the number of studies on gas sensors, as depicted in Figure 1-2a, an indication of growing interest and research efforts in this field. Significant progress has been made in sensing performance, operational conditions and evaluation methods to bridge the gap between laboratory research and targeted real-world applications. The bulk of the effort is concentrated in the field of sensing materials, which

form the core part of gas sensors. The development of sensing materials and/or catalysts has been focused on exploiting novel materials for high-performance gas sensing. Examples in Figure 1-2b include metal oxides (such as SnO_2, WO_3, and ZnO), carbon materials (carbon nanotube,[39] and graphene[32]), and quantum dots[21]. For SGSs, the sensing performance is greatly enhanced by employing nanostructured materials, such as nanowires, nanopores, and nanoparticles[40] as shown in Figure 1-2c.[41] It is crucial to note that different gases may have varied interactions with semiconductor materials, resulting in different sensitivity levels and response times. Therefore, these sensors are often designed and calibrated for specific gases or gas families.

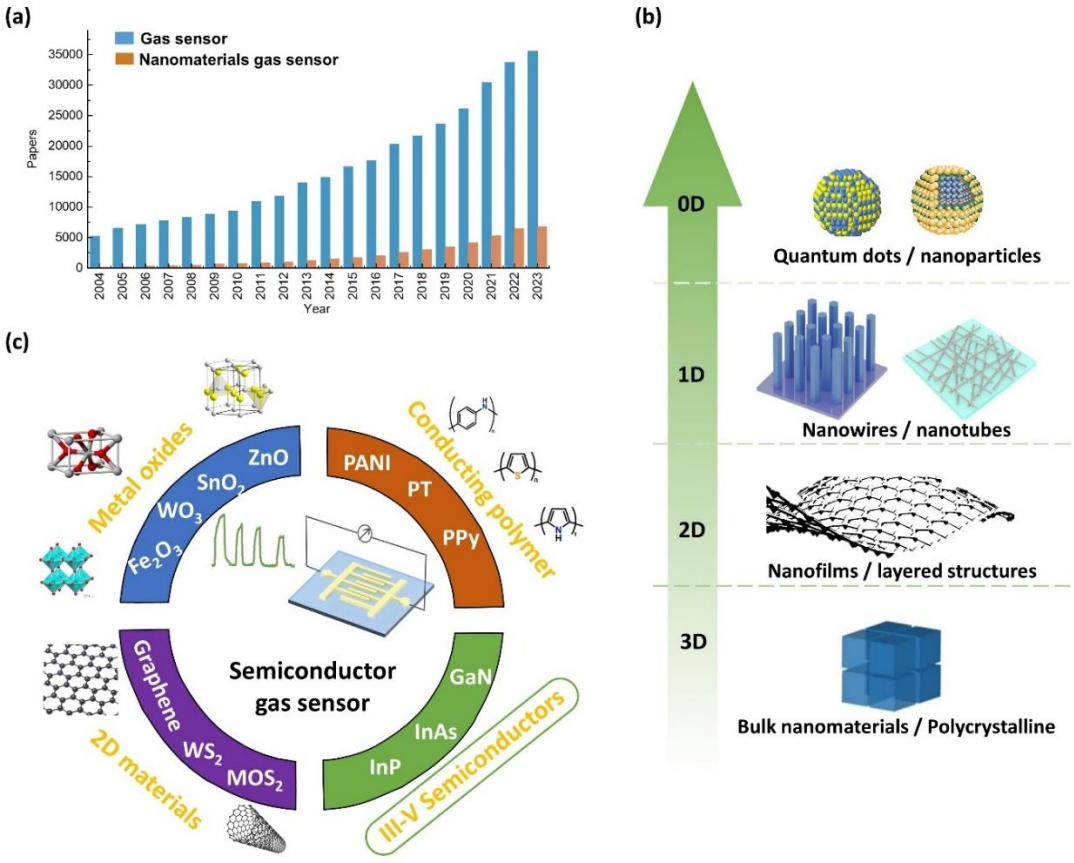

Figure 1-2. (a) Number of published papers versus year of publication (Source: ScienceDirect). (b) The types of 0D, 1D, 2D, and 3D structures used for gas sensing. (c) Materials used for the active layer of SGSs. (Adapted from [39])

Among the various sensing materials, nanomaterials, defined as materials with a single unit sized between 1 and 100 nm in at least one dimension, exhibit significant potential for the development of high-performance SGSs, facilitated by advancements in nanotechnology as shown in Figure 1-2b.[42] Materials with nanoscale structures often possess unique optical, electrical, thermo-physical and/or mechanical properties,[43-44] which, combined with their small size, high surface area and quantum effects, making them ideal candidates for gas sensing applications.[45] Key aspects and advantages of nanomaterial-based gas sensors include:

1) Increased surface area: The large surface area-to-volume ratio of nanomaterials facilitates gas molecules interaction. This enhances sensitivity, enabling the detection of gases at lower concentrations. Nanomaterials are particularly suitable for detecting trace amounts of hazardous or toxic gases.[46]

2) Fast response speed: Due to their small size and efficient gas-molecule interactions, nanomaterials exhibit fast response and recovery times, leading to real-time monitoring and reduced power requirements and energy-efficient operation.[47]

3) Tailored selectivity: Nanomaterials can be engineered to exhibit high selectivity towards specific gases by modifying their surface or functionalizing them with specific chemical groups.[48]

4) Miniaturisation: The nanoscale dimensions and high surface-to-volume ratio of nanomaterials allow for the miniaturisation of SGSs. This enables their integration into small devices and systems for various applications. Moreover, nanomaterials can be seamlessly integrated into existing semiconductor fabrication processes, enabling cost-effective mass production.

In addition to progress in sensing materials, advancements in gas sensors have been focused on the development of sensors capable of detecting multiple gases

simultaneously. Multiplexed-gas sensors offer improved applicability and sensitivity tunability.[49] Miniaturisation of sensors can also be achieved through microelectromechanical systems (MEMS) technology, creating compact and highly sensitive MEMS-based gas sensors.[50] These sensors offer advantages such as low power consumption, fast response times and compatibility with integrated circuits. Sensor arrays consisting of multiple sensors with different selectivity have been employed to enhance gas recognition and discrimination. Furthermore, multiplexed gas sensor arrays benefit from advanced data analysis techniques, including machine learning and pattern recognition algorithm,[51] to interpret sensor responses and identify specific gases or gas mixtures and achieve improved performance.

1.2 Recent progress on nanomaterial-based gas sensor research

The development of nanotechnology and nanomaterials has driven the miniaturisation of gas sensors, making them portable and wearable. These devices are now capable of monitoring personal exposure to gases and for a variety of applications, in particular for industrial safety.[52] These sensors can be integrated into small handheld devices such as smart watches, wristbands or even clothing,[53] offering real-time personal monitoring of air quality and potential hazards. These user-friendly device design could also be employed to measuring biomarkers in exhaled breath and monitor physical health conditions to provide clinical assistance, especially for initial disease diagnosis and health management.[54]

The real-world application requirements mentioned above demand high sensing performance, including sensitivity, selectivity, stability and low cost.[55] Nanomaterials provide opportunities for performance improvement due to their unique properties and

large surface area compared to bulk materials.[56] To enhance sensing performance, increasing the surface area through nanomaterials such as nanowires (NWs), nanoparticles (NPs) or porous nanostructures (see Figure 1-2c) becomes crucial. This enhances the number of active sites available for gas adsorption, resulting in improved sensitivity to low gas concentrations as shown in Figure 1-3a.[57] For example, Xu, et al created active adsorption sites with an SnO_2 layer coated on a polystyrene substrate with nanoscale triangle array embossment, leading to an adsorption sites-dependent sensitivity. This work presented a low detection limit of around 6 ppm ethanol gas at room temperature.[58]

Different materials have varying affinities for specific gases.[59] The ability of the sensing material to bind with the target gas molecules depends largely on the chemical composition and surface condition, determining the tendency to receive or donate electrons toward the gas.[60] The sensing properties can be further tuned by doping or alloying.[61] The experimental studies by Cho et al. demonstrated good selectivity of MoS_2 sensors toward NO_2 gas,[61] which is consistent with theoretical calculation showing that the adsorption energies of NO_2/NO gases on MoS_2 are generally lower and the number of electrons transferred are higher as compared to that toward other gases including CO, CO_2, NH_3, NO, NO_2, CH_4, H_2O, N_2, O_2 and SO_2.

Specific functional groups or coatings which modify/functionalise the nanomaterial surface could enhance its interaction with target gas molecules. Noble metal nanoparticles are the common surface functionalisation materials such as Au, Ag, Pd and Pt.[62] Their chemical sensitisation effect increases the number of reactive oxygen molecules involved in the reaction process and at the same time providing more active sites. The Schottky junctions formed between semiconductors and noble metals decrease the electrons

concentration in the conduction band of semiconductor, increasing the thickness of the electron depletion layer. This effect, known as electronic sensitisation,[63] improves sensitivity, selectivity and reduces cross-sensitivity of SGSs (Figure 1-3c).[64-65]

Also, the heterostructures formed by nanomaterials can promote electron-hole separation and transfer, and modify the gas interaction properties, making them widely studied for gas sensors (Figure 1-3b).[66] The distinctively different chemical and physical parameters between the two materials, such as band structure, dielectric constant, lattice constant and electron affinity can induce a mismatch phenomenon at the interface. This phenomenon endows the heterojunction with many novel properties that can be finely tailored to enhance sensitivity and selectivity. A study by Jian et al. reported an ultrasensitive NH_3 gas sensor featuring n-type semiconductor TiO_2 microfibers attached by a p-type polymer polyaniline nanograin,[67] achieving a very low detection limit of 50 ppt in the air.

Furthermore, integrating nanomaterials gas sensors with nanoelectronics, such as field-effect transistors (FETs) or nanowire transistors, can amplify sensitivity and enable real-time gas sensing.[68-69] This type of integration has the additional advantage of decoupling the chemically sensitive region from the conducting channel, reducing the drive voltage and enhancing the device reliability by liberating the active layer from continuous electrical stress.[70]

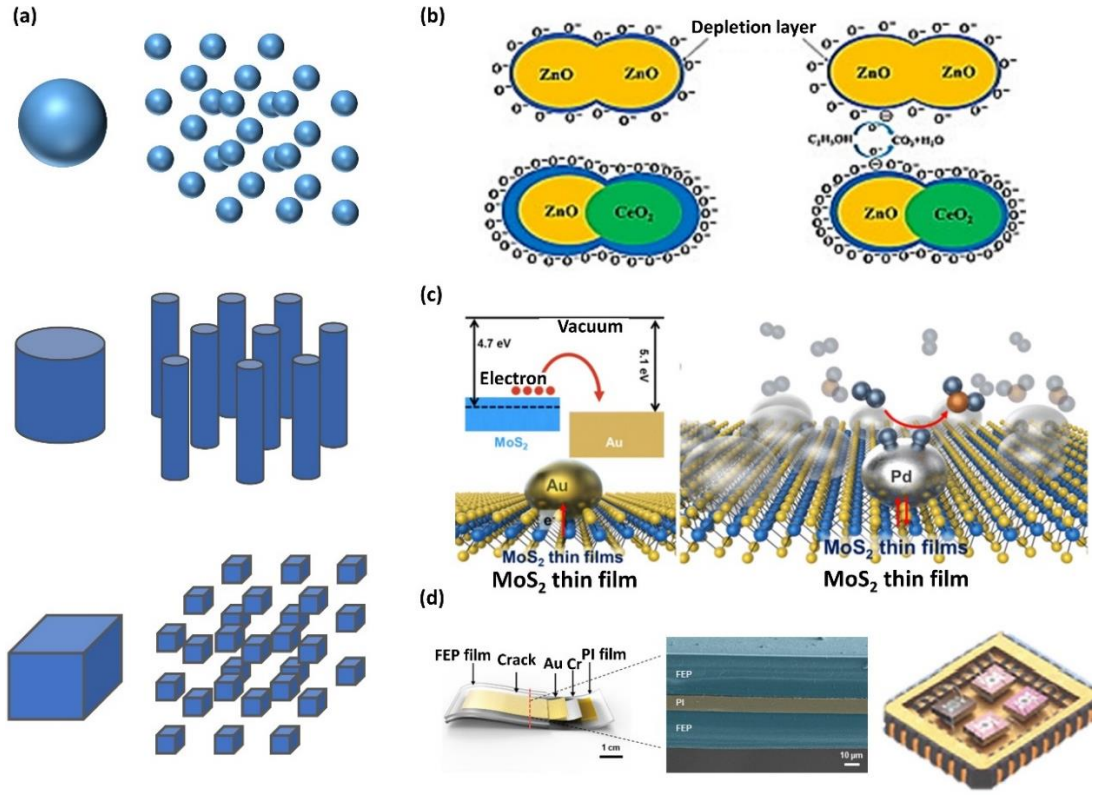

Figure 1-3. Common strategies used in nanomaterials gas sensors for performance enhancement: (a) surface-to-volume ratio, (b) heterojunction configuration, (c) surface-functionalisation and (d) packaging and encapsulation. (Adapted from [71-73])

Portable gas sensor devices have wide applications. Given the challenging environmental fluctuation and the requirement of compactness, there is a need to continually miniaturise the device size and enhance the reliability of sensors against interference.[74] Gas sensors developed in the laboratory must undergo calibration and validation to ensure accurate and reliable measurements in real-world conditions. This process involves comparing the sensing response to known gas concentrations and establishing calibration curves or algorithms.[75] Conducting extensive field testing and validation is crucial to assess the performance of nanomaterials gas sensors to provide valuable insights and feedback for further performance optimisation.[76]

Another critical aspect for practical applications is the stability of nanomaterial gas sensors. Stability is typically categorised into two types: one pertaining to the reproducibility of sensor characteristics over a specified period under working conditions, including high temperatures and the presence of a known analyte, known as active stability. The other type of stability is associated with maintaining sensitivity and selectivity over time under normal storage conditions, such as room temperature and ambient humidity, referred to as long-term stability.[77] In real-world environments, especially for long-term applications that involve continuous monitoring of sensing performance over an extended period under realistic conditions, stability is paramount.[78] Issues like drift, aging, or degradation may emerge from prolonged operation, and investigating these matters offers insights into the reliability of gas sensors over time.

To address concerns related to environmental factors like temperature, humidity and contaminants that could compromise reliability, designing suitable packaging to encapsulate the sensor and implementing protective measurements are proved to be an efficient method. Packaging must be customised based on the intended application to ensure durability, stability and compatibility with the targeted measurement environment (see Figure 1-3d). Nowak et al[78] employed a low temperature co-fired ceramics (LTCC) with thick-film technologies. This LTCC technology is favoured for its simple connection of electrical or optical signals and integration capabilities with passive components such as heaters, sensors and converters. In the study, the LTCC package was designed for a SiC-based hydrogen gas sensor. It serves the dual purposes of safeguarding the sensor against mechanical damage and facilitating an easy connection of electrical signals. Moreover, incorporated heaters and temperature sensors ensure the acquisition of accurate temperature for sensing measurements. The integration of lab-developed gas sensors into measurement systems or devices is important for practical use and calls for

the development of electronics, firmware and software interfaces to streamline data acquisition, processing and analysis. The investigation into these aspects is vital for enhancing the performance and applicability of nanomaterials gas sensors in real-world scenarios.[79]

1.3 III-V semiconductor nanowires for gas sensors

As discussed, when incorporated with nanomaterials SGSs exhibit exceptional advantages in terms of sensitivity, selectivity, stability, compatibility of miniaturisation and integration with electronics and is cost-effective.[80] SGSs often employ device structures such as chemiresistor,[19] FET,[81] Schottky diode,[82] or heterostructure,[83] for detecting gases like CO, NO_2 and ozone. More recently, there has been emerging research revealing their sensitivity towards VOCs, especially for potential applications in exhale breath analysis.[83-85] Despite significant progress in sensing performance of SGSs, there are still challenges and issues to be addressed:

a) Many SGSs require heating at elevated temperature (100-500 °C) to activate the sensing reaction and to enhance sensitivity and selectivity.[86] The high working temperature of the SGSs can result in circuit integration complexity, additional power consumption, cost and safety related issues. The high-power consumption would also need to be addressed in portable and battery-operated devices.

b) One of the primary challenges is achieving high selectivity and minimising cross-sensitivity to other gases. Many gas sensors exhibit response to multiple gases, which can lead to interference and false readings.[65] Developing sensor materials and strategies that can discriminate between target gases and minimise interference from other compounds is an ongoing challenge.

c) Some SGSs suffer from drift, aging or degradation over time, especially for those requiring high operation temperatures, which can affect their accuracy and consistency.[87] It is critical to develop materials and sensor designs for ambient temperature operation and with reliability and long-term stability.

d) Long response / recovery times for some of SGSs hinder their capability to achieve effective real-time detection, especially for toxic gases monitoring.[88]

e) Cost is a significant factor for widespread adoption of gas sensors in various applications. Some cost-effective manufacturing techniques and materials to reduce the overall cost of SGSs may compromise their performance and reliability.

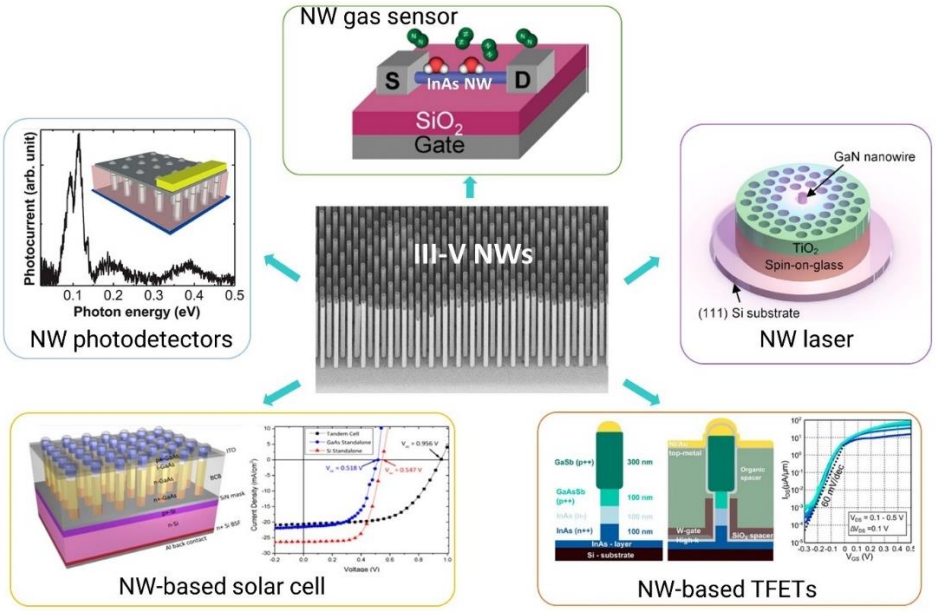

Figure 1-4. III-V NW based devices for various applications. (Adapted from [89])

Addressing these challenges requires interdisciplinary research effort, encompassing the materials science, surface chemistry, device engineering and packaging, and data science. Recently, SGSs based on III-V compound semiconductor NWs have shown promising properties and performances to overcome the aforementioned challenges. III-V compound semiconductors refer to compounds made from elements in the III and V groups of the periodic table, such as GaN, InAs and InP.[90] As one of the most studied

nanostructures, NWs based on III-V semiconductors have been investigated in terms of material growth/synthesis and optoelectronic device applications as lasers, LEDs, photodetectors and solar cells, as shown in Figure 1-4 based on single, array and random configurations.[91-92] On the other hand, although they have excellent potential in optoelectronic device applications, research on III-V NW based gas sensors is still in its infancy.

Similar to the applications for electronic/optoelectronic devices, the key advantages of III-V NW-based gas sensors arise from their superior electrical and/or optical properties, high tunability through varying bandgap energy, doping, surface functionalisation and well-established fabrication technology.[93] Their high carrier mobility enhances sensor sensitivity to surface charge modulation caused by gas adsorption or chemical reactions, and electric field and drift velocity enables fast sensor response/recovery times. Due to their high surface-to-volume ratio, III-V NWs exhibit high sensitivity to a broad range of gases.[94] For cross-sensitivity, III-V NWs can be engineered and functionalized to show selective responses to specific gases by tailoring surface chemistry or modifying material composition.[95] Their nanoscale dimensions enable quick diffusion and adsorption of gas molecules, resulting in faster response times compared to traditional sensors. III-V semiconductor materials possess excellent stability and durability, ensuring the long-term reliability of gas sensors. III-V NWs can be fabricated into miniaturised devices and integrated into compact and portable systems, thereby facilitating the development of wearable gas sensors, wireless sensor networks and other applications where size and portability are critical.[96]

Among the different types of III-V NWs, GaN NWs is one of the most studied SGSs materials which have shown sensitivity towards both oxidation (e.g. NO_2, SO_2) and

reduction gases (e.g. H_2, methanol).[97] Surface-functionalisation method with materials including metal oxides, noble metal nanoparticles and carbon materials has been applied to enhance sensitivity to target analytes.[98] UV illumination has been shown to be able to decrease the operation temperature of several types of sensors, although it poses hazards to human health.[99] In addition to group III-nitrides NWs, InAs NWs have also been studied for sensing NO_2 and ethanol in both single and array NW device configurations. However, they showed a detection limit higher than 0.1 ppm, long response and recovery times (> 600 s) and recovery issue (baseline drifting).[100] On the other hand, the DFT study indicates that the NO_2 molecules are more competitive in adsorbing on InP surface with higher adsorption energy, which could facilitate the selectivity.[101] Such that, core-shell InAs/InP NW sensors with InP shell as passivation layer exhibited a higher sensitivity (detection range: 50 - 1000 ppb) under a decreased operation temperature 50 °C comparing with bare InAs NWs.[89] Furthermore, it has been reported that InP epitaxial layer could achieve ~0.1 ppm level sensitivity to NO_2 at relatively lower working temperature (80-150 ˚C) indicating their potential for room-temperature NO_2 sensing.[102] Considering the superior air stability, NO_2 adsorption capability, low operation temperature and mature fabrication techniques, InP NWs appear to be one of the best candidates for gas sensors, however there are very few reports of InP NWs as gas sensors.

In fact, research on III-V NW based SGSs is still at an early stage, offering ample opportunities to explore new material and device designs based on different sensing mechanisms. In this thesis, we investigate InP nanowire array based gas sensors and our research strategies on sensor device design and performance optimisation include:

- Nanowire doping: introducing dopants into III-V NWs can tune the charge carrier concentration, bandgap, or surface reactivity of the NWs, thereby influencing their

gas response characteristics.[103] The p-n junction formed by doping NWs could generate photovoltaic effect leading to the self-powered operation capability.[91]

- Nanowire diameter and pitch design and optimisation: NW size, geometry and configuration can significantly affect gas sensing performance due to their tunability to the surface-to-volume ratio and electrical property of NW.[104]
- Junction formation: owing to the well-established materials growth and processing techniques, high quality Schottky junction, heterojunction, homojunction, with well-defined interfaces, thicknesses, and compositions can be easily implemented in NW structures.[65] With a tuneable depletion layer and photovoltaic effect, proper junction design could enable high sensitivity and self-powered gas sensing capability.
- Surface-functionalisation: functionalising the sensing surface with specific chemical functional groups or molecules that have strong affinity with the target gases could greatly enhance the cross-sensitivity and selectivity. New functionalisation materials including 2D materials,[105] polymers,[106] metal oxides,[107] or organic compounds,[108] have been reported to increase chemical reactivity and thus enhance the sensor selectivity of the target gas.[87, 109] By incorporating different functional groups for each target gas, a single sensor material may be able to be fabricated into different sensor units to detect different to achieve multiplexed gas sensing functionality. Surface-functionalisation normally involves the deposition of thin films or coatings of the reagents onto the sensing surface to create specific chemical interactions using techniques such as spin-coating or thermal evaporation.

1.4 Aim and scope

This thesis is focused on the development and investigation of NO_2 and acetone gas sensors for environment and health monitoring based on InP NWs. NO_2 exhausted in air

has raised serious concerns due to the irreversible damage it causes to human health and various ecosystems.[60] Reactions of NO_2 with water, oxygen and other chemicals in the atmosphere can lead to acid rain which is hazardous to the sensitive ecosystems and the formation of photochemical smog that may cause eye and lung damage,[110] highlighting the necessity for real-time monitoring at low concentration (100 ppb). On the other hand, for diabetes diagnostic and monitoring, the finger-prick test using ketone strips is the most common method currently used in medical treatment, however their invasive nature contributes to low levels of compliance, especially in children and younger individuals.[111] In the meanwhile, it has been found that acetone concentrations in human breath exhibit a direct correlation with blood ketone levels making it an ideal non-invasive biomarker for diabetes detection in future point-of-care and self-use diagnostic tools.[112] It also emphasizes the significance of the study on high performance acetone sensor for breath testing application.

In this thesis, we report the investigation of InP NW arrays as a new SGS platform for potential environmental and health monitoring applications. We demonstrate new NO_2 and acetone gas sensor design, based on the strategies of NW structure/device design, surface-functionalisation and pixels array construction. At first, the NW geometrical effect, namely, the diameter and density, is studied and tailored for optimum sensitivity to NO_2. Secondly, p-n and Schottky junctions were introduce to the NWs to demonstrate sensing performance enhancement and photovoltaic (PV) based self-powered operation for NO_2 and acetone sensing, respectively. Thirdly, an effective surface-functionalisation approach was developed which achieved excellent sensitivity for acetone sensing. Finally, multi-pixel NW array sensors were constructed for cross-sensitivity enhancement and multi-analytes sensing. Based on these strategies, high-performance prototype NO_2 and acetone sensors have been developed and tested in real-world environments to reveal their

great potential for practical applications.

1.5 Thesis outline

After this introductory chapter, a general review of III-V NWs based SGSs is presented in Chapter 2. This includes the basic concepts, background knowledge, material properties of InP NWs. Then, in Chapter 3, the experimental techniques employed in the thesis are introduced including both top-down and bottom-up approaches for InP NW array growth/fabrication, material characterization, device fabrication, and device testing techniques.

In Chapter 4, vertical InP NW array were fabricated by top-down etching method for NO_2 sensing.[60] A novel tilt-angle deposition based NW array sensor device fabrication method has been developed for the first time. The effect of the array geometry, including NW diameter and pitch size on the chemical sensing performance, was investigated to optimise the device design. Selectivity and air stability were also characterised to determine the reliability of these NW sensors. An analytical model was built for binding affinity kinetics analysis, combined with electrical simulation to gain a comprehensive understanding of the gas sensing mechanism in the NWs.

In Chapter 5, a novel PV self-powered NO_2 sensors were demonstrated based on bottom-up growth axial p–i–n homojunction InP NW arrays to further improve the sensing performance.[101] An InP NW array photovoltaic sensor device was designed and optimised by numerical simulation for insights into sensing mechanisms and performance enhancement. Without a power source, the InP NW sensors achieve an 84% sensing response to 1 ppm NO_2 and record a limit of detection down to the sub-ppb level.[110]

The sensor was integrated into a commercial microchip interface to evaluate its performance in the context of dynamic environmental monitoring of motor vehicle exhaust. The results show that InP NW arrays can form promising self-powered sensing platforms with ultrahigh sensitivity, suitable for IoT systems.

In Chapter 6, InP/Pt/chitosan NWs arrays were designed and fabricated for acetone sensing application. By incorporating chitosan as a surface-functional layer and a Pt Schottky contact for efficient charge transfer processes and photovoltaic effect, self-powered, highly selective acetone sensing has been achieved.[111] The sensors exhibit an ultra-wide acetone detection range from sub-ppb to >100,000 ppm level at room temperature, covering those in the exhaled breath from healthy individuals (300-800 ppb) to people at high-risk of DKA (> 75 ppm). The NW sensors were also successfully integrated into a handheld breath testing prototype, the 'Ketowhistle', which can successfully detect different ranges of acetone concentrations in simulated breath and provides an immediate potential for non-invasive ketone monitoring for people living with diabetes, in particular for DKA prevention.

In Chapter 7, InP NWs array with various diameters were grown as different pixels on the same substrate using bottom-up approach to achieve multiple sensor functions.[112] An innovative fabrication method was introduced for vertically assembling and transferring the NWs array to a flexible substrate.[113] A signal decoupling strategy was designed based on the fabrication optimisation, surface-functionalisation and electrode contacting metals, with the aim of maximising the functionality of each array element for body temperature, pulse, NO_2 and acetone sensing. This work provides a new material platform with a signal decoupling feature and processing pathway towards the

development of wearable devices with a more comprehensive healthcare monitoring setup capable of simultaneous detection of both physical and chemical stimuli.

Finally, Chapter 8 summarises the main results and findings of this thesis and proposes future work on the promising research directions for further development of InP and other III-V nanomaterials based sensors. Future development targets on broadening detectable analytes while achieving high sensing performance and power/cost-effectiveness, for applications in future smart home, IoT and healthcare systems.

References

[1] R. Paul, B. Das and R. Ghosh, Novel approaches towards design of metal oxide based hetero-structures for room temperature gas sensor and its sensing mechanism: A recent progress. *Journal of Alloys and Compounds*, **941**, 168943 (2023).

[2] S. R. Sriram, S. R. Parne, N. Pothukanuri and D. R. Edla, Prospects of spray pyrolysis technique for gas sensor applications – A comprehensive review. *Journal of Analytical and Applied Pyrolysis*, **164**, 105527 (2022).

[3] F. J. Kelly and J. C. Fussell, Air pollution and airway disease. *Clinical and Experimental Allergy*, **41**, 1059-1071 (2011).

[4] X. H. Chen, M. Leishman, D. Bagnall and N. Nasiri, Nanostructured Gas Sensors: From Air Quality and Environmental Monitoring to Healthcare and Medical Applications. *Nanomaterials*, **11**, 5910-5932 (2021).

[5] M. Javaid, A. Haleem, S. Rab, R. Pratap Singh and R. Suman, Sensors for daily life: A review. *Sensors International*, **2**, 100121 (2021).

[6] M. Ahmadipour, A. L. Pang, M. R. Ardani, S.-Y. Pung, P. C. Ooi, A. A. Hamzah, M. F. Mohd Razip Wee, M. Aniq Shazni Mohammad Haniff, C. F. Dee, E. Mahmoudi, A. Arsad, M. Z. Ahmad, U. Pal, K. M. Chahrour and S. A. Haddadi, Detection of breath acetone by semiconductor metal oxide nanostructures-based gas sensors: A review. *Materials Science in Semiconductor Processing*, **149**, 106897 (2022).

[7] S. Dhall, B. R. Mehta, A. K. Tyagi and K. Sood, A review on environmental gas sensors: Materials and technologies. *Sensors International*, **2**, 100116 (2021).

[8] P. Achakulwisut, M. Brauer, P. Hystad and S. C. Anenberg, Global, national, and urban burdens of paediatric asthma incidence attributable to ambient NO_2 pollution: estimates from global datasets. *The Lancet Planetary Health*, **3**, e166-e178 (2019).

[9] W. U. Anake and E. A. Nnamani, Indoor air quality in day-care centres: a global review. *Air Quality Atmosphere and Health*, **16**, 997-1022 (2023).

[10] P. Saxena and P. Shukla, A review on recent developments and advances in environmental gas sensors to monitor toxic gas pollutants. *Environmental Progress & Sustainable Energy*, **56**, 14126 (2023).

[11] K. Liu and C. Zhang, Volatile organic compounds gas sensor based on quartz crystal microbalance for fruit freshness detection: A review. *Food Chemistry*, **334**, 127615 (2021).

[12] Amann, L. Costello Bde, W. Miekisch, J. Schubert, B. Buszewski, J. Pleil, N. Ratcliffe and T. Risby, The human volatilome: volatile organic compounds (VOCs) in exhaled breath, skin emanations, urine, feces and saliva. *J Breath Res*, **8**, 034001 (2014).

[13] R. A. B. John and A. Ruban Kumar, A review on resistive-based gas sensors for the detection of volatile organic compounds using metal-oxide nanostructures. *Inorganic Chemistry Communications*, **133**, 108893 (2021).

[14] S. Matindoust, G. Farzi, M. B. Nejad and M. H. Shahrokhabadi, Polymer-based gas sensors to detect meat spoilage: A review. *Reactive and Functional Polymers*, **165**, 104962 (2021).

[15] D. E. Williams, Electrochemical sensors for environmental gas analysis. *Current Opinion in Electrochemistry*, **22**, 145-153 (2020).

[16] C.-O. Park, J. Fergus, N. Miura, J. Park and A. Choi, Solid-state electrochemical gas sensors. *Ionics*, **15**, 261-284 (2009).

[17] J. W. Fergus, Materials for high temperature electrochemical NO_x gas sensors. *Sensors and Actuators B: Chemical*, **121**, 652-663 (2007).

[18] E. A. Symons, in *Gas Sensors: Principles, Operation and Developments*, (Ed: G. Sberveglieri), Springer Netherlands, Dordrecht **1992**, p. 169-185.

[19] Y. Tang, Y. Zhao and H. Liu, Room-Temperature Semiconductor Gas Sensors: Challenges and Opportunities. *Acs Sensors*, **7**, 3582-3597 (2022).

[20] P. Raju and Q. Li, Review—Semiconductor Materials and Devices for Gas Sensors. *Journal of the Electrochemical Society*, **169**, 057518 (2022).

[21] E. Stauffer, J. A. Dolan and R. Newman, in *Fire Debris Analysis*, (Eds: E. Stauffer, J. A. Dolan and R. Newman), Academic Press, Burlington **2008**, p. 131-161.

[22] C. F. Poole, Ionization-based detectors for gas chromatography. *Journal of Chromatography A*, **1421**, 137-153 (2015).

[23] T.-V. Dinh, I.-Y. Choi, Y.-S. Son and J.-C. Kim, A review on non-dispersive infrared gas sensors: Improvement of sensor detection limit and interference correction. *Sensors and Actuators B: Chemical*, **231**, 529-538 (2016).

[24] D. Popa and F. Udrea, Towards integrated mid-infrared gas sensors. *Sensors*, **19**, 2076 (2019).

[25] S. Tabassum, S. Nayemuzzaman, M. Kala, A. Kumar Mishra and S. K. Mishra, Metasurfaces for Sensing Applications: Gas, Bio and Chemical. *Sensors*, **22**, 6896 (2022).

[26] D. R. Smith, J. B. Pendry and M. C. Wiltshire, Metamaterials and negative refractive index. *science*, **305**, 788-792 (2004).

[27] Alipour, A. Farmani and A. Mir, High sensitivity and tunable nanoscale sensor based on plasmon-induced transparency in plasmonic metasurface. *Ieee Sensors Journal*, **18**, 7047-7054 (2018).

[28] Lochbaum, A. Dorodnyy, U. Koch, S. M. Koepfli, S. Volk, Y. Fedoryshyn, V. Wood and J. Leuthold, Compact mid-infrared gas sensing enabled by an all-metamaterial design. *Nano Letters*, **20**, 4169-4176 (2020).

[29] P. T. Moseley, Solid state gas sensors. *Measurement Science and technology*, **8**, 223 (1997).

[30] Y. Nemirovsky, S. Stolyarova, T. Blank, S. Bar-Lev, A. Svetlitza, A. Zviagintsev and I. Brouk, A new pellistor-like gas sensor based on micromachined CMOS transistor. *IEEE Transactions on Electron Devices*, **65**, 5494-5498 (2018).

[31] S. M. Majhi, A. Mirzaei, H. W. Kim, S. S. Kim and T. W. Kim, Recent advances in energy-saving chemiresistive gas sensors: A review. *Nano Energy*, **79**, 105369 (2021).

[32] K. Sharma and A. Mahajan, in *Carbon Nanomaterials and their Nanocomposite-Based Chemiresistive Gas Sensors*, (Ed: S. Dhall), Elsevier **2023**, p. 223-245.

[33] V. R. Naganaboina and S. G. Singh, Chemiresistive gas sensors: From novel gas-sensing materials to electrode structure. *Chemical Physics Reviews*, **4**, 021306 (2023).

[34] J. Lin, M. Kilani and G. Mao, Recent Advances in Integrating 1D Nanomaterials into Chemiresistive Gas Sensor Devices. *Advanced Materials Technologies*, **8**, 2202038 (2023).

[35] T. John, K. Murugappan, D. R. Nisbet and A. Tricoli, An Outlook of Recent Advances in Chemiresistive Sensor-Based Electronic Nose Systems for Food Quality and Environmental Monitoring. *Sensors (Basel)*, **21**, 2271 (2021).

[36] M. V. Nikolic, V. Milovanovic, Z. Z. Vasiljevic and Z. Stamenkovic, Semiconductor Gas Sensors: Materials, Technology, Design, and Application. *Sensors (Basel)*, **20**, 6694 (2020).

[37] Schütze, T. Baur, M. Leidinger, W. Reimringer, R. Jung, T. Conrad and T. Sauerwald, Highly sensitive and selective VOC sensor systems based on semiconductor gas sensors: how to? *Environments*, **4**, 20 (2017).

[38] D. Wang, J. Pan, X. Huang, J. Chu, H. Yuan, A. Yang, N. Koratkar, X. Wang and M. Rong, Virtual alternating current measurements advance semiconductor gas sensors' performance in the internet of things. *IEEE Internet of Things Journal*, **9**, 5502-5510 (2021).

[39] S. Das, S. Mojumder, D. Saha and M. Pal, Influence of major parameters on the sensing mechanism of semiconductor metal oxide based chemiresistive gas sensors: A review focused on personalized healthcare. *Sensors and Actuators B: Chemical*, **352**, 131066 (2022).

[40] H. Zhai, Z. Wu and Z. Fang, Recent progress of Ga2O3-based gas sensors. *Ceramics International*, **48**, 24213-24233 (2022).

[41] L. Kong, Z. Yuan, H. Gao and F. Meng, Recent progress of gas sensors based on metal oxide composites derived from bimetallic metal-organic frameworks. *TrAC Trends in Analytical Chemistry*, **166**, 117199 (2023).

[42] D. Lun and K. Xu, Recent Progress in Gas Sensor Based on Nanomaterials. *Micromachines (Basel)*, **13**, 919 (2022).

[43] R. Sadri, M. Hosseini, S. N. Kazi, S. Bagheri, A. H. Abdelrazek, G. Ahmadi, N. Zubir, R. Ahmad and N. I. Z. Abidin, A facile, bio-based, novel approach for synthesis of covalently functionalized graphene nanoplatelet nano-coolants toward improved thermo-physical and heat transfer properties. *Journal of Colloid and Interface Science*, **509**, 140-152 (2018).

[44] M. Portela, A. Vidyasagar, S. Krödel, T. Weissenbach, D. W. Yee, J. R. Greer and D. M. Kochmann, Extreme mechanical resilience of self-assembled nanolabyrinthine materials. *Proceedings of the National Academy of Sciences*, **117**, 5686-5693 (2020).

[45] T. T. Zhou and T. Zhang, Recent Progress of Nanostructured Sensing Materials from 0D to 3D: Overview of Structure-Property-Application Relationship for Gas Sensors. *Small Methods*, **5**, 2100515 (2021).

[46] V. Galstyan, A. Moumen, G. W. C. Kumarage and E. Comini, Progress towards chemical gas sensors: Nanowires and 2D semiconductors. *Sensors and Actuators B: Chemical*, **357**, 131466 (2022).

[47] N. Wongkaew, M. Simsek, C. Griesche and A. J. Baeumner, Functional Nanomaterials and Nanostructures Enhancing Electrochemical Biosensors and Lab-on-a-Chip Performances: Recent Progress, Applications, and Future Perspective. *Chemical Reviews*, **119**, 120-194 (2019).

[48] E. Barrigon, M. Heurlin, Z. X. Bi, B. Monemar and L. Samuelson, Synthesis and Applications of III-V Nanowires. *Chemical Reviews*, **119**, 9170-9220 (2019).

[49] H. M. Fahad, H. Shiraki, M. Amani, C. C. Zhang, V. S. Hebbar, W. Gao, H. Ota, M. Hettick, D. Kiriya, Y. Z. Chen, Y. L. Chueh and A. Javey, Room temperature multiplexed gas sensing using chemical-sensitive 3.5-nm-thin silicon transistors. *Science Advances*, **3**, 8 (2017).

[50] G. Niu and F. Wang, A review of MEMS-based metal oxide semiconductors gas sensor in Mainland China. *Journal of Micromechanics and Microengineering*, **32**, 054003 (2022).

[51] Z. Chen, Z. Chen, Z. Song, W. Ye and Z. Fan, Smart gas sensor arrays powered by artificial intelligence. *Journal of Semiconductors*, **40**, 111601 (2019).

[52] W. W. Wu and H. Haick, Materials and Wearable Devices for Autonomous Monitoring of Physiological Markers. *Advanced Materials*, **30**, 17 (2018).

[53] Y. J. Su, J. J. Wang, B. Wang, T. N. Yang, B. X. Yang, G. Z. Xie, Y. H. Zhou, S. L. Zhang, H. L. Tai, Z. X. Cai, G. R. Chen, Y. D. Jiang, L. Q. Chen and J. Chen, Alveolus-Inspired Active Membrane Sensors for Self-Powered Wearable Chemical Sensing and Breath Analysis. *Acs Nano*, **14**, 6067-6075 (2020).

[54] T. C. Nguyen, M. Schwartz, X. T. Vu, J. Blinn and S. Ingebrandt, Handheld readout system for field-effect transistor biosensor arrays for label-free detection of biomolecules. *Physica Status Solidi a-Applications and Materials Science*, **212**, 1313-1319 (2015).

[55] Ossai and N. Raghavan, Nanostructure and nanomaterial characterization, growth mechanisms, and applications. *Nanotechnology Reviews*, **7**, 209-231 (2018).

[56] S. D. Lawaniya, S. Kumar, Y. Yu, H.-G. Rubahn, Y. K. Mishra and K. Awasthi, Functional nanomaterials in flexible gas sensors: recent progress and future prospects. *Materials Today Chemistry*, **29**, 101428 (2023).

[57] V. Galstyan, "Quantum dots: Perspectives in next-generation chemical gas sensors" – A review. *Analytica Chimica Acta*, **1152**, 238192 (2021).

[58] Salvini, M. Re Fiorentin, F. Risplendi, F. Raffone and G. Cicero, Active Surface Structure of SnO_2 Catalysts for CO_2 Reduction Revealed by Ab Initio Simulations. *The Journal of Physical Chemistry C*, **126**, 14441-14447 (2022).

[59] Y. Liu, Z. Zhao, Y. Zhang, L. Zhou, X. Qin, Z. Zhao, H. Ji and K. Chai, Integration of multi-affinity sites into confined channels allows a bismuth-based metal-organic framework to sequestrate multi-component impurities from methane. *Microporous and Mesoporous Materials*, **354**, 112530 (2023).

[60] J. Cao, Q. Chen, X. Wang, Q. Zhang, H. D. Yu, X. Huang and W. Huang, Recent Development of Gas Sensing Platforms Based on 2D Atomic Crystals. *Research (Wash D C)*, **2021**, 9863038 (2021).

[61] S.-Y. Cho, S. J. Kim, Y. Lee, J.-S. Kim, W.-B. Jung, H.-W. Yoo, J. Kim and H.-T. Jung, Highly enhanced gas adsorption properties in vertically aligned MoS_2 layers. *Acs Nano*, **9**, 9314-9321 (2015).

[62] Meng, H. Zheng, Y. Sun, M. Li and J. Liu, Trimethylamine sensors based on Au-modified hierarchical porous single-crystalline ZnO nanosheets. *Sensors*, **17**, 1478 (2017).

[63] Z. Yuan, R. Li, F. Meng, J. Zhang, K. Zuo and E. Han, Approaches to Enhancing Gas Sensing Properties: A Review. *Sensors (Basel)*, **19**, 1946 (2019).

[64] M. W. Hoffmann, L. Mayrhofer, O. Casals, L. Caccamo, F. Hernandez‐Ramirez, G. Lilienkamp, W. Daum, M. Moseler, A. Waag and H. Shen, A highly selective and self‐powered gas sensor via organic surface functionalization of p‐Si/n‐ZnO diodes. *Advanced Materials*, **26**, 8017-8022 (2014).

[65] J. Walker, P. Karnati, S. A. Akbar and P. A. Morris, Selectivity mechanisms in resistive-type metal oxide heterostructural gas sensors. *Sensors and Actuators B: Chemical*, **355**, 131242 (2022).

[66] M. Bai, H. Huang, Z. Liu, T. T. Zhan, S. F. Xia, X. G. Li, N. Sibirev, A. Bouravleuv, V. G. Dubrovskii and G. Cirlin, InAs/InP core/shell nanowire gas sensor: Effects of InP shell on sensitivity and long-term stability. *Applied Surface Science*, **498**, 143756 (2019).

[67] J. Gong, Y. Li, Z. Hu, Z. Zhou and Y. Deng, Ultrasensitive NH_3 gas sensor from polyaniline nanograin enchased TiO2 fibers. *The Journal of Physical Chemistry C*, **114**, 9970-9974 (2010).

[68] T. Hamada and M. Sugiyama, Fabrication of solar cells with CO_2 gas sensing capabilities based on a NiO/ZnO p-n junction for developing self-powered gas sensors. *Japanese Journal of Applied Physics*, **61**, 054022 (2022).

[69] X. L. Liu, Y. Zhao, W. J. Wang, S. X. Ma, X. J. Ning, L. Zhao and J. Zhuang, Photovoltaic Self-Powered Gas Sensing: A Review. *Ieee Sensors Journal*, **21**, 5628-5644 (2021).

[70] J.-W. Han, T. Rim, C.-K. Baek and M. Meyyappan, Chemical Gated Field Effect Transistor by Hybrid Integration of One-Dimensional Silicon Nanowire and Two-Dimensional Tin

Oxide Thin Film for Low Power Gas Sensor. *Acs Applied Materials & Interfaces*, **7**, 21263-21269 (2015).

[71] Hui, M. Zhu, X. Yang, J. Liu, G. Pan and Z. Wang, Highly sensitive ethanol gas sensor based on CeO_2/ZnO binary heterojunction composite. *Materials Letters*, **278**, 128453 (2020).

[72] J. M. Suh, Y.-S. Shim, K. C. Kwon, J.-M. Jeon, T. H. Lee, M. Shokouhimehr and H. W. Jang, Pd- and Au-Decorated MoS_2 Gas Sensors for Enhanced Selectivity. *Electronic Materials Letters*, **15**, 368-376 (2019).

[73] M. Mariello, K. Kim, K. Wu, S. Lacour and Y. Leterrier, Recent Advances in Encapsulation of Flexible Bioelectronic Implants: Materials, Technologies, and Characterization Methods. *Advanced Materials*, **34**, 2201129 (2022).

[74] C. A. Betty, S. Choudhury and K. G. Girija, Reliability studies of highly sensitive and specific multi-gas sensor based on nanocrystalline SnO_2 film. *Sensors and Actuators B: Chemical*, **193**, 484-491 (2014).

[75] S. Russell, L. B. Frederickson, S. Kwiatkowski, A. P. M. Emygdio, P. Kumar, J. A. Schmidt, O. Hertel and M. S. Johnson, Enhanced Ambient Sensing Environment— A New Method for Calibrating Low-Cost Gas Sensors. *Sensors*, **22**, 7238 (2022).

[76] T. Baur, J. Amann, C. Schultealbert and A. Schütze, Field Study of Metal Oxide Semiconductor Gas Sensors in Temperature Cycled Operation for Selective VOC Monitoring in Indoor Air. *Atmosphere*, **12**, 647 (2021).

[77] Dey, Semiconductor metal oxide gas sensors: A review. *Materials Science and Engineering: B*, **229**, 206-217 (2018).

[78] X. Chen, M. Leishman, D. Bagnall and N. Nasiri, Nanostructured gas sensors: From air quality and environmental monitoring to healthcare and medical applications. *Nanomaterials*, **11**, 1927 (2021).

[79] J. Kneer, A. Eberhardt, P. Walden, A. Ortiz Pérez, J. Wöllenstein and S. Palzer, Apparatus to characterize gas sensor response under real-world conditions in the lab. *Review of Scientific Instruments*, **85**, 055006 (2014).

[80] J. Li, H. Yan, H. Dang and F. Meng, Structure design and application of hollow core microstructured optical fiber gas sensor: A review. *Optics & Laser Technology*, **135**, 106658 (2021).

[81] S. M. Majhi, A. Mirzaei, H. W. Kim, S. S. Kim and T. W. Kim, Recent advances in energy-saving chemiresistive gas sensors: A review. *Nano Energy*, **79**, 105369 (2021).

[82] S. A. Zakaria, S. H. Ahmadi and M. H. Amini, Chemiresistive gas sensors based on layered double hydroxides (LDHs) structures: A review. *Sensors and Actuators A: Physical*, **346**, 113827 (2022).

[83] M. Reddeppa, S. B. Mitta, T. Chandrakalavathi, B. G. Park, G. Murali, R. Jeyalakshmi, S. G. Kim, S. H. Park and M. D. Kim, Solution-processed Au@rGO/GaN nanorods hybrid-

structure for self-powered UV, visible photodetector and CO gas sensors. *Current Applied Physics*, **19**, 938-945 (2019).

[84] T. Pham, G. Li, E. Bekyarova, M. E. Itkis and A. Mulchandani, MoS_2-Based Optoelectronic Gas Sensor with Sub-parts-per-billion Limit of NO_2 Gas Detection. *Acs Nano*, **13**, 3196-3205 (2019).

[85] Rydosz, Sensors for Enhanced Detection of Acetone as a Potential Tool for Noninvasive Diabetes Monitoring. *Sensors*, **18**, 2298 (2018).

[86] Wang, G. J. Fan, Z. X. Yang, N. Han, Y. F. Chen and J. Yang, Low-Temperature As-Doped In2O3 Nanowires for Room Temperature NO_2 Gas Sensing. *Acs Applied Nano Materials*, **5**, 7983-7992 (2022).

[87] D. N. Zhao, H. Huang, S. J. Chen, Z. R. Li, S. D. Li, M. Y. Wang, H. C. Zhu and X. M. Chen, In Situ Growth of Leakage-Free Direct-Bridging GaN Nanowires: Application to Gas Sensors for Long-Term Stability, Low Power Consumption, and Sub-ppb Detection Limit. *Nano Letters*, **19**, 3448-3456 (2019).

[88] M. Reddeppa, B. G. Park, N. D. Chinh, D. Kim, J. E. Oh, T. G. Kim and M. D. Kim, A novel low-temperature resistive NO gas sensor based on InGaN/GaN multi-quantum well-embedded p-i-n GaN nanorods. *Dalton Transactions*, **48**, 1367-1375 (2019).

[89] E. Barrigón, M. Heurlin, Z. Bi, B. Monemar and L. Samuelson, Synthesis and Applications of III–V Nanowires. *Chemical Reviews*, **119**, 9170-9220 (2019).

[90] F. Geisz, R. M. France, K. L. Schulte, M. A. Steiner, A. G. Norman, H. L. Guthrey, M. R. Young, T. Song and T. Moriarty, Six-junction III-V solar cells with 47.1% conversion efficiency under 143 Suns concentration. *Nature Energy*, **5**, 326 (2020).

[91] D. Liang, J. Du and X. P. A. Gao, InAs Nanowire Devices with Strong Gate Tunability: Fundamental Electron Transport Properties and Application Prospects: A Review. *Journal of Materials Science & Technology*, **31**, 542-555 (2015).

[92] P. Offermans, M. Crego-Calama and S. H. Brongersma, Gas Detection with Vertical InAs Nanowire Arrays. *Nano Letters*, **10**, 2412-2415 (2010).

[93] M. A. Garcia, M. Losurdo, S. D. Wolter, W. V. Lampert, J. Bonaventura, G. Bruno, C. Yi and A. S. Brown, Comparison of Functionalized III-V Semiconductor Response for Nitric Oxide. *Sensor Letters*, **6**, 627-634 (2008).

[94] W. C. Yi, X. Chen, Z. X. Wang, Y. C. Ding, B. C. Yang and X. B. Liu, A novel two-dimensional delta-InP_3 monolayer with high stability, tunable bandgap, high carrier mobility, and gas sensing of NO_2. *Journal of Materials Chemistry C*, **7**, 7352-7359 (2019).

[95] M. A. H. Khan and M. V. Rao, Gallium Nitride (GaN) Nanostructures and Their Gas Sensing Properties: A Review. *Sensors*, **20**, 3889 (2020).

[96] G. D. Sun, P. Zhao, W. X. Zhang, H. Li and C. He, Adsorption of gas molecules on armchair AlN nanoribbons with a dangling bond defect by using density functional theory. *Materials Chemistry and Physics*, **186**, 305-311 (2017).

[97] Q. N. Abdullah, A. R. Ahmed, A. M. Ali, F. K. Yam, Z. Hassan, M. Bououdina and M. A. Almessiere, Growth and characterization of GaN nanostructures under various ammoniating time with fabricated Schottky gas sensor based on Si substrate. *Superlattices and Microstructures*, **117**, 92-104 (2018).

[98] B. M. Ming, Z. L. Zheng, C. H. Wang, G. C. Guo, B. R. Wang, H. Yan and R. Z. Wang, Enhancement mechanism of H-2 sensing in metal-functionalized GaN nanowires. *Applied Surface Science*, **486**, 212-218 (2019).

[99] M. Z. Peng, X. H. Zheng, Z. G. Ma, H. Chen, S. J. Liu, Y. F. He and M. L. Li, Ni-pattern guided GaN nanowire-array humidity sensor with high sensitivity enhanced by UV photoexcitation. *Sensors and Actuators B-Chemical*, **256**, 367-373 (2018).

[100] Du, D. Liang, H. Tang and X. P. A. Gao, InAs Nanowire Transistors as Gas Sensor and the Response Mechanism. *Nano Letters*, **9**, 4348-4351 (2009).

[101] S. Wei, Z. Li, K. Murugappan, Z. Li, F. Zhang, A. G. Saraswathyvilasam, M. Lysevych, H. H. Tan, C. Jagadish, A. Tricoli and L. Fu, A Self-Powered Portable Nanowire Array Gas Sensor for Dynamic NO_2 Monitoring at Room Temperature. *Advanced Materials*, **35**, 2207199 (2023).

[102] V. Battut, J. P. Blanc, E. Goumet, V. Soulière and Y. Monteil, NO_2 sensor based on InP epitaxial thin layers. *Thin Solid Films*, **348**, 266-272 (1999).

[103] M. A. H. Khan, B. Thomson, A. Motayed, Q. L. Li and M. V. Rao, Functionalization of GaN Nanowire Sensors With Metal Oxides: An Experimental and DFT Investigation. *Ieee Sensors Journal*, **20**, 7138-7147 (2020).

[104] H. Du, H. Wang, P. Yao, J. Wang and Y. Sun, In_2O_3 nanofibers surface modified by low-temperature RF plasma and their gas sensing properties. *Materials Chemistry and Physics*, **215**, 316-326 (2018).

[105] M. Reddeppa, B. G. Park, M. D. Kim, K. R. Peta, N. D. Chinh, D. Kim, S. G. Kim and G. Murali, H-2, H_2S gas sensing properties of rGO/GaN nanorods at room temperature: Effect of UV illumination. *Sensors and Actuators B-Chemical*, **264**, 353-362 (2018).

[106] D. Ohayon, G. Nikiforidis, A. Savva, A. Giugni, S. Wustoni, T. Palanisamy, X. X. Chen, I. P. Maria, E. Di Fabrizio, P. Costa, I. McCulloch and S. Inal, Biofuel powered glucose detection in bodily fluids with an n-type conjugated polymer. *Nature Materials*, **19**, 456 (2020).

[107] M. A. H. Khan, B. Thomson, J. Yu, R. Debnath, A. Motayed and M. V. Rao, Scalable metal oxide functionalized GaN nanowire for precise SO_2 detection. *Sensors and Actuators B-Chemical*, **318**, 128223 (2020).

[108] M. W. G. Hoffmann, L. Mayrhofer, O. Casals, L. Caccamo, F. Hernandez-Ramirez, G. Lilienkamp, W. Daum, M. Moseler, A. Waag, H. Shen and J. D. Prades, A Highly Selective and Self-Powered Gas Sensor Via Organic Surface Functionalization of p-Si/n-ZnO Diodes. *Advanced Materials*, **26**, 8017-8022 (2014).

[109] M. Shafa, S. A. Aravindh, M. N. Hedhili, S. T. Mahmoud, Y. Pan, T. K. Ng, B. S. Ooi and A. Najar, Improved H-2 detection performance of GaN sensor with Pt/Sulfide treatment of porous active layer prepared by metal electroless etching. *International Journal of Hydrogen Energy*, **46**, 4614-4625 (2021).

[110] Q. Gao, Z. Y. Li, L. Li, K. Vora, Z. Li, A. Alabadla, F. Wang, Y. A. Guo, K. Peng, Y. C. Wenas, S. Mokkapati, F. Karouta, H. H. Tan, C. Jagadish and L. Fu, Axial p-n junction design and characterization for InP nanowire array solar cells. *Progress in Photovoltaics*, **27**, 237-244 (2019).

[111] H.-I. Chen, Y.-I. Chou and C.-Y. Chu, A novel high-sensitive Pd/InP hydrogen sensor fabricated by electroless plating. *Sensors and Actuators B: Chemical*, **85**, 10-18 (2002).

[112] Q. Gao, D. Saxena, F. Wang, L. Fu, S. Mokkapati, Y. A. Guo, L. Li, J. Wong-Leung, P. Caroff, H. H. Tan and C. Jagadish, Selective-Area Epitaxy of Pure Wurtzite InP Nanowires: High Quantum Efficiency and Room-Temperature Lasing. *Nano Letters*, **14**, 5206-5211 (2014).

[113] S. Pouladi, M. Rathi, D. Khatiwada, M. Asadirad, S. K. Oh, P. Dutta, Y. Yao, Y. Gao, S. C. Sun, Y. K. Li, S. Shervin, K. H. Lee, V. Selvamanickam and J. H. Ryou, High-efficiency flexible III-V photovoltaic solar cells based on single-crystal-like thin films directly grown on metallic tapes. *Progress in Photovoltaics*, **27**, 30-36 (2019).

Chapter 2. Background

This chapter begin with the introduction of background knowledge of III-V nanowire (NW) based semiconductor gas sensors (SGSs), including the sensing mechanisms and key parameters for assessment of gas sensing performance. Then, it provides a literature review on the research progress and existing challenges of III-V NW based SGSs in recent years. Subsequently, this chapter discusses the material properties of InP NWs, and particularly their potential to overcome the existing challenges in SGSs research to achieve high gas sensing performance. Lastly, the surface functionalisation method for gas sensing performance enhancement is presented.

2.1 Background

2.1.1 Categories of semiconductor gas sensors

In general, based on device structure, the categories of SGSs include resistors (chemiresistive sensor), Schottky diode, and field-effect transistor (FET) sensors. For chemiresistive SGSs, the fundamental mechanism is the change of electrical conductivity of the sensor material as it interacts with the gas molecules by extract or donate electrons from the adsorbed molecules to the active layer. As a result, the sensor current/resistance is modulated in proportion to the analyte concentration.[1] For other types of devices such as FET, other electric parameters could also be modulated, such as mobility, threshold voltage, etc.[2]

In this thesis, we focus on chemiresistive SGSs that are normally based on metal oxides, two-dimensional (2D) materials, etc., due to their simple device configuration and low

power consumption comparing to other types of sensors. The detailed sensing mechanism varies depending on the sensing materials. For metal oxides, the gas sensing process involves the chemisorption of O_2, resulting from the oxygen vacancy on surface[3] to form oxygen ions species (i.e. O_2^-, O^-, O^{2-}), that will subsequently react with gas molecules on metal oxides surface. The reaction normally leads to trapping or donating electrons to the metal oxides and thus a change of the conductance. For 2D materials such as graphene[4] and transition metal dichalcogenides (TMDs), the sensing process arises from physisorption (through van der Waals interaction or hydrogen bonding) or chemisorption of gas molecules, resulting in the changes of carrier concentration and resistivity.[5] During chemisorption, transfer of charge carriers between the gas molecule and the sensing material takes place.[6] The sensing mechanism of III-V NW based SGSs also varies with the sensing materials as will be discussed in section 2.1.3.

2.1.2 Semiconductor gas sensor performance parameters

For SGSs, several key parameters are used to evaluate the sensor performance:

Sensitivity: Sensitivity of a sensor can be defined as the slope of the output characteristic curve or, more generally, the minimum perturbation of physical parameters that will create a detectable output change.[7] Some reports also use the response value calculated by $R = \Delta I/I_0$ to represent the sensitivity, correlated with the concentration.[8] In this thesis, we also used these two parameters for InP NW sensitivity characterisation in following chapters. The site-binding hypothesis assumes that atoms on the surface of sensing materials can act as binding sites for analyte adsorption, and thus the conductance change of the device would be related to the surface occupancy of the analyte molecules on the sensing materials.[9-10]

Limit of detection (LOD): The LOD is the smallest concentration of an analyte that can be reliably distinguished from its absence. The determining LODs involves exposing a sensing device to known concentrations of the analyte to generate a calibration curve for the slope (S) of this curve. The LOD can be obtained by equation: $LOD = 3*(SD_{noise}^2/S)$, where the SD_{noise}^2 is the standard deviation of signal noise and S is the sensitivity.[11]

Selectivity: Selectivity is the ability of an analytical method to discriminate between analytes of interest and other interfering components. It can be estimated directly by comparing signal levels obtained from analytes and interferences and/or through statistical analysis (e.g., principal component analysis) or computational modelling (e.g., DFT). The enhancement of selectivity may be achieved through surface functionalisation on sensing materials with specific receptors corresponding to the analytes.[12] The multipixel array device is a recently emerging method to enhance selectivity with the assistance of statistical analysis.[13]

Response/recovery time (R_{es}/R_{ec}): R_{es} is the time required to reach a stable and certain percentage (e.g., 90%) of its stabilised value output reading upon exposure to analytes. The specific requirement for the response time is often dictated by the application of sensors, such as health condition and toxic monitoring, which requires a fast response in millisecond range. R_{ec} is considered the inverse of the response time, and it is defined as the time required for the sensor signal to return to certain percentage (e.g., 90%) of its initial value after analyte exposure.[14]

The above three parameters are the most important for gas sensing research and have been carefully studied in the following chapters to characterise the sensing properties of our

InP NW SGSs. Other important parameters in particular for real applications are listed below:

Dynamic response range: Dynamic response range is defined as the concentration range corresponding to the maximum and minimum operable analytical signal that can be precisely measured by a sensing system.

Reproducibility: Reproducibility is the ability of the analytical device to produce the same signal output after the experimental conditions have been altered. It can be quantified by measuring the variation in calibration data obtained for different devices, using the same test protocols and test equipment.

Reversibility and Stability: reversibility is the capability of signal recovering to its initial state after analyte exposure. This is paramount for practical applications of sensors for continuous sample monitoring. Stability is the ability of a sensor to produce the same output signal when performing the same analytical measurement over a period, particularly important for the devices employed for continuous monitoring of analytes, such as environmental monitoring. It can be quantified by comparing the response produced by an aged device with a new device.

2.1.3 III-V nanowire-based oxidising gas sensors

In recently years, III-V compound semiconductor NW based SGSs have emerged, as they offer stable operation under various radiation and atmosphere conditions due to their superior electrical performance and air/humidity stability.[15-17] With highly tuneable NW configurations and material compositions, many III-V NW SGSs have overcome issues such as high working temperature and large power consumption.[18-22] Moreover,

their capability to be fabricated on Si substrates allows for easy integration into the CMOS infrastructure. These advantages are critical for the implementation of gas sensors in air quality monitoring, smart homes, agriculture, transportation and healthcare applications et al., and thus the development of the next-generation Internet of Things (IoT).[23] This IoT system is of great significance for monitoring urban environmental and public health pollutants. The gaseous pollutants mainly composed by the oxidising gases including in O_3, SO_2, NO, NO_2, etc., originating from the combustion of fossil fuels in oil refineries, power stations, industrial plants and motor vehicles. As acknowledged by the US Environmental Protection Agency (US EPA),[24] the real-time monitoring of these gases in a low concentration range (~50 ppb) holds great significance.

Gallium Nitride (GaN) NWs have demonstrated sensitivity towards SO_2, NO, and NO_2.[25-26] New NW configurations have been explored to enhance the performance in gas sensing applications. Maddaka Reddeppa et al.[25] designed GaN NWs grown on a V-grooved Si(100) substrate with Si(111) facets for NO_2 gas sensor applications, as illustrated in Figure 2-1a with high photocurrent conversion efficiency, increased sensitivity, and a reduced working temperature (from 150 to 27 °C).

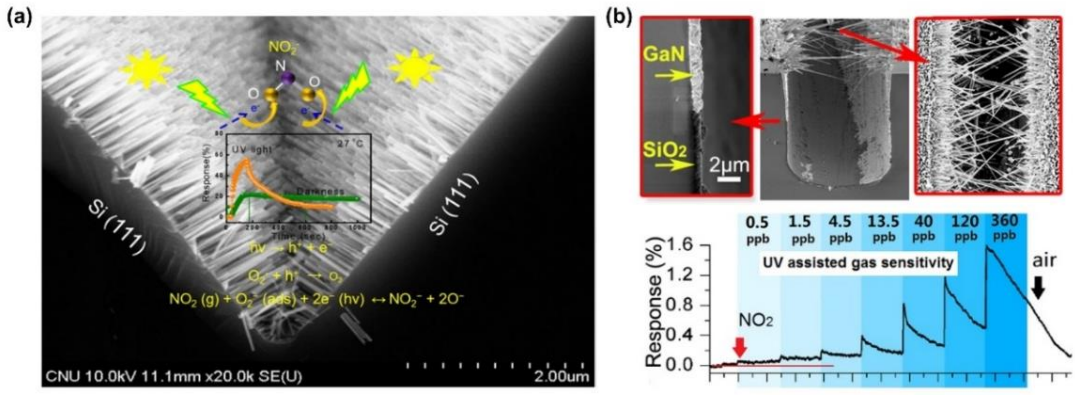

Figure 2-1. The NO_2 sensors based on GaN NWs. (a) SEM images of the bottom point of GaN NWs grown on V-grooved Si; the inset shows the dynamic NO_2 gas response of this device under

darkness and UV illumination, respectively. (adapted from [25]) (b) SEM images of bridge growth of aligned GaN NWs and the corresponding UV assisted NO_2 response. (adapted from [26])

Danna Zhao et al.[26] proposed a direct-bridge growth of aligned GaN NWs. This structure facilitates robust connections and eliminates a contact barrier in bridging NWs. With these features and the assistance of UV light, the LOD improved from 4.5 to 0.5 ppb as shown in Figure 2-1b. The GaN SGSs sensing mechanism involves in chemisorption of O_2, as illustrated in following equations[25]:

$$O_{2(ads)} + e^- \rightarrow O_2^-{}_{(ads)}$$

$$O_2^-{}_{(ads)} + 2AM_{(ads)} \rightarrow 2AMO^- \text{ (oxidative)}$$

where AMs is analyte molecules. During this sensing reaction, the chemisorbed oxygen molecule (O_2^-) act as a surface defect active site, which chemisorbed AMs, causing surface potential modification of GaN NWs through dynamic trapping and de-trapping of charge carriers.[27] Due to the involvement of O_2^-, GaN NW based sensor typically require a higher working temperature (>100 °C) or the assistance of UV illumination to facilitate ionisation of the adsorbed O_2 molecules, as depicted in Figure 2-2.[28]

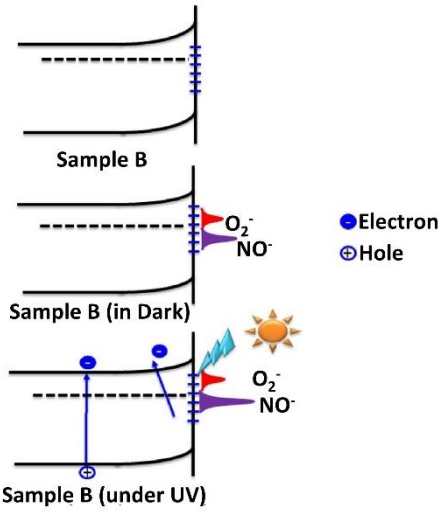

Figure 2-2. Schematic band diagram of GaN NWs after H_2O_2 treatment (top), in NO_2 ambient (middle), in NO_2 ambient under UV illumination (bottom). (adapted from [8])

In fact, UV illumination is widely applied to reduce the operation temperature GaN NW SGSs,[25] considering the large band gap of GaN. Upon UV illumination, electron-hole pairs are generated in GaN, desorbing $O_2^-{}_{(ads)}$ and releasing the surface sites for successive NO_2 adsorption.[29] Thus, a rapid and significant response can be achieved under UV light.

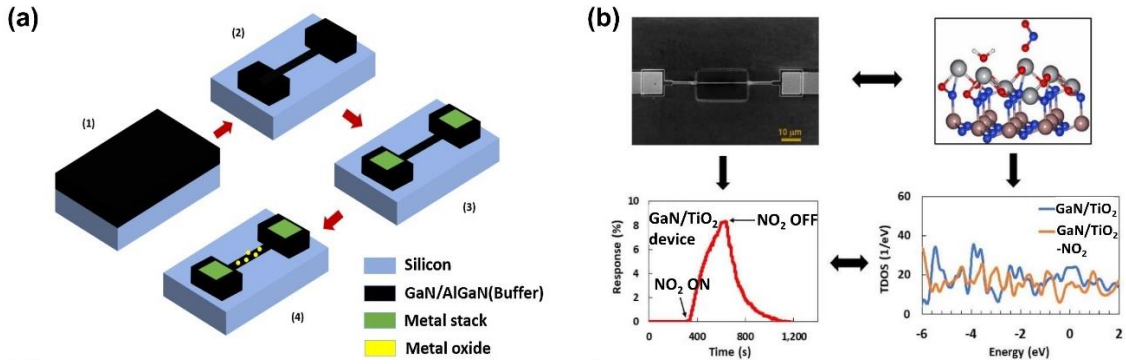

Figure 2-3. (a) Schematic process flow for the fabrication of GaN NW SGSs with metal-oxides surface-functionalisation. (adapted from [27]) (b) SEM image of the metal-oxide/GaN single NW for gas sensing experimental and DFT result. (adapted from [30])

By forming a heterostructure or surface treatment using metal oxides,[27] 2D materials,[29, 31] and hydrogen peroxide treatment[8], gas sensing performance of a single GaN NW SGSs can be further enhanced. Md Ashfaque Hossain Khan et al.[27] deposited metal oxides (ZnO, WO_3 and SnO_2) onto GaN NWs formed on a Si substrate (Figure 2-3a). The charge transfer between the metal oxide and GaN increased with the depletion region width within the GaN by reducing the sensor current, which enhanced sensitivity. Further studies from this group demonstrated that the deposition of a TiO_2 on GaN single NW device led to a very high response to NO_2 due to the large NO_2 adsorption energy of the TiO_2 functionalisation, which was studied via DFT, as depicted in Figure 2-3b.

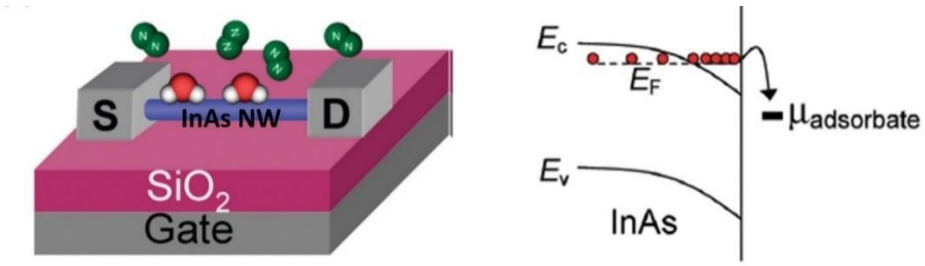

Figure 2-4. Schematic of InAs NW device in ambient N_2 environment with chemical vapor molecules adsorbed on the surface (Left panel). Schematic of electron transfer between the InAs NW and adsorbate molecules (Right panel). The InAs NW is shown to have Fermi level pinned above the bottom of conduction band and an electron accumulation layer on surface. (adapted from [2])

Apart from GaN, InAs NWs have also been investigated as SGSs due to the rich surface states and the formation of a surface electron accumulation layer, leading to pinning of the Fermi level (E_F) above the conduction band minimum as shown in Figure 2-4. This property can make them highly sensitive to molecules adsorbed on the surface.[32] The strong oxidative gases NO_2 with high electron affinity of 220 kJ/mol attribute to the role of an electron acceptor,[33] such that it captures the electrons from NW surface, following equation: $NO_2+e^- \rightarrow NO_2^-$.[34] Peter Offermans et al., realised a remarkable NO_2 LOD of 115 ppb by InAs NWs at room temperature. However, an intrinsic drawback of InAs NWs is their gradually oxidisation in air, leading to a degradation in electrical and sensing performance over time.[33] To address this issue, InAs/InP core/shell NWs have been fabricated, resulting in significantly improved long-term stability.[35]

2.1.4 III-V nanowire-based reducing gas sensors

Sensors designed for reductive gases, including hydrogen (H_2), hydrogen sulphide (H_2S), methane (CH_4) and some volatile organic compounds (VOCs), are in high demand because of their significance in H_2 energy industry, environmental and health monitoring,

etc. Many of these gases, particularly those promising for breath biomarkers,[36] have applications for various disease diagnostics.[37-39]

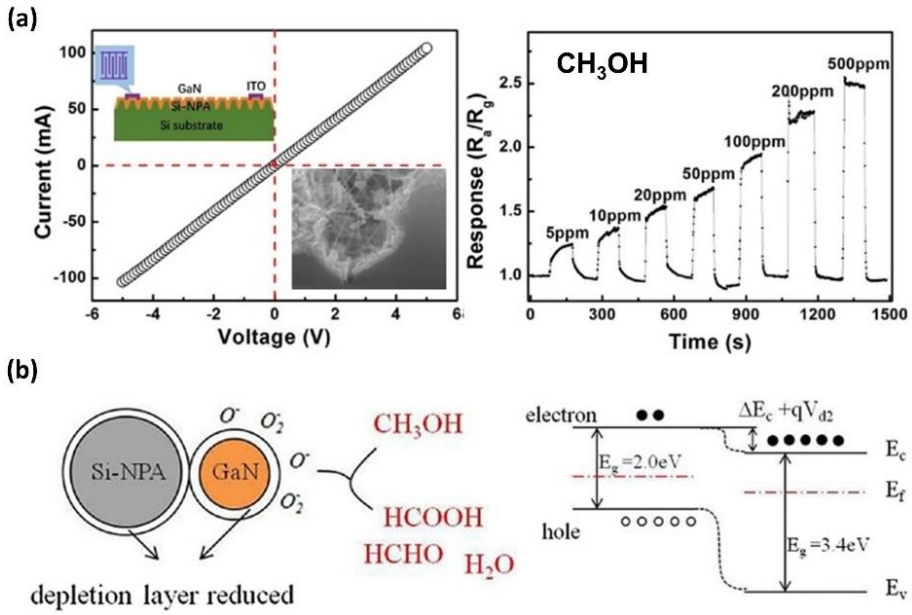

Figure 2-5. The GaN/Si-NPA structure based SGSs. (a) left panel: I–V curve of a coplanar GaN/Si-NPA structure. The inset illustrates the schematic diagram of the GaN/Si-NPA SGSs. Right panel: Response of GaN/Si-NPA SGSs to methanol and selectivity measurement. (b) Energy band diagrams of GaN/Si-NPA with methanol absorption. (adapted from [40])

H. F. Ji et al. fabricated GaN NW SGSs on a silicon nanoporous pillar array (Si-NPA) which exhibited robust sensing responses to methanol within a dynamic range of 5-200 ppm at 350°C as depicted in Figure 2-5.[40] The n-GaN/p-Si heterojunction significantly contributed to enhancing sensitivity to methanol by the built-in electric field formation which facilitated the chemisorption of O_2 and the formation of O^- and O_2^-. The reductive gas sensing reaction could be summarised as follows:

$$O_{2(ads)}^{-} + 2AM_{(ads)} \rightarrow 2AMO + e^{-} \text{ (reductive)}$$

where the electrons captured by the chemisorbed oxygen ion species returned to the GaN through this reaction with reductive gases, increasing the charge carrier concentration (n-type).

InAs NW SGSs exhibited a conductance and mobility change based on the single NW FET device arising from absorbed analytes in gate response experiments.[2] Exposure of InAs NWs to reducing gas decreases carrier concentration by nearly an order of magnitude and improves the NW mobility by almost a factor of six,[32-33] because chemisorption weakening the surface band bending and reducing the electron density of the surface accumulation layer.[41]

Table 2-1. Summary of materials and configuration of III-V NW based gas sensors

Materials	Gas	Sensitivity (S) or Response (R)	LOD	R_{es}/R_{ec} (s)	Working Condition	Ref
InP-NWs array	NO_2	R = 12.9% (1 ppm)	0.01 ppm	43/127	25 °C	[35]
p-i-n InP-NWs array	NO_2	R = 84.1% (1 ppm)	0.1 ppb	50/140	25 °C, solar simulator P = 42.3 $mW \cdot cm^{-2}$	[42]
InAs/InP-NWs (horizontal) array	NO_2	R = 150% (30 ppb)	0.8 ppb	350/-	20 °C	[34]
InAs-single NW	NO_2	S_{NO2}= 0.19 ppm^{-1} R_{NO2} = 90% (5 ppm)	5 ppm	1860/780	25 °C	[43]
	Ethanol	S_{Eth} = 0.002 ppm^{-1} R_{Eth} = 110% (6000 ppm)	4000 ppm	2700/1440		
InAs-single NW	NO_2	R = 4% (10 ppm)	-	-	180 °C	[44]
Graphene GaN-NWs array	NO_2	R = 2300%	10 ppm	107/309	25 °C, λ = 250-350 nm, P = 7 $mW \cdot cm^{-2}$	[29]
Direct-bridging GaN NWs (horizontal) array	NO_2	R = 3.6% (360 ppb)	0.5 ppb	18/300	25 °C, λ = 340 nm, P = 1.4 $mW \cdot cm^{-2}$	[26]

In_2O_3/InN core-shell NWs array	NO_2	R = 52.1%, (50 ppm)	23.25 ppb	47/430	80 °C	[45]
TiO_2/GaN-single NW	NO_2	S = 1.26 ppm^{-1} R =4.5% (1 ppm)	0.5 ppm	240/280	20 °C, λ = 365 nm P = 470 $mW{\cdot}cm^{-2}$	[30]
g-C_3N_4/GaN-NWs array	NO_2	R = 7.8 % (5 ppm)	0.5 ppm	33/218	27 °C, λ = 392 nm P = 1.35 $mW{\cdot}cm^{-2}$	[31]
GaN NWs (random)	H_2	R = 43.50% (200 ppm)	-	100/120	25 °C	[39]
rGO/GaN-NWs array	H_2 H_2S	R = 6.10% (100 ppm) R = 15.20% (100 ppm)	20 ppm	-	30 °C, λ = 365 nm P = 20 $mW{\cdot}cm^{-2}$	[46]
ZnO/GaN-single NW	SO_2	R = 6.26% (1 ppm) S = 1.95 ppm^{-1}	0.5 ppm	230/275	20 °C, λ = 365 nm P = 470 $mW{\cdot}cm^{-2}$	[27]
p-i-n GaN-NWs array	NO	R = 32% (100 ppm）	10 ppm	-	35 °C, λ = 367 nm P = 20 $mW{\cdot}cm^{-2}$	[47]
GaN-NWs array	H_2O	R=24,037% (15%)	15%	-	25 °C, λ = 370 nm P = 80 $mW{\cdot}cm^{-2}$	[48]
GaN/Si- NWs (random)	Methanol	R = 1.22% (5 ppm）	5 ppm	8/7	350 °C	[40]
GaAs-NWs arrays	Methanol	R = 1.37% (406 ppm)	91 ppm	100/500	25 °C	[49]
$Al_{0.07}Ga_{0.93}N$ NWs (random)	CH_4	R = 20% (500 ppm）	100 ppm	33/42	50 °C	[50]

Among all III-V semiconductors, GaN NWs have been extensively studied for SGSs, demonstrating sensitivity to both oxidising and reducing gases. Surface-functionalisation technique, involving metal oxides and graphene, have been employed to enhance

sensitivity to target analytes. UV illumination has been proven effective to be able to decrease the operation temperature of various sensors. However, research efforts are needed to address critical issues such as the fabrication complexity, reproducibility, and reliability, directly impacting their practical applications and mass production. Moreover, the UV illumination and/or high temperature operation pose safety issues, limiting its real-world applicability.

2.2 InP nanowires for gas sensing

As mentioned earlier, a previous study[51] has demonstrated an the InP thin film SGS with ppb level sensitivity and relatively low working temperature (80 ˚C). These results indicate a promising potential to address the existing challenges such as high working temperature, limited sensitivity/selectivity and slow response speed through further sensor design and optimisation, such as employing of nanostructures such as NWs.

Similar to other NW nanostructured materials, NWs have a large surface area and a substantial surface-to-volume ratio compared to bulk material, making the surface properties of InP NWs pivotal in determining their electrical and optical properties, and thus the overall performance across various applications.[35] In particular, the large surface area offers unique advantages for sensor applications. The number of available active sites on NW SGSs for gas adsorption and reaction is significantly higher than that of planar SGSs, elevating the probability of gas adsorption, hence improving the sensitivity. The NW structure also shortens the diffusion path for gas molecules to reach the NW surface, resulting in faster gas reaction kinetics for a rapid response time ideal for real-time detection. Apart from these general features, the unique properties of InP

NWs may also play a critical role in device performance, as discussed in following sections.

However, research on InP NW SGSs is currently lacking in the literature. This gap can be attributed to several possible reasons: 1. Most of the NW sensors mentioned earlier adopt a single NW device configuration, causing challenging fabrication processes such as precise lithography alignments for electrode contacting, which can be cumbersome. 2. Single NW devices face issues of poor stability and reproducibility. 3. In the case of vertical NW array devices, there is a lack of a suitable electrical contacting method to establish connections among each NW in the array while simultaneously exposing the NW surface for interaction with the target gas molecules. The following sections also provide the potential solutions to address these issues, aim at realising the implementation of InP NW array in SGSs.

2.2.1 Basic semiconductor properties

Crystal structure determines the intrinsic properties of semiconductors, such as band gap energy, optical, electrical and mechanical characteristics. The zinc blende (ZB) is based on a face-centred cubic arrangement of anions, with cations occupying one of the two types of tetrahedral holes present as shown in Figure 2-6a. On the other hand, the wurtzite (WZ) structure comprises a hexagonal close-packed array of oxygen anions, with half of the tetrahedral interstices filled by metal cations (Figure 2-6b). While the nearest neighbour connections are similar in both structures, the distances and angles to further neighbours differ.[52] As one of a binary III–V semiconductors, bulk InP are naturally formed with the ZB structure. Interestingly, the InP NWs synthesized by bottom-up epitaxial growth method could exhibit either WZ [53] or a mixture of WZ and ZB crystal phases [54].

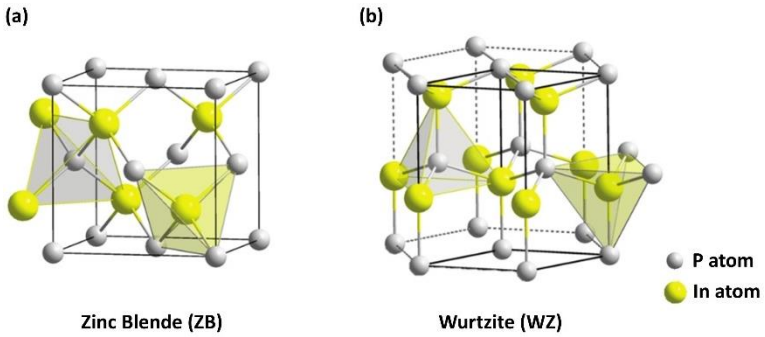

Figure 2-6. The zinc-blende (a) and wurtzite (b) crystal structure. (Adapted from [55])

The precise tailoring of either WZ or ZB phases add an extra tunability to III–V NW properties. Recent research indicates that the tuning of bottom-up growth conditions can obtain both ZB and WZ crystal structures, determining by growth conditions, i.e. temperature, III/V ratio, precursor flow rates, and the presence of specific catalysts or dopants.[53, 56-57] Due to the axial-direction-dominated growth in the WZ structure, the resulting InP NW diameter is mainly determined by the pattern size, allowing for more precise and easier tailoring of NW diameter. The geometry of the NW arrays, i.e. diameter and density, is critical for the gas sensing performance. Therefore, in our study, we choose to grow WZ structure InP NWs for SGSs fabrication. For the NW arrays fabricated by top-down approach, the crystal structure is determined by the crystalline structure of the substrate, i.e. ZB (100) in this work. Due to the smallest atom density in the (100) facet, it features the highest etching rate compared to other facets and is typically chosen for the dry etching process.

The crystal structure determines the electronic band structure of InP NWs which fundamentally governs their semiconducting properties. As a direct bandgap semiconductor, InP NWs exhibit efficient light emission and absorption properties, making it excellent candidates for optoelectronic devices like lasers/LEDs,[58] photodetectors,[59] and solar cells[60]. For gas sensor applications, the light illumination

could provide energy to excite electron-hole pairs to facilitate sensing reactions. The excellent optical properties of InP NWs ensures good photoelectrical conversion efficiency, enabling the low power consumption or even self-powered gas sensing, as demonstrated in Chapter 6.

Doping is another critical factor that significantly influences the material properties of InP NWs and serves as an effective strategy for regulating gas sensing properties. A doping effect study of the epitaxial n-InP thin film sensor (100 nm thickness) revealed that the device with a low doping level 5×10^{15} cm^{-3} exhibited the highest response compared with those doped at higher levels due to suppressed baseline current.[19]

2.2.2 Electrical properties

The excellent charge carrier mobility of InP NWs also facilitate efficient electron and hole transport through the NW channels.[60-61] For gas sensor application, carrier mobility and drift velocity impact the speed of charge carriers moving through the sensing material and generating a measurable electrical signal when exposed to gas molecules. Faster carrier transport results in shorter response times. Efficient charge carrier transport can also reduce the power consumption of gas sensors, making them suitable for battery-powered and energy-efficient applications.[62]

To characterise their electrical properties, electrode contact on NWs requires a delicate and intricate fabrication process, compared to thin film materials.[63] Based on the NW configuration, NW devices are typically classified into single NW devices[64] and NW array devices[65] following different fabrication processes, as shown in Figure 2-7. Single NW devices as aforementioned suffer from complex fabrication process and a lack of reproducibility/stability.[65-66]

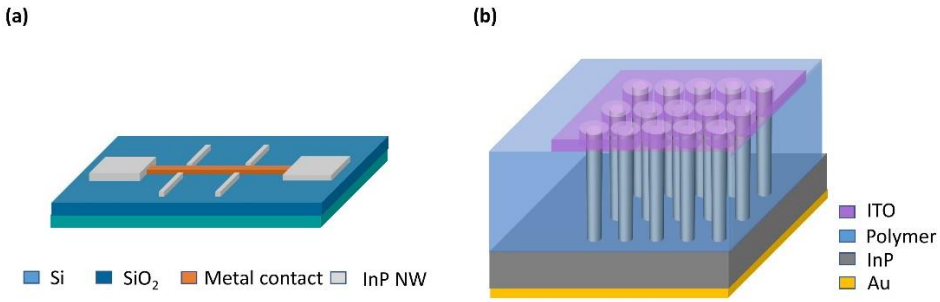

Figure 2-7. (a) The schematics of single NW metal electrodes contact, and (b) the NWs array electrodes contact.

On the other hand, NW arrays harness the collective properties of multiple NWs. The three-dimensional nature of vertical NW arrays ensures precise control over dimensions, offering greater tunability including diameter, length and density, contributing to an increased overall surface area (Figure 2-7b).[67] This tunability is advantageous for tailoring devices to realise different functions and meet specific application requirements.[68] The NW array configuration can be fabricated using scalable techniques, enabling the production of devices in large quantities, which is crucial for commercial applications where mass production is essential.[69] Owing to these features, this NW array configuration was implemented in the SGSs studies in the thesis. It is worth noting that in most of the reported NW array devices [70], the NWs are entirely embedded in a layer of polymer and the top-contact layers as shown in Figure 2-7b. This device configuration cannot be applied to gas sensors as it prohibits the interaction between NWs and the gas molecules. In this thesis, a new NW array gas sensor device fabrication process has been developed for the first time and is detailed in Chapter 3.

2.2.3 Mechanical Properties

Due to their small sizes, the mechanical properties of InP NWs are commonly investigated through theoretical modelling, simulation, and indirect characterisation techniques such as atomic/piezo-response force microscopy (AFM/PFM) as illustrated in Figure 2-8a. Young's modulus represents the stiffness of the NW and its ability to resist deformation under an applied load. InP NWs typically exhibit a high Young's modulus, similar to bulk InP, ranging from 90-120 GPa. This high elastic modulus allows InP NWs to possess high strength and fracture toughness. Despite their small size and high aspect ratio, InP NWs are quite flexible, allowing them to be manipulated or assembled into specific structures, including wearable devices as demonstrated in Chapter 7.

The mechanical deformation of InP NWs could also lead to the generation of electric charges or a voltage, which is known as the piezoelectric effect, resulted from the linear electromechanical interaction between the mechanical and electrical states in crystalline materials with no inversion symmetry as shown in Figure 2-8b. Various device applications are based on the piezoelectricity effect, including energy harvesting, pressure sensors, wireless communication, piezoelectric motors, etc.[71] As mentioned in section 2.2.1, the crystalline structures of InP NWs are either WZ or ZB. The WZ InP NW has demonstrated a higher piezoelectrical effect compared to the ZB NW, making it more suitable for relevant applications.[72] In this case, this piezoelectric property allows WZ InP NWs to be applied as pressure sensors, as demonstrated in Chapter 7.

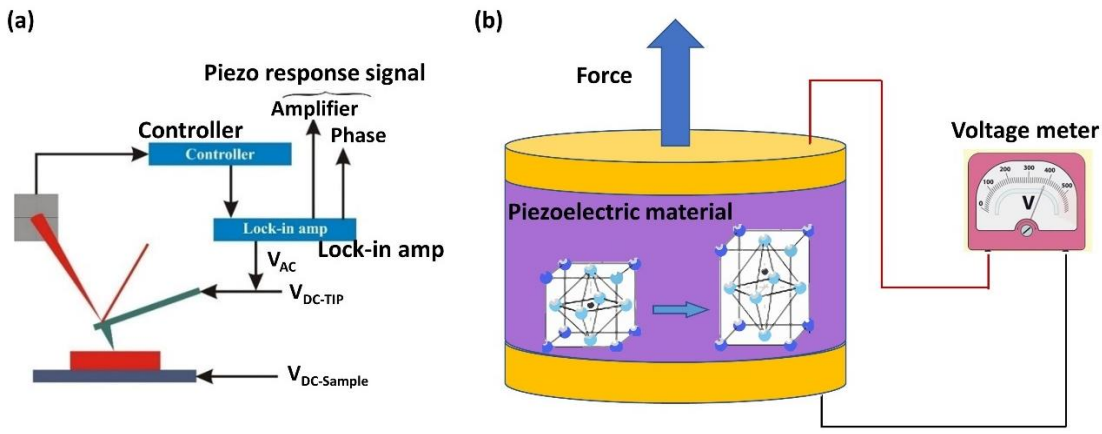

Figure 2-8. (a) The schematic of PFM system and (b) piezoelectric effect measurement based on mechanism with the crystal deformation.[71]

2.2.4 Thermal properties

Compared to other semiconductors, such as Si, InP exhibits relatively high thermal conductivity.[73] This property enables InP NW-based devices to efficiently dissipate heat, reducing the risk of overheating and improving device reliability. At elevated temperatures, the thermal energy possessed by lattice vibrations (phonons) may be sufficient to overcome the bandgap energy, such that the electrons can transition from the valence band to the conduction band, leaving behind a positively charged hole in the valence band.[74] The thermal generation of carriers is of great significance in thermal devices, such as thermophotovoltaic systems and energy harvesting devices. By measuring the change of resistance as a function of temperature dependent thermal carrier generation in a semiconductor material, the temperature of the surrounding environment can be obtained.[74] Based on this, in this thesis we also demonstrate InP NW array temperature sensor (i.e. thermistor) in Chapter 7.

2.3 Surface-functionalisation

Owing to the large surface-to-volume ratio, surface functionalisation of NWs can easily tailor their surface chemistry, allowing the modification of their surface properties for selective gas adsorption.[75] This facilitates differentiation between gases and reduces interference from the environment.[76] By modifying the NW surface with the surface functionalising material, the sensitivity, selectivity, and stability of SGSs may be improved. A variety of materials have been researched as the surface functionalisation reagents for gas sensors, including:

- Metal oxide nanoparticles or nanoclusters: Deposition of metal oxide nanoparticles or nanoclusters on the semiconductor surface such as SnO_2, ZnO, and WO_3 can increase the active surface area and promote gas adsorption, leading to enhanced sensitivity and response speed.[77]

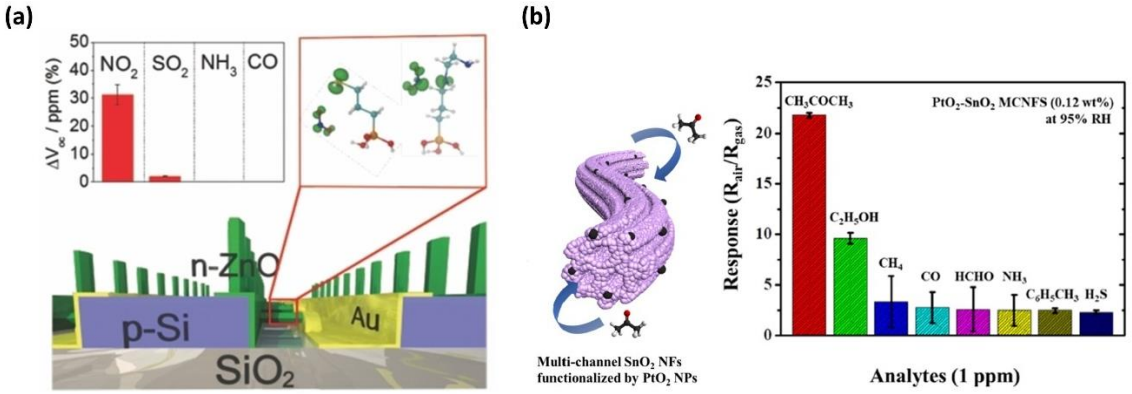

Figure 2-9. The surface-functionalisation gas sensors with (a) SAMs of trimethoxylsilane [78] and (b) metallic nanoparticles [79] with enhanced selectivity.

- Chemically modified layers: Introducing chemical groups or functional molecules on the semiconductor surface can enhance selectivity to specific gases. Chemical modification can increase the affinity of the sensor material to certain gas molecules, improving the sensor's ability to discriminate between different gases. For example, different self-assembled monolayers (SAMs) surface functionalisation reagents have

been fabricated on the surface of active layer of the SGSs, and the formation of single molecular layers can be tailored to interact specifically with certain gas molecules (Figure 2-9a).[80]

- Catalytic materials: Coating the semiconductor surface with catalytic materials, such as noble metals (Pt, Pd, Au) in Figure 2-9b, can also improve gas sensor performance. The catalytic coating facilitates gas adsorption and enhances chemical reactions on the sensor surface, leading to improved sensitivity to certain gases (e.g., Pt nanoparticles for H_2 sensing).[81]

References

[1] R. J. Rath, S. Farajikhah, F. Oveissi, F. Dehghani and S. Naficy, Chemiresistive Sensor Arrays for Gas/Volatile Organic Compounds Monitoring: A Review. *Advanced Engineering Materials*, **25**, 2200830 (2023).

[2] J. Du, D. Liang, H. Tang and X. P. Gao, InAs nanowire transistors as gas sensor and the response mechanism. *Nano Lett*, **9**, 4348-51 (2009).

[3] M. Z. Asadzadeh, A. Köck, M. Popov, S. Steinhauer, J. Spitaler and L. Romaner, Response modeling of single SnO_2 nanowire gas sensors. *Sensors and Actuators B: Chemical*, **295**, 22-29 (2019).

[4] H. Chi, L. J. Ze, X. M. Zhou and F. K. Wang, GO film on flexible substrate: An approach to wearable colorimetric humidity sensor. *Dyes and Pigments*, **185**, 108916(2021).

[5] B. Cho, M. G. Hahm, M. Choi, J. Yoon, A. R. Kim, Y.-J. Lee, S.-G. Park, J.-D. Kwon, C. S. Kim, M. Song, Y. Jeong, K.-S. Nam, S. Lee, T. J. Yoo, C. G. Kang, B. H. Lee, H. C. Ko, P. M. Ajayan and D.-H. Kim, Charge-transfer-based Gas Sensing Using Atomic-layer MoS_2. *Scientific Reports*, **5**, 8052 (2015).

[6] Z. R. Zhang, Y. X. Wu, H. Y. Du, Y. H. Sun, S. P. Sun, S. K. Xu, L. Y. Cong and P. C. Sun, Acetone sensing mechanism of Ar/O_2 plasma modified indium oxide electrospun fibers: A combined DFT and experimental study. *Journal of Alloys and Compounds*, **895**, 162017 (2022).

[7] S.-Y. Guo, P.-X. Hou, F. Zhang, C. Liu and H.-M. Cheng, Gas Sensors Based on Single-Wall Carbon Nanotubes. *Molecules*, **27**, 5381 (2022).

[8] M. Reddeppa, T. K. P. Nguyen, B. G. Park, S. G. Kim and M. D. Kim, Low operating temperature NO gas sensors based hydrogen peroxide treated GaN nanorods. *Physica E-Low-Dimensional Systems & Nanostructures*, **116**, 113725 (2020).

[9] C. Shi, A. Rani, B. Thomson, R. Debnath, A. Motayed, D. E. Ioannou and Q. L. Li, High-performance room-temperature TiO_2-functionalized GaN nanowire gas sensors. *Applied Physics Letters*, **115**, 121602 (2019).

[10] Najar, M. Shafa and D. Anjum, Synthesis, optical properties and residual strain effect of GaN nanowires generated via metal-assisted photochemical electroless etching. *Rsc Advances*, **7**, 21697-21702 (2017).

[11] Z. Meng, R. M. Stolz, L. Mendecki and K. A. Mirica, Electrically-Transduced Chemical Sensors Based on Two Dimensional Nanomaterials. *Chemical Reviews*, **119**, 478-598 (2019).

[12] Dedigama, M. Angelo, P. Torrione, T. H. Kim, S. Wolter, W. Lampert, A. Atewologun, M. Edirisoorya, L. Collins, T. F. Kuech, M. Losurdo, G. Bruno and A. Brown, Hemin-Functionalized InAs-Based High Sensitivity Room Temperature NO Gas Sensors. *Journal of Physical Chemistry C*, **116**, 826-833 (2012).

[13] M. A. H. Khan, B. Thomson, R. Debnath, A. Motayed and M. V. Rao, Nanowire-Based Sensor Array for Detection of Cross-Sensitive Gases Using PCA and Machine Learning Algorithms. *Ieee Sensors Journal*, **20**, 6020-6028 (2020).

[14] S. Chizhov, N. E. Mordvinova, M. N. Rumyantseva, I. V. Krylov, K. A. Drozdov, X. G. Li and A. M. Gas'kov, The Effect of CdSe and InP Quantum Dots on the Interaction of ZnO with NO_2 under Visible Light Irradiation. *Russian Journal of Inorganic Chemistry*, **63**, 512-518 (2018).

[15] S. Pouladi, M. Rathi, D. Khatiwada, M. Asadirad, S. K. Oh, P. Dutta, Y. Yao, Y. Gao, S. C. Sun, Y. K. Li, S. Shervin, K. H. Lee, V. Selvamanickam and J. H. Ryou, High-efficiency flexible III-V photovoltaic solar cells based on single-crystal-like thin films directly grown on metallic tapes. *Progress in Photovoltaics*, **27**, 30-36 (2019).

[16] E. Barrigón, M. Heurlin, Z. Bi, B. Monemar and L. Samuelson, Synthesis and Applications of III–V Nanowires. *Chemical Reviews*, **119**, 9170-9220 (2019).

[17] J. F. Geisz, R. M. France, K. L. Schulte, M. A. Steiner, A. G. Norman, H. L. Guthrey, M. R. Young, T. Song and T. Moriarty, Six-junction III-V solar cells with 47.1% conversion efficiency under 143 Suns concentration. *Nature Energy*, **5**, 326 (2020).

[18] Z. Y. Li, H. H. Tan, C. Jagadish and L. Fu, III-V Semiconductor Single Nanowire Solar Cells: A Review. *Advanced Materials Technologies*, **3**, 180005 (2018).

[19] V. Battut, J. P. Blanc, E. Goumet, V. Soulière and Y. Monteil, NO_2 sensor based on InP epitaxial thin layers. *Thin Solid Films*, **348**, 266-272 (1999).

[20] L. Talazac, F. Barbarin, C. Varenne and Y. Cuminal, Highly NO_2 sensitive pseudo Schottky barrier diodes on p-type InP with improved electrical characteristics. *Sensors and Actuators B-Chemical*, **77**, 447-454 (2001).

[21] K. Wierzbowska, B. Adamowicz, L. Mazet, J. Brunet, A. Pauly, L. Bideux, C. Varenne, B. Laure and J. P. Germain, High-sensitivity NO_2 sensor based on n-type InP epitaxial layers. *Optica Applicata*, **35**, 655-662 (2005).

[22] J. Wong-Leung, I. Yang, Z. Y. Li, S. K. Karuturi, L. Fu, H. H. Tan and C. Jagadish, Engineering III-V Semiconductor Nanowires for Device Applications. *Advanced Materials*, **32**, 14 (2020).

[23] X. L. Liu, Y. Zhao, W. J. Wang, S. X. Ma, X. J. Ning, L. Zhao and J. Zhuang, Photovoltaic Self-Powered Gas Sensing: A Review. *Ieee Sensors Journal*, **21**, 5628-5644 (2021).

[24] F. Karagulian, M. Barbiere, A. Kotsev, L. Spinelle, M. Gerboles, F. Lagler, N. Redon, S. Crunaire and A. Borowiak, Review of the Performance of Low-Cost Sensors for Air Quality Monitoring. *Atmosphere*, **10**, 506 (2019).

[25] M. Reddeppa, D. J. Nam, N. H. Bak, K. S. Pasupuleti, H. Woo, S. G. Kim, J. E. Oh and M. D. Kim, Proliferation of the Light and Gas Interaction with GaN Nanorods Grown on a V-

Grooved Si(111) Substrate for UV Photodetector and NO_2 Gas Sensor Applications. *Acs Applied Materials & Interfaces*, **13**, 30146-30154 (2021).

[26] D. N. Zhao, H. Huang, S. J. Chen, Z. R. Li, S. D. Li, M. Y. Wang, H. C. Zhu and X. M. Chen, In Situ Growth of Leakage-Free Direct-Bridging GaN Nanowires: Application to Gas Sensors for Long-Term Stability, Low Power Consumption, and Sub-ppb Detection Limit. *Nano Letters*, **19**, 3448-3456 (2019).

[27] M. A. H. Khan, B. Thomson, J. Yu, R. Debnath, A. Motayed and M. V. Rao, Scalable metal oxide functionalized GaN nanowire for precise SO_2 detection. *Sensors and Actuators B-Chemical*, **318**, 128223 (2020).

[28] Q. C. Bui, L. Largeau, M. Morassi, N. Jegenyes, O. Mauguin, L. Travers, X. Lafosse, C. Dupuis, J. C. Harmand, M. Tchernycheva and N. Gogneau, GaN/Ga_2O_3 Core/Shell Nanowires Growth: Towards High Response Gas Sensors. *Applied Sciences-Basel*, **9**, 3528 (2019).

[29] J. Shin, S. Han, S. Noh, Y. T. Yu and J. S. Kim, Room-temperature operation of light-assisted NO_2 gas sensor based on GaN nanowires and graphene. *Nanotechnology*, **32**, 505201 (2021).

[30] M. A. H. Khan, B. Thomson, A. Motayed, Q. L. Li and M. V. Rao, Functionalization of GaN Nanowire Sensors With Metal Oxides: An Experimental and DFT Investigation. *Ieee Sensors Journal*, **20**, 7138-7147 (2020).

[31] M. Reddeppa, N. T. KimPhung, G. Murali, K. S. Pasupuleti, B. G. Park, I. In and M. D. Kim, Interaction activated interfacial charge transfer in 2D g-C_3N_4/GaN nanorods heterostructure for self-powered UV photodetector and room temperature NO_2 gas sensor at ppb level. *Sensors and Actuators B-Chemical*, **329**, 129175 (2021).

[32] D. Liang, J. Du and X. P. A. Gao, InAs Nanowire Devices with Strong Gate Tunability: Fundamental Electron Transport Properties and Application Prospects: A Review. *Journal of Materials Science & Technology*, **31**, 542-555 (2015).

[33] P. Offermans, M. Crego-Calama and S. H. Brongersma, Gas Detection with Vertical InAs Nanowire Arrays. *Nano Letters*, **10**, 2412-2415 (2010).

[34] M. Bai, H. Huang, Z. Liu, T. T. Zhan, S. F. Xia, X. G. Li, N. Sibirev, A. Bouravleuv, V. G. Dubrovskii and G. Cirlin, InAs/InP core/shell nanowire gas sensor: Effects of InP shell on sensitivity and long-term stability. *Applied Surface Science*, **498**, 143756 (2019).

[35] S. Y. Wei, Z. Li, A. John, B. I. Karawdeniya, Z. Y. Li, F. L. Zhang, K. Vora, H. H. Tan, C. Jagadish, K. Murugappan, A. Tricoli and L. Fu, Semiconductor Nanowire Arrays for High-Performance Miniaturized Chemical Sensing. *Advanced Functional Materials*, **32**, 2107596 (2022).

[36] M. Khatib and H. Haick, Sensors for Volatile Organic Compounds. *Acs Nano*, **16**, 7080-7115 (2022).

[37] K. Prasad, P. K. Sahoo, S. Dhara, S. Dash and A. K. Tyagi, Differences in hydrogen absorption over Pd and Pt functionalized CVD-grown GaN nanowires. *Materials Chemistry and Physics*, **211**, 355-360 (2018).

[38] S. B. Wang, X. Q. Wang, Z. Y. Chen, P. Wang, Q. Qi, X. T. Zheng, B. W. Sheng, H. P. Liu, T. Wang, X. Rong, M. Li, J. Zhang, X. L. Yang, F. J. Xu and B. Shen, Enhanced Hydrogen Detection Based on Mg-Doped InN Epilayer. *Sensors*, **18**, 10 (2018).

[39] Q. N. Abdullah, A. R. Ahmed, A. M. Ali, F. K. Yam, Z. Hassan, M. Bououdina and M. A. Almessiere, Growth and characterization of GaN nanostructures under various ammoniating time with fabricated Schottky gas sensor based on Si substrate. *Superlattices and Microstructures*, **117**, 92-104 (2018).

[40] H. F. Ji, W. K. Liu, S. Li, Y. Li, Z. F. Shi, Y. T. Tian and X. J. Li, High-performance methanol sensor based on GaN nanostructures grown on silicon nanoporous pillar array. *Sensors and Actuators B-Chemical*, **250**, 518-524 (2017).

[41] C. Tseng, D. Lynall, I. Savelyev, M. Blumin, S. L. Wang and H. E. Ruda, Sensing Responses Based on Transfer Characteristics of InAs Nanowire Field-Effect Transistors. *Sensors*, **17**, 1640 (2017).

[42] S. Y. Wei, Z. Li, K. Murugappan, Z. Y. Li, F. L. Zhang, A. G. Saraswathyvilasam, M. Lysevych, H. H. Tan, C. Jagadish, A. Tricoli and L. Fu, A Self-Powered Portable Nanowire Array Gas Sensor for Dynamic NO_2 Monitoring at Room Temperature. *Advanced Materials*, **35**, 2207199 (2022).

[43] V. Demontis, M. Rocci, M. Donarelli, R. Maiti, V. Zannier, F. Beltram, L. Sorba, S. Roddaro, F. Rossella and C. Baratto, Conductometric Sensing with Individual InAs Nanowires. *Sensors*, **19**, 2994 (2019).

[44] S. K. Jangir, H. K. Malik, P. Saho, R. Muralidharan, T. Srinivasan and P. Mishra, Electrical transport and gas sensing characteristics of dielectrophoretically aligned MBE grown catalyst free InAs nanowires. *Nanotechnology*, **30**, 105706 (2019).

[45] B. G. Park, M. Reddeppa, Y. H. Kim, S. G. Kim and M. D. Kim, Hydrogenation-produced In_2O_3/InN core-shell nanorod and its effect on NO_2 gas sensing behavior. *Nanotechnology*, **31**, 335503 (2020).

[46] M. Reddeppa, B. G. Park, M. D. Kim, K. R. Peta, N. D. Chinh, D. Kim, S. G. Kim and G. Murali, H_2, H_2S gas sensing properties of rGO/GaN nanorods at room temperature: Effect of UV illumination. *Sensors and Actuators B-Chemical*, **264**, 353-362 (2018).

[47] M. Reddeppa, B. G. Park, N. D. Chinh, D. Kim, J. E. Oh, T. G. Kim and M. D. Kim, A novel low-temperature resistive NO gas sensor based on InGaN/GaN multi-quantum well-embedded p-i-n GaN nanorods. *Dalton Transactions*, **48**, 1367-1375 (2019).

[48] M. Z. Peng, X. H. Zheng, Z. G. Ma, H. Chen, S. J. Liu, Y. F. He and M. L. Li, Ni-pattern guided GaN nanowire-array humidity sensor with high sensitivity enhanced by UV photoexcitation. *Sensors and Actuators B-Chemical*, **256**, 367-373 (2018).

[49] X. X. Wang, S. Ermez, H. Goktas, S. Gradecak and K. Gleason, Room Temperature Sensing Achieved by GaAs Nanowires and oCVD Polymer Coating. *Macromolecular Rapid Communications*, **38**, 1700055 (2017).

[50] S. Parida, A. Das, A. K. Prasad, J. Ghatak and S. Dhara, Native defect-assisted enhanced response to CH_4 near room temperature by $Al_{0.07}Ga_{0.93}N$ nanowires. *Physical Chemistry Chemical Physics*, **20**, 18391-18399 (2018).

[51] L. Talazac, J. P. Blanc, J. P. Germain and A. Pauly, NO_2 detection by a resistive device based on n-InP epitaxial layers. *Sensors and Actuators B: Chemical*, **59**, 89-93 (1999).

[52] P. M. de Wolff, N. V. Belov, E. F. Bertaut, M. J. Buerger, J. D. H. Donnay, W. Fischer, T. Hahn, V. A. Koptsik, A. L. Mackay, H. Wondratschek, A. J. C. Wilson and S. C. Abrahams, Nomenclature for crystal families, Bravais-lattice types and arithmetic classes. Report of the International Union of Crystallography Ad-Hoc Committee on the Nomenclature of Symmetry. *Acta Crystallographica Section A*, **41**, 278-280 (1985).

[53] Q. Gao, V. G. Dubrovskii, P. Caroff, J. Wong-Leung, L. Li, Y. Guo, L. Fu, H. H. Tan and C. Jagadish, Simultaneous Selective-Area and Vapor–Liquid–Solid Growth of InP Nanowire Arrays. *Nano Letters*, **16**, 4361-4367 (2016).

[54] Q. Gao, Z. Li, L. Li, K. Vora, Z. Li, A. Alabadla, F. Wang, Y. Guo, K. Peng, Y. C. Wenas, S. Mokkapati, F. Karouta, H. H. Tan, C. Jagadish and L. Fu, Axial p-n junction design and characterization for InP nanowire array solar cells. *Progress in Photovoltaics: Research and Applications*, **27**, 237-244 (2019).

[55] Boyce, C. Barrie, I. Samson and A. Williams-Jones, Current perspectives on zinc deposits. *Irish Association for Economic Geology*, (Eds: Piercey, S. J.) **2015**, p. 17-35.

[56] F. Ishizaka, Y. Hiraya, K. Tomioka, J. Motohisa and T. Fukui, Growth of All-Wurtzite InP/AlInP Core–Multishell Nanowire Array. *Nano Letters*, **17**, 1350-1355 (2017).

[57] H. J. Chu, T. W. Yeh, L. Stewart and P. D. Dapkus, Wurtzite InP nanowire arrays grown by selective area MOCVD. *physica status solidi c*, **7**, 2494-2497 (2010).

[58] X. Duan, Y. Huang, Y. Cui, J. Wang and C. M. Lieber, Indium phosphide nanowires as building blocks for nanoscale electronic and optoelectronic devices. *Nature*, **409**, 66-69 (2001).

[59] Z. Zhong, Z. Li, Q. Gao, Z. Li, K. Peng, L. Li, S. Mokkapati, K. Vora, J. Wu and G. Zhang, Efficiency enhancement of axial junction InP single nanowire solar cells by dielectric coating. *Nano Energy*, **28**, 106-114 (2016).

[60] S. De Franceschi, J. Van Dam, E. Bakkers, L. Feiner, L. Gurevich and L. P. Kouwenhoven, Single-electron tunneling in InP nanowires. *Applied Physics Letters*, **83**, 344-346 (2003).

[61] N. S. Mohammad, Understanding quantum confinement in nanowires: basics, applications and possible laws. *Journal of Physics: Condensed Matter*, **26**, 423202 (2014).

[62] G. Shen, P.-C. Chen, Y. Bando, D. Golberg and C. Zhou, Pearl-like ZnS-decorated InP nanowire heterostructures and their electric behaviors. *Chemistry of Materials*, **20**, 6779-6783 (2008).

[63] F. Zafar and A. Iqbal, Indium phosphide nanowires and their applications in optoelectronic devices. *Proceedings of the Royal Society A: Mathematical, Physical and Engineering Sciences*, **472**, 20150804 (2016).

[64] G. Otnes, E. Barrigón, C. Sundvall, K. E. Svensson, M. Heurlin, G. Siefer, L. Samuelson, I. Åberg and M. T. Borgström, Understanding InP nanowire array solar cell performance by nanoprobe-enabled single nanowire measurements. *Nano Letters*, **18**, 3038-3046 (2018).

[65] Nowzari, M. Heurlin, V. Jain, K. Storm, A. Hosseinnia, N. Anttu, M. T. Borgström, H. k. Pettersson and L. Samuelson, A comparative study of absorption in vertically and laterally oriented InP core–shell nanowire photovoltaic devices. *Nano Letters*, **15**, 1809-1814 (2015).

[66] D. Jevtics, B. Guilhabert, A. Hurtado, M. Dawson and M. Strain, Deterministic integration of single nanowire devices with on-chip photonics and electronics. *Progress in Quantum Electronics*, 100394 (2022).

[67] J. Wallentin, N. Anttu, D. Asoli, M. Huffman, I. Åberg, M. H. Magnusson, G. Siefer, P. Fuss-Kailuweit, F. Dimroth and B. Witzigmann, InP nanowire array solar cells achieving 13.8% efficiency by exceeding the ray optics limit. *Science*, **339**, 1057-1060 (2013).

[68] Y. Huang, X. Duan and C. M. Lieber, Nanowires for integrated multicolor nanophotonics. *Small*, **1**, 142-147 (2005).

[69] N. Anttu, A. Abrand, D. Asoli, M. Heurlin, I. Åberg, L. Samuelson and M. Borgström, Absorption of light in InP nanowire arrays. *Nano Research*, **7**, 816-823 (2014).

[70] M. Karimi, V. Jain, M. Heurlin, A. Nowzari, L. Hussain, D. Lindgren, J. E. Stehr, I. A. Buyanova, A. Gustafsson and L. Samuelson, Room-temperature InP/InAsP quantum discs-in-nanowire infrared photodetectors. *Nano Letters*, **17**, 3356-3362 (2017).

[71] Manbachi and R. S. C. Cobbold, Development and Application of Piezoelectric Materials for Ultrasound Generation and Detection. *Ultrasound*, **19**, 187-196 (2011).

[72] M. Dunaevskiy, P. Geydt, E. Lahderanta, P. Alekseev, T. Haggren, J. P. Kakko, H. Jiang and H. Lipsanen, Young's Modulus of Wurtzite and Zinc Blende InP Nanowires. *Nano Letters*, **17**, 3441-3446 (2017).

[73] Kudman and E. Steigmeier, Thermal conductivity and Seebeck coefficient of InP. *Physical Review*, **133**, A1665 (1964).

[74] X. Jiang, Q. Xiong, S. Nam, F. Qian, Y. Li and C. M. Lieber, InAs/InP radial nanowire heterostructures as high electron mobility devices. *Nano letters*, **7**, 3214-3218 (2007).

[75] M. Wusiman and F. Taghipour, Methods and mechanisms of gas sensor selectivity. *Critical Reviews in Solid State and Materials Sciences*, **47**, 416-435 (2022).

[76] X. Chen, C. K. Wong, C. A. Yuan and G. Zhang, Nanowire-based gas sensors. *Sensors and Actuators B: Chemical*, **177**, 178-195 (2013).

[77] Kolmakov and M. Moskovits, Chemical sensing and catalysis by one-dimensional metal-oxide nanostructures. *Annu. Rev. Mater. Res.*, **34**, 151-180 (2004).

[78] M. W. G. Hoffmann, L. Mayrhofer, O. Casals, L. Caccamo, F. Hernandez-Ramirez, G. Lilienkamp, W. Daum, M. Moseler, A. Waag, H. Shen and J. D. Prades, A Highly Selective and Self-Powered Gas Sensor Via Organic Surface Functionalization of p-Si/n-ZnO Diodes. *Advanced Materials*, **26**, 8017-8022 (2014).

[79] Y. J. Jeong, W. T. Koo, J. S. Jang, D. H. Kim, M. H. Kim and I. D. Kim, Nanoscale PtO_2 Catalysts-Loaded SnO_2 Multichannel Nanofibers toward Highly Sensitive Acetone Sensor. *Acs Applied Materials & Interfaces*, **10**, 2016-2025 (2018).

[80] S. Onclin, B. J. Ravoo and D. N. Reinhoudt, Engineering silicon oxide surfaces using self-assembled monolayers. *Angewandte Chemie International Edition*, **44**, 6282-6304 (2005).

[81] Kolmakov, X. Chen and M. Moskovits, Functionalizing nanowires with catalytic nanoparticles for gas sensing application. *Journal of Nanoscience and Nanotechnology*, **8**, 111-121 (2008).

Chapter 3. Experimental Techniques

This chapter introduces the main experimental techniques employed in this thesis, including InP nanowire (NW) array synthesize/fabrication, material characterisation, sensor device fabrication and measurements. Primary focuses are the introduction of the fundamental principles of key techniques and development of new NW sensor fabrication processes.

3.1 Top-down approach for NW array fabrication

The top-down etching approach for NW array fabrication offers several advantages, such as simplicity, high uniformity, and scalability which is compatible with standard microelectronics industry processes.[1] In this thesis, this method was also used to fabricate InP NW arrays for gas sensing from undoped semi-insulating InP (100) wafer with a carrier concentration of (1-10) × 10^{15} cm^{-3} (AXT Inc.) following the process outlined below.

3.1.1 Substrate preparation

The substrate preparation steps for the top-down InP (100) include:

- SiO_2 layer deposition: A 600 nm SiO_2 layer is deposited onto the undoped InP wafer using plasma-enhanced chemical vapor deposition (PECVD).[2] The SiO_2 crystal layer is deposited at 300 °C under a pressure of 87 Pa and a radio frequency power of 200 W, utilizing source gases of $SiH_4/N_2O/N_2$ (flow rate 9/70/161 sccm) to achieve a uniform and dense dielectric layer. The thickness of the SiO_2 layer was measured by an ellipsometry (JA Woollam M2000D).

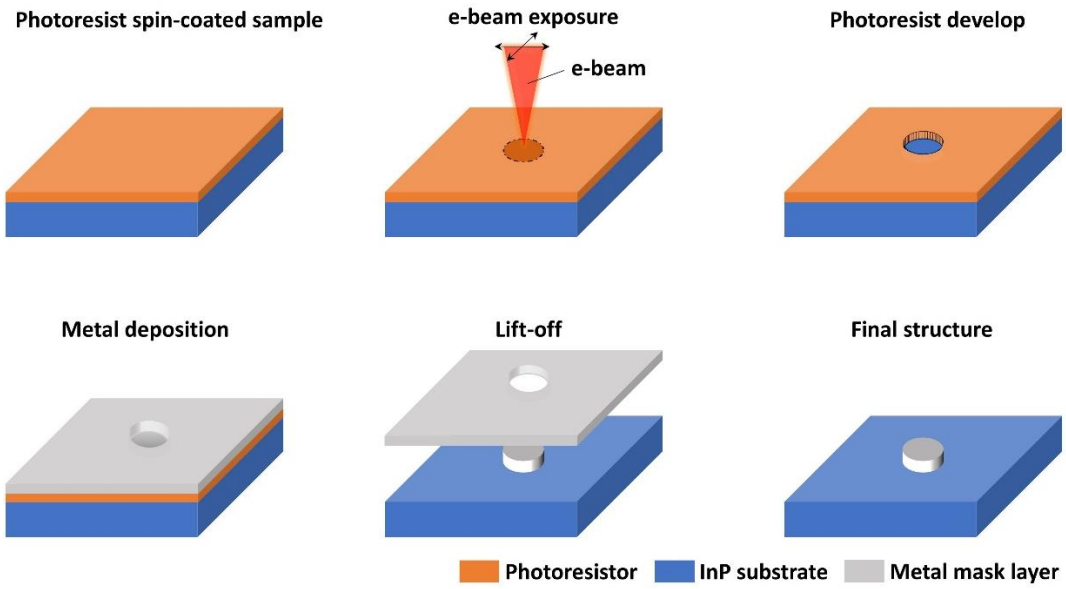

Figure 3-1. The schematic of EBL working process for the SiO_2/InP wafer substrate patterning.

- NW array patterning: The NW array is patterned using electron beam lithography (EBL) to define a circular dot array pattern on the InP substrate, by spin-coating the AR6200.09 (Kirsten Hackenbroich) resist onto the SiO_2/InP wafer for electron beam exposure of a pre-designed pattern using an RAITH150 system[3], as illustrated in Figure 3-1.

- Photoresist developing of and etching mask deposition: A patterned resist layer is created by developing the exposed photoresist layer by EBL using the developer (AR600).[4] The remaining photoresist layer serves as the mask for the subsequent metal deposition step, as depicted in Figure 3-1. A 70 nm layer of Ni is deposited on top of the patterned substrate using electron-beam evaporation technique.[5-6] This step is followed by soaking the wafer in ZEP remover (Kirsten Hackenbroich) for 1 hour for the lift-off process, leaving the patterned Ni layer on top of SiO_2 layer forming a Ni/SiO_2 bilayer as the mask for subsequent InP etching.

3.1.2 Dry Etching

Among various dry etching techniques, the Inductively Coupled Plasma (ICP) etching exhibits anisotropic etching characteristics, being able to achieve vertical sidewalls required by many device applications. The ICP etching method is a standard semiconductor processing technique used in the semiconductor industry. It has well developed processes for various material systems, including InP, and was employed in this work to transfer the EBL defined pattern to the InP substrate for NW array fabrication with high precision and reproducibility.

Before the etching of InP layer, the exposed SiO_2 layer should be etched first by the ICP with fluorian gas (ICP-F). The SiO_2 etching process was conducted under CHF_3/Ar gas flow, with a small chamber pressure of 0.1 pa and high radio frequency (RF) power. Then, the InP wafer was etched by $SiCl_4$/Ar gas flow, with RF power, leading to the formation of NW array with well-defined geometry.[7] It was observed that chamber pressure, etching gas flow rate, ICP power, and RF power are critical parameters influencing the etching rate, and the resultant morphology and dimension of the InP NWs.[8] Through careful tuning of these parameters, vertically configured NW arrays with smooth sidewalls can be obtained. For the etching masks with different pattern densities, the chamber pressure needs to be adjusted accordingly, as will be discussed in the next section. Finally, the Ni/SiO_2 etching mask is removed by HF solution with concentration of 10 %, and the InP NWs are fabricated. The process of the top-down approach for InP NW array fabrication is illustrated in Figure 3-2, with detailed processing parameters provided in Table 3-1.

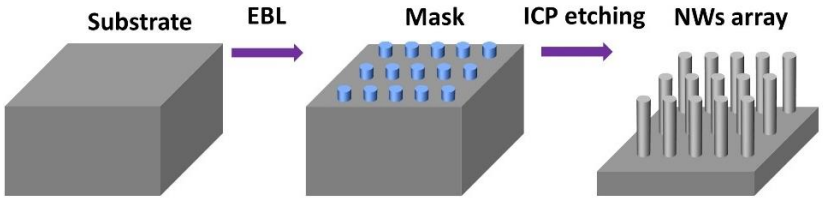

Figure 3-2. The top-down etching steps for InP NW array fabrication, including in EBL patterning of the Ni/SiO_2 bilayer mask on the InP wafer and the following ICP-CL etching.

Table 3-1. Detailed experimental parameters used for InP NW array fabricated by top-down etching.

Step	Process detail	equipment
SiO_2 deposition	PECVD 600 nm for top-down etching mask and 30 nm of SA-MOVPE growth @ 300 °C / 87 Pa / 200 W / $SiH_4/N_2O/N_2$ (flow rate 9/70/161 sccm)	PECVD
Thickness measurement	SiO_2 on InP	Ellipsometer
AR6200.09 coating	5s @500rpm/60s @3000rpm	Spinner
Bake out	1 min @150 °C	Hotplate
EBL pattern	EHT 10 kV/ Aperture 10 µm / writing field 100 µm / Step size 0.01 µm / dose 60 µC/cm^2	EBL
Development	60s @AR600 developer / 45s @IPA/ 30s DI water	Wet station
Metal deposition	70 nm Ni for dry etching mask Ti 10 nm / Au 80 nm for contact electrodes Ti 10 nm / Pt 60 nm for Schottky contact	e-beam evaporation
Lift-off	>1 hour @ZEP remover /IPA flushing	Wet station
HF etching	20s @ Buffered HF (1%) for native oxide removal	Wet station
SEM	NWs morphology examination @ electron beam voltage of 2 kV and current of 13 pA	SEM
Plasma strip	Oxygen plasma 2 min 300 sccm / 0.2 mbar / 100W	Barrel etcher
ICP-F	SiO_2 layer etching @ CHF_3 20 sccm /Ar 10 sccm / 0.1-0.3 mbar/ ICP power 400 W/ RF power 80 W	ICP-F etcher
ICP-CL	InP layer etching @ $SiCl_4$ 1.5 sccm / Ar 25 sccm / ICP power 200 W/ RF power 50 W	ICP-CL etcher

3.1.3 Tailoring of nanowire array geometry

To tailor the NW array geometry in terms of diameter and pitch size, the EBL patterns are designed with different diameters of 300, 200, and 100 nm and varied pitch sizes (interspace between NWs) of 1000, 800, 600, and 400 nm, respectively. Initially, the pitch size is set at 1000 nm to investigate the diameter tuning effect, with samples labelled as D100P1000, D200P1000, and D300P1000 (D: diameter; P: pitch size). These samples undergo etching under the same optimised conditions to achieve a vertical cylinder-shaped array. With the same NW density in these three samples, the same etching conditions are used to with a similar etching rate.

The NW arrays with varied pitch sizes are designed with the diameter fixed at 100 nm. Higher ICP etching pressure shortens the mean free path of particles in the chamber and increases the probability of collisions between particles, leading to a loss of energy. Hence, the density of reactive $SiCl_4$ radicals and the number of ions reaching the etched surface are decreased, reducing the efficiency of atomic bond breaking on the surface. For higher density masks (smaller NW pitch size), a reduced chamber pressure is adopted to ensure that sufficient reactive $SiCl_4$ radicals penetrate down to the narrow gap between mask patterns to obtain higher density NW arrays.[9-10] With a decreased chamber pressure, a constant etching rate can be achieved despite of the increased NW density.

It is noteworthy that the surface of as-etched NWs could be damaged during multiple etching and chemical treatments. Post-processing steps are crucial for surface recovery to restore the desired optical/electrical properties and functionality of the NWs for further device fabrication. In this case, subsequent cleaning steps are performed to remove any etch residues, byproducts, or contaminants that may have accumulated on the NW surfaces after etching. Chemical treatments can also be applied to passivate the etched

NW surfaces to reduce surface defects and improve surface quality. In this study, the fabricated InP NW array was subjected to surface cleaning in a barrel-etcher with an O_2 flow rate of 100 sccm and RF power of 100 W, and surface treatment by 1 % HF. The material characterisation results of top-down etched InP NW arrays are presented in Chapter 4.

3.2 Bottom-up growth of InP nanowire arrays

Nanowire arrays can also be grown using bottom-up approaches by epitaxial techniques such molecular beam epitaxy (MBE) or metal-organic vapour phase epitaxy (MOVPE). For MOVPE technique, the growth occurs near thermodynamic equilibrium leading to excellent crystallinity and has the advantage of high growth rate for bulk layers.[11] In this work, we also employed the MOVPE technique to grow InP NW arrays. The bottom-up NWs by this technique can be grown via different mechanisms, such as vapour-liquid-solid (VLS) or selective area metal-organic vapor-phase epitaxy (SA-MOVPE).[12]

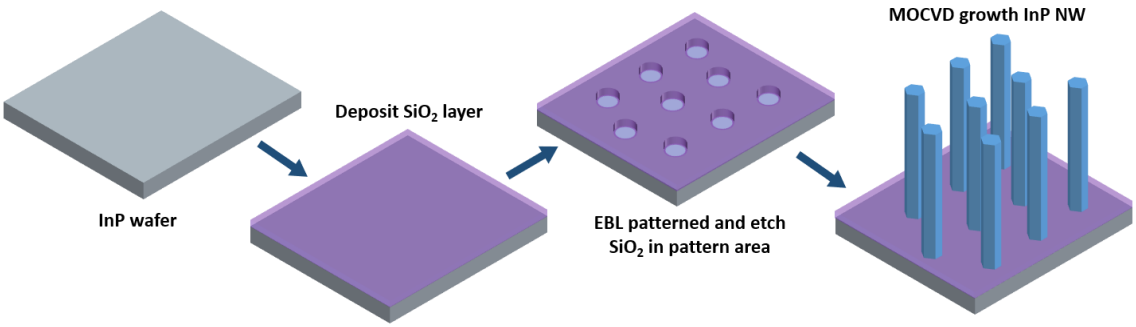

Figure 3-3. The schematic of SA-MOVPE process for InP NW array growth.

The VLS method uses metal catalysts (usually Au nanoparticles) as the nucleation sites for the NW growth.[13] The enhancement in growth rate can be explained by a reduced nucleation barrier underneath the seed particle compared to the substrate and NW side facets. For SA-MOVPE as shown in Figure 3-3, a hard template is used to limit the crystal

surface available for epitaxy. While different mask materials have been studied, a 20-50 nm thick SiO_2 or Si_3N_4 mask patterned by EBL onto substrates is typically used.[14] Holes are defined and opened using ICP dry etch. Similar to VLS growth, by changing the growth conditions, both radial and axial structures can be produced. While SA-MOVPE is more complex and has lower throughput than VLS growth, the use of Au as a catalyst in VLS growth raises concerns about Au incorporation within the NWs.[10] Although the position define of VLS method could be facilitated by EBL patterning of the droplets of metal catalyst, VLS-based methods are reliant on the liquid catalyst and the composition of the NWs grown is limited by the solubilities of the relevant precursors within the liquid catalyst. Consequently, this method has challenges with control over NW doping and composition of their heterostructures.[15] The SA-MOVPE is preferrable for defining the location and NW structures, where no extrinsic catalyst is incorporated,[16] featuring non-tapering, highly tuneable growth dimension, doping and composition.[17] Hence, the SA-MOVPE technique was employed in this thesis, following the process outlined below.

3.2.1 Substrate fabrication

To facilitate the SA-MOVPE growth of InP NWs, a series of substrate preparation steps are undertaken to ensure high-quality and reproducible NW growth. In this work, the growth substrate was InP (111)A wafer, either p-doped or n-doped, with a concentration of (0.8-8) $\times 10^{18}$ cm^{-3}. Figure 3-3 illustrates the processes involved in preparation for NW growth.[18] Firstly, a 30 nm SiO_2 layer was deposited on the (111)A InP substrate using PECVD at 300 °C. The thickness of the SiO_2 layer was measured and calibrated by an ellipsometry. Subsequently, a negative resist (AR6200.09) was spin-coated onto the SiO_2 layer and baked at 150°C for 1 minute on a hotplate. The resist was then exposed by EBL based on a designed pattern consisting of a 200 × 200 μm hexagonal dot array with a size

of 80 nm and a pitch of 600 nm. The exposed pattern area was developed and further cleaned by the oxygen plasma as discussed in the last section.

The exposed pattern was subsequently etched by ICP to remove the SiO_2 layer on the InP substrate followed by a trim etching to ensure the quality of the InP surface for MOCVD growth. The trim etching includes 2 minutes 10% H_2O_2 to oxidise the InP layer, followed by a 10% H_3PO_4 etching to remove the oxide layer for 2 minutes.[19] These steps were repeated sequentially for five times, after which the sample was promptly transferred into the MOVPE reactor for NW growth.

3.2.2 InP NW array growth by SA-MOVPE

The equipment used for SA-MOVPE growth in this work is an AIXTRON 200/4 reactor. A typical MOVPE process for InP epitaxial growth is schematically illustrated in Figure 3-4. To initiate the InP NW array growth process, the substrates are exposed to precursors and hydrogen carrier gas, which operates at a base pressure of 100 mbar, utilising H_2 as a carrier gas under a total flow rate of 14.5 l/min. Trimethylindium (TMIn) and phosphine (PH_3) serve as precursors for the group III (In) and group V (P) elements, respectively. The corresponding idealised chemical reaction for the growth is:[20-21]

$In(CH_3)_3 + PH_3 = InP + 3CH_4$

Doping introduces impurity atoms into the crystal lattice of the semiconductor material, either to increase electron or hole concentration, allowing the formation of an electrical structures such as p-n junction during the growth process.[22] In this work, silane (SiH_4) and diethylzinc (DEZn) are introduced during the growth for the n-type doping and p-type doping respectively, with all other parameters kept the same as those used for the growth of the undoped InP.[23] Achieving the desired doping concentration involves adjusting the flow rate ratio of the dopant precursor to the III-V precursor.[24] In this

thesis, i-n and i-p InP NWs were grown on p-doped and n-doped substrates, respectively, to form n-i-p and p-i-n junctions for the study of self-powered photovoltaic NO_2 sensors, as will be presented in Chapter 5.

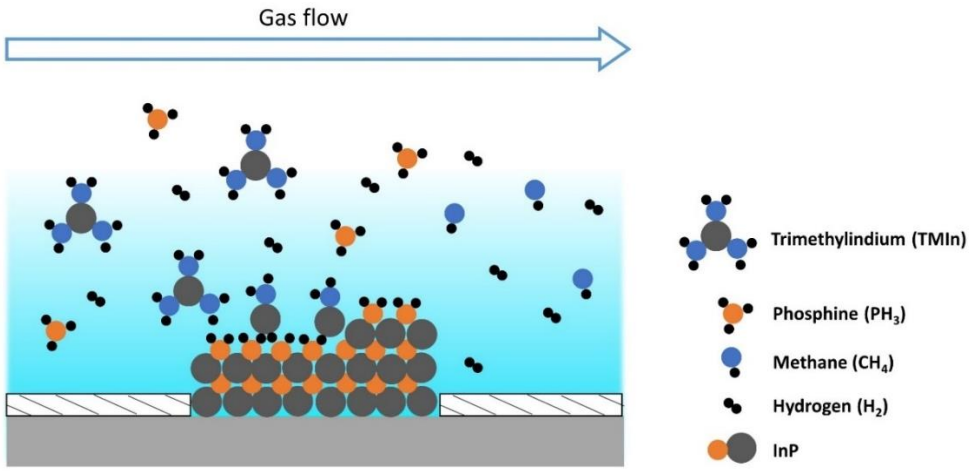

Figure 3-4. The schematic of InP epitaxial growth principle by SA-MOVPE technique.

3.3 Device fabrication

Given the unique structure of the NW arrays, the process of device fabrication requires a careful design to preserve the vertically aligned NW array configuration and ensure proper electrical contact for all the NWs within the arrays.[25] For different NW configurations and device applications, different device fabrication processes are required. For instance, for optoelectronic devices such as photodetectors and solar cells, the NW arrays are normally embedded in an insulating polymer material with the tip of the NWs exposed and deposited with a metal contact layer transparent at the working wavelength.[26] However, for chemical sensor applications, the NW surface needs to be exposed to react with target analytes, requiring a completely different device configuration and fabrication process, as will be described in Chapters 4 and 5.

3.4 Nanowire material characterisation

In this thesis, a series of techniques has been employed to characterise the material properties of the InP NWs, including morphology, doping and crystalline structure to obtain desirable NW size and quality.

The morphology of the as-fabricated InP NW arrays was characterised using scanning electron microscopy (SEM, FEI VERIOS 460),[27] which is an electron microscope that generates images of a sample by scanning the surface with a focused beam of electrons. These electrons interact with atoms in the sample, producing various signals containing information about the surface topography and composition.[28] As the most common SEM operation mode, secondary electrons emitted by atoms are excited by the electron beam and detected using a secondary electron detector (Everhart-Thornley detector). The signal intensity, depending on specimen topography, is obtained by combining the position of the scanned electron beam with the intensity of the detected signal to produce an image.[29] The working principle of SEM requires that the samples be conductive or semi-conductive for efficient electron interaction. InP NWs have good electrical conductivity, allowing direct characterisation by SEM without additional treatment like Au sputtering, which is typically used to facilitate the measurement of materials with poor conductivity.

The crystal structure of the InP NWs is determined through transmission electron microscopy (TEM) using the JEOL 2100F instrument.[30] TEM is a microscopy technique wherein a beam of electrons is transmitted through an ultrathin sample, usually less than 100 nm, to create an image.[31] In this study, since the NWs were designed and obtained with very thin thicknesses (<100 nm) for chemical sensing applications, they

were directly transferred from the original substrate to the copper mesh for TEM measurement.

Cathodoluminescence (CL) technique was applied to single NWs that are transferred from the NW array to a Si substrate to characterise their optical properties (Figure 3-5).[32] CL is one of a luminescence mode, created during irradiation of a solid surface with an excited electron beam as shown in Figure 3-5a.[33] After an electron beam with high energy raster-scanned over the sample surface, the emission of photons is collected to form CL spectroscopy (Figure 3-5b). Its combination with SEM, CL is a powerful technique for nanoscale optical characterisation.[34-35] In this thesis, the CL images of NWs are acquired using an SEM equipped Gatan MONO CL 4 under an electron excitation voltage of 10 kV and a current of 0.8 nA at room temperature.

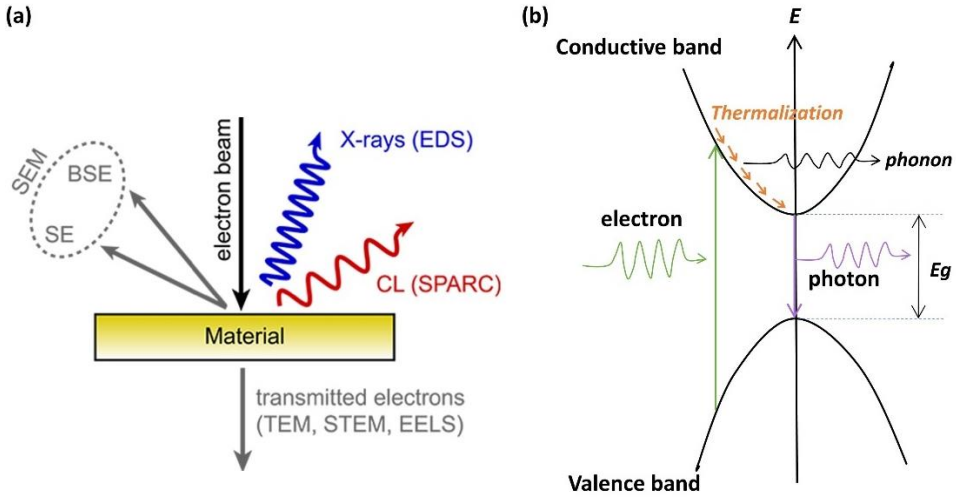

Figure 3-5. The working principle of CL (a). The radiative recombination process in a direct bandgap material (b).

Also, the NWs are transferred to a SiO_2/Si substrate for micro-photoluminescence (PL) and time-resolve PL (TRPL) analysis at room temperature. PL is the process of material absorbing photons (or electromagnetic waves) and re-radiating photons (or electromagnetic waves).[36] TRPL is used to detect the radioactive decay of the samples

in which excited electrons have a radioactive decay channel, such that it can probe excited-state recombination dynamics, including effective carrier lifetimes.[37] The micro-PL system used here comprises a Horiba LabRAM system equipped with confocal optics as shown in Figure 3-6, a diode-pumped solid-state (DPSS) 532 nm laser, and a liquid nitrogen-cooled array InGaAs detector. The laser beam was focused through a 100x microscope objective lens, resulting in a spot size of 0.36 μm (in radius), estimated by vector diffraction calculation. For TRPL, the emission was collected by the same objective lens and detected by a single-photon avalanche diode, which is connected to the Picoharp 300 time-correlated single-photon counting (TCSPC) system.[38] Micro-PL spectra and TRPL are acquired along a single NW from the top to the bottom position. The minority carrier lifetime in the NWs was extracted from the single exponential fitting of the TRPL decay curve.[39]

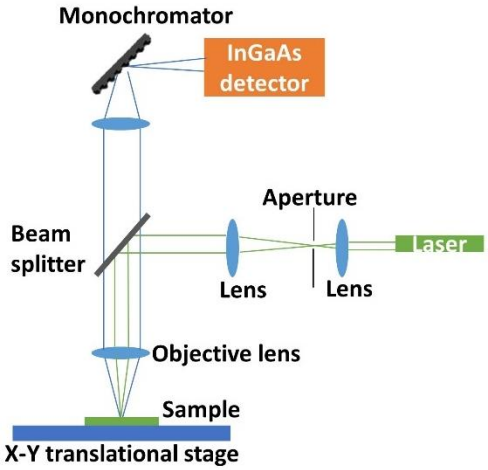

Figure 3-6. The Schematic diagram of the micro-PL system used in this work.

3.5 Gas sensor device characterisation

After fabrication, the InP NW array sensor devices are characterised by both dark and light current-voltage (I-V) measurements using the Keysight B2902A source/measurement unit, integrated with a solar simulator.[40]

The gas sensing performance was measured by home-made sensing setup which consists of a Linkam chamber with a sample stage and Au probes for electrical contact, mass flow controllers (MFCs Bronkhorst), a solar simulator @1.5M and gas cylinders as shown in Figure 3-7. The Linkam chamber ensures an isolated environment of gas testing and the MFCs can precisely control the gas flow rate and the consequently the gas concentration delivered into the Linkam chamber. The cover of the Linkam chamber contains a glass window which allow the light illumination during the measurement. The electric signal is measured by the Potentiostat (CHI) for several type of electrical signal output by its software.

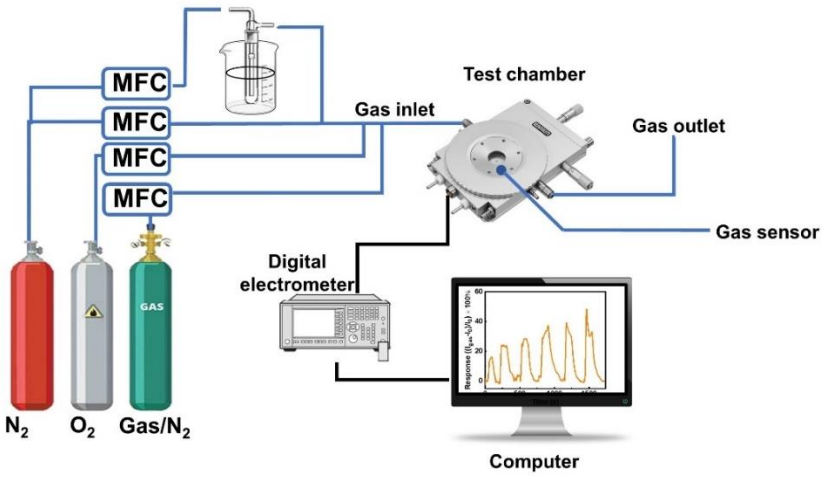

Figure 3-7. The schematic of the home-made gas sensing setup system.

For the gas sensing measurements, the carrier gas is simulated air with volume ratio of N_2 to O_2 at 4 (V_{N2}/V_{O2} = 4, N_2 and O_2, BOC gas). The gas flow rates are controlled by MFCs while the total gas flow rate is kept at 1 l/min for ppm level concentration test and 0.5 l/min for sub-ppm level concentration test. For the measurement of analyte gas, volatile organic compounds (VOCs) (ethanol, 9.91 ppm in N_2, Coregas; acetone, 10.1 ppm in N_2, Coregas; methanol, 10 ppm in N_2, BOC gas) or NO_2 gas are diluted to desired concentrations before being purged into the chamber. The selectivity is measured by

comparing the sensing response of the target gas and the potential interference gases. This measurement can also be performed by mixing the target gas and competing gases during the sensing measurement, comparing the sensing response with and without the competing gases.

For humidity test, the water vapor is produced by the same bubbler setup as above, where the organic solvent is replaced by DI water in the bubbler. The water vapor is injected into the gas chamber with a consistent N_2 flow rate during the whole sensing process, and the relative humidity (RH) is controlled by the N_2 flow rate, as shown in Table 3-2.

Table 3-2. The humidity test at different RHs controlled by flow rates of the mass flow controller.

RH (%)	N_2 to the bubbler ($L \cdot min^{-1}$)	Simulated air ($L \cdot min^{-1}$)
20	0.2	0.8
50	0.5	0.5
65	0.65	0.35

References

[1] H. Ohmi, J. Sato, Y. Shirasu, T. Hirano, H. Kakiuchi and K. Yasutake, Significant Improvement of Copper Dry Etching Property of a High-Pressure Hydrogen-Based Plasma by Nitrogen Gas Addition. *Acs Omega*, **4**, 4360-4366 (2019).

[2] K. Zuber, R. Radjef and C. Hall, in *Frontiers of Nanoscience*, (Eds: M. Benelmekki and A. Erbe), Elsevier **2019**, p. 141-179.

[3] A. Tseng, K. Chen, C. D. Chen and K. J. Ma, Electron beam lithography in nanoscale fabrication: recent development. *IEEE Transactions on electronics packaging manufacturing*, **26**, 141-149 (2003).

[4] D. R. Sahu, S.-Y. Lin and J.-L. Huang, Improved properties of Al-doped ZnO film by electron beam evaporation technique. *Microelectronics Journal*, **38**, 245-250 (2007).

[5] G. Myburg and F. Auret, Influence of the electron beam evaporation rate of Pt and the semiconductor carrier density on the characteristics of Pt/n-GaAs Schottky contacts. *Journal of applied physics*, **71**, 6172-6176 (1992).

[6] Y. Zhu, V. Raj, Z. Li, H. H. Tan, C. Jagadish and L. Fu, Self-Powered InP Nanowire Photodetector for Single-Photon Level Detection at Room Temperature. *Advanced Materials*, **33**, 2105729 (2021).

[7] Y. Han, S. Xue, W. Guo, Y. Luo, Z. Hao and C. Sun, Highly Selective Dry Etching of GaN over AlGaN Using Inductively Coupled $Cl_2/N_2/O_2$ Plasmas. *Japanese Journal of Applied Physics*, **42**, L1139 (2003).

[8] H. Ahmad, Z. Engel, M. Zia, A. S. Weidenbach, C. M. Matthews, B. Zivasatienraj, M. S. Bakir and W. A. Doolittle, Cascaded Ni hard mask to create chlorine-based ICP dry etched deep mesas for high-power devices. *Semiconductor Science and Technology*, **36**, 125016 (2021).

[9] W. W. Wong, N. Wang, B. D. Esser, S. A. Church, L. Li, M. Lockrey, I. Aharonovich, P. Parkinson, J. Etheridge and C. Jagadish, Bottom-up, Chip-Scale Engineering of Low Threshold, Multi-Quantum-Well Microring Lasers. *Acs Nano*, **15**, 15065–15076 (2023).

[10] E. Barrigon, M. Heurlin, Z. X. Bi, B. Monemar and L. Samuelson, Synthesis and Applications of III-V Nanowires. *Chemical Reviews*, **119**, 9170-9220 (2019).

[11] V. G. Dubrovskii, in *Semiconductor Nanowires I: Growth and Theory*, (Eds: A. F. I. Morral, S. A. Dayeh and C. Jagadish), Elsevier Academic Press Inc, San Diego **2015**, p. 1-78.

[12] J. Nah, H. Fang, C. Wang, K. Takei, M. H. Lee, E. Plis, S. Krishna and A. Javey, III-V Complementary Metal-Oxide-Semiconductor Electronics on Silicon Substrates. *Nano Letters*, **12**, 3592-3595 (2012).

[13] K. Rishinaramangalam, M. Nami, D. M. Shima, G. Balakrishnan, S. R. J. Brueck and D. F. Feezell, Reduction of reverse-leakage current in selective-area-grown GaN-based core-shell

nanostructure LEDs using AlGaN layers. *Physica Status Solidi a-Applications and Materials Science*, **214**, 1600776 (2017).

[14] Y. B. Fan, J. Wang, J. Li, H. Y. Yin, H. Y. Hu, Z. Y. Yang, X. Wei, Y. Q. Huang and X. M. Ren, Epitaxial Lateral Overgrowth of InP on Nanopatterned GaAs Substrates by Metal-Organic Chemical Vapor Deposition. *Journal of Electronic Materials*, **47**, 5518-5524 (2018).

[15] Q. Gao, Z. Y. Li, L. Li, K. Vora, Z. Li, A. Alabadla, F. Wang, Y. A. Guo, K. Peng, Y. C. Wenas, S. Mokkapati, F. Karouta, H. H. Tan, C. Jagadish and L. Fu, Axial p-n junction design and characterization for InP nanowire array solar cells. *Progress in Photovoltaics*, **27**, 237-244 (2019).

[16] S. Maeda, K. Tomioka, S. Hara and J. Motohisa, Fabrication and Characterization of InP Nanowire Light-Emitting Diodes. *Japanese Journal of Applied Physics*, **51**, 02BN03 (2012).

[17] J. Bauer, V. Gottschalch, H. Paetzelt, G. Wagner, B. Fuhrmann and H. Leipner, MOVPE growth and real structure of vertical-aligned GaAs nanowires. *Journal of crystal growth*, **298**, 625-630 (2007).

[18] I.-T. Im, H. J. Oh, M. Sugiyama, Y. Nakano and Y. Shimogaki, Fundamental kinetics determining growth rate profiles of InP and GaAs in MOCVD with horizontal reactor. *Journal of crystal growth*, **261**, 214-224 (2004).

[19] S. Hasan, A. Mamun, K. Hussain, M. Gaevski, I. Ahmad and A. Khan, Growth evolution of high-quality MOCVD aluminum nitride using nitrogen as carrier gas on the sapphire substrate. *Journal of Materials Research*, **36**, 4360-4369 (2021).

[20] D. Lindgren, O. Hultin, M. Heurlin, K. Storm, M. T. Borgström, L. Samuelson and A. Gustafsson, Study of carrier concentration in single InP nanowires by luminescence and Hall measurements. *Nanotechnology*, **26**, 045705 (2015).

[21] Z. Zhong, Z. Li, Q. Gao, Z. Li, K. Peng, L. Li, S. Mokkapati, K. Vora, J. Wu and G. Zhang, Efficiency enhancement of axial junction InP single nanowire solar cells by dielectric coating. *Nano Energy*, **28**, 106-114 (2016).

[22] D. Ruhstorfer, M. Döblinger, H. Riedl, J. J. Finley and G. Koblmüller, Role of twin defects on growth dynamics and size distribution of undoped and Si-doped GaAs nanowires by selective area epitaxy. *Journal of Applied Physics*, **132**, 204302 (2022).

[23] M. Kwiat, S. Cohen, A. Pevzner and F. Patolsky, Large-scale ordered 1D-nanomaterials arrays: Assembly or not? *Nano Today*, **8**, 677-694 (2013).

[24] X. M. Zhang, M. Y. Lu, Y. Zhang, L. J. Chen and Z. L. Wang, Fabrication of a high-brightness blue-light-emitting diode using a ZnO-nanowire array grown on p-GaN thin film. *Advanced Materials*, **21**, 2767-2770 (2009).

[25] K. Akhtar, S. A. Khan, S. B. Khan and A. M. Asiri, Scanning electron microscopy: Principle and applications in nanomaterials characterization. *Handbook of materials characterization*, 113-145 (2018).

[26] M. Abd Mutalib, M. Rahman, M. Othman, A. Ismail and J. Jaafar, in *Membrane characterization*, Elsevier **2017**, p. 161-179.

[27] J. Wang, S. Plissard, M. Hocevar, T. T. Vu, T. Zehender, G. G. Immink, M. A. Verheijen, J. Haverkort and E. P. Bakkers, Position-controlled [100] InP nanowire arrays. *Applied Physics Letters*, **100**, 053107(2012).

[28] M. Kannan, Transmission electron microscope—Principle, components and applications. *A textbook on fundamentals and applications of nanotechnology*, 93-102 (2018).

[29] J. Götze, Application of cathodoluminescence microscopy and spectroscopy in geosciences. *Microscopy and Microanalysis*, **18**, 1270-1284 (2012).

[30] P. R. Edwards and R. W. Martin, Cathodoluminescence nano-characterization of semiconductors. *Semiconductor Science and Technology*, **26**, 064005 (2011).

[31] Rahman and A. K. Rahman, Nanoscale metrology of line patterns on semiconductor by continuous wave terahertz multispectral reconstructive 3-D imaging overcoming the abbe diffraction limit. *IEEE Transactions on Semiconductor Manufacturing*, **32**, 7-13 (2018).

[32] Q. Li, M. Anpo, J. You, T. Yan and X. Wang, in *Springer Handbook of Advanced Catalyst Characterization*, (Eds: I. E. Wachs and M. A. Bañares), Springer International Publishing, Cham **2023**, p. 295-321.

[33] D. Grinberg and Y. Paz, Recent progress in transient spectroscopy studies of solid statephotocatalysts. *Current Opinion in Green and Sustainable Chemistry*, **41**, 100768 (2023).

[34] G. S. Buller, S. Fancey, J. Massa, A. C. Walker, S. Cova and A. Lacaita, Time-resolved photoluminescence measurements of InGaAs/InP multiple-quantum-well structures at 1.3-μm wavelengths by use of germanium single-photon avalanche photodiodes. *Applied Optics*, **35**, 916-921 (1996).

[35] S. Reitzenstein, S. Münch, C. Hofmann, A. Forchel, S. Crankshaw, L. C. Chuang, M. Moewe and C. Chang-Hasnain, Time resolved microphotoluminescence studies of single InP nanowires grown by low pressure metal organic chemical vapor deposition. *Applied Physics Letters*, **91**, 091103 (2007).

[36] Z. Zhong, Z. Li, Q. Gao, Z. Li, K. Peng, L. Li, S. Mokkapati, K. Vora, J. Wu, G. Zhang, Z. Wang, L. Fu, H. H. Tan and C. Jagadish, Efficiency enhancement of axial junction InP single nanowire solar cells by dielectric coating. *Nano Energy*, **28**, 106-114 (2016).

Chapter 4. High-Performance InP Nanowire Arrays for NO_2 sensing

As discussed in Chapter 1, gas sensors find widespread applications in our daily lives and industries. Among these applications, gas sensors have attracted particular interest for air pollution monitoring. Managing local air pollution is one of the primary challenges of modern society.[1-2] Nitrogen Dioxide (NO_2) is a poisonous and toxic gas produced as a byproduct from the combustion processes of fuels (such as coal, gas, oil, wood, or even non-green H_2) in vehicles, industrial plants, and household gas appliances.[3-5] In Australia, the Time Weighted Average (TWA) limit for NO_2 is 200 ppb (10102-44-0 Safe Work Australia, 2020).[6-8] Such a low concentration is beyond the sensitivity of many commercial NO_2 detectors, highlighting the significance of next-generation NO_2 sensors.[9-10] As mentioned in Chapter 1, chemiresisitive sensors present a promising technique due to their low-cost, superior sensitivity, fast response times, and feasibility for miniaturisation and integration into microchips.[11-14]

In this chapter, we demonstrated the potential of InP nanowires (NWs) for selectively detection of NO_2 by fabricating them into a miniaturised and integrated chemiresistor device. Firstly, a novel NWs array gas sensor device was developed by employing a tilt-angle deposition method[15] to connect each NW in the array for electrical contacts while partially exposing the NW surface for gas sensing. Then, we investigated the impact of array geometry, including NW diameter and pitch size, on chemical sensing performance to optimise device design. Selectivity and air stability were characterised to assess the reliability of these NW sensors, achieving a limit of detection of 3.1 ppb at room temperature and outstanding selectivity and long-term stability. Lastly, an analytical

model by kinetic analysis was built for binding affinity kinetics analysis,[16] combining with electrical simulation of the NW chemiresistive properties for a comprehensive understanding of the NW array geometry correlated gas sensing mechanism.[17]

4.1 Experimental

4.1.1. InP NW array fabrication

A top-down etching approach was used to fabricate InP NW array from undoped InP wafer with a carrier concentration of (1-10) × 10^{15} cm^{-3} (AXT Inc.), as aforementioned in Chapter 3, section 3.2. This top-down approach for InP NWs is illustrated in Figure 4-1 and summarised as following: (a) 600 nm SiO_2 was deposited on the undoped InP wafer by PECVD process. SiO_2 was deposited at 300 °C under a pressure of 87 Pa and radio frequency (RF) power of 200 W with the source gases $SiH_4/N_2O/N_2$ (flow rate 9/70/161 sccm). (b) The electron-resist AR6200.09 (Kirsten Hackenbroich) was spin-coated on the SiO_2/InP wafer for RAITH150 EBL patterning. As the key step of this top-down method, EBL was used to achieve precise pattern definition for subsequent Ni mask deposition and ICP-RIE etching for the NW arrays. (c) Deposition of 70 nm Ni on the top of the EBL pattern by e-beam evaporation. This was followed by soaking the wafer in ZEP remover (Kirsten Hackenbroich) for 3 hours for lift-off. (d) ICP (Florine) was used to etch the exposed SiO_2 layer to form a Ni/SiO_2 bilayer as the mask for subsequent InP etching. This SiO_2 etching process was carried out under CHF_3/Ar gas flow (20/10 sccm) and chamber pressure of 0.1 Pa under the ICP power of 400 W and RF power of 80 W. (e) InP with Ni/SiO_2 mask was etched by ICP-RIE, under 0.1-0.3 Pa chamber pressure and $SiCl_4$/Ar gas flow (1.5/25 sccm) with the ICP power of 200 W and RF power of 50 W. Samples with varying diameter (D), named by D100P1000, D200P1000, D300P1000,

were etched under chamber pressure of 0.3 Pa with an etching rate of ~ 3.33 nm/s. The etching time was 10 min in NW length of around 2 µm.

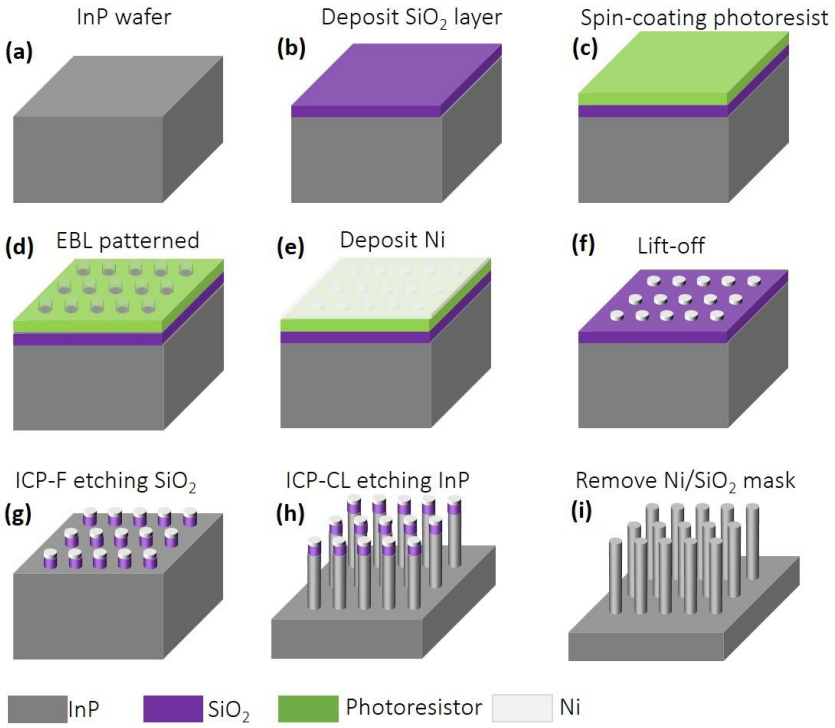

Figure 4-1. Top-down etching process for InP NW array fabrication. (a) InP undoped (n-type): (1-10) × 10^{15} cm^{-3} wafer. (b) PECVD deposition of 600 nm SiO_2. (c) Spin-coating AR6200.09 photoresist on the deposited SiO_2. (d) EBL patterning to open up holes for subsequent etching mask deposition. (e, f) 70 nm Ni deposition by e-beam evaporation on the EBL patterned substrate followed by lift-off to form the Ni mask pattern. (g) ICP of SiO_2 to form the SiO_2/Ni mask. (h) ICP of InP with the SiO_2/Ni mask. (i) Removal of SiO_2/Ni mask by 10% HF solution.

To vary the array pitch size (P), the etching condition was further optimised. With the decrease of NW pitch size, the chamber pressure was decreased to 0.2 Pa for pitch size 600 nm and 800 nm sample (D100P600, D100P800) and 0.1 Pa for pitch size 400 nm sample (D100P400) to maintain a vertical configuration of the NWs. The etching rate was also maintained with the decreased chamber pressure even though the NW density was increased more than a factor of two. Ni/SiO_2 mask was removed by soaking in 10% HF

solution for 5 minutes. Then, the fabricated InP NWs array was cleaned in barrel-etcher with an O_2 flow rate of 100 sccm and RF power of 100 W.

4.1.2 InP NW array characterisation

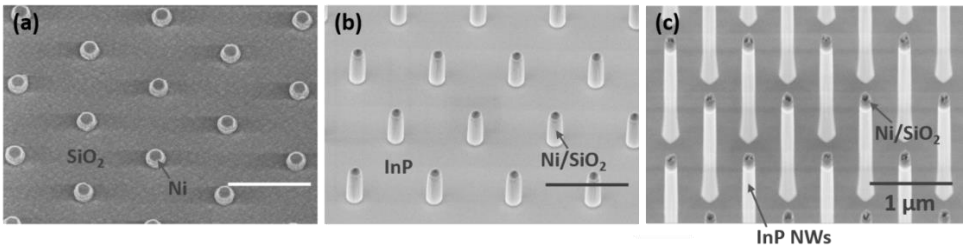

Figure 4-2. SEM images of InP NWs fabricated by top-down etching approach (viewed at a tilt angle of 30°). (a) Ni mask after EBL patterning and lift-off. (b) Results after ICP (Florine) etching of SiO_2. (c) Results after ICP-RIE of InP. These images correspond to Figure 4-1 (f-h), respectively.

The morphology of top-down fabrication process of an InP NW array was imaged by scanning electron microscope (SEM) under an accelerating voltage of 2.0 kV and a current of 13 pA, as shown in Figure 4-2. After careful optimisation of the top-down etching conditions, the NWs exhibit a vertical and cylindrical geometry with uniform length, shape, and size across the array. It is noted that each set of NWs display a slightly hourglass-like shape, which is also observed in previous top-down etched III-V NW studies due to a slight lateral etching during this process.[18]

The optical property of the NWs was characterised by room temperature photoluminescence (PL) and time-resolved photoluminescence (TRPL) measurements as mentioned in Chapter 3, section 3.5. As shown in Figure 4-3a, the PL peak intensity is diameter-related: the larger diameter has higher peak intensity in the PL spectrum, due to the higher ratio of surface-to-bulk. The PL lifetime was extracted by fitting a single-exponential decay of the TRPL intensity decay at the peak wavelength, see Figure 4-3b,

c, showing a similar trend. It is well known that the carrier lifetime of the semiconductor materials is extremely sensitive to a small density of impurities or intrinsic defects and hence an ideal parameter for evaluation of material quality and process control. Since the NWs are obtain from the same undoped InP wafer featuring very high purity, the surface defects caused by plasma-induced damage during top-down etching process are the main reason for the variation in lifetime of NWs from different NW arrays.

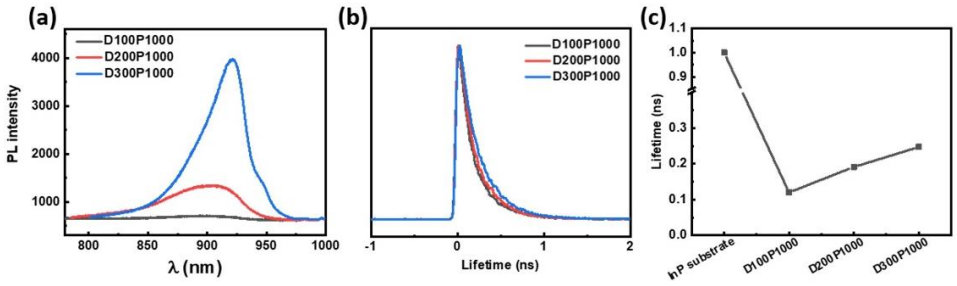

Figure 4-3. PL spectra of single InP NWs transferred from NW arrays (a). Normalised PL intensity and lifetime extracted from TRPL measurement results (b, c).

4.1.3 Chemiresistive nanowire array sensor fabrication

To enable chemiresistive sensing measurements, each single NW needs to be electrically contacted such that their resistivity change can be measured. A tilt-angle deposition method[15] was employed to contact/connect each NW in the array to allow for electrical measurements while partially exposing the NW surface at the same time for gas sensing, following the detailed fabrication process as schematically illustrated in Figure 4-4:

i) Photoresist SU8-2 (Kirsten Hackenbroich) was spin-coated on the NW array to fully covered all the NWs.

ii) The SU8-2 was etched back by a barrel-etcher (PVA Tepla Gigabatch 310 M) to expose half of the InP NWs for further electrical contact.

iii) After that, the sample was flood exposed under UV illumination and baked at 200 °C to cure the SU8-2. Here the SU8-2 acts as an isolation layer to prevent the deposited Au electrode (on NWs) from contacting the substrate.

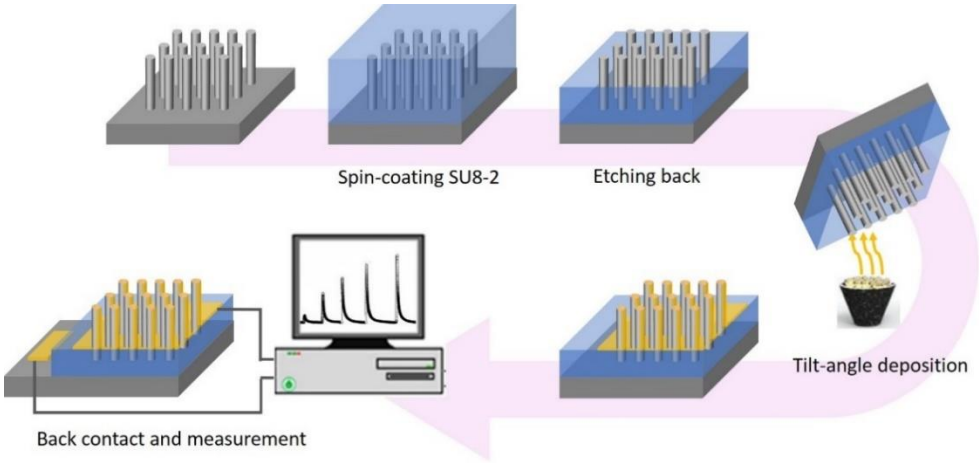

Figure 4-4. Schematic of the fabrication process for InP NW array chemiresistor.

iv) An e-beam evaporator was used to deposit a Ti 10nm/ Au 80 nm Au film on the NWs for contacting and the samples were mounted on a special holder to enable tilt-angle deposition. Deposition at an angle ensures that part of the NWs surface is exposed for reaction with the analytes, while the metal contacts will serve as contacts on etch NWs in array for electrical measurements or connections.

v) Finally, a 200 nm-thick Au layer was deposited on the InP substrate for bottom contact. The fabricated devices were then characterised for their sensing performance.

Figure 4-5 presents the SEM images of the InP NW array taken after each fabrication step, with Figure 4-5a showing the as-fabricated InP NW array, Figure 4-5b showing the planarization of NW array by spin-coating of SU8-2 to cover the bottom of the NWs. Figure 4-5c shows the tilt-angle deposition of Au on one side of NWs to connect every NW in the array. It is also clear that at least half of the NW surface is exposed in air, to allow analyte to directly reach the active layer of each NW. A cross-sectional image in

Figure 4-5d was obtained by cutting the NW array in the middle, confirming that the SU8-2 layer uniformly covered the substrate to not only prevent the Au layer from shorting the InP substrate but also to improve the mechanical stability of the NWs.

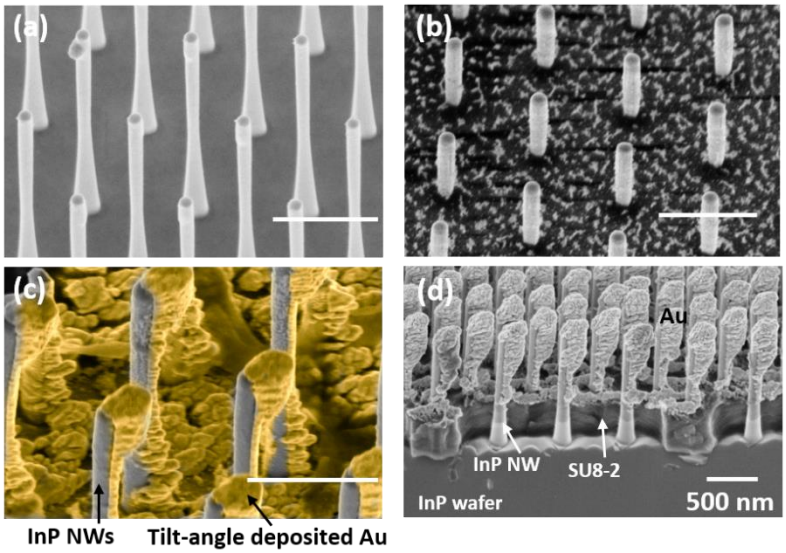

Figure 4-5. SEM images of InP NW sensor fabrication process with the step of (a) as-fabricated InP NWs. (b) InP NWs planarized by SU8-2. (c) Tilt-angle deposition of the Au contact layer. The yellow color in this image was modified by Adobe Photoshop. (d) Cross-sectional image of the NW array after tilt-angle deposition. All the scale bars are 500 nm.

4.1.4 Nanowire sensor measurements

The gas sensing performance was measured by a home-made sensing setup as mentioned in Chapter 3, section 3.5. For all gas sensing measurements, the carrier gas was simulated air with N_2 and O_2 (V_{N2}/V_{O2} = 4, N_2 and O_2 purity 99.99%). The gas flow rate was controlled by MFCs, with the total gas flow rate kept at 1 $L \cdot min^{-1}$ for ppm level concentrations and selectivity measurements for sample D100P1000. The gas flow rate was kept at 0.5 $L \cdot min^{-1}$ for sub-ppm level concentration test and selectivity measurements for sample D100P400. The NO_2 sensing measurements were performed at room-temperature in dark condition. The current (I) was measured at a bias voltage of 0.5 V.

As shown in Figure 4-6, when the NW array is exposed to NO_2, the current decreases immediately and then reach saturation. When air is injected from the inlet to remove the adsorbed NO_2 from the NWs,[18-19] the current increases again to the initial background level.

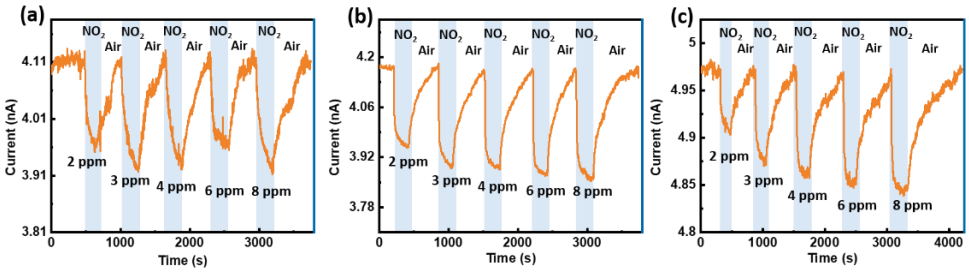

Figure 4-6. Raw data from sensing measurement system with samples D300P1000 (a), D200P1000 (b), D100P1000 (c).

It is noteworthy that the power (P) requirement for operation of our InP NW array sensor is around 2.06 nW ($P = I \times V$= 4.11 nA × 0.5 V, I: current; V: voltage) with a baseline current of ~ 4.11 nA under the bias voltage of 0.5 V, owing to the small device size (400 μm × 400 μm NW array) and nano-scale InP NWs. Such power consumption is way below the near-zero power applications threshold of 10 nW, as defined by "The Near Zero Power RF and Sensor Operations (N-ZERO) program from DARPA".[19]

To find out the optimised NO_2 sensing measurement condition, the sensing experiment was measured under different temperatures of 25, 50, 100, and 150 °C as shown in Figure 4-7, showing an enhancement with temperature rising from 25 to 100 °C. This is consistent with a previous study on an InP epitaxy layer based NO_2 sensor,[18] ascribing the increased response to more activated NO_2 adsorption at higher temperature. However, when the temperature was further increased to 150 °C, the sensing responses decrease to the values similar to those measured at 50 °C. This may be due to the large increase of semiconductor conductivity to > 10^{-3} S·cm^{-1} at high temperature (>100 °C) and thus an

increased the baseline current, leading to a decrease in calculated sensing response. It is worth noting that the response and recovery time (25 / 70 s) measured at 150 °C is much shorter than those at lower temperatures (43 / 160 s at 25 °C), which may be ascribed to the accelerated gas molecular movement and collision frequency with NWs that speed up the gas molecule adsorption and desorption processes at higher temperatures.

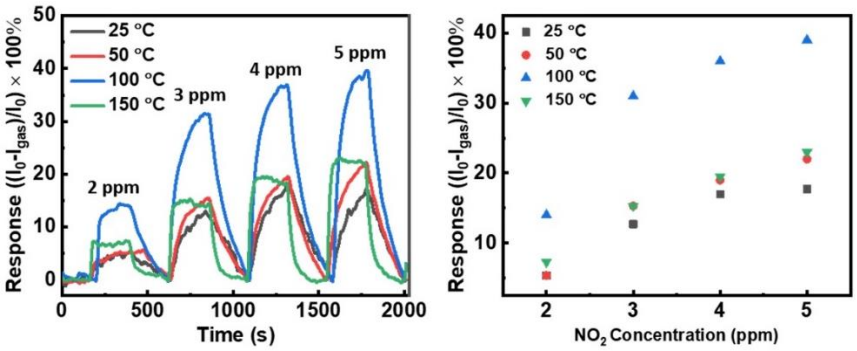

Figure 4-7. Time-dependent NO_2 sensing measurement at temperature of 25-150 °C, and the corresponding sensing response against NO_2 concentration.

4.2 Investigation of NW array geometry effect

4.2.1 Nanowire diameter effect

The resulting array morphologies with different diameter (D) and pitch size (P) are shown in the SEM images of Figure 4-8. To quantify the sensing performance, the change in current ratio, $R = (I_{air} - I_{gas}) / I_{air} \times 100\%$ is calculated and plotted in Figure 4-9 a-c for sensors with a diameter of 100, 200, 300 nm and pitch size of 1000 nm (D100P1000, D200P1000, D300P1000).[20-22] It can be clearly observed that the sensing response increases dramatically with decreasing NW diameter. The sample with 100 nm diameter (D100P1000) shows the highest response reaching 13.9% at 8 ppm NO_2, while those from the 200 nm diameter sample (D200P1000) and 300 nm diameter sample (D300P1000) are 8.1% and 4.0%, respectively. The overall sensing response shows a concentration-dependent trend for each sample (Figure 4-9d), with an improved sensitivity and linearity

with the decrease of NW diameter. This is closely related to the NW sensing mechanism and will be further discussed in detail.

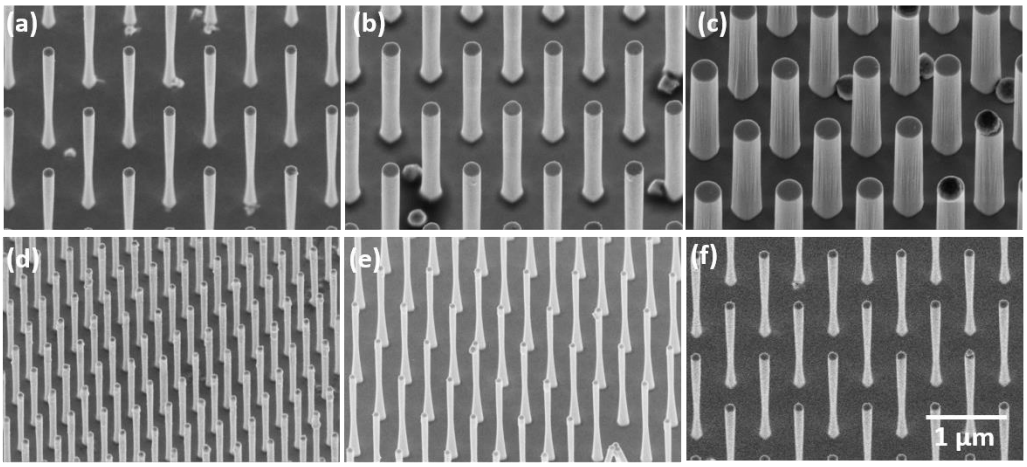

Figure 4-8. SEM images of top-down etched InP NWs array with different diameter and pitch size. (a) D100P1000 (b) D200P1000 (c) D300P1000 (d) D100P400 (e) D100P600 (f) D100P800. (D: diameter; P: pitch size in nm)

The response/recovery time is another important sensor performance of merit and is defined by the time taken for the sensing signal to change from the baseline with or without the analyte to 90% maximum/minimum value. As shown in Figure 4-9e, the response time of our NW arrays is in the range of 40 - 140 s with a slightly shorter response time to higher NO_2 concentrations. This is substantially faster than those measured from bulk InP sensors which display a typical response time in the range of 20 min.[23-24] We attribute the fast response time of NW array sensors to their nanoscale size and the NW array geometry. The selectivity of the D100P1000 sample was also investigated by measuring the sensing response to other common VOCs and gases in the environment (methanol (CH_3OH), ethanol (C_2H_5OH), methyl nitrite (CH_3NO_2), and propane (C_3H_8)) with concentration of 2 ppm and carbon dioxide (CO_2) of 2%. The sensing response to NO_2 is significantly higher than the response against other gases, indicating that InP NWs are highly selective towards NO_2 (Figure 4-9f) as a result of its

higher electron affinity (2.27 eV) [25] than the other gases tested here such as CO_2 (-0.60 eV)[26]. For reducing gases such as propane, methanol and ethanol, the D100P1000 sample shows a negative response which may arise from the reaction between the reducing gas and oxygen species pre-adsorbed on NW surface to release electrons to the NW.

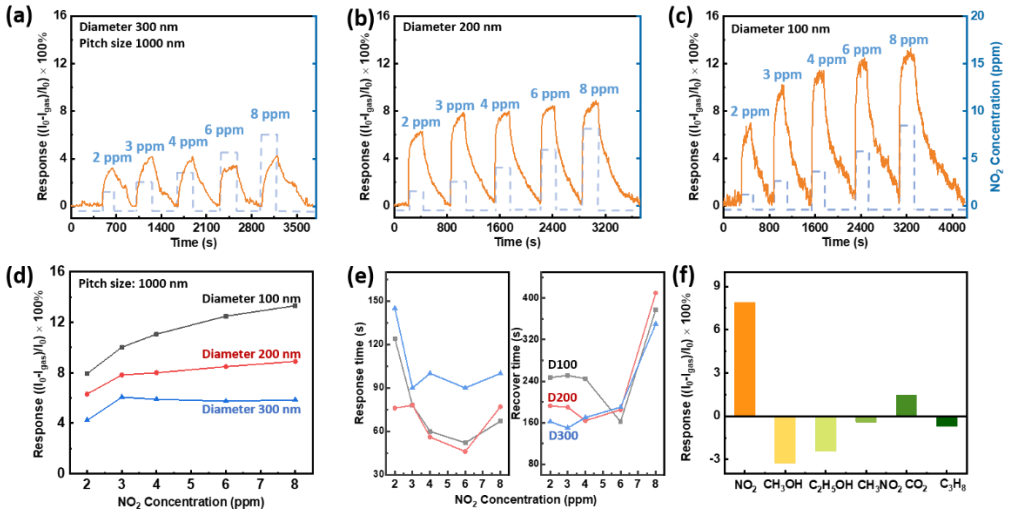

Figure 4-9. Time-dependent sensor response of D300P1000, D200P1000, D100P1000 InP NWs to the NO_2 concentration of 2-8 ppm (a-c). NO_2 concentration dependent sensor response: $R = (I_0 - I_{gas})/I_0$ and response time (d, e). Selectivity measurement on D100P1000 with 2 ppm NO_2, methanol, methyl nitrite, ethanol, CO_2, and propane (f).

4.2.2 Nanowire pitch (density) effect

To further investigate the relationship between the NW geometry and the sensing performance, InP NWs with 100 nm in diameter and smaller pitch sizes of 400 and 600 nm were fabricated. The sensing response measured under a lower NO_2 concentration range from 200 - 1000 ppb for these NW arrays are presented in Figure 4-10 a-c, respectively. The 400 nm NW pitch (D100P400) array achieves the highest sensitivity to NO_2 among all three samples with a sensing response of up to 8.7 % to 200 ppb NO_2, which is approximately 3 times higher than that of the 600 nm pitch (D100P600) sample

(2.9 %), and more than 10 times higher than that of the 1000 nm pitch sample D100P1000 (< 1%).

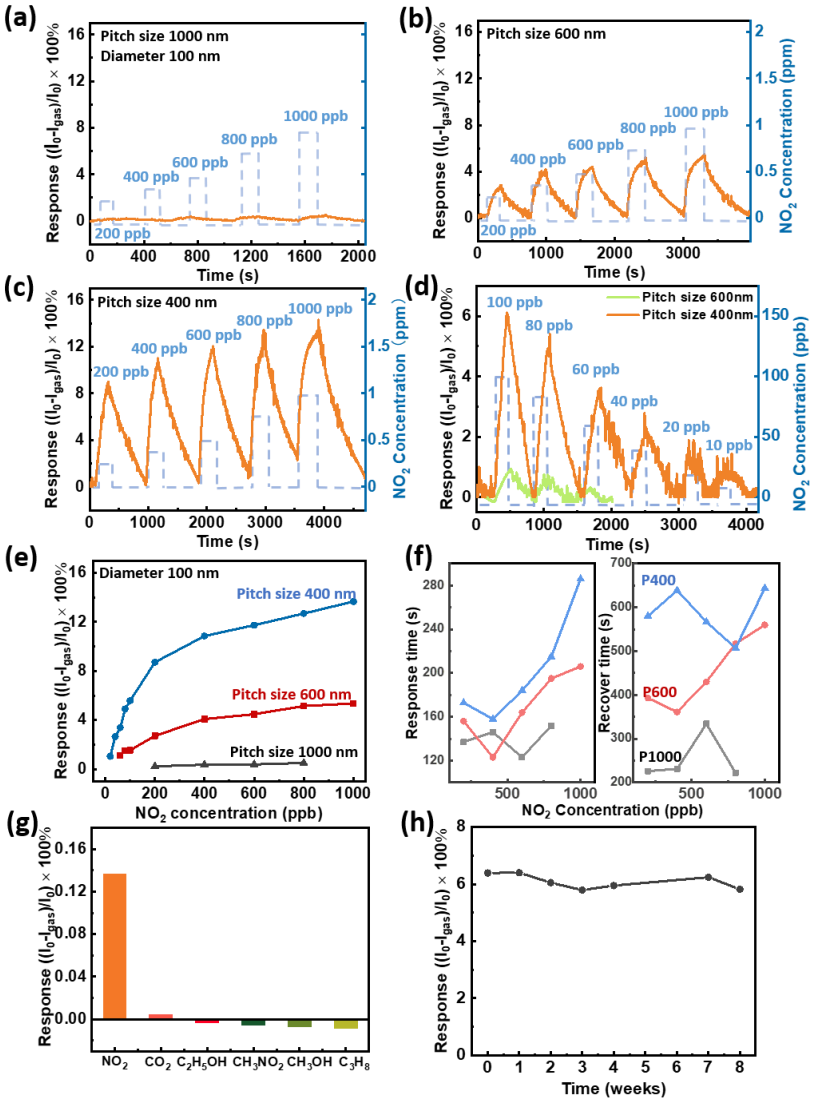

Figure 4-10. Time-dependent sensor response of D100P1000, D100P600, D100P400 to NO_2 with the concentration of 200-1000 ppb (a-c). (d) Limit of detection measurement for samples D100P600 and D100P400. (e, f) NO_2 concentration dependent sensing response and response time. (g) Selectivity measurement with 1 ppm NO_2, methyl nitrite (CH_3NO_2), acetone (C_3H_6O), propane (C_3H_8), ethanol (C_2H_5OH), and carbon dioxide (CO_2) of 1% (h) Air stability of D100P400 sensing response with 100 ppb NO_2 measured on a weekly basis for two months.

To obtain the limit of detection (LOD) of these NW sensors, a lower concentration range 10 - 100 ppb was further measured (Figure 4-10d) and calculated based on the theory in

Chapter 2, section 2.3.[27-28] With the linear fitting result in Figure 4-11, an extremely low theoretical LOD of ~ 3.1 ppb (slope = 0.056 %/ppb) is exhibited by sample D100P400.

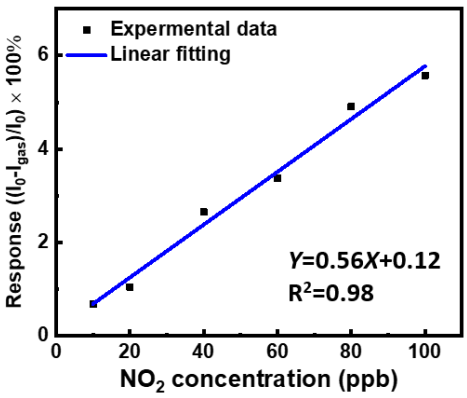

Figure 4-11. Concentration dependent sensor response from sample D100P400 and the linear fitting result.

Furthermore, the concentration-response curves of the samples are also plotted in Figure 4-10e again showing a trend of saturation in the slope with the lowest on-set observed for the sample with 1000 nm pitch size, suggesting that the saturation effect arises from the low density of adsorption sites. Although sample D100P400 features the highest response, it is also noted from Figure 4-10f that its response / recovery times (160-290 s; 500-650 s) are longer than those of D100P600 and D100P1000 at the same concentrations. This is attributed to the high NW density which may form a diffusion barrier for gas molecules to diffuse and adsorb. As can be noted from Figure 4-10d and f, the recovery time of D100P400 at low analyte concentrations (10 - 40 ppb) is much shorter than that at high concentrations, decreasing from 600 s to 300 s, which may be due to the longer time required to equilibrate the high concentration analyte on the NW surface. To ensure the practical application of the sensors and to investigate the robustness of the sensors, the air stability of the D100P400 array was investigated for 8 consecutive weeks. The device was stored in ambient condition during this process. Figure 4-10h shows that the sensing

performance of the device can be maintained at around 95 % of its original response level over a period of two months, confirming the excellent stability of these InP NW arrays.

The selectivity of D100P400 towards NO_2 is also enhanced with an improvement in NO_2 sensing response (12.9% @1 ppm), which is more than 20 times higher than response to other gases at the same concentration of 1 ppm. To highlight the selective response towards NO_2, sensing measurements were also performed in the presence of competing gases, such as ethanol, CO_2, propane and acetone as detailed in Chapter 3, section 3.5, confirming that our InP NW array maintains high sensitivity towards NO_2 even with higher competing gas concentrations as shown in Figure 4-12. This ensured that the concentration of competing gases was higher than that of the analyte, NO_2. As shown in Figure 4-12a, the NO_2 sensing response decreased in the presence of competing gases, especially with reducing gases such as acetone, ethanol and propane. However, the decline of the sensing response is still less than 50%, compared to that without competing gases. Figure 4-12b shows that the sensing response to NO_2 is concentration-dependent under the presence of the competing gases. Figure 4-12c summarises the sensing response to 5 ppm NO_2 and competing gases (with/without mixing), highlighting the good sensing selectivity of our InP NW array sensor towards NO_2 even in the presence of high concentration of competing gases.

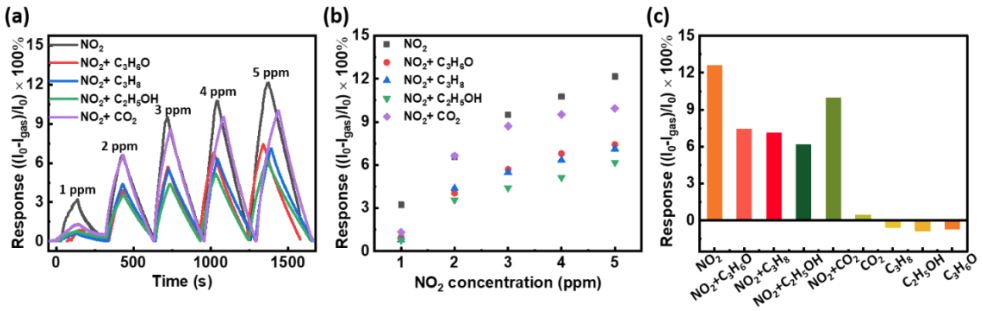

Figure 4-12. Time-dependent NO_2 sensing measurement for an InP NW array sensor (D100P400) mixed with competing gases: acetone, propane, and ethanol at concentration of 5 ppm, and carbon

dioxide of 5 % with NO_2 concentration 1-5 ppm (a). (b) Calculated response vs concentration results from (a). (c) Selectivity measurement by measuring the response from NO_2, C_3H_6O, C_3H_8, C_2H_5OH, and CO_2, in comparison with the competing gas study result.

Sensing measurements were performed with the D100P400 NW sensor under relative humidity (RH) from 10% to 90 %, as shown in Figure 4-13. The results show that even with a high concentration of water vapour (RH 90%), the NW sensor still demonstrates high sensitivity (linear fitting slope = 182 %/ppm), despite a small degradation (around 35% from its original level), demonstrating excellent humidity tolerance compared with other sensing materials such as carbon nanotubes[29] and metal oxides.[30]

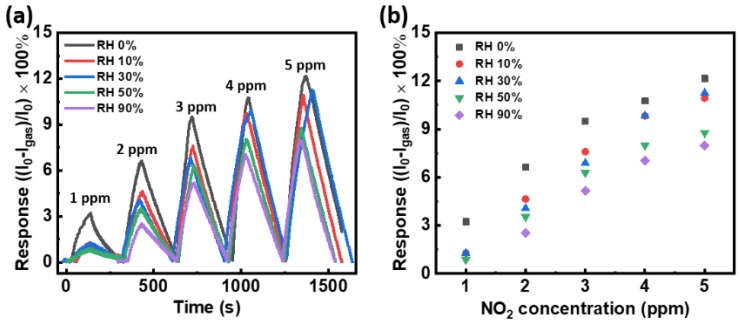

Figure 4-13. Time-dependent NO_2 sensing response from a D100P400 NW array under relative humidity (RH) 10%, 30%, 50% and 90% (a). (b) Calculated response vs concentration results from (a).

4.3 Investigation of NO_2 sensing mechanism

Chemiresistive sensor relies on resistance change during their operation as a result of electron transfer between the active layer and the analyte. For InP NWs studied in this work, the sensing mechanism can be explained by via a two-step surface adsorption-charge transfer mechanism proposed in previous studies[18, 31]: 1) NO_2 gas molecules adsorption on the surface of InP NW as $NO_{2(ad)}$ molecules; and 2) $NO_{2(ad)}$ molecules

ionised into chemisorbed species such as NO_2^- at relatively low temperature (<150 °C) by capturing electrons from the InP NW because of its high electron affinity (2.273 eV). This process creates an electron surface depletion layer on the NW, turning it into a high resistance state. These two steps can be summarised as follows:

$$NO_{2(gas)} \leftrightarrow NO_{2(ad)} \quad (1)$$

$$NO_{2(ad)} + e^- \leftrightarrow {NO_2}^-_{(ad)} \quad (2)$$

It is noted that the native oxide layer (such as In_2O_3) on the surface of InP NWs could also contribute to the sensing response based on a different sensing mechanism found in metal-oxide gas sensors.[19] However, as shown by the previous reports,[32] the working temperatures of various nanostructured In_2O_3 sensors are required to be between 100 - 300 °C for good sensing response. Therefore, the highly sensitive room temperature performance of our InP NW array devices indicates that such mechanism may not play a dominant role during the sensing process.

To investigate the adsorption kinetics of the NO_2 gas molecules on the InP NWs during the sensing process (step (1)), an exponential fitting was employed to quantify molecular binding affinities based on the Langmuir isotherm model.[16] Through fitting the sensing response vs time curves from all NW samples, as shown in Figure 4-14a, b, the kinetic adsorption of gas molecules in sensing reaction (assuming the NWs surface is homogeneous) can be described using the following equations[18]:

$$[\mathrm{AB}]_{\mathrm{adsorption}} = \frac{k_a[\mathrm{B}]\times[\mathrm{A}]}{k_a[\mathrm{A}]+k_d}(1 - e^{-(k_a[A]+k_d)t}) \quad (3)$$

$$[\mathrm{AB}]_{\mathrm{desorption}} = \frac{k_a[\mathrm{B}]\times[\mathrm{A}]}{k_a[\mathrm{A}]+k_d}(e^{-k_d t}) \quad (4)$$

where [AB] is the NO_2 gas molecule involved in the reaction; k_a (unit: $M^{-1}s^{-1}$) and k_d (unit: s^{-1}) are association and dissociation rate constants, respectively; [A] is the molarity concentration of NO_2; and [B] is the number of binding sites per unit area.

After fitting the experimental sensing response with these two equations, k_a and k_d can be obtained. K_A represents the affinity of gas molecule with InP NWs, and gas adsorption is one of the key steps of the sensing process, directly affecting the sensing performance. Figure 4-14c shows that there is a clear correlation between K_A and NW diameter and density (corresponding to pitch size). For the NW samples with the same diameter (D100P1000, D100P600, D100P400), K_A and sensing response increase with NW density (Figure 4-14c, left panel), due to increased adsorption sites corresponding to the surface area (D100P1000: 4.7×10^4 μm^2, D100P600: 8.9×10^4 μm^2, D100P400: 18.0×10^4 μm^2). However, for the NW array with the same pitch size, i.e., the same NW density, a negative correlation between K_A and NW diameter can be found in Figure 4-14c (right panel), showing better sensing performance for smaller diameter NWs. This is associated with step (2) of the InP NW sensing process, when NO_2(ad) molecules are ionised into NO_2^- by capturing electrons from the NW surface, as studied by the electrical simulation below.

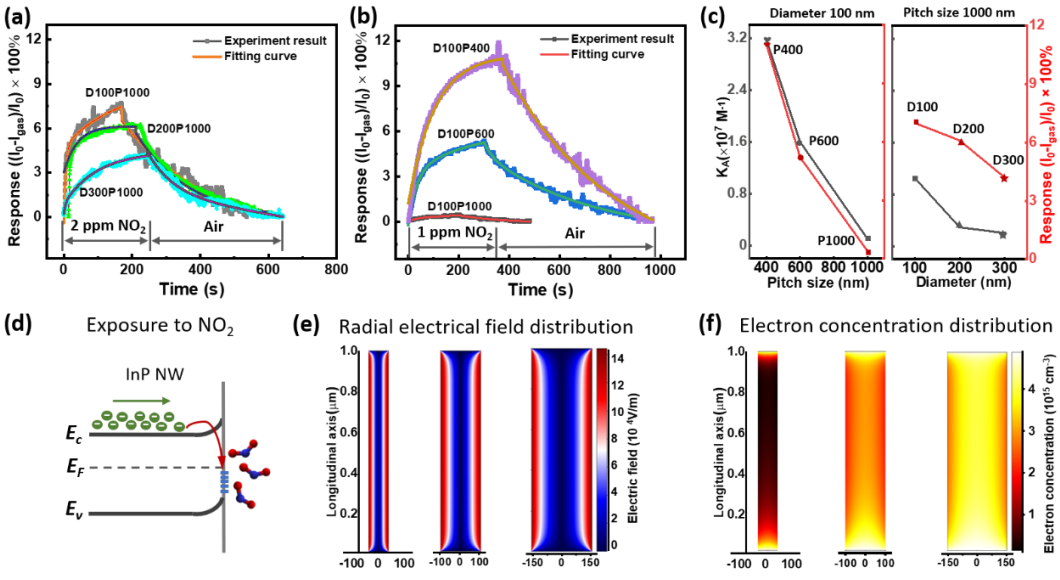

Figure 4-14. Quantification of the affinities of NO_2 with InP NWs by fitting real-time sensor responses to the Langmuir isotherm model (a, b). (c) Calculated association constant K_A and the corresponding response for samples of different pitch size and diameter. (d) Schematic energy

band diagram of the InP NW during NO_2 exposure. (e, f) Simulated electric field and electron concentration distributions across the InP NWs with diameter of 100, 200, 300 nm during NO_2 exposure.

The charge transfer process on the NW surface and its effect on chemiresistor performance of NWs with different diameters (step (2)) was studied by modelling of the electrical properties of InP NWs using the semiconductor module in COMSOL Multiphysics (The simulation studied was conducted by Dr. Zhe Li).[32-33] Ohmic contact was assumed at the top and the bottom of the NW and a uniform N-type doping profile of 5×10^{15} cm^{-3}. To fully utilise the device symmetry, a 2D axis-symmetric geometry was used, as an approximation of the 3D cylindrical structure of the NW. The resistivity change of the NWs during gas sensing is modelled by introducing defect centre at NW surface, since the adsorption of oxidative gas such as NO_2 at the n-type NW surface creates acceptor-like surface states that can capture electrons, thus forming a surface depletion layer and leading to reduced conductivity as shown in (Figure 4-14d).[34] The simulation was performed for three samples: D100P1000, D200P1000 and D300P1000, subjected to the same surface defect density (SRV 10^{10} cm^{-2}) and surface recombination velocity (10^4 cm/s). The SRV was calculated based on the measured lifetime data equation $(1/\tau_{mc}) = (1/\tau_{bulk}) + (4SRV/d)$, where τ_{mc}, τ_{bulk} and d are the NW, bulk minority carrier lifetime and NW diameter, respectively.[35] As shown in Figure 4-3, the minority carrier lifetimes of samples D300P1000, D200P1000, D100P1000 are 0.24, 0.19, 0.13 ns, respectively.

Figure 4-14e, f shows the distributions of radial electric field and electron concentration over the cross-section of the NW at a bias of 0.5 V, together with an illustrative band diagram in Figure 4-14d highlighting carrier depletion due to surface band bending.

Figure 4-14e shows that the magnitude of radial electric field is the same for all three cases since they are subjected to similar surface conditions; however, thicker NWs can preserve a highly conductive channel in their central region and thus is much less affected by the surface depletion as compared to thinner NWs. This is further evident in Figure 4-14f, where the electron concentration in the middle region of D100P1000 sample is nearly five times smaller than its background doping concentration, whereas for D300P1000, the electron concentration in the centre is only slightly less than the background doping concentration. Clearly, surface depletion has a much stronger impact on small-diameter NWs leading to a highly sensitive sensing performance. The simulation results in this work can also explain the similar characteristics observed in other material systems. For example, Qin et.al. reported that thinner WO_3 NWs showed a rapid response and a relative higher response value to the same concentration of NO_2 gas compared to nanorods, due to their smaller diameter.[36] As enabled by the highly uniform ordered NW array platform, our combined kinetic analysis and electrical simulation illustrate the significant effect of NW geometry on NO_2 sensing response, which could inspire future design and implementation of electrical structures such as p-n junctions in NWs and/or surface functionalization approaches for broader sensing applications.

Finally, to benchmark the performance of our NW array sensors, we compare their key performance parameters with various types of chemiresistive NO_2 sensors reported in recent years, as summarised in Table 4-1, including bulk InP, InAs NWs, and metal-oxide materials. In comparison, our InP NW array NO_2 sensor studied in this work demonstrates the lowest LOD (10 ppb), the shortest response time (43 s) and room-temperature operation with excellent air stability, indicating a strong potential for gas sensing application. It is also worth highlighting that based on the top-down etching approach, multiple NW arrays with different geometries can be easily designed and fabricated

simultaneously to form sensor arrays to detect multiple gas species and/or generate multi-channel sensing signal to realise high performance on-field real-time gas monitoring sensor module.[16]

Table 4-1. Sensing performance of NO_2 sensor in this work in comparison with recently reported chemiresistive NO_2 sensors.

Material	Sensitivity (%) (1 ppm)	LOD (ppm)	Response/recovery time	Working temperature (°C)	Ref
InP-NWs	12.9	0.01	43/127 s	25	This work
n-InP-epitaxy layer	6	0.1	1800/3600 s	80	[18]
InAs/InP -NWs	21	0.03	-	50	[37]
InAs-NWs	17	0.15	2400/2200 s	25	[38]
Pd-In_2O_3-NWs	6	1	71/100 s	110	[32]
ZnO	12	0.03	-	150	[39]
ZnO/Graphene	21	0.05	182/234 s	110	[40]
SnO_2-NWs	81	0.05	-	300	[41]
Pt/WO_3	18	0.5	198/225 s	400	[42]
MoS_2/Graphene	12	0.05	-	200	[43]
Ni-MOF	85	0.5	2700/- s	50	[44]

4.4 Summary

A novel miniaturised room-temperature NO_2 gas sensor design based on vertical array of InP NWs has been successfully demonstrated in the chapter. The NW sensors were fabricated by a top-down etching approach with precise control of the NW diameter and pitch size, followed by a tilt-angle deposition technique to contact/connect the vertical NWs to form the chemiresistive sensing devices. Owing to their nanoscale size and unique one-dimensional geometry, the NW sensors achieved room-temperature operation with fast response/recover time, <10 ppb level of sensitivity, excellent selectivity and air stability, outperforming most recently reported NO_2 gas sensors. A systematic investigation of the impact of NW diameter and pitch size on the sensing response show

that larger NW density (smaller pitch) and smaller NW diameter lead to better sensing performance. The sensing mechanism is studied by theoretical modelling of the NW array adsorption kinetics and electrical simulation of NW structures, revealing a strong NW geometry related gas adsorption and electron transfer/depletion process. Owing to the flexibility in InP NW material composition, geometry and electrical designs, InP NW arrays present a promising new nanomaterial platform for the development of future miniaturised, high performance, multifunctional on-chip chemical sensing technology.

References

[1] J. G. Chen, R. M. Crooks, L. C. Seefeldt, K. L. Bren, R. M. Bullock, M. Y. Darensbourg, P. L. Holland, B. Hoffman, M. J. Janik, A. K. Jones, M. G. Kanatzidis, P. King, K. M. Lancaster, S. V. Lymar, P. Pfromm, W. F. Schneider and R. R. Schrock, Beyond fossil fuel-driven nitrogen transformations. *Science*, **360**, 7 (2018).

[2] M. Eeftens, J. Beekhuizen, R. Beelen, M. Wang, R. Vermeulen, B. Brunekreef, A. Huss and G. Hoek, Quantifying urban street configuration for improvements in air pollution models. *Atmospheric Environment*, **72**, 1-9 (2013).

[3] Rosenbaum, S. Hartley, C. Holder, A. Turley and S. Graham, Nitrogen Dioxide (NO_2) Exposure Assessment in Support of US EPA's NAAQS Review: Application of AERMOD and APEX to Philadelphia County. *Epidemiology*, **19**, S344-S345 (2008).

[4] E. D. Lebel, C. J. Finnegan, Z. Ouyang and R. B. Jackson, Methane and NOx Emissions from Natural Gas Stoves, Cooktops, and Ovens in Residential Homes. *Environmental Science & Technology*, **56**, 2529-2539 (2022).

[5] F. O'Leary, A. B. Hill, K. G. Akers, H. J. Esparra-Escalera, A. Lucas, G. Raoufi, Y. X. Huang, N. Mariscal, S. K. Mohanty, C. M. Tummala and T. M. Dittrich, Air quality monitoring and measurement in an urban airshed: Contextualizing datasets from the Detroit Michigan area from 1952 to 2020. *Science of the Total Environment*, **809**, 152120 (2022).

[6] J. W. Leonhardt, A new ppb-gas analyzer by means of GC-ion mobility spectrometry (GC-IMS). *Journal of Radioanalytical and Nuclear Chemistry*, **257**, 133-139 (2003).

[7] H. W. Jin, R. Z. Hu, P. H. Xie, H. Chen, Z. Y. Li, F. Y. Wang, Y. H. Wang and C. Lin, Photo-acoustic technology applied to ppb level NO_2 detection by using low power blue diode laser. *Acta Physica Sinica*, **68**, 8 (2019).

[8] T. Takayanagi, X. L. Su, P. K. Dasgupta, K. Martinelango, G. G. Li, R. S. Al-Horr and R. W. Shaw, Chemiluminometric measurement of atmospheric ozone with photoactivated chromotropic acid. *Analytical Chemistry*, **75**, 5916-5925 (2003).

[9] S. Schutting, S. M. Borisov and I. Klimant, Diketo-Pyrrolo-Pyrrole Dyes as New Colorimetric and Fluorescent pH Indicators for Optical Carbon Dioxide Sensors. *Analytical Chemistry*, **85**, 3271-3279 (2013).

[10] X. Zhou, S. Lee, Z. C. Xu and J. Yoon, Recent Progress on the Development of Chemosensors for Gases. *Chemical Reviews*, **115**, 7944-8000 (2015).

[11] G. Barillaro and L. M. Strambini, An integrated CMOS sensing chip for NO_2 detection. *Sensors and Actuators B-Chemical*, **134**, 585-590 (2008).

[12] G. Guillaud, J. Simon and J. P. Germain, Metallophthalocyanines - Gas sensors, resistors and field effect transistors. *Coordination Chemistry Reviews*, **178**, 1433-1484 (1998).

[13] K. Murugappan and M. R. Castell, Bridging electrode gaps with conducting polymers around the electrical percolation threshold. *Electrochemistry Communications*, **87**, 40-43 (2018).

[14] N. Mkhize, K. Murugappan, M. R. Castell and H. Bhaskaran, Electrohydrodynamic jet printed conducting polymer for enhanced chemiresistive gas sensors dagger. *Journal of Materials Chemistry C*, **9**, 4591-4596 (2021).

[15] K. Ren, K. M. Azizur-Rahman, Z. X. Rong, B. C. Juang, S. Somasundaram, M. Shahili, A. C. Farrell, B. S. Williams and D. L. Huffaker, Room-Temperature Midwavelength Infrared InAsSb Nanowire Photodetector Arrays with Al_2O_3 Passivation. *Nano Letters*, **19**, 2793-2802 (2019).

[16] H. G. Moon, Y. Jung, B. Shin, Y. G. Song, J. H. Kim, T. Lee, S. Lee, S. C. Jun, R. B. Kaner, C. Y. Kang and C. Kim, On-Chip Chemiresistive Sensor Array for On-Road $NO_{(x)}$ Monitoring with Quantification. *Advanced Science*, **7**, 9 (2020).

[17] X. X. Duan, Y. Li, N. K. Rajan, D. A. Routenberg, Y. Modis and M. A. Reed, Quantification of the affinities and kinetics of protein interactions using silicon nanowire biosensors. *Nature Nanotechnology*, **7**, 401-407 (2012).

[18] V. Battut, J. P. Blanc, E. Goumet, V. Souliere and Y. Monteil, NO_2 sensor based on InP epitaxial thin layers. *Thin Solid Films*, **348**, 266-272 (1999).

[19] L. Talazac, J. P. Blanc, J. P. Germain and A. Pauly, NO_2 detection by a resistive device based on n-InP epitaxial layers. *Sensors and Actuators B-Chemical*, **59**, 89-93 (1999).

[20] V. Raj, K. Vora, L. Fu, H. H. Tan and C. Jagadish, High-Efficiency Solar Cells from Extremely Low Minority Carrier Lifetime Substrates Using Radial Junction Nanowire Architecture. *ACS Nano*, **13**, 12015-12023 (2019).

[21] H. Wang, M. H. Sun, K. Ding, M. T. Hill and C. Z. Ning, A Top-down Approach to Fabrication of High Quality Vertical Heterostructure Nanowire Arrays. *Nano Letters*, **11**, 1646-1650 (2011).

[22] X. Zhao and J. A. del Alamo, Nanometer-Scale Vertical-Sidewall Reactive Ion Etching of InGaAs for 3-D III-V MOSFETs. *Ieee Electron Device Letters*, **35**, 521-523 (2014).

[23] L. Talazac, F. Barbarin, C. Varenne and Y. Cuminal, Highly NO_2 sensitive pseudo Schottky barrier diodes on p-type InP with improved electrical characteristics. *Sensors and Actuators B-Chemical*, **77**, 447-454 (2001).

[24] K. Wierzbowska, B. Adamowicz, L. Mazet, J. Brunet, A. Pauly, L. Bideux, C. Varenne, B. Laure and J. P. Germain, High-sensitivity NO_2 sensor based on n-type InP epitaxial layers. *Optica Applicata*, **35**, 655-662 (2005).

[25] K. M. Ervin, J. Ho and W. C. Lineberger, Ultraviolet photoelectron spectrum of nitrite anion. *The Journal of Physical Chemistry*, **92**, 5405-5412 (1988).

[26] M. Knapp, O. Echt, D. Kreisle, T. D. Mark and E. Recknagel, FORMATION OF LONG-LIVED CO_2-,N_2O-, AND THEIR DIMER ANIONS, BY ELECTRON-ATTACHMENT TO VANDERWAALS CLUSTERS. *Chemical Physics Letters*, **126**, 225-231 (1986).

[27] T. Pham, G. H. Li, E. Bekyarova, M. E. Itkis and A. Mulchandani, MoS_2-Based Optoelectronic Gas Sensor with Sub-parts-per-billion Limit of NO_2 Gas Detection. *Acs Nano*, **13**, 3196-3205 (2019).

[28] W. Yang, H. T. Chen and J. M. Lu, Assembly of stacked In_2O_3 nanosheets for detecting trace NO_2 with ultrahigh selectivity and promoted recovery. *Applied Surface Science*, **539**, 9 (2021).

[29] M. Shooshtari, A. Salehi and S. Vollebregt, Effect of humidity on gas sensing performance of carbon nanotube gas sensors operated at room temperature. *IEEE Sensors Journal*, **21**, 5763-5770 (2020).

[30] Nasriddinov, M. Rumyantseva, E. Konstantinova, A. Marikutsa, S. Tokarev, P. Yaltseva, O. Fedorova and A. Gaskov, Effect of humidity on light-activated NO and NO_2 gas sensing by hybrid materials. *Nanomaterials*, **10**, 915 (2020).

[31] K. Y. Ko, J. G. Song, Y. Kim, T. Choi, S. Shin, C. W. Lee, K. Lee, J. Koo, H. Lee, J. Kim, T. Lee, J. Park and H. Kim, Improvement of Gas-Sensing Performance of Large-Area Tungsten Disulfide Nanosheets by Surface Functionalization. *Acs Nano*, **10**, 9287-9296 (2016).

[32] M. Q. Huang, Z. D. Cui, X. J. Yang, S. L. Zhu, Z. Y. Li and Y. Q. Liang, Pd-loaded In_2O_3 nanowire-like network synthesized using carbon nanotube templates for enhancing NO_2 sensing performance. *Rsc Advances*, **5**, 30038-30045 (2015).

[33] Yang, Z. Y. Li, J. Wong-Leung, Y. Zhu, Z. Li, N. Gagrani, L. Li, M. N. Lockrey, H. Nguyen, Y. R. Lu, H. H. Tan, C. Jagadish and L. Fu, Multiwavelength Single Nanowire InGaAs/InP Quantum Well Light-Emitting Diodes. *Nano Letters*, **19**, 3821-3829 (2019).

[34] Y. Kim, S. Lee, J. G. Song, K. Y. Ko, W. J. Woo, S. W. Lee, M. Park, H. Lee, Z. Lee, H. Choi, W. H. Kim, J. Park and H. Kim, 2D Transition Metal Dichalcogenide Heterostructures for p- and n-Type Photovoltaic Self-Powered Gas Sensor. *Advanced Functional Materials*, **30**, 2003360 (2020).

[35] Q. Gao, D. Saxena, F. Wang, L. Fu, S. Mokkapati, Y. A. Guo, L. Li, J. Wong-Leung, P. Caroff, H. H. Tan and C. Jagadish, Selective-Area Epitaxy of Pure Wurtzite InP Nanowires: High Quantum Efficiency and Room-Temperature Lasing. *Nano Letters*, **14**, 5206-5211 (2014).

[36] Y. X. Qin, X. Li, F. Wang and M. Hu, Solvothermally synthesized tungsten oxide nanowires/nanorods for NO_2 gas sensor applications. *Journal of Alloys and Compounds*, **509**, 8401-8406 (2011).

[37] A. Gupta, P. J. Barrios, J. Lapointe, G. C. Aers and C. Storey, Single-mode 2.4 mu m InGaAsSb/AlGaAsSb distributed feedback lasers for gas sensing. *Applied Physics Letters*, **95**, 3 (2009).

[38] P. Offermans, M. Crego-Calama and S. H. Brongersma, Gas Detection with Vertical InAs Nanowire Arrays. *Nano Letters*, **10**, 2412-2415 (2010).

[39] Z. G. Xue, M. Y. Yan, X. Yu, Y. J. Tong, H. Zhou, Y. F. Zhao, Z. Y. Wang, Y. S. Zhang, C. Xiong, J. Yang, X. Hong, J. Luo, Y. Lin, W. X. Huang, Y. F. Li and Y. E. Wu, One-Dimensional Segregated Single Au Sites on Step-Rich ZnO Ladder for Ultrasensitive NO_2 Sensors. *Chem*, **6**, 3364-3373 (2020).

[40] P. J. Cao, Y. Z. Cai, D. Pawar, S. T. Navale, C. N. Rao, S. Han, W. Y. Xu, M. Fang, X. K. Liu, Y. X. Zeng, W. J. Liu, D. L. Zhu and Y. M. Lu, Down to ppb level NO_2 detection by ZnO/rGO heterojunction based chemiresistive sensors. *Chemical Engineering Journal*, **401**, 10 (2020).

[41] H. Kim, A. Mirzaei, J. Y. Kim, J. H. Lee, H. W. Kim, S. Hishita and S. S. Kim, Enhancement of gas sensing by implantation of Sb-ions in SnO_2 nanowires. *Sensors and Actuators B-Chemical*, **304**, 10 (2020).

[42] Q. A. Drmosh, Y. A. Al Wajih, R. Al-Rammah, M. Qamar and Z. H. Yamani, Surface-engineered WO_3 thin films for efficient NO_2 sensing. *Applied Surface Science*, **517**, 10 (2020).

[43] H. Long, A. Harley-Trochimczyk, T. Pham, Z. R. Tang, T. L. Shi, A. Zettl, C. Carraro, M. A. Worsley and R. Maboudian, High Surface Area MoS_2/Graphene Hybrid Aerogel for Ultrasensitive NO_2 Detection. *Advanced Functional Materials*, **26**, 5158-5165 (2016).

[44] J. Small, S. E. Henkelis, D. X. Rademacher, M. E. Schindelholz, J. L. Krumhansl, D. J. Vogel and T. M. Nenoff, Near-Zero Power MOF-Based Sensors for $NO_{(2)}$ Detection. *Advanced Functional Materials*, **30**, 8 (2020).

Chapter 5. Self-Powered Photovoltaic InP Nanowire Array Sensors for Dynamic NO_2 Monitoring

Self-powered sensing systems emerge as one of the most promising solutions to overcome the external-power supply issue for the development of Internet of Things (IoT),[1-3] by harvesting energy from the environment.[4-6] Among various types of self-powered gas sensors, photovoltaic (PV) effect-based sensors have been intensively explored, as the PV effect and gas sensing function can be achieved simultaneously within the same semiconductor active layer, making them highly compact for miniaturisation at relatively low cost.[7-12] However, most of the reported self-powered gas sensors show issues such as limited PV efficiency, sensitivity and selectivity at room temperature,[13] signal drifts and lack of stability over time.[14-15] InP NWs show direct and tuneable bandgap, superior optical and electronic properties, lower surface recombination velocity and higher carrier mobility, which is ideal for PV solar cell applications.[16] Combining their superior PV properties and NO_2 sensitivity, InP NW array is a promising candidate for self-powered sensing.[15-16] To date, despite that a few different III–V NW materials were investigated for gas and biomolecule sensing, InP NWs have rarely been studied as self-powered gas sensors.

In this chapter, a novel InP NW array based gas sensor architecture was demonstrated that combines a PV junction and an active sensing region to achieve highly sensitive, selective, and reproducible self-powered NO_2 sensing at room temperature. Prior to NW growth, the NW and device structure were designed via numerical simulation that models PV NW sensing mechanisms and optimises performance. Then, axial junction based InP NW arrays were grown according to the simulation optimised structures by bottom-up

approach with a careful characterisation. The NW array sensor devices were designed and fabricated to enable robust contacts for signal extraction, while maintaining a large, exposed NW active area for gas sensing. This device presented a high selectivity, and a sub-ppb level limit of detection (LOD), even under a much weaker light intensity than a standard one sun illumination. Finally, this NW sensor can be readily integrated onto a microchip board for on-field dynamic NO_2 concentration measurements from vehicle exhaust pollutant.

5.1 Electrical simulation for the nanowire based self-powered NO_2 sensor

The self-powered InP NW array device design was guided by numerical simulation for insight into sensing mechanism and performance enhancement, performing with the semiconductor module of COMSOL Multiphysics (the simulation study was conducted by Dr. Zhe Li). According to the sensing mechanism discussed in Chapter 4, once the NO_2 molecules adsorb onto the NW surface, the resultant acceptor-like surface states capture electrons from the NW surface,[17] turning it into a high resistance state and leading to a measurable signal of the adsorbed NO_2. Under light illumination, a photocurrent is generated in the p-n junction embedded NWs i.e., a short-circuit current (I_{SC}) without externally supplied power. NO_2 exposure effectively modulates the photocurrent flowing through the p-n junction due to the charge (electrons) transfer from the NWs to the adsorbed NO_2 molecules, causing significant change of the photocurrent. Based on this fundamental mechanism and PV effect attainable by the formation of a p–n junction NWs, we have conceptualised an InP NW array PV sensor to achieve gas sensing and self-powered carrier collection simultaneously. Therefore, the p-n junction-based sensing response can be defined as:

$$R = \frac{(I_0 - I_{gas})}{I_0} \times 100\% \quad (1)$$

where I_0 and I_{gas} denote the initial I_{SC} in air and the final I_{SC} in response to gas adsorption, respectively. I_{gas} can be either greater or smaller than I_0 as will be discussed later, leading to either a positive or negative value for the measured response.

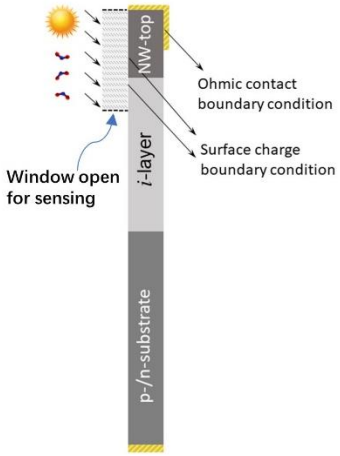

Figure 5-1. Schematic of the architecture used in the two-dimensional simulation domain deployed in COMSOL Multiphysics.

To understand the PV NW sensing mechanism, we investigated and compared two common axial p-n junction structures: an NW array with i-(intrinsic) and n-doped segments grown on a p-doped InP substrate, referred as p-i-n hereafter, and an NW array with i-(intrinsic) and p-doped segments grown on a n-doped InP substrate, referred as n-i-p hereafter (Figure 5-1a). To allow effective gas sensing and NW top contact fabrication for signal extraction, a light illumination window is created at the top of the NW for gas exposure with the length of 700 nm (500 nm of the doping segment and 200 nm of the exposure window depth). It is a realistic size that can be achieved reliably by device fabrication. All simulation related condition and parameters are presented in Figure 5-1b and Table 5-1.

Table 5-1. Material and Model Parameters in the Numerical Simulations

Material/Model Parameters	Value	Comments
Electron mobility	120 cm^2 ($V^{-1}s^{-1}$)	[18]
Hole mobility	100 cm^2 ($V^{-1}s^{-1}$)	[19]
SRH recombination lifetime	190 ps	Based on TRPL measurement; see Chapter 3
Doping concentration top P-doped NW	1×10^{17} cm^{-3}	[19]
Doping concentration i-region	1×10^{16} cm^{-3}	[19]
Doping concentration top N-doped NW	3×10^{18} cm^{-3}	[19]
Doping concentration P-/N-doped substrate	1×10^{18} cm^{-3}	[19]
Top N-/P-doped NW segment thickness	Adjustable parameter	Varied from 350 nm to 1800 nm
i-region thickness	Adjustable parameter	Total thickness of top NW segment plus i-region is 3 μm; i-region thickness changes correspondingly.
InP nanowire radius	100 nm	

We simulated I_{SC} before and after gas exposure to calculate sensing response by equation (1) and found that the relative position of i-n or i-p junction with respect to the exposure window plays a critical role in sensing performance. For p-i-n structure, large positive responses are obtained as plotted in Figure 5-2c, whereas for n-i-p structure, the response changes from positive to negative within a small range of values with increasing junction depth as shown in Figure 5-2d. The polarity of the sensing response for different structures can be explained with the aid of a band diagram of the NW top junction as shown in Figure 5-2e, f, where the case of n-/p-doped top segment length is exemplarily set as 450 nm. For the case of a p-i-n structure under illumination, NO_2 gas molecules adsorbing on the top n-doped segment and i-region (lightly n-doped due to background impurity doping during bottom-up growth[20]) as electron acceptors, giving rise to an

upward surface band bending as shown in Figure 5-2e.[21-22] As a result, the majority carrier (i.e. electron) concentration in both top n-doped segment and i-region is reduced, leading to decreased photocurrent and hence a positive sensing response as calculated by equation (1). Since the top n-segment is highly doped to 3×10^{18} cm^{-3}, the corresponding band bending (and carrier depletion) is much less evident than that in the i-region, subjected to same amount of gas adsorption. Therefore, the sensing response of p-i-n structure decreases sharply as the top n-segment length increases until longer than exposure window where no i-region is exposed for sensing, since most carrier depletion occurs within the i-layer.

When an n-i-p NW sensor is exposed to NO_2, the resultant upward band bending in the top p-doped segment increases majority carrier (i.e. hole) concentration and thus photocurrent shows an enhancement as plotted in Figure 5-2f. However, the i-region as mentioned still exhibited unintentionally n-doped and the band bending depletes electrons, leading to decreased photocurrent in contrast to the p-segment. For a shallow i-p junction that exposes both p- and i-regions for NO_2 sensing, due to the larger band bending in the i-segment, electron depletion plays a dominant role than the hole enhancement in the top p-doped segment, leading to the net photocurrent decrease and positive sensing response. As the junction depth increases and only the p-segment is exposed for sensing, the majority carrier (hole) concentration increases, presenting a negative sensing response due to the increased photocurrent. By comparing the response curves for the two structures, the p-i-n-based device is a better candidate for high-performance oxidative gas sensing. The length of the top n-segment plays a critical role, which should be kept as short as possible just enough for the electrical contact, so that the i-region can be sufficiently exposed for a better sensing performance. For n-i-p structure, varying junction depth plays limited role due to its bipolar sensing response in top p-segment and

i-region. As a result, the absolute response is less than 5% with all junction depths included.

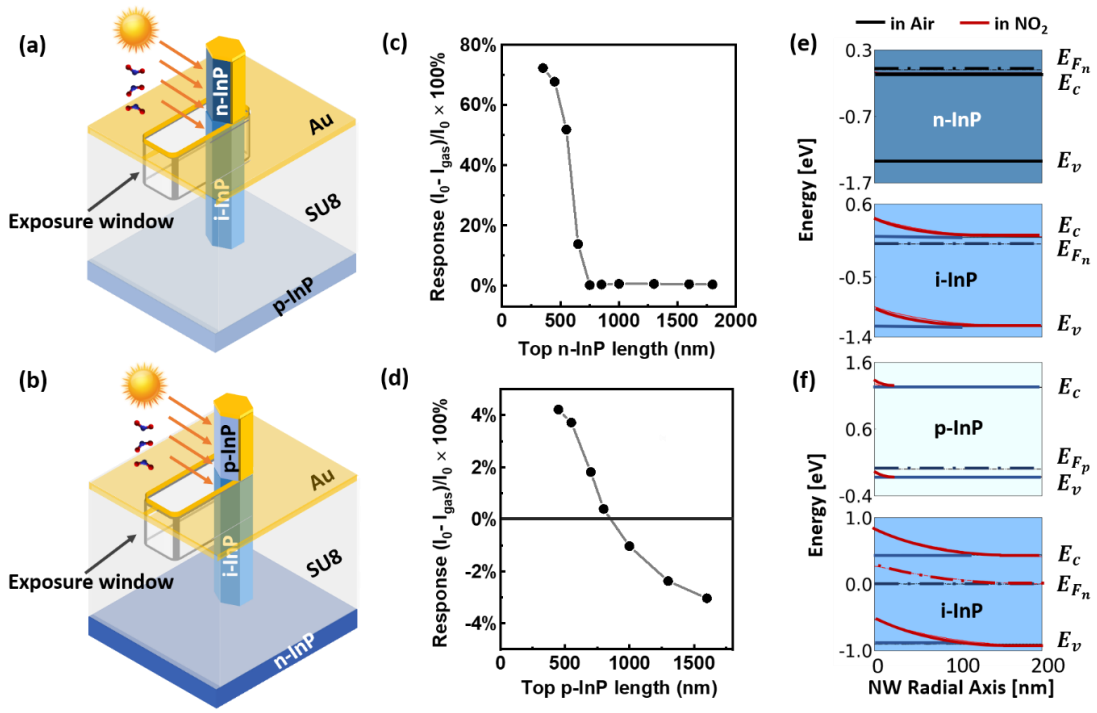

Figure 5-2. Simulation result of the p-n junction NW based NO_2 sensor. (a, b) Three-dimensional schematics of a unit cell of the p-i-n and n-i-p NW based sensor, respectively. (c, d) Simulated gas sensing response vs NW top segment length. (e, f) Band diagram of the respective structures before (i.e. in air) and after gas exposure (i.e. in NO_2). Due to the background impurity doping, the unintentionally doped i-segment grown by SA-MOVPE is slightly n-type (n^-).

5.2 Experimental

5.2.1 Substrate processing

The detailed substate preparation steps are described in Chapter 3, section 3.2.1. Through this process, a 30 nm SiO_2 layer was deposited on both n-doped and p-doped InP (111)A wafer, (doping concentration: (0.8–8) × 10^{18} cm^{-3}), with opened holes as pattern consisting of 200 × 200 μm^2 hexagonal dot array, diameter of 80 nm and inter-spacing of 600 nm.

5.2.2 p-i-n/n-i-p InP NW growth

The InP NW arrays were grown by bottom-up selective-area metal-organic vapor-phase epitaxy (SA-MOVPE), with details in Chapter 3, section 3.2.2. Molar fractions of trimethylindium (TMIn) and phosphine (PH_3) were set to be 9.38×10^{-6} and 7.59×10^{-4}, respectively, corresponding to a V/III ratio of 80. During the growth, all samples were firstly baked at 750 °C for 10 min under the PH_3 flow and grown for 4 min at 730 °C for undoped segment (i-InP). Then, Silane (SiH_4) and diethylzinc (DEZn) were introduced during the growth of n-doped segment and p-doped segment for 2 min, respectively. All the other parameters kept the same as those used for the growth of undoped InP segment. With this two-step growth process, the i-n and i-p InP NW were grown on p-doped and n-doped substrate, respectively, to form p-i-n (Figure 5-3a) and n-i-p (Figure 5-3b) junctions.

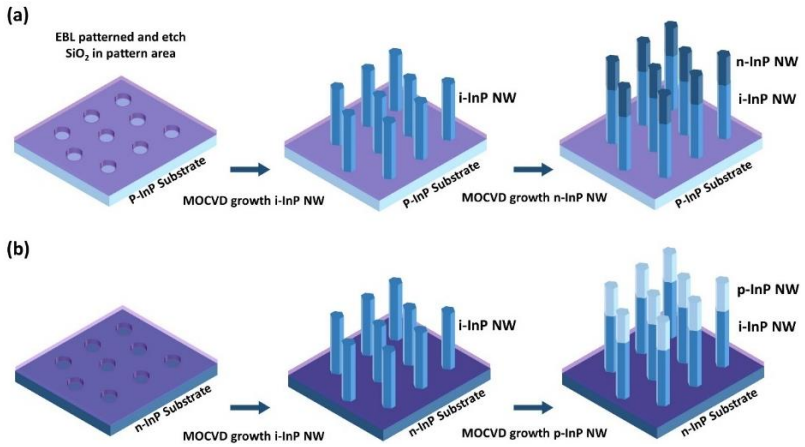

Figure 5-3. Schematic diagrams of NW growth process by SA-MOVPE for the p-i-n (a) and n-i-p (b) axial junction based structures.

5.3 Characterisation of the p-n junction InP nanowires

5.3.1 Morphological and microstructural characterisation

The morphology of the as-grown p-i-n and n-i-p InP NW arrays was characterised by SEM (FEI VERIOS 460 SEM) with electron beam voltage of 2 kV and current of 13

pA.[23] The SEM images shown in Figure 5-4, highlight the well-ordered InP NW arrays with taper-free hexagonal-cylinder shape. The two structures display a similar configuration due to the same growth time and substrate pattern design, with a diameter of around 110 nm, a length of 3-4 µm, and the inter-spacing of 600 nm.

The doping profiles of the two NW structures were characterised by cathodoluminescence (CL) of single NWs as mentioned in Chapter 3, section 3.4,[24] transferred from the NW arrays to a Si substrate. The bright-and-dark contrast of the CL panchromatic image[25] arises from different doping type and level of NW along the axial direction. Figure 5-4d shows that the n-segment has a much stronger luminescence than the i-segment, due to higher electron concentration, which increases transition probability of donor-valence band transition, in comparison to intrinsic-valence band transition. While for the p-doped top segment (Figure 5-4h), the transition probability of acceptor-valence band transition is lower than that of intrinsic-valence band transition, leading to a lower luminescence in the p-segment than that in the i-segment. The SEM-CL characterisation indicates that both n-i-p and p-i-n structures grown by SA-MOVPE method present well-defined junctions.

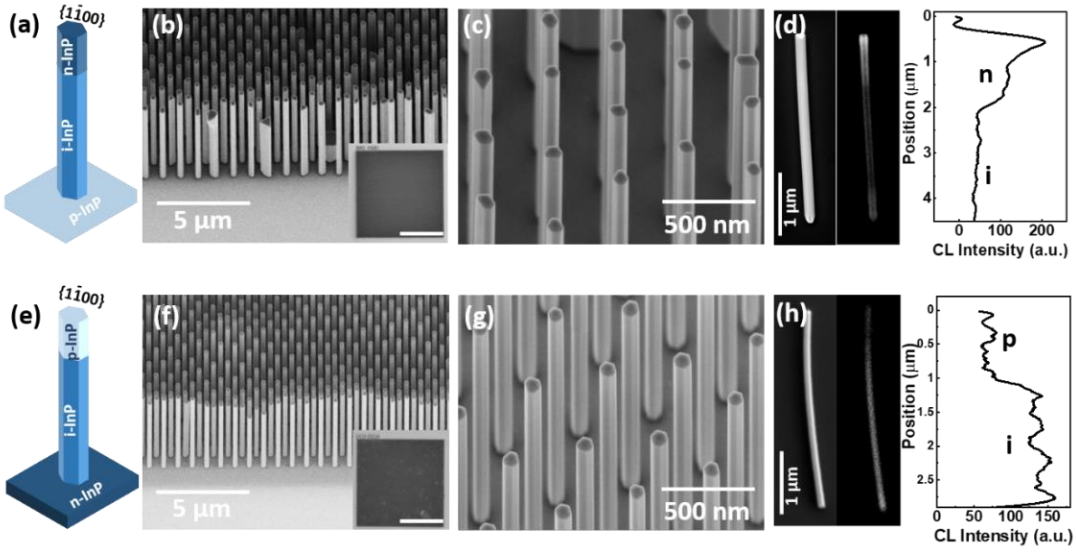

Figure 5-4. The Morphological and microstructural characterisation of p-n junction InP NWs. (a,

b, c) Schematic and SEM images of i-n InP NW on p-doped InP substrate (p-i-n). (e, f, g) Schematic and SEM images of i-p InP NW on n-doped InP substrate (n-i-p). (d, h) SEM and corresponding cathodoluminescence (CL) image with CL spectrum intensity profile of p-i-n and n-i-p InP NW, respectively.

The crystal structure is determined by transmission electron microscopy (TEM) analysis. NWs were directly transferred from original array to a copper mesh for TEM. Figure 5-5 presents the TEM images taken along zone axis from top and bottom region of a i-n NW confirming that NW was grown in wurtzite phase with barely any crystalline defects, and the dopants have negligible effect to the NW crystallinity.

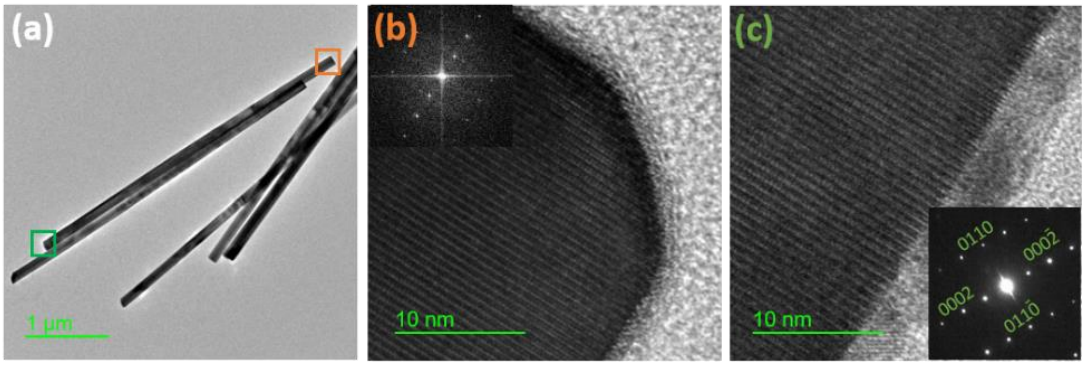

Figure 5-5. TEM characterisation of InP NWs. (a) Bright-field TEM image showing the morphology of a typical i-n InP NW grown at 730 °C. (b, c) High-resolution TEM images taken along [110] zone axis from the top and bottom regions of the InP NW shown in (a). Inset of (b) is the fast Fourier transform (FFT) image. Inset of (c) shows the selected area electron diffraction pattern confirming the WZ crystalline structure of the NW.

5.3.2 Optical property characterisation

The NWs were also transferred to SiO_2/Si substrate for time-resolved photoluminescence (TRPL) measurement for optical property characterisation. PL spectra were acquired along a single NW from top to bottom position (P1 to P3) at room temperature as shown in Figure 5-6. It is found that the lifetimes of i-p and i-n NW segments are ~0.7-0.4 and

~0.3-0.1 ns, respectively. The lifetime of i-p NW is decreasing along the length from P3 to P1 due to the Zn dopant interstitials.[26] It is also noticeable that the lifetime of n-i-p is much smaller than p-i-n, because the n-doping concentration (~3 × 10^{18} cm^{-3}) is higher than p-doping (~1 × 10^{17} cm^{-3}) from previous research reported by our group and higher impurity level decreases the lifetime. Although these values are lower than the best lifetime values reported previously by our group,[26-27] it is adequate to realise the PV effect for the self-powered sensing application.

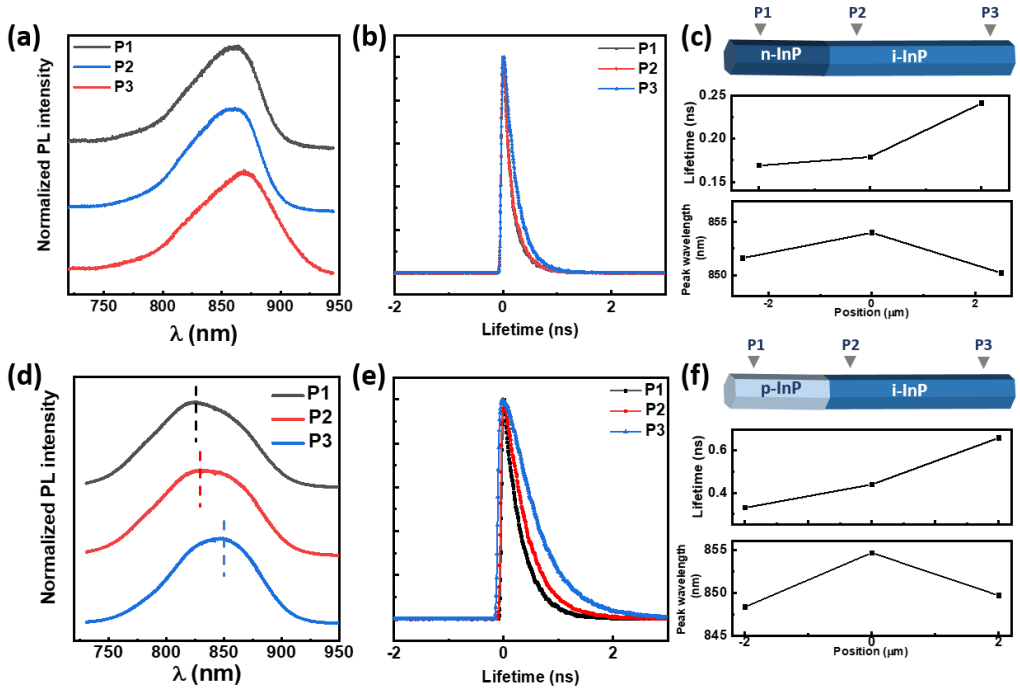

Figure 5-6. Room-temperature PL spectra of i-n InP and i-p InP NWs measured at top, middle and bottom position, respectively (a, d). TRPL decays measured at the peak emission wavelength of i-n InP and i-p InP at the same position (b, e). (c, f) Minority carrier lifetimes and peak wavelength extracted from TRPL measurement (a-d).

5.3.3 Photovoltaic effect characterisation

For PV effect and sensing measurements, the as-grown NW arrays were then fabricated into NW PV sensors according to the designed structure as illustrated in Figure 5-7.[28] The fabrication started with spin-coating SU8-5 on the NWs for planarization. Then SU8-

5 was etched back by barrel-etcher to expose ~500 nm of the top of InP NWs for subsequent electrical contact (Figure 5-7a, e). Since the top junction is deeper than 500 nm, the i-region of NW is embedded in SU8-5, which prevents shorting of the junction and provides necessary mechanical support to the NWs. A Ti 10nm/ Au 80 nm Au film layer was tilt-angle deposited on NWs using electron-beam evaporator for top contact (Figure 5-7b, f), as previously discussed in Chapter 4, section 4.1.

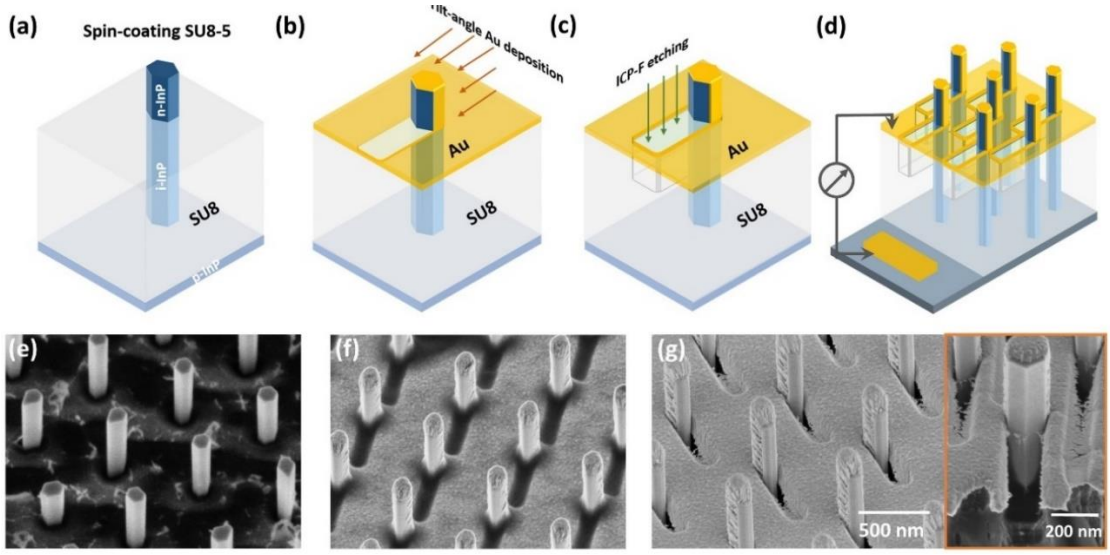

Figure 5-7. Schematic of device fabrication process based on as-grown InP NWs including (a) spin-coating of SU8-5, (b) tilt-angle deposition of Au, (c) ICP (fluorine) etching, and (d) the as-fabricated InP NW array sensor with electrical contacts. (e-g) SEM images corresponding to the fabrication process (a-c) and a cross-sectional view (orange box) highlighting the window at the top junction region opened for gas sensing in the right panel of (g).

The method left a shadow area behind each NW covered by SU8-5, which can be further etched to extend the exposure window below the top junction by inductively coupled plasma (ICP). The etching rate of ICP has been well calibrated such that another ~500 nm of SU8-5 was removed precisely, which formed a hole besides each NW (Figure 5-7c, g), successfully realising the designed exposure window. Then, a 200 nm Au layer

was deposited on the back of InP substrate as bottom contact as shown in Figure 5-7d, which also shows the schematic electrical contact.

The electrical properties of two NW device structures (p-i-n and n-i-p) were characterised by standard dark/light current-voltage (I-V) measurement as shown in Figure 5-8a, d. The dark I-V curves of both devices show typical diode characteristic. When illuminated under a solar simulator @AM1.5 at 42.3 mW/cm^2, both devices show photovoltaic behaviour, indicating successful device fabrication. The p-i-n and n-i-p structures have a short-circuit current (I_{SC}) density of 0.19 and 0.13 mA/cm^2 (device area of 200 × 200 μm^2), and an open-circuit voltage (V_{OC}) of 0.16 and 0.25 V, respectively. The time-dependent photo-responses are shown in Figure 5-8b, e and Figure 5-8c, f for I_{SC} and V_{OC}, where distinct 'ON' and 'OFF' photovoltaic states can be well manipulated to fit into the subsequent self-powered gas sensing measurements.

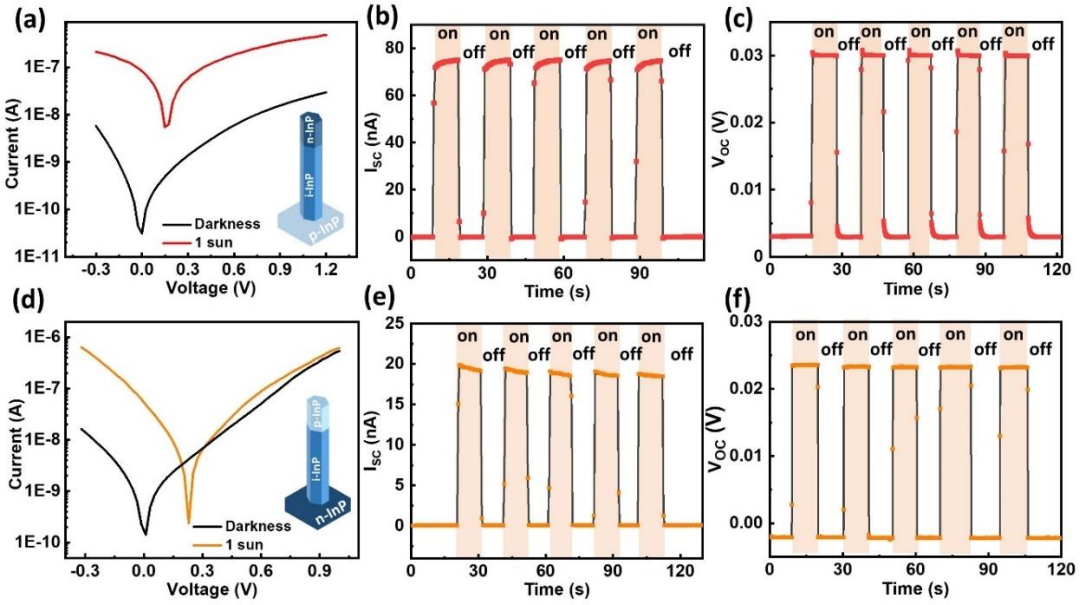

Figure 5-8. Photovoltaic characterisation of the p-n junction InP NW device. (a, d) Dark/light I−V characteristics of the p-i-n and n-i-p InP NW arrays (light source: solar simulator @AM1.5, 42.3 mW/cm^2). (b, e) Time-dependent I_{SC} of p-i-n and n-i-p InP NW device, respectively; 'on' and 'off' correspond to states with and without illumination. (c, f) Time-dependent V_{OC} of p-i-n and n-i-p

InP NW devices, respectively.

5.4 NO_2 sensing measurement

5.4.1 Self-powered gas sensing measurement setup

The gas sensing performance was measured using a home-made sensing setup as aforementioned in Chapter 3, section 3.5, with an additional solar simulator for light illumination.

5.4.2 The electrical signals employed for self-powered gas sensing

Prior to gas injection, the device was placed in the gas sensing chamber with illumination, zero bias voltage and constant air flow to generate steady-state I_{SC}. As NO_2 gas injection is introduced into the chamber, I_{SC} of the p-i-n device decreases and I_{SC} of the n-i-p device increases as shown in Figure 5-9a, b, consistent with the mechanism discussed in section 5.1.[21]

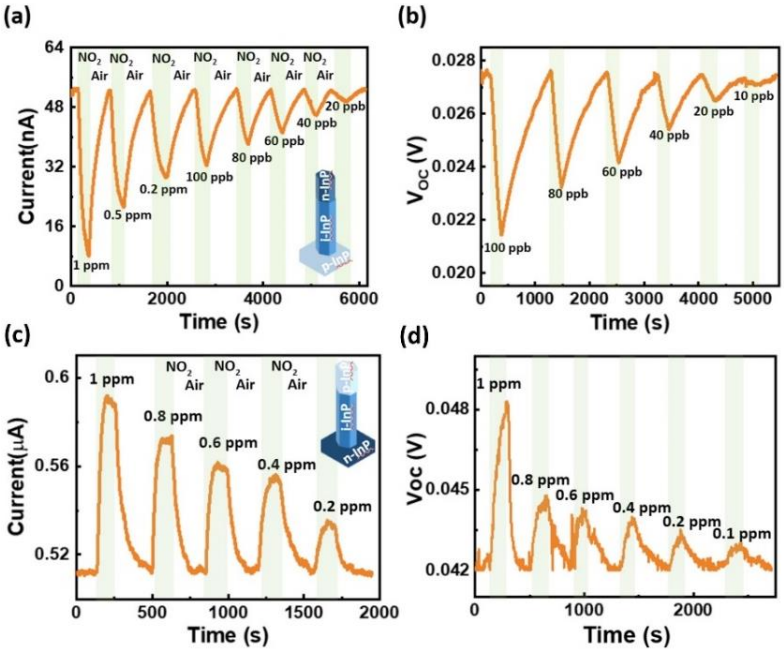

Figure 5-9. Raw data from p-i-n and n-i-p InP NW photocurrent sensing measurement (a, c), and V_{OC} as output signal for NO_2 sensing measurement (b, d).

The response of I_{SC} reaches a saturation state in ~ 200 s. When NO_2 gas is removed off and air flow resumed, I_{SC} recovers back to initial base level. Besides I_{SC}, the time-dependent V_{OC} in Figure 5-9c, d can be also measured as an alternative readout signal that is also concentration dependent and can be useful for integration with digital microchip circuit board.[29-30]

5.4.3 Light intensity effect on sensing performance

To find out the threshold light intensity for our self-powered NW sensor operation and the capacity of the device working under various illumination conditions, the p-i-n device was measured under a series of attenuated light intensity tuned by a neutral density filter. Figure 5-10a shows that with 100 ppb NO_2, the sensing response is consistent within the standard deviation range (22 ± 4.9 %, shaded area) under light intensity decreasing from original 42.3 mW/cm^2 to 10 % of this original level (or <5% 1sun condition). Under reduced light intensity, the baseline I_{SC} (i.e., I_0) and the gas adsorption induced I_{SC} (i.e., I_{gas}) decreases simultaneously, such that the response calculated by equation (1) remains at a similar value. Such light-intensity independent performance is highly desirable for sensing in realistic environment, since atmosphere solar irradiation usually varies drastically during a day.

5.4.4 Self-powered NO_2 sensing performance

Figure 5b summarises the concentration-dependent sensing response for both p-i-n and n-i-p sample with their linear-fitting slope (L) which is defined as device sensitivity, as discussed in Chapter 2.[15, 31] Figure 5-10c, d shows the time-dependent sensing response of the p-i-n based device in concentration range 1 - 1000 ppb, and the n-i-p sample results are illustrated in Figure 5-10e, f, with concentration 20 - 1000 ppb. It is

noticeable that the absolute value of response at 1000 ppb and the device sensitivity for n-i-p structure (15.9 %, 0.014 %/ppb) is much smaller than p-i-n structure (84.1 %, 0.62 %/ppb). This result essentially verifies the numerical simulation that the responses from top p- and i-segment of the bipolar n-i-p junction structure offset each other, leading to a much weaker response.

For the more sensitive p–i–n structure, a linear correlation of response versus concentration can be observed at two separate concentration regimes, with a smaller slope at the high concentration range (>100 ppb). This phenomenon also exists in previously reported work,[17] which indicates that the sensor saturates gradually due to the limited number of surface adsorption sites.

The superior sensitivity performance of p-i-n structure is also indicated from the measurement of extremely low NO_2 concentration (1 ppb), where a distinguishable sensing response of 2% can still be obtained as shown in Figure 5-10d. From the baseline in Figure 5-10e, the RMS_{noise} is 0.10 % and L is 0.62 %/ppb obtained from the inset of Figure 5-10c, so the calculated limit of detection (LOD) is 0.49 ppb, which is the lowest record achieved by a self-powered gas sensor to the best of our knowledge. Furthermore, both the n-i-p and p-i-n devices demonstrated a high selectivity to NO_2 as shown in Figure 5-10g, h. At 1 ppm level, their sensing response to other organic vapours and common atmosphere gases (methanol (CH_3OH), ethanol (C_2H_5OH), methyl nitrite (CH_3NO_2), carbon dioxide (CO_2) and propane (C_3H_8)) are negligible compared to NO_2.

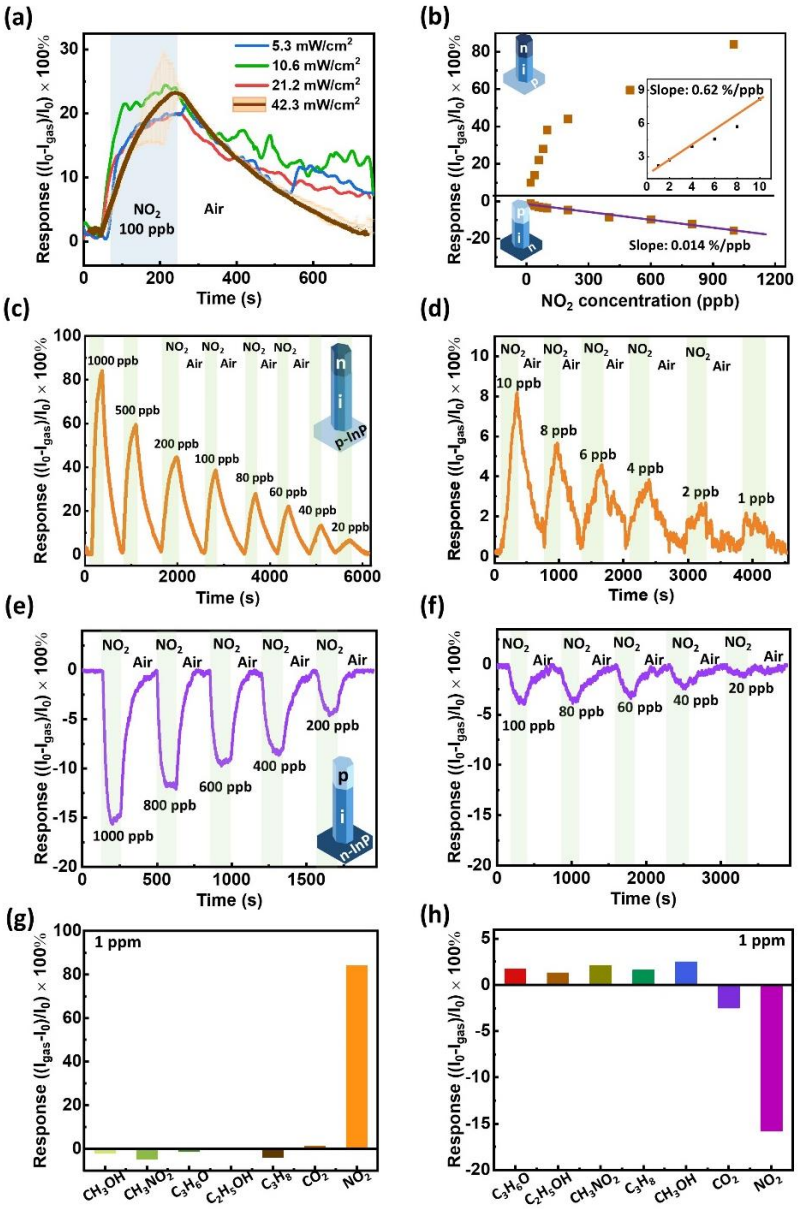

Figure 5-10. Self-powered NO_2 sensing performance of p-i-n and n-i-p InP NW. (a) Time dependent sensing response measured from the p-i-n device under different illumination intensities. The averaged time-dependent sensing response and standard deviation range under light intensity 42.3 mW/cm^2 is shown as the shaded area. (b) Response of the p-i-n (upper panel) and n-i-p (lower panel) NW structures under different NO_2 concentrations. The inset shows an enlarged graph of p-i-n sensing responses from 1-10 ppb NO_2. (c-f) Sensing response measured from (c, d) p-i-n, and (e, f) n-i-p NW structures. (g, h) Selectivity measurements of the p-i-n (g) and n-i-p (h) NW structures, respectively, with gas concentration of 1 ppm for methanol, methyl nitrides, acetone, ethanol, propane, NO_2 and 1% for CO_2.

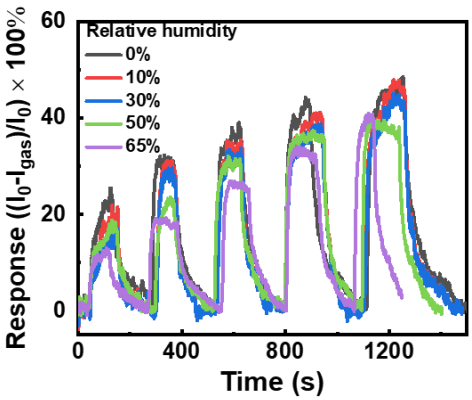

Figure 5-11. Time-dependent sensing response to NO_2 concentration of 200 ppb from a p-i-n device under the relative humidity levels of 0%, 30%, 50% and 65%.

Also, the effect of humidity on the p-i-n sensor was investigated under various relative humidity (RH) levels (Figure 5-11). Even with a high concentration of water vapour (RH 65%), the NW sensor maintains its high sensitivity despite a small degradation in sensing response (< 30%) compared to the dry condition (RH 0%), demonstrating excellent humidity tolerance. Compared with different types of recently reported PV self-powered gas-sensing devices as summarised in Table 5-2, our p-i-n InP NW-based sensor shows an overall outstanding performance with a high response (84% to 1 ppm NO_2), the lowest LOD (1 ppb), dual measurable signal (I_{SC} and V_{OC}) and ability to work stably under natural light source with different intensities other than a specific wavelength or intensity.[32]

Table 5-2**.** Comparison of typical sensing performance parameters from self-powered gas sensors reported in the literature (room temperature operation).

Device structure	Light source	Measured signal	Target gas (LOD)	Response 100% (gas concentration)	Response / recovery time (s)	Ref
p-i-n InP NW	Solar simulator (AM 1.5)	I_{SC} (nA) V_{OC} (mV)	NO_2 (1 ppb)	84% (1 ppm)	200 / 400	This work

p-Si/n-ZnO (amine-/thiol-functionalization)	Solar simulator (AM 1.5)	V_{OC} (mV)	NO_2 (170 ppb)	Amine: 7.5% Thiol: 9.8% (250 ppb)	~1000	[10]
CNT-SiNW	Solar simulator (AM 1.5)	V_{OC} (V)	NO_2 (10 ppm)	46% (10 ppm)	4-6	[12]
SWNTs/Si	λ = 600 nm, P = 1.8 mW cm^{-2}	V_{OC} (mV)	NO_2 (100 ppb)	2.23% (400 ppb)	~50	[33]
NiO/ZnO/ITO	Solar simulator 100 mW cm^{-2} AM1.5	V_{OC} (V)	CO_2	0.1%	150/100	[34]
$CsPbBr_3$	Solar simulator (AM 1.5)	I_{SC} (nA)	Acetone (1 ppm)	3% (1 ppm)	10/5	[11]
$CsPbBr_2I$	Solar simulator (AM 1.5)	I_{SC} (nA)	Acetone (1 ppm)	16% (1 ppm)	150	[35]
Gr/WS_2/Gr	White light P = 100 mW cm^{-2}	I_{SC} (μA) or V_{OC} (mV)	NO_2 (5ppm), H_2 (50ppm)	NO_2: 70% (5ppm), H_2: 17% (50ppm)	~500	[9]
SiNWs/ITO	Red LED λ = 576 nm, P = 20 mW cm^{-2}	I_{SC} (μA)	NO_2 (5ppb)	90% (1 ppm)	80/850	[32]
Au@rGO/GaN nanorods	UV LED λ = 382 nm, P = 1.71 mW cm^{-2}	I_{SC} (μA)	CO (5 ppm)	38% (20 ppm)	400/1000	[36]
FMCPIB	Solar simulator (AM 1.5)	I_{SC} (nA)	NO_2 (1 ppm)	8% (8 ppm)	17/126	[37]

5.5 On-Field Gas Sensing

Based on the laboratory sensing measurement results, the p-i-n NW sensor was chosen to confirm its applicability in a real environment. A real-time on-field measurement was enabled by connecting our NW device to a portable microprocessor with USB interface (JLM Innovation with supplementary software JLMlogSP), where the electrical signal generated by the NW sensor is transmitted and processed. A prototype workflow from the on-field sensing measurement to the data analysis and output result is illustrated in Figure 5-12. Prior to on-field operation, the sensor was calibrated in self-powering mode in the lab as shown in Figure 5-12a, which correlates the sensing response value with the NO_2 concentration. This calibration was performed in the laboratory gas sensing setup where the injected gas concentration was known and can be precisely controlled. However, when the NW sensor was connected to the portable USB microprocessor, it could no longer be fitted into the same sensing setup. In this case, the calibration was then performed in a home-made 3D-printing enclosure (with an LED light source) that can accommodate the NW sensor integrated USB system. In this case, the enclosure was not completely sealed and isolated from the ambient atmosphere as in a standard gas sensing chamber. Hence, the measured sensing response tends to overestimate the injected gas concentration (i.e., consider a small amount of gas leakage).

The portable NW sensor system was then brought to the real environment for on-field measurement with the exposure of a 4-cylinder gasoline car exhaust. An example time-dependent response curve shows that the value and shape of response pulse vary in different accelerator pedal pressing duration and revolutions per minute (RPM) of the engine, as NO_2 concentration in exhaust gas depending on these parameters (Figure 5-12b). The measured response curve, together with the calibration results, was transmitted

to a data evaluation unit (e.g., a laptop, or an embedded system with USB or Bluetooth interface) for processing. Here, we demonstrate a simple pipeline of data acquisition and processing for a vehicle exhaust at 2500 RPM where the gas pedal was pressed four times, each of which lasted approximately 25 s. The raw data from the measurement was then evaluated with a logistic filter to remove noise (e.g. a double-logistic filter in this demonstration) to extract sensing response values as shown in (Figure 5-12c).

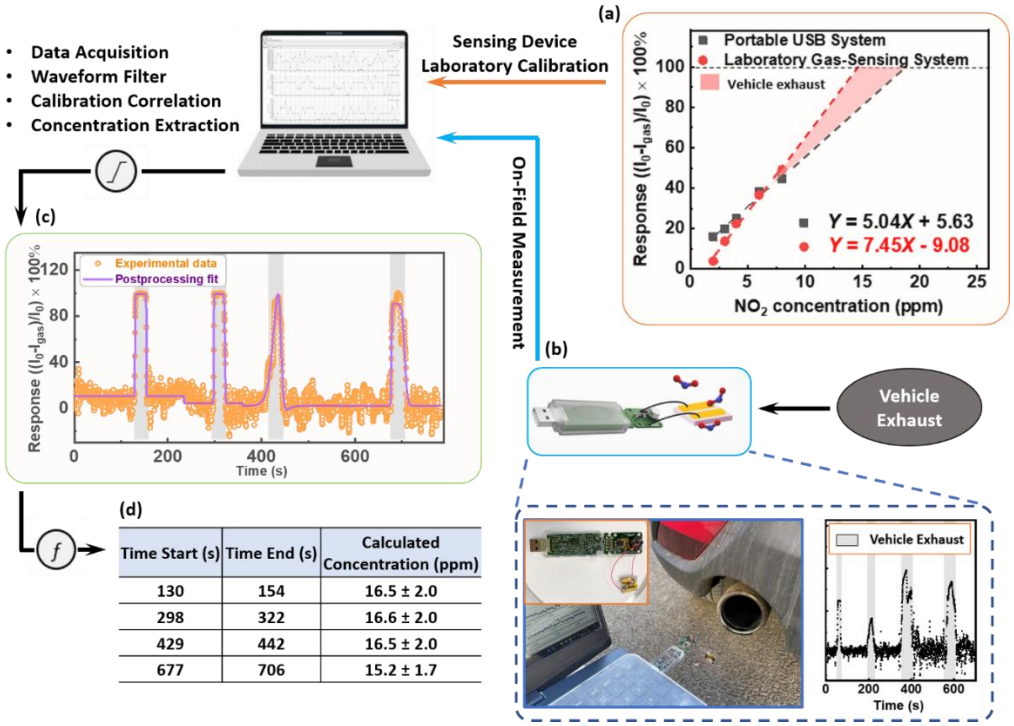

Figure 5-12. A prototype workflow for practical on-field gas sensing measurement. (a) The NW sensor concentration calibration in laboratory environment (portable USB microprocessor system and laboratory gas sensing system). (b) The schematic and on-site photos of on-field vehicle exhaust measurement based on the NW sensor integrated with the USB interface and an example of acquired data. (c) Data measured by this USB interface and the corresponding post-processed fitting result by user-specified data filters to remove noise and extract sensing response values; (d) By correlating with the laboratory calibration, the NO_2 concentration can be dynamically monitored.

To further confirm the reliability of the NW sensor, a commercial NO_2 air quality sensor (KEMET USEQGCDAN82100) was also integrated to this USB interface for the same vehicle exhaust measurement except that it requires an external power source (2.5 V), as shown in Figure 5-13a. The commercial sensor was calibrated in the laboratory setup with injected NO_2 in the range of 2-10 ppm, obtaining a linear relation between sensing response and NO_2 concentration (red dots) with response ranging 20-30 % (Figure 5-13b).

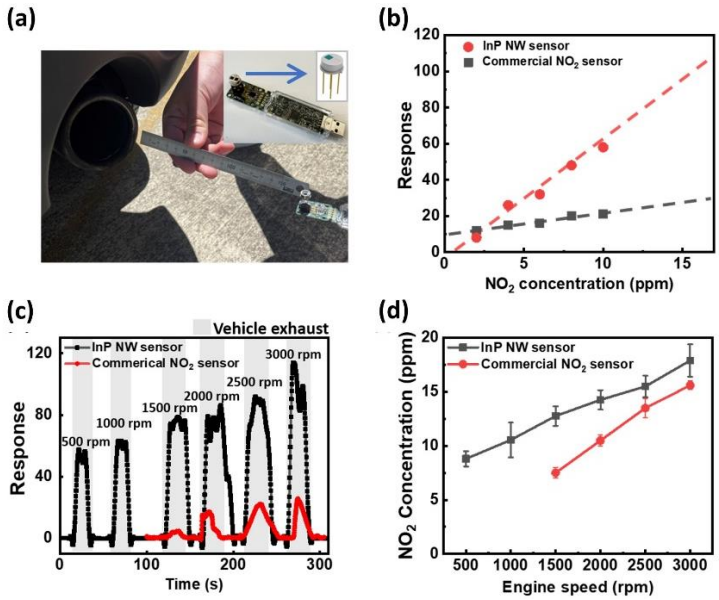

Figure 5-13. The performance comparison with commercial KEMET NO_2 sensor. (a) Photo of the on-field vehicle exhaust measurement with a commercial KEMET NO_2 sensor (inset) integrated on the USB interface. (b) Calibration between sensing response and NO_2 concentration (with linear fitting) for the commercial device and InP NW sensor. (c) Sensing response measured with InP NW sensor and commercial sensor at an engine speed of 500 – 3000 RPM, and (d) the engine speed correlated NO_2 concentration (measured three times for each device).

The sensing response measured from the vehicle exhaust with varying engine speed is shown in Figure 5-13c, validated by previous study that the NO_2 concentration in vehicle exhaust increases with engine speed.[38] It is noted that our InP NW sensor can detect vehicle exhaust with engine speed down to 500 RPM, while the commercial sensor shows no response with engine speed below 1500 RPM. Also, our self-powered InP NW sensor

produces a much larger sensing responses with less variation in value, indicating a more sensitive performance. The obtained NO_2 concentration, as shown in Figure 5-13d, is calculated based on the sensing response results in Figure 5-13b and the result from this commercial sensor is 8.9-13.0 ppm at 2500 RPM, relatively consistent with our p-i-n InP NW sensor (15.2-16.6 ppm).

5.6 Summary

In this chapter, a novel self-powered sensor architecture is successfully designed and demonstrated based on bottom-up grown p-n homojunction InP NW arrays. We designed the p-n junction-based NW sensor structure and explored the sensing mechanism via numerical simulation. The fabricated sensors exhibited outstanding sensitivity with a limit of detection down to sub-ppb level, and high selectivity to NO_2 without the need for applied bias. These results promise a new family of sensing platform to achieve high-performance gas sensing under self-powered operation mode enabled by photovoltaic effect. The integration of the NW sensor with a portable USB interface for practical dynamic on-field measurement is further demonstrated, precisely quantifying NO_2 concentration from a motor vehicle exhaust. Our prototype InP NW sensor design paves a way towards battery-free, highly integrable and compatible sensing platform for applications such as environmental monitoring, industrial safety and hazard alarming. It is a promising step forward for next generation sensing network for Internet of Things.

References

[1] Z. Y. Qian, S. H. Kang, V. Rajaram, C. Cassella, N. E. McGruer and M. Rinaldi, Zero-power infrared digitizers based on plasmonically enhanced micromechanical photoswitches. *Nature Nanotechnology*, **12**, 969-973 (2017).

[2] X. Li, C. Q. Luo, H. Ji, Y. D. Zhuang, H. L. Zhang and V. C. M. Leung, Energy consumption optimization for self-powered IoT networks with non-orthogonal multiple access. *International Journal of Communication Systems*, **33**, (2020).

[3] Ahmed, I. Hassan, M. F. El-Kady, A. Radhi, C. K. Jeong, P. R. Selvaganapathy, J. Zu, S. Ren, Q. Wang and R. B. Kaner, Integrated Triboelectric Nanogenerators in the Era of the Internet of Things. *Advanced Science*, **6**, (2019).

[4] Z. Y. Wu, T. H. Cheng and Z. L. Wang, Self-Powered Sensors and Systems Based on Nanogenerators. *Sensors*, **20**, e4174(2020).

[5] Z. L. Song, W. H. Ye, Z. Chen, Z. S. Chen, M. T. Li, W. Y. Tang, C. Wang, Z. A. Wan, S. Poddar, X. L. Wen, X. F. Pan, Y. J. Lin, Q. F. Zhou and Z. Y. Fan, Wireless Self-Powered High-Performance Integrated Nanostructured-Gas-Sensor Network for Future Smart Homes. *Acs Nano*, **15**, 7659-7667 (2021).

[6] E. Lee and H. Yoo, Self-Powered Sensors: New Opportunities and Challenges from Two-Dimensional Nanomaterials. *Molecules*, **26**, 5056 (2021).

[7] X. L. Liu, Y. Zhao, W. J. Wang, S. X. Ma, X. J. Ning, L. Zhao and J. Zhuang, Photovoltaic Self-Powered Gas Sensing: A Review. *Ieee Sensors Journal*, **21**, 5628-5644 (2021).

[8] Y. Kim, S. Lee, J.-G. Song, K. Y. Ko, W. J. Woo, S. W. Lee, M. Park, H. Lee, Z. Lee, H. Choi, W.-H. Kim, J. Park and H. Kim, 2D Transition Metal Dichalcogenide Heterostructures for p- and n-Type Photovoltaic Self-Powered Gas Sensor. *Advanced Functional Materials*, **30**, 2003360 (2020).

[9] D. Lee, H. Park, S. D. Han, S. H. Kim, W. Huh, J. Y. Lee, Y. S. Kim, M. J. Park, W. I. Park, C.-Y. Kang and C.-H. Lee, Self-Powered Chemical Sensing Driven by Graphene-Based Photovoltaic Heterojunctions with Chemically Tunable Built-In Potentials. *Small*, **15**, 1804303 (2019).

[10] M. W. G. Hoffmann, L. Mayrhofer, O. Casals, L. Caccamo, F. Hernandez-Ramirez, G. Lilienkamp, W. Daum, M. Moseler, A. Waag, H. Shen and J. D. Prades, A Highly Selective and Self-Powered Gas Sensor Via Organic Surface Functionalization of p-Si/n-ZnO Diodes. *Advanced Materials*, **26**, 8017-8022 (2014).

[11] H. Chen, M. Zhang, R. Bo, C. Barugkin, J. Zheng, Q. Ma, S. Huang, A. W. Y. Ho-Baillie, K. R. Catchpole and A. Tricoli, Superior Self-Powered Room-Temperature Chemical Sensing with Light-Activated Inorganic Halides Perovskites. *Small*, **14**, 1702571 (2018).

[12] Y. Jia, Z. Zhang, L. Xiao and R. Lv, Carbon Nanotube-Silicon Nanowire Heterojunction Solar Cells with Gas-Dependent Photovoltaic Performances and Their Application in Self-Powered NO_2 Detecting. *Nanoscale Research Letters*, **11**, 299 (2016).

[13] M. W. G. Hoffmann, O. Casals, A. E. Gad, L. Mayrhofer, C. Fabrega, L. Caccamo, F. Hernandez-Ramirez, G. Lilienkamp, W. Daum, M. Moseler, H. Shen, A. Waag and J. D. Prades, in *Eurosensors 2015*, (Eds: G. Urban, J. Wollenstein and J. Kieninger) **2015**, p. 623-627.

[14] E. Modaresinezhad and S. Darbari, Realization of a room-temperature/self-powered humidity sensor, based on ZnO nanosheets. *Sensors and Actuators B-Chemical*, **237**, 358-366 (2016).

[15] X.-L. Liu, Y. Zhao, S.-X. Ma, S.-W. Zhu, X.-J. Ning, L. Zhao and J. Zhuang, Rapid and Wide-Range Detection of NO_x Gas by N-Hyperdoped Silicon with the Assistance of a Photovoltaic Self-Powered Sensing Mode. *ACS Sensors*, **4**, 3056-3065 (2019).

[16] M. A. Green, E. D. Dunlop, J. Hohl-Ebinger, M. Yoshita, N. Kopidakis, K. Bothe, D. Hinken, M. Rauer and X. Hao, Solar cell efficiency tables (Version 60). *Progress in Photovoltaics: Research and Applications*, **30**, 687-701 (2022).

[17] S. Y. Wei, Z. Li, A. John, B. I. Karawdeniya, Z. Y. Li, F. L. Zhang, K. Vora, H. H. Tan, C. Jagadish, K. Murugappan, A. Tricoli and L. Fu, Semiconductor Nanowire Arrays for High-Performance Miniaturized Chemical Sensing. *Advanced Functional Materials*, 35, 2207357 (2022)

[18] F. Wang, Q. Gao, K. Peng, Z. Li, Z. Li, Y. Guo, L. Fu, L. M. Smith, H. H. Tan and C. Jagadish, Spatially Resolved Doping Concentration and Nonradiative Lifetime Profiles in Single Si-Doped InP Nanowires Using Photoluminescence Mapping. *Nano Letters*, **15**, 3017-3023 (2015).

[19] Q. Gao, Z. Li, L. Li, K. Vora, Z. Li, A. Alabadla, F. Wang, Y. Guo, K. Peng and Y. C. Wenas, Axial p‐n junction design and characterization for InP nanowire array solar cells. *Progress in Photovoltaics: Research and Applications*, **27**, 237-244 (2019).

[20] Q. Gao, Z. Li, L. Li, K. Vora, Z. Li, A. Alabadla, F. Wang, Y. Guo, K. Peng, Y. C. Wenas, S. Mokkapati, F. Karouta, H. H. Tan, C. Jagadish and L. Fu, Axial p-n junction design and characterization for InP nanowire array solar cells. *Progress in Photovoltaics: Research and Applications*, **27**, 237-244 (2019).

[21] Y. Kim, S. Lee, J. G. Song, K. Y. Ko, W. J. Woo, S. W. Lee, M. Park, H. Lee, Z. Lee, H. Choi, W. H. Kim, J. Park and H. Kim, 2D Transition Metal Dichalcogenide Heterostructures for p- and n-Type Photovoltaic Self-Powered Gas Sensor. *Advanced Functional Materials*, **30**, 2003360 (2020).

[22] M. Bai, H. Huang, Z. Liu, T. T. Zhan, S. F. Xia, X. G. Li, N. Sibirev, A. Bouravleuv, V. G. Dubrovskii and G. Cirlin, InAs/InP core/shell nanowire gas sensor: Effects of InP shell on sensitivity and long-term stability. *Applied Surface Science*, **498**, 143756 (2019).

[23] Q. Gao, Z. Y. Li, L. Li, K. Vora, Z. Li, A. Alabadla, F. Wang, Y. A. Guo, K. Peng, Y. C. Wenas, S. Mokkapati, F. Karouta, H. H. Tan, C. Jagadish and L. Fu, Axial p-n junction design and characterization for InP nanowire array solar cells. *Progress in Photovoltaics*, **27**, 237-244 (2019).

[24] Z. Y. Li, I. Yang, L. Li, Q. Gao, J. S. Chong, Z. Li, M. N. Lockrey, H. H. Tan, C. Jagadish and L. Fu, Reducing Zn diffusion in single axial junction InP nanowire solar cells for improved performance. *Progress in Natural Science-Materials International*, **28**, 178-182 (2018).

[25] Yang, X. Zhang, C. L. Zheng, Q. Gao, Z. Y. Li, L. Li, M. N. Lockrey, H. Nguyen, P. Caroff, J. Etheridge, H. H. Tan, C. Jagadish, J. Wong-Leung and L. Fu, Radial Growth Evolution of InGaAs/InP Multi Quantum-Well Nanowires Grown by Selective-Area Metal Organic Vapor-Phase Epitaxy. *Acs Nano*, **12**, 10374-10382 (2018).

[26] J. Wallentin, M. T. Borgström, L. Samuelson, M. Ekawa and K. Kawaguchi, Photoluminescence study of Zn-doped wurtzite InP core-shell nanowires. *Applied Physics Letters*, **102**, 032105 (2013).

[27] V. Dagytė, E. Barrigón, W. Zhang, X. Zeng, M. Heurlin, G. Otnes, N. Anttu and M. T. Borgström, Time-resolved photoluminescence characterization of GaAs nanowire arrays on native substrate. *Nanotechnology*, **28**, 505706 (2017).

[28] S. Wei, Z. Li, A. John, B. I. Karawdeniya, Z. Li, F. Zhang, K. Vora, H. H. Tan, C. Jagadish, K. Murugappan, A. Tricoli and L. Fu, Semiconductor Nanowire Arrays for High-Performance Miniaturized Chemical Sensing. *Advanced Functional Materials*, **32**, 2107596 (2022).

[29] D. Lynall, A. C. Tseng, S. V. Nair, I. G. Savelyev, M. Blumin, S. L. Wang, Z. M. M. Wang and H. E. Ruda, Nonlinear Chemical Sensitivity Enhancement of Nanowires in the Ultralow Concentration Regime. *Acs Nano*, **14**, 964-973 (2020).

[30] H. Long, A. Harley-Trochimczyk, T. Pham, Z. R. Tang, T. L. Shi, A. Zettl, C. Carraro, M. A. Worsley and R. Maboudian, High Surface Area MoS_2/Graphene Hybrid Aerogel for Ultrasensitive NO_2 Detection. *Advanced Functional Materials*, **26**, 5158-5165 (2016).

[31] X. Zhou, J. Y. Liu, C. Wang, P. Sun, X. L. Hu, X. W. Li, K. Shimanoe, N. Yamazoe and G. Y. Lu, Highly sensitive acetone gas sensor based on porous $ZnFe_2O_4$ nanospheres. *Sensors and Actuators B-Chemical*, **206**, 577-583 (2015).

[32] D. Liu, Q. Chen, A. Chen and J. Wu, Self-powered gas sensor based on SiNWs/ITO photodiode. *RSC Advances*, **9**, 23554-23559 (2019).

[33] L. Liu, G. H. Li, Y. Wang, Y. Y. Wang, T. Li, T. Zhang and S. J. Qin, A photovoltaic self-powered gas sensor based on a single-walled carbon nanotube/Si heterojunction. *Nanoscale*, **9**, 18579-18583 (2017).

[34] T. Hamada and M. Sugiyama, Fabrication of solar cells with CO_2 gas sensing capabilities based on a NiO/ZnO p-n junction for developing self-powered gas sensors. *Japanese Journal of Applied Physics*, **61**, 054002 (2022).

[35] H. Chen, M. Zhang, X. Fu, Z. Fusco, R. Bo, B. Xing, H. T. Nguyen, C. Barugkin, J. Zheng, C. F. J. Lau, S. Huang, A. W. Y. Ho-Baillie, K. R. Catchpole and A. Tricoli, Light-activated inorganic $CsPbBr_2I$ perovskite for room-temperature self-powered chemical sensing. *Physical Chemistry Chemical Physics*, **21**, 24187-24193 (2019).

[36] M. Reddeppa, S. B. Mitta, T. Chandrakalavathi, B. G. Park, G. Murali, R. Jeyalakshmi, S. G. Kim, S. H. Park and M. D. Kim, Solution-processed Au@rGO/GaN nanorods hybrid-structure for self-powered UV, visible photodetector and CO gas sensors. *Current Applied Physics*, **19**, 938-945 (2019).

[37] H. Chen, M. Zhang, B. Xing, X. Fu, R. Bo, H. K. Mulmudi, S. Huang, A. W. Y. Ho-Baillie, K. R. Catchpole and A. Tricoli, Superior Self-Charged and -Powered Chemical Sensing with High Performance for NO_2 Detection at Room Temperature. *Advanced Optical Materials*, **8**, 1901863 (2020).

[38] Q. B. Jamali, M. T. Bhatti, Q. A. Qazi, B. H. Kaurejo, I. A. Qazi, S. H. Solangi and A. S. Jamali, Analysis of CO_2, CO, NO, NO_2, and PM particulates of a diesel engine exhaust. *Engineering, Technology & Applied Science Research*, **9**, 4912-4916 (2019).

Chapter 6. Self-Powered, Portable InP Nanowire Acetone Sensors for Breath Testing

In Chapter 4 and 5, the InP nanowires (NWs) sensors display specific sensitivity to NO_2, but are insensitive to weak oxidation gases or reducing gases including some of the organic volatile gases (VOCs) such as ethanol, methanol, propane, and acetone. However, the detection of VOCs has important application. For example, a large number of VOCs present in human exhaled breath and analysing them as biomarkers is a non-invasive and valuable approach for early disease detection, treatment response and overall health monitoring.[1] Acetone is one of the typical VOCs whose concentrations in breath have a direct correlation with blood ketone levels, making it an ideal biomarker for diabetes monitoring in particular prevention of diabetes acidosis (DKA), a severe and life-threatening condition.[2] Current clinical ketone detection methods largely rely on blood and urine assays. Although finger-prick tests using ketone strips are the most prevalent means of monitoring ketone levels, their invasive nature contributes to low levels of compliance, especially in children and younger individuals.[2-3] Urine testing is usually not recommended, as it is inconvenient and lower accuracy.[4] The detection of acetone in breath provides a new method for non-invasive DKA monitoring. For now, only a few breath tests have been extended to clinical applications, and these applications seldom employ portable, self-use, real-time diagnostic devices, highlighting the demand for suitable novel technologies to realise non-invasive breath tests.

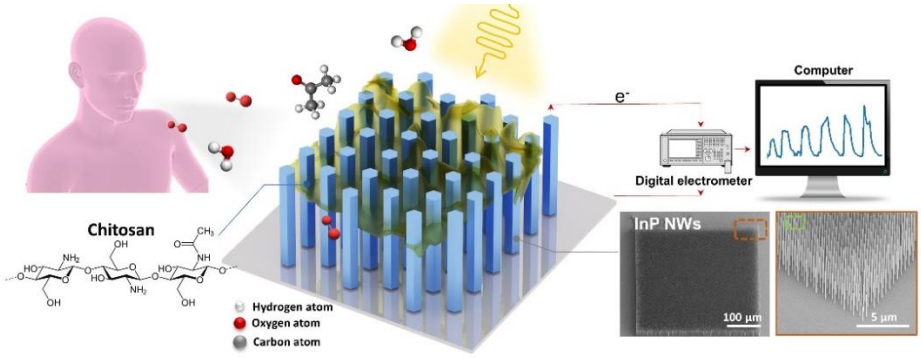

Figure 6-1. Schematic overview of the InP NW array based acetone sensing.

In this chapter, again based on the InP NW-based technology, we demonstrate a new NW device design, utilising a chitosan surface-functional layer to achieve acetone specific sensing for breath acetone sensing and diabetes monitoring. Chitosan is a cost-effective, renewable, and eco-friendly biopolymer with superb water solubility, biodegradability, renewability, antimicrobial activity, biocompatibility, and adsorption properties. The amine group ($-NH_2$) in chitosan interacts with the carbonyl groups of acetone, contributing to a high acetone specificity. Previously, chitosan has been used as the active layer of acetone sensors, however they have shown inadequate selectivity and/or sensitivity to fulfill the clinical requirements. Here, by utilising chitosan as the surface-functional layer, along with a Pt Schottky contact formed on the ultrathin InP NWs, as shown in Figure 6-1, a self-powered acetone sensor has been achieved at room temperature. It shows high selectivity and sensitivity covering the whole diabetes relevant range (from sub-ppb to >100,000 ppm level). The acetone sensing mechanism was studied through numerical simulations and experimental investigations, revealing an oxygen-facilitated two-step charge transfer process enabling acetone redox reaction. Finally, the NW sensor has been integrated into a portable electronic setup, the Ketowhistle, serving as a prototype breath-testing device that successfully detects simulated exhaled breath containing different ranges of acetone concentrations.

6.1 Experimental

The 400 × 400 μm InP NW arrays for acetone sensor were fabricated by both bottom-up and top-down method, aiming at producing NWs with small diameter to enhance sensitivity, as investigated and discussed in Chapter 4, section 4.4.

6.1.1 Bottom-up method

This method is based on the selective area metal-organic chemical vapour deposition (SA-MOCVD) technique, obtaining a NW array with the diameter of 50 - 60 nm, pitch size of 600 nm and length of ~ 4 μm on n-doped (Si) (111)A InP substrate($(1\text{-}10)\times10^{-18}$ cm^{-3}), as shown in Figure 6-2a. The growth condition was optimised to produce pure wurtzite crystal structure due to dominant axial growth versus radial growth,[4] following the substrate preparation and SA-MOCVD growth processes described in Chapter 5, section 5.2. The bottom-up grown NW sample is named as b-InP NW in this chapter.

6.1.2 Top-down method

The top-down method follows the fabrication process described in Chapter 4, section 4.1.[5] The NW diameter is determined by the mask and the ICP etching process. The smallest mask size that can be achieved is ~ 40-50 nm by electron beam lithography. The obtained NWs in Figure 6-2b show a large tapering because of the etching of already-exposed sidewalls during the deep etching of the substrate, leading to the variation of diameter along a NW from ~< 30 nm at the top to ~130 nm at the bottom. Another limitation of the top-down approach is the shorter NW length due to the etching selectivity of the mask and InP substrate, as the mask for ICP etching will be slowly removed during the etching process. Therefore, the average length of top-down etched NWs is ~2 μm,

considerably shorter than that of the bottom-up grown NWs (> 4 μm). The top-down NW is named as t-InP NW in this chapter.

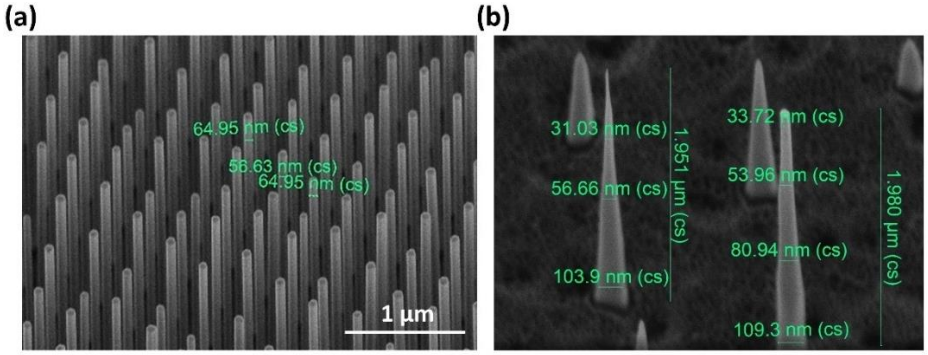

Figure 6-2. The SEM images of InP NWs obtained by bottom-up (a) and top-down (b) approaches.

6.1.3 Acetone sensor fabrication

The InP NW array acetone sensor was fabricated following the standard process of the chemiresistive gas sensor described in Chapter 4, section 4.1.3, as illustrated in Figure 6-3 a-c: 1) planarization of NW array with SU8-5 photoresist, 2) oxygen plasma etching to expose uniformly the top segments of the NWs, 3) tilt-angle deposition of Pt (< 50 nm) on exposed NWs. Finally, a diluted chitosan acetic acid aqueous solution with a concentration of 2.5 % (diluted at a 1:10 ratio from the saturated solution, concentration of 28 %) was drop-casted over the NW/Pt array and baked on a hotplate at 50 °C to remove the solvent functionalising the exposed NW surface. As shown in Figure 6-3d, through the drop-casting process a parafilm-like chitosan film forms over the tip of NWs but does not fill up the regions between the NWs. A Ti/Au contact was fabricated on top of the InP substrate next to the NW array as the bottom electrode to complete the fabrication of the acetone sensor based on b-InP NW and t-InP NW, i.e., the b-InP/Pt/chitosan NW and the t-InP/Pt/chitosan NW sensor, respectively (Figure 6-3e).

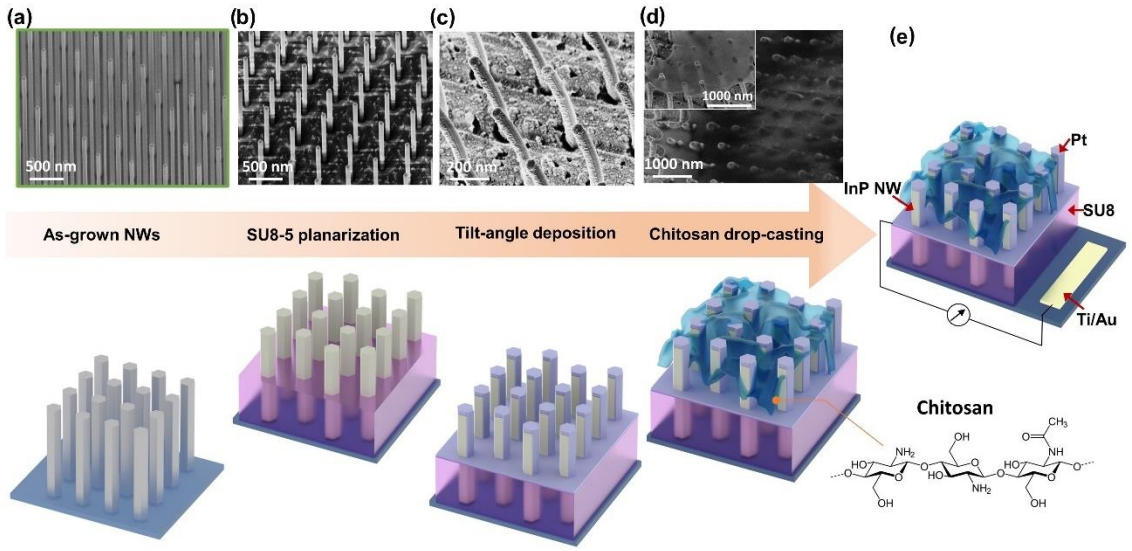

Figure 6-3. Overview of the chitosan functionalized InP NW acetone sensor and the fabrication process. The SEM images in the middle panel with the corresponding schematics in the bottom panel represent the various stage during the fabrication process, showing (a) the as-grown NWs; (b) SU8-5 planarized NWs; (c) tilt-angle deposition of Pt electrode; (d) drop-casted chitosan functionalisation; and (e) the Ti/Au bottom contact fabrication next to the NW array for electrical connection.

It is the notable that the morphology of t-chitosan/Pt/InP NW is different from the b-chitosan/Pt/InP NW because of the tapering and sharp tip of t-InP NWs, resulting in the Pt layer slightly peeled-off from t-InP NWs (Figure 6-4). This deformation may slightly affect the device electrical property because it damages the contact between the NW and Pt electrode.

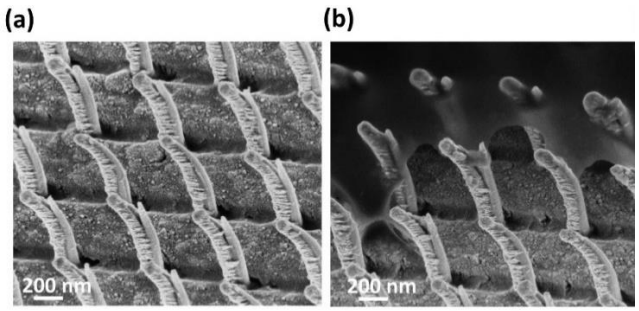

Figure 6-4. SEM images of t-InP NWs after device fabrication steps of SU8-5 planarization, tilt-angle deposition of 60 nm Pt (a) and the InP NWs devices after drop-casting of the chitosan solution (b).

6.1.4 Electrical property characterisation

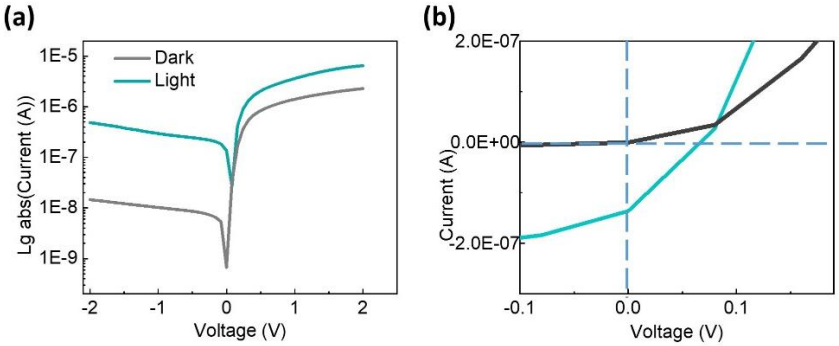

Figure 6-5. I-V measurement of the acetone sensor under dark/light conditions (a) and magnified plot of the I-V curve to determine I_{SC} and V_{OC} (b).

After the sensor fabrication, photo-electrical and gas sensing measurements were performed using a gas sensing system with solar simulator as the light source as mentioned in Chapter 5, section 5.4. As shown in Figure 6-5, the electrical properties of the sensors were characterised by standard dark/light current-voltage (I-V) measurements, exhibiting a typical Schottky diode characteristic.[6] Under illumination from a solar simulator @AM1.5 at a power of 100 $mW \cdot cm^{-2}$ (1 sun), the device demonstrated a short circuit current (I_{SC}) of 1.4×10^{-7} A (an increase from $< 10^{-9}$ A in the dark condition) and an open-circuit voltage (V_{OC}) of 80 mV,[7] indicating the self-powered operation capability of sensor.

6.1.5 Acetone sensing measurements

For the sensing measurement, the baseline I_{SC} signal was measured under 1 sun illumination with constant airflow and zero external power (self-powered).[8] Before gas

injection, the sensor was placed in the chamber under light illumination and constant simulated airflow to generate steady-state baseline I_{SC}. As acetone gas is injected, I_{SC} increased and then reached saturation. For the experiments shown below, we kept the acetone exposure time constant at (100 s) as we noted that the response reached saturation <100 s. The variation between saturated and baseline I_{SC} was calculated as the sensing response, as defined Chapter 2, section 2.1.2.[9] When acetone gas was turned off and airflow resumed, I_{SC} returned to the initial baseline current level.

6.2 Chitosan/Pt/InP NWs acetone sensing performance

6.2.1 Acetone sensing performance of b-InP/Pt/chitosan NW sensor

The sensing performance of the b-InP/Pt/chitosan NW sensor was investigated at low acetone concentrations ranging from 0.4 ppb to 10 ppm. As shown in Figure 6-6 a-d, the response of NW sensor exhibits a strong concentration dependence, demonstrating high sensitivity at both ppb and ppm levels. The linear fitting results in Figure 6-6f and g illustrate response as a function of acetone concentration with a slope that defines the device sensitivity.[10]

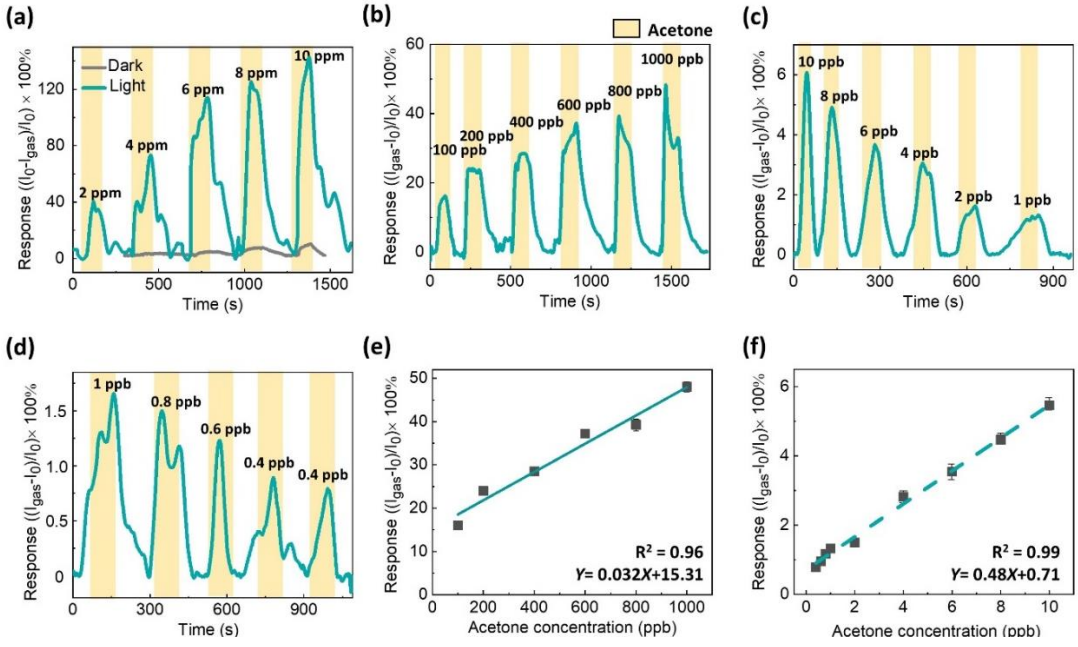

Figure 6-6. Acetone sensing performance of the b-chitosan/Pt/InP NW. (a, b, c) Time-dependent sensing response measured from short-circuit current under dark (bias voltage 0.5 V, to obtain a similar current level with I_{SC} under light condition) and light condition (bias voltage 0 V). Time-dependent sensing response in acetone concentration range (d) 100 - 1000 ppb, (e) 1 - 10 ppb, and (f) 0.4 - 1 ppb. The yellow strips indicate acetone exposure.

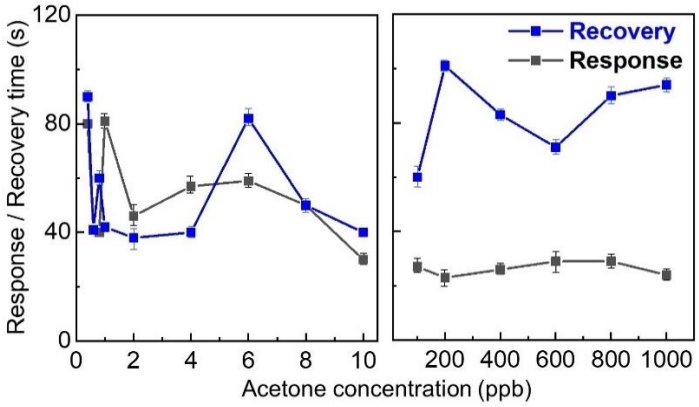

Figure 6-7. The response and recovery time corresponding to acetone concentration 0.4-1000 ppb with the standard deviation as the error bars obtained by 10 cycles of sensing measurements.

The sensitivity in the higher concentration range (100 - 1000 ppb) is 0.032 %/ppb, smaller than that in the 0.4 - 10 ppb range (0.48 %/ppb). The decreased sensitivity at a higher concentration range results from the charge-release saturation due to increased analyte concentration, given that there are only a finite number of active surface sites. Based on the linear fitting result, the limit of detection (LOD) of our acetone sensor is calculated to be 0.18 ppb (calculation details in Chapter 2, section 2.1.2). This LOD and detectable concentration range covers the clinical requirement in the lower-level breath acetone detection from healthy individuals (300-800 ppb) to people with well-managed type 1 and type 2 diabetes exhibit slightly elevated breath acetone level of 1 - 2 ppm.[11-13] Notably, our sensor features a rapid response time (T_{res}: ~25 s) and recovery time (T_{rec}: ~39 s), as shown in Figure 6-7, making it promising for real-time testing. The reproducibility of the b-InP/Pt/chitosan NW sensor was assessed by repeating 16 cycles

of acetone sensing measurement at 10, 2 and 0.1 ppm Figure 6-8. The obtained response values remain relatively consistent over time for a given concentration, with a maximum standard deviation of only 5.45%, indicating excellent stability and reproducibility in self-powered operation.

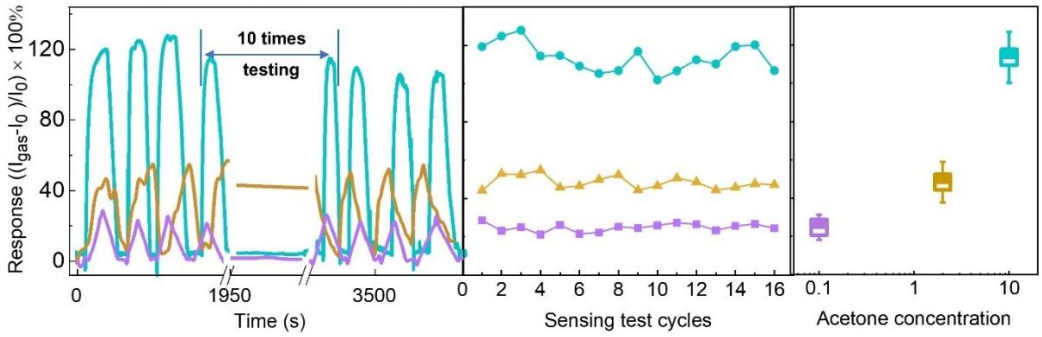

Figure 6-8. The reproducibility of b-chitosan/Pt/InP NW after 16 cycles of measurements.

Apart from the high sensitivity, achieving adequate selectivity to acetone is also critical because numerous VOCs in human breath with concentrations varying from ppt to ppm levels could act as interfering agents. A selective sensor is required to distinguish acetone from these interfering VOCs for breath ketone testing. Hence, the sensitivity of the NW sensor to a series of VOCs and atmospheric gases, including acetone (CH_3COCH_3), methyl nitrides (CH_3NO_2), ethanol (C_2H_5OH), and propane (C_6H_6) was evaluated at a concentration of 1 ppm. Notably, the sensor response to carbon dioxide (CO_2), one of the main gas components in exhaled breath, was investigated at 1% (~10,000 ppm). As shown in Figure 6-9a, the sensing responses for these gases were less than 5% of that from acetone (49 ± 2%), indicating an excellent selectivity towards acetone. In particular, ethanol is one of the most common interfering VOCs in breath; however, the acetone selectivity over ethanol interference ($R_{acetone}$ / $R_{ethanol}$) was > 40, much higher than those obtained in previous studies.

The bubbler setup, built to connect to the gas sensing system shown in Chapter 3, section 3.5, was further used to evaporate acetone and 2-butanone solvents at higher concentrations to fulfill the DKA breath acetone ranges from 75 to 1200 ppm.[1, 14-15] A high concentration vapour can be produced by a bubbler setup with a N_2 tube inlet into the relevant solvent and evaporating saturated vapor to the gas sensing chamber. To stabilise the temperature, the bubbler is placed in a bath of water at room-temperature during the whole sensing measurement process. The vapor concentration (Conc) was calculated by following equations:[16]

$$F_{output} = \left(\frac{P}{P_o - P}\right) F_c = \alpha F_c \quad (2)$$

$$Conc = \frac{10^6 F_{output}}{F_{dilute} + F_{carrier} + F_{output}} = \frac{10^6 \alpha}{(F_{dilute}/F_{carrier}) + 1 + \alpha} \quad (3)$$

where F_{output}, $F_{carrier}$, and F_{dilute} are the output, carrier, and dilute flow rate of acetone vapour from the bubbler, respectively, in standard cubic centimeter per minute (sccm), and α is the vapor pickup efficiency defined as the relative ratio of the output sample flow rate to the carrier flow. P_o is the outlet pressure in the bubbler, defined by $P_o = P_i + P_{th}$. P_i is the inlet pressure to the bubbler (1.6 bar), and P_{th} is the thermodynamic vapour pressure of the analyte sample. When the carrier gas is completely saturated with analyte vapour, P_{th} becomes the saturated vapor pressure, P_s, which can be calculated from the empirical Antoine equation[17]:

$$log_{10} P_s = A - \frac{B}{C + T} \quad (4)$$

where T is temperature (in Kelvin, K), and A, B, and C are component-specific constants of 4.42, 1312.25, and -32.45, respectively, for acetone at room temperature. The calculated P_s of acetone is 30.6 kPa (298 K) (https://webbook.nist.gov/cgi/cbook.cgi?ID=C67641). With different dilution ratios of simulated air, a series of high concentration acetone from 0.45 % (4,500 ppm) to 13.12% (131,200 ppm) can be obtained through this setup (Table 6-1).

Table 6-1. Parameters used for calculating acetone concentration produced from the bubbler.

$F_{carrier}$ (sccm)	F_{vapor} (sccm)	$F_{dilution}$ (sccm)	α	Vapour Conc (ppm)	Vapour Conc (%)
1000	151.01	0	0.15	131194.19	13.12
830	125.33	170	0.15	111375.18	11.14
660	99.66	340	0.15	90630.85	9.06
500	75.50	500	0.15	70202.15	7.02
330	49.83	670	0.15	47466.38	4.75
170	25.67	830	0.15	25028.38	2.50
130	19.63	870	0.15	19252.73	1.93
100	15.10	900	0.15	14875.89	1.49
66	9.97	973	0.15	9501.11	0.95
30	4.53	970	0.15	4509.73	0.45

As shown in Figure 6-9b, the sensor response exhibits a consistent correlation with the concentration from 0.57% (5,700 ppm) to 13.7% (137,000 ppm). This indicates a wide dynamic range that effectively encompasses the clinically significant range, from sub-ppm (non-diabetic person) to 1000 ppm (DKA).[18] It is worth noting that even though both acetone and 2-butanone molecules are small ketones, our NW sensor only exhibits a high sensitivity to acetone. A possible reason could be that the activation energy required for the 2-butanone sensing reaction is higher than that required for acetone. This selectivity is of great significance for clinical breath analysis since 2-butanone is a small four-carbon ketone (acetone is a three-carbon ketone), which is also a breath biomarker for lung cancer. The capability to distinguish it from acetone will greatly reduce the risk of false positives.[19]

Another major challenge in breath analysis is moisture in the breath, which could impact the sensor behaviour by saturating the sensor and decreasing the material sensitivity to the target gas. The effect of humidity on the acetone sensing performance was characterised on b-InP/Pt/chitosan NW devices by the same bubbler setup to create a humid condition. As shown in Figure 6-9c, compared to the dry air condition, the sensing response decrease by 10 ± 2 %, 30 ± 6 %, and 50 ± 12 % under a relative humidity (RH) of 20%, 50%, and 65%, respectively. Nevertheless, according to the slope of the sensing response plot in Figure 6-9d, the device still maintained a consistent sensitivity to acetone, indicating that the sensitivity of this device was not compromised in a humid environment.

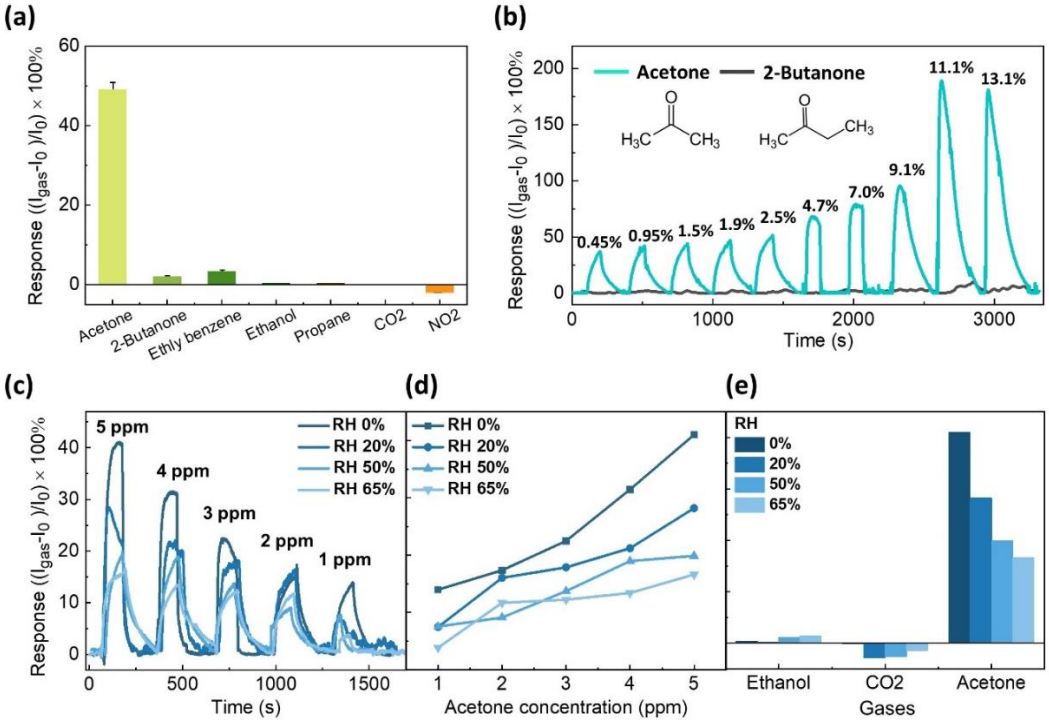

Figure 6-9. Selectivity and humidity test for the b-chitosan/Pt/InP NW sensor. (a) Gas sensing selectivity measurement performed under a concentration of 1 ppm of acetone, 2-butanone, ethly benzene ethanol, propane, NO_2, as well as 1 % CO_2, with the standard deviation as the error bars obtained by 10 cycles of sensing measurements. (b) Time-dependent sensing response of acetone and 2-butanone in concentrations ranging from 1% (10,000 ppm) to 11% (110,000 ppm). (c, d) Time-dependent sensing response to the acetone concentration of 1-5 ppm under the RH levels

of 0%, 30%, 50% and 65%. (e) Gas sensing selectivity measurement at 1 ppm compared to similar concentration of ethanol and CO_2 under different RH.

The cross-sensitivity to interrupting molecules that may be present in exhaled breath, such as ethanol and CO_2, was also measured under different RH conditions separately, as shown in Figure 6-9e, confirming the high selectivity towards acetone, with an almost ×10 higher response compared to the interfering gases under the same RH conditions.

6.2.2 Acetone sensing performance of t-InP/Pt/chitosan NW sensor

From above results, the bottom-up b-InP/Pt/chitosan NW sensor achieved a high performance metrics i.e. sub-ppb level detection, rapid response/recovery speed, and an ultra-broad dynamic range covering different types of diabetes and metabolic conditions, satisfying the basic clinical requirements for breath testing. However, evaluating the usability of this device for DKA monitoring, we identified one drawback of using the b-InP/Pt/chitosan sensor, it relies on specialised epitaxial growth equipment and technique, which is of high cost and difficult to scale up. Therefore, the top-down approach fabricated t-InP/Pt/chitosan NW sensors with an intention for mass production and commercialisation,[20] as this approach is highly scalable, more accessible, cost-effective and compatible with the well-established complementary metal-oxide semiconductor (CMOS) processes.

The details on the device processing and sensing performance result are provided in section 6.1.2 and Figure 6-10a and b. The acetone sensing response of this t-chitosan/Pt/InP NW device (20%, 1 ppm) is smaller than the b-chitosan/InP NW (49%, 1 ppm), and the LOD of this device (82 ppb) is larger than the b-chitosan/InP NW. However, the t-chitosan/InP NW has a high sensitivity of 6.61 %/ppm to acetone in the diabetic

diagnosis concentration range of 0.1-10 ppm (Figure 6-10c, e). Moreover, the acetone response only decreases slightly from 6.5 % to 4.7 % at 1 ppm, with the reduction in light intensity from 42.3 to 4.2 mW·cm^{-2}. This small dependence of the light intensity could further approach the environmental fidelity.[21] It exhibits shorter T_{res} (~5 s) and T_{rec} (~7 s), higher humidity tolerance, light intensity fidelity, selectivity, and ease of fabrication as shown in Figure 6-10d, f, despite slightly lower sensitivity. A summary of and the sensor parameters are listed in Table 6-2. Considering the fabrication cost and scalability issue, the top-down fabricated device was chosen for integration into the Ketowhistle.[22]

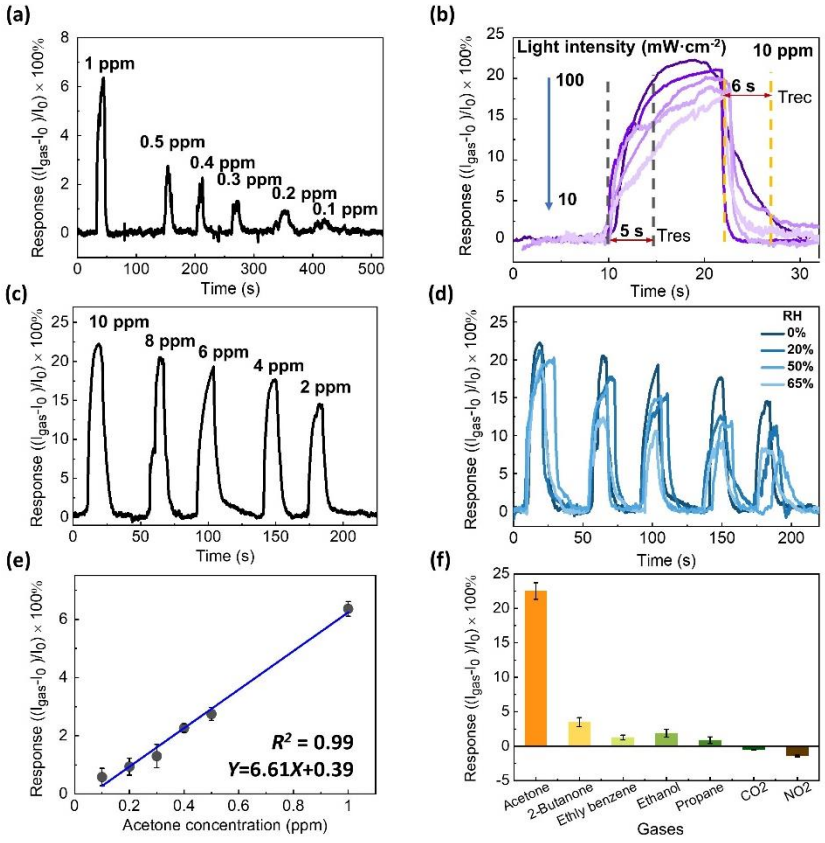

Figure 6-10. Acetone sensing performance of the top-down method fabricated NW sensor (t-InP/Pt/chitosan). (a) Time-dependent sensing response measured for an acetone concentration of 0.1-1 ppm. (b) Acetone sensing response under different light illumination intensities from 100 to 10 mW·cm^{-2}, with the response and recovery times. (c) Time-dependent sensing response curve with an acetone concentration range of 2-10 ppm. (d) Time-dependent sensing response to the acetone concentration of 2-10 ppm under the RH levels of 0%, 20%, 50% and 65%. (e) Sensor

response vs concentration curve with linear fitting to the data. (f) Gas sensing selectivity measurement comparing the response to 10 ppm acetone, 2-butanone, ethyl benzene, ethanol, propane, NO_2, and 10% CO_2. The error bars in (e, f) indicate the standard deviation obtained from 10 cycles of sensing measurements.

The key performance parameters of the b-InP/Pt/chitosan NW and t-InP/Pt/chitosan NW sensor, along with those of other chemiresistive acetone sensors reported in recent years are compared in Table 6-2. Our NW sensors show superior performance in all key metrics, including It is also noteworthy to the best of our knowledge, it is the first demonstration of acetone sensor with self-powered room-temperature operation capability, which effectively addresses the power consumption and safety concerns typically encountered by most of metal-oxide based devices.

Table 6-2. Comparison of the sensing performance of chemiresistive acetone sensors from recent literature.

Materials	Working temperature (°C)	Response (concentration)	Limit of detection	Response/ recover time (s)	Ref
Chitosan/Pt/InP NW	25	48% (1 ppm)	0.4 ppb	25 / 39	This work
t-InP/Pt/chitosan NW	25	6.5% (1 ppm)	82 ppb	5 / 6	
$NiO/NiWO_4/WO_3$ (p–p–n) NW	400	29 (30 ppm)	0.7 ppm	-	[23]
Pt/WO_3 hemitubes	350	4.11 (2 ppm)	120 ppb	-	[24]
Si/WO_3	135	5.4 (1 ppm)	50 ppb	-	[25]
Rh/SnO_2 nanofibers	200	2.7 (1 ppm)	-	2 / 64	[26]
chitosan–Pt SnO_2 nanofibers	350	2.9 (5 ppb)	5 ppb	12 / 84	[27]

Au- ZnO/Ag core-shell films	150	43% (0.5 ppm)	0.5 ppm	45 / 160	[28]
Na/ZnO Nanoflowers	25, (UV light, 5 $mW \cdot cm^{-2}$)	1.51 (1 ppm)	0.2 ppm	18 / 63	[29]
Zn_3N_2 / ZnO	200	5.1 (1 ppm)	0.07 ppm	15 / 27	[30]
In_2O_3 fibers	275	24 (1ppm)	0.3 ppm	-	[31]
Chitosan thin film	25	12.3% (1 ppm)	0.1 ppm	-	[32]

6.3 Acetone sensing mechanism

To understand the sensing mechanism of the InP/Pt/chitosan NW acetone sensor, a series of controlled experiments (Figure 6-11a, b) and simulation studies (Figure 6-11c, f) were performed. Contrary to previous studies in which chitosan acts as the active sensing layer[33], in our study, the chitosan layer was drop-casted on top of the NW array after metal electrode deposition, as the surface functionalisation layer and was not electrically connected to the sensing circuit. To clarify the effect of chitosan on acetone sensing, a similar device without the chitosan layer was fabricated and used as a reference sample. Figure 6-11a compares the baseline I_{SC} of the b-Pt/InP NW device with/without chitosan under light illumination. Compared with the device without chitosan, the chitosan-coated device has a significantly lower baseline current under illumination. We ascribed it to the ability of chitosan to absorb and release oxygen.[34] The presence of chitosan effectively absorbs O_2 from the simulated air, trapping O_2 molecules at the chitosan/InP interface, as denoted in equation (1) as shown below. This would facilitate O_2 ionisation (equation (2)) by the photogenerated electrons that drift to the InP NW surface due to the built-in electric field formed with the Pt/InP Schottky contact. This depletion of electrons leads to a decreased baseline current (I_{SC}) of the chitosan-coated device.[35]

$$O_{2(gas)} \leftrightarrow O_{2(ads)} \quad (1)$$

$$O_{2(ads)} + e^- \leftrightarrow O_2^-{}_{(ads)} \quad (2)$$

$$CH_3COCH_{3\,(ads)} + 4O_2^-{}_{(ads)} \rightarrow 3CO_2 + 3H_2O + 4e^- \quad (3)$$

In contrast, the device without chitosan has much less O_2 adsorption on the InP NW surface, and thus, a negligible baseline I_{SC} change is observed. As the main mechanism for most chemiresistive acetone sensors, these chemisorbed oxygen ions (i.e., O_2^-, O^-, and O^{2-})[32, 35-37] are the indispensable reactant to enable a redox reaction with acetone, producing CO_2, H_2O and electrons,[38] as represented in equation (3). Therefore, it is clear that chitosan plays a critical role in achieving sensitivity and selectivity to acetone, possibly through its -NH_2 groups interacting with acetone, and by improving O_2 adsorption. As can be seen from Figure 6-11b, with the simulated air, the acetone sensing response obtained from the chitosan-coated device is significantly higher (>120% at 10 ppm) than the device without chitosan (< 5% at 10 ppm). However, under the O_2 eliminated condition (only pure N_2 as the carrier gas for sensing measurement), the sensing response of the chitosan-coated device decreased from > 120% (with O_2) to < 15% (without O_2), as shown in the middle panel of Figure 6-11b, confirming the vital role of the $O_{2(ads)}$ and ionic oxygen species like O_2^- in the acetone sensing reaction.[39]

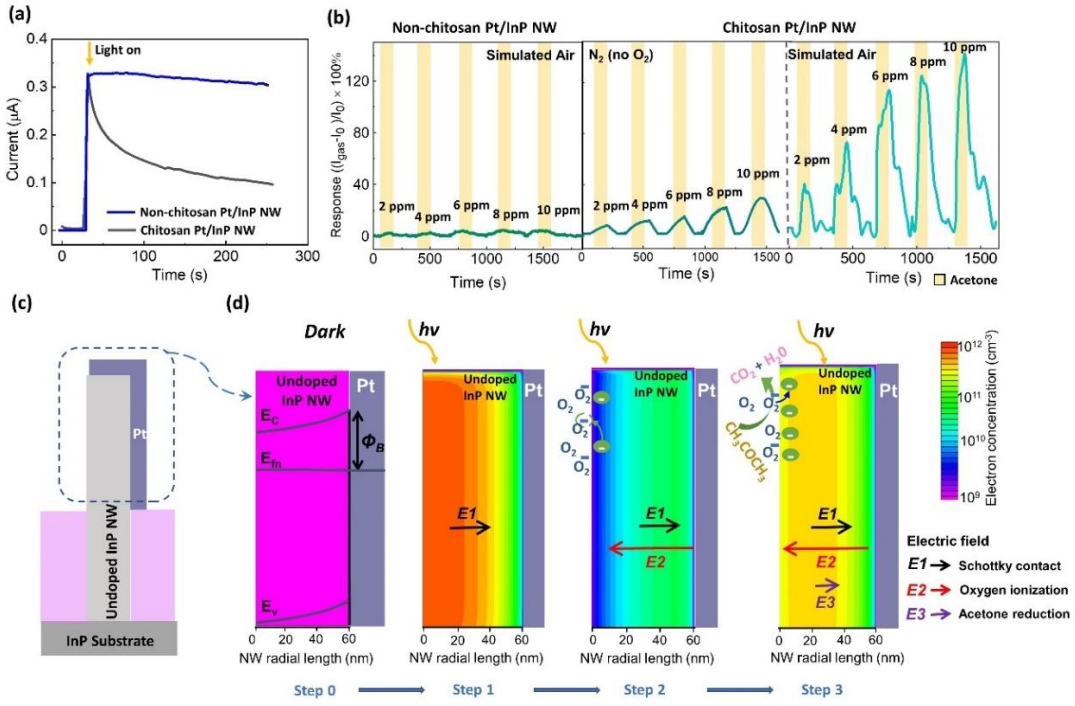

Figure 6-11. Acetone sensing mechanism investigation. (a) Temporal short-circuit current (I_{SC}) response of the b-Pt/InP NW device with and without chitosan under light illumination. (b) Time-dependent acetone sensing response of the sensor with and without chitosan (under low oxygen conditions and in simulated air). (c) Schematic of an InP NW with Pt contact used for the simulation study. (d) Energy band diagram of the structure with the simulated electron concentration, corresponding to the various critical condition/steps of acetone sensing process. E_c, E_v, and E_{fn} represent the conduction band, valence band, and electron quasi-Femi level, respectively.

A simulation study by COMSOL Multiphysics (this part of work was conducted by Dr. Zhe Li) was performed to investigate the effect of Pt/NW Schottky contact by calculating the energy band diagram of the device and electron concentration distribution within a single NW as depicted in Figures 6-11c and d. The effect of chitosan on the NW surface was also modelled through the surface charge boundary condition in the simulation. As shown in Figure 6-11d, the Pt layer forms a Schottky contact on the InP NW side wall under dark condition (Step 0). Due to the band alignment of the Fermi level between the InP NW and Pt contact, an electron depletion layer is first created that drastically decreases the electron concentration within the NW due to the small NW diameter (50 - 60 nm), indicating the importance of the geometric optimisation. Upon light illumination, the built-in electric field generated by the Schottky contact drives photo-generated electrons towards the NW surface (Step 1), resulting in surface accumulation of electrons. This facilitates the ionisation of adsorbed O_2 on the NW interface (Step 2), as enhanced by chitosan functionalisation and expressed in equations (1) and (2). The enhancement of O_2 ionisation enables the acetone reduction reaction (equation (3)), resulting in the release of electrons back to the InP NW that significantly increases the carrier concentration in the NW (Step 3).[40]

6.4 Portable breath sensor prototype (Ketowhistle) development, calibration, and testing

To demonstrate the applicability of the chitosan/Pt/InP NWs acetone sensor and test the point-of-care application, a prototype portable device has been demonstrated for exhaled breath testing [22] by integrating the t-InP/Pt/chitosan NW sensor onto a handheld apparatus named Ketowhistle, as shown in Figure 6-12a. The handheld Ketowhistle apparatus contains the NW acetone sensor, a commercial CO_2 sensor (to ensure the utilisation of end-tidal breath most reflective of blood acetone concentrations[41]), a signal-processing circuitry, and an OLED screen for data display. The NW acetone sensor is illuminated by a low-power red LED, which is placed right on top of the sensor to ensure stable illumination and sensing response, as shown in Figure 6-12a. A wide concentration range calibration of the Ketowhistle for the acetone analysis was performed using the laboratory-based gas sensing system. Figure 6-12c presents the Ketowhistle calibration curve for acetone concentration ranging from 0.1-1000 ppm to cover the entire breath acetone spectrum. The measured electrical signal readouts from the Ketowhistle exhibit two distinct regions, with a slope of 6.11 mV/ppm and 0.013 mV/ppm corresponding to two ranges of acetone concentrations, i.e., Range 1 (0.1 - 10 ppm) and Range 2 (50 - 500 ppm), respectively. Within each range, there is a linear correlation between the electrical readout and the acetone concentration. It is worth noting that the low acetone concentration Range 1 covers the range that reflects normal eating patterns, whereas Range 2 indicates significant ketosis with a high risk of DKA. For persons with established diabetes, a device giving a digital readout of concentrations would be ideal in the management of sick days, as the trend in levels will indicate improvement or deterioration.[42-45]

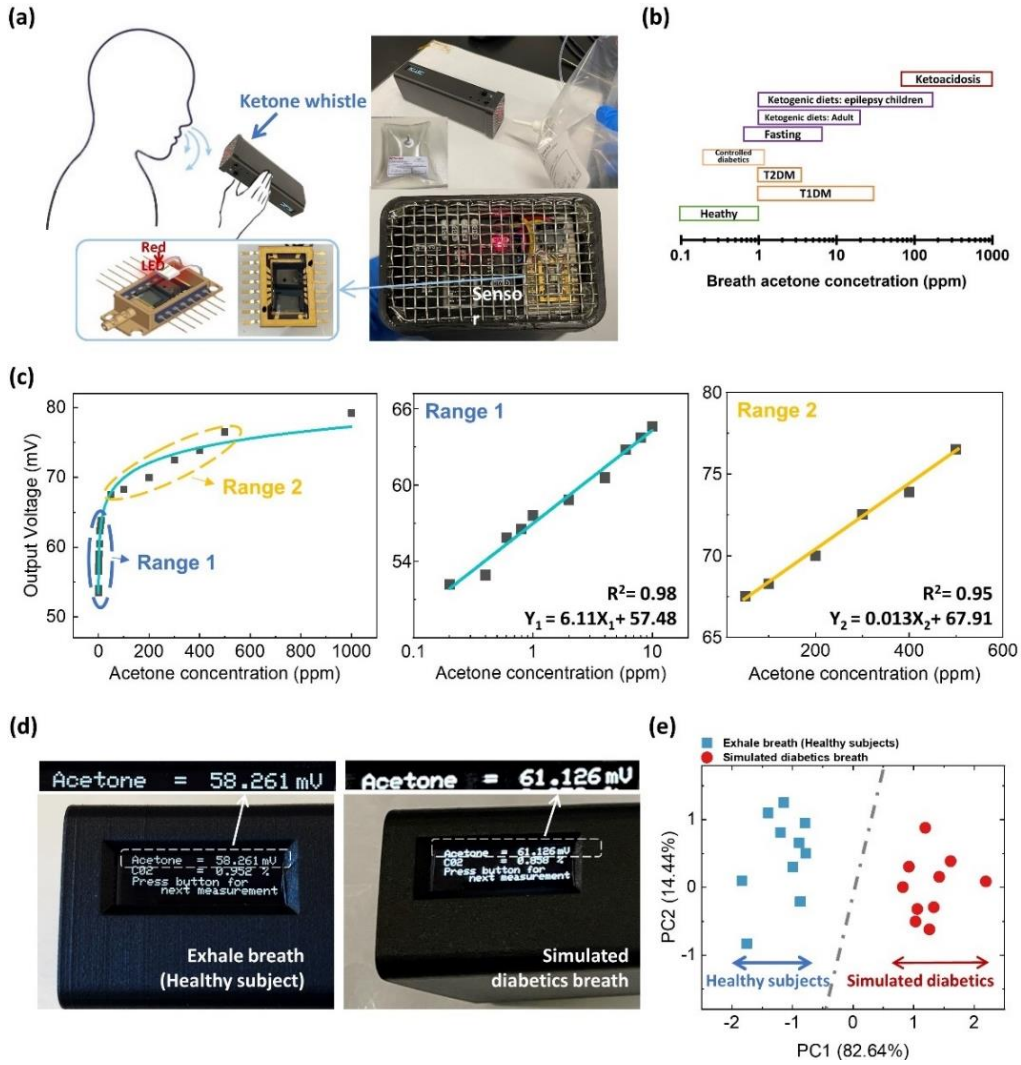

Figure 6-12. The Ketowhistle for simulated breath test. (a) Pictures of the portable Ketowhistle prototype using Tedlar bags for collection of simulated breath samples. (b) Chart showing the ranges of breath acetone concentration corresponding to various physiological states and ketosis ranges. [44] (c) Ketowhistle calibration for acetone concentration ranging from 0.1-1000 ppm to cover the entire breath acetone spectrum. (d) OLED screen displaying the response of an exhaled breath sample of a non-diabetic (left) and a simulated diabetic breath sample (right). (e) PCA for non-diabetic breath samples and simulated diabetic breath samples.

For the exhaled breath test, Tedlar bags (PVDF 0.6 L, Sigma-Aldrich), suitable for VOC sampling, were used to collect the breath samples from non-diabetic subjects and simulated diabetic breath,[46] as shown by the inset in Figure 6-12a. Tedlar bags with the

Push/Pull Lock Valve (PLV) on bags allow them to fill in, short-term stock and release exhale breath for the breath sample collection. For the exhaled breath test, the concentration of simulated breath of diabetics was adjusted to ~ 5 ppm by filling the Tedlar bags with ~50 % (v) of non-diabetic exhaled breath and ~50 % of 10 ppm acetone in simulated air. The measurement result captured by the Ketowhistle is displayed on the OLED screen, as shown in Figure 6-12d. Principal component analysis (PCA) was applied to analyse the output voltage-dependent breath test results in Figure 6-12b),[47] where 10 simulated diabetic breath samples and 10 non-diabetic subjects were clearly categorised into two distinguishable clusters without any overlap. The stability and reproducibility of the Ketowhistle prototype have been further demonstrated by repeated breath tests from the same person for two months and the standard deviation is only 0.375 mV, variation <0.6%,[48-49] indicating excellent consistency essential for clinical applications as shown in Figure 6-13.[50]

For future work, the next step is for the InP/Pt/chitosan NW sensor based Ketowhistle prototype to be assessed in pilot clinical studies, including persons living with type 1 (well and during episodes of DKA), type 2 diabetes (including those using SGLT2 inhibitor medications), and overweight/obese persons using ketogenic diets in weight loss programs. To enhance device performance, the chitosan functionalization layer can be further modified to optimise NW coverage by changing its concentration (by dilution) and/or composition.[33, 38] Guided by this study, using various functionalisation materials with functional groups specific to other breath VOCs could realise a variety of NW array-based multiplexed breath sensor devices.

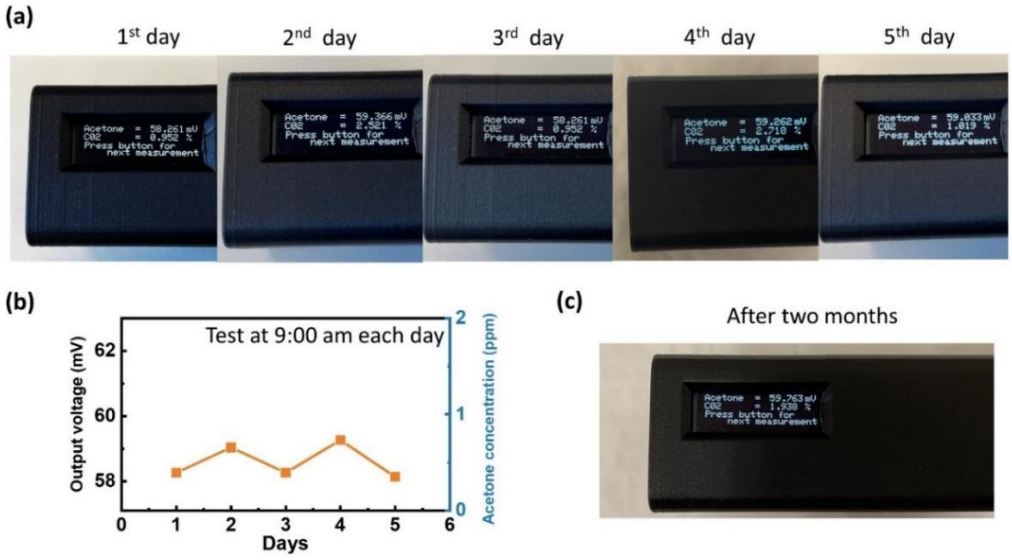

Figure 6-13. (a)The stability of Ketowhistle breath test results at 9:00 am during consecutive five days of testing and (b) the corresponding acetone concentration from the calibration in Figure 6-12c. (c) Ketowhistle breath test result from the same person with after Ketowhistle has been stored in ambient condition for two months.

6.5 Summary

In this chapter, a novel high-performance, non-invasive, self-powered chitosan/Pt/InP NW acetone sensor has been successfully demonstrated for the first time. The sensor device exhibits superior sensitivity in a wide dynamic range, from the concentration of sub-ppb level up to >110,000 ppm, as well as high selectivity against other VOCs, including other small gaseous ketones. The sensing mechanism of this device is thoroughly investigated by control experiments and numerical simulations, revealing an oxygen-facilitated two-step charge transfer process for acetone reduction, enabled by chitosan functionalisation and Pt/InP Schottky contact. Finally, by incorporating the NW sensor into a portable breath testing prototype, the Ketowhistle, we showed their immediate potential for non-invasive ketone testing and monitoring for persons with

diabetes, particularly for DKA prevention. This study also provides an exciting pathway towards future reliable breath analysis for diabetes diagnosis, management and beyond.

References

[1] Alkedeh and R. Priefer, The Ketogenic Diet: Breath Acetone Sensing Technology. *Biosensors-Basel*, **11**, 26 (2021).

[2] S. Wei, Z. Li, A. John, B. I. Karawdeniya, Z. Li, F. Zhang, K. Vora, H. H. Tan, C. Jagadish, K. Murugappan, A. Tricoli and L. Fu, Semiconductor Nanowire Arrays for High-Performance Miniaturized Chemical Sensing. *Advanced Functional Materials*, **32**, 2107596 (2022).

[3] S. Wei, Z. Li, K. Murugappan, Z. Li, F. Zhang, A. G. Saraswathyvilasam, M. Lysevych, H. H. Tan, C. Jagadish and A. Tricoli, A Self‐Powered Portable Nanowire Array Gas Sensor for Dynamic NO_2 Monitoring at Room Temperature. *Advanced Materials*, **35**, 2207199 (2023).

[4] J. Wong-Leung, I. Yang, Z. Y. Li, S. K. Karuturi, L. Fu, H. H. Tan and C. Jagadish, Engineering III-V Semiconductor Nanowires for Device Applications. *Advanced Materials*, **32**, 1904359 (2020).

[5] S. Y. Wei, Z. Li, A. John, B. I. Karawdeniya, Z. Y. Li, F. L. Zhang, K. Vora, H. H. Tan, C. Jagadish, K. Murugappan, A. Tricoli and L. Fu, Semiconductor Nanowire Arrays for High-Performance Miniaturized Chemical Sensing. *Advanced Functional Materials*, **32**, 2107596 (2022).

[6] Q. Gao, Z. Y. Li, L. Li, K. Vora, Z. Li, A. Alabadla, F. Wang, Y. A. Guo, K. Peng, Y. C. Wenas, S. Mokkapati, F. Karouta, H. H. Tan, C. Jagadish and L. Fu, Axial p-n junction design and characterization for InP nanowire array solar cells. *Progress in Photovoltaics*, **27**, 237-244 (2019).

[7] J. Wallentin, N. Anttu, D. Asoli, M. Huffman, I. Aberg, M. H. Magnusson, G. Siefer, P. Fuss-Kailuweit, F. Dimroth, B. Witzigmann, H. Q. Xu, L. Samuelson, K. Deppert and M. T. Borgstrom, InP Nanowire Array Solar Cells Achieving 13.8% Efficiency by Exceeding the Ray Optics Limit. *Science*, **339**, 1057-1060 (2013).

[8] M. B. Reddy, V. Janardhanam, A. A. Kumar, V. R. Reddy, P. N. Reddy, C. J. Choi, R. Jung and S. Hur, The influence of rapid thermal annealing on electrical and structural properties of Pt/Au Schottky contacts to n-type InP. *Journal of Materials Science-Materials in Electronics*, **21**, 804-810 (2010).

[9] Q. Gao, Z. Li, L. Li, K. Vora, Z. Li, A. Alabadla, F. Wang, Y. Guo, K. Peng, Y. C. Wenas, S. Mokkapati, F. Karouta, H. H. Tan, C. Jagadish and L. Fu, Axial p-n junction design and characterization for InP nanowire array solar cells. *Progress in Photovoltaics: Research and Applications*, **27**, 237-244 (2019).

[10] T. Pham, G. H. Li, E. Bekyarova, M. E. Itkis and A. Mulchandani, MoS_2-Based Optoelectronic Gas Sensor with Sub-parts-per-billion Limit of NO_2 Gas Detection. *Acs Nano*, **13**, 3196-3205 (2019).

[11] Rydosz, A Negative Correlation Between Blood Glucose and Acetone Measured in Healthy and Type 1 Diabetes Mellitus Patient Breath. *J Diabetes Sci Technol*, **9**, 881-4 (2015).

[12] M. Sun, Z. Chen, Z. Gong, X. Zhao, C. Jiang, Y. Yuan, Z. Wang, Y. Li and C. Wang, Determination of breath acetone in 149 Type 2 diabetic patients using a ringdown breath-acetone analyzer. *Analytical and bioanalytical chemistry*, **407**, 1641-1650 (2015).

[13] V. Saasa, T. Malwela, M. Beukes, M. Mokgotho, C. P. Liu and B. Mwakikunga, Sensing Technologies for Detection of Acetone in Human Breath for Diabetes Diagnosis and Monitoring. *Diagnostics*, **8**, 12 (2018).

[14] J. C. Anderson, Measuring breath acetone for monitoring fat loss: Review. *Obesity*, **23**, 2327-2334 (2015).

[15] H. L. Tai, S. Wang, Z. H. Duan and Y. D. Jiang, Evolution of breath analysis based on humidity and gas sensors: Potential and challenges. *Sensors and Actuators B-Chemical*, **318**, 128104 (2020).

[16] Y. S. Kim, S. C. Ha, H. Yang and Y. T. Kim, Gas sensor measurement system capable of sampling volatile organic compounds (VOCs) in wide concentration range. *Sensors and Actuators B-Chemical*, **122**, 211-218 (2007).

[17] E. Araujo-Lopez, J. S. Lopez-Echeverry and S. Reif-Acherman, The Antoine equation of state: Rediscovering the potential of an almost forgotten expression for calculating volumetric properties of pure compounds. *Chemical Engineering Science*, **177**, 89-109 (2018).

[18] Go, S. R. Park, Y. Ku, M. Sun, S. Yeon, J.-K. Lee, S. W. Lee and M.-H. Lee, Highly Sensitive Electrochemical Sensor for Diagnosis of Diabetic Ketoacidosis (DKA) by Measuring Ketone Bodies in Urine. *Sensors*, **21**, 4902 (2021).

[19] M. Hakim, Y. Y. Broza, O. Barash, N. Peled, M. Phillips, A. Amann and H. Haick, Volatile Organic Compounds of Lung Cancer and Possible Biochemical Pathways. *Chemical Reviews*, **112**, 5949-5966 (2012).

[20] M. Tintelott, V. Pachauri, S. Ingebrandt and X. T. Vu, Process Variability in Top-Down Fabrication of Silicon Nanowire-Based Biosensor Arrays. *Sensors*, **21**, 5153 (2021).

[21] R. G. Hobbs, N. Petkov and J. D. Holmes, Semiconductor Nanowire Fabrication by Bottom-Up and Top-Down Paradigms. *Chemistry of Materials*, **24**, 1975-1991 (2012).

[22] P. C. McIntyre and A. F. I. Morral, Semiconductor nanowires: to grow or not to grow? *Materials Today Nano*, **9**, 100058 (2020).

[23] N. Kaur, D. Zappa, V. A. Maraloiu and E. Comini, Novel Christmas Branched Like NiO/NiWO4/WO3 (p-p-n) Nanowire Heterostructures for Chemical Sensing. *Advanced Functional Materials*, **31**, 2104416 (2021).

[24] S. J. Choi, I. Lee, B. H. Jang, D. Y. Youn, W. H. Ryu, C. O. Park and I. D. Kim, Selective Diagnosis of Diabetes Using Pt-Functionalized WO_3 Hemitube Networks As a Sensing Layer of Acetone in Exhaled Breath. *Analytical Chemistry*, **85**, 1792-1796 (2013).

[25] C. Weber, H. P. Braun, F. Krumeich, A. T. Guntner and S. E. Pratsinis, Superior Acetone Selectivity in Gas Mixtures by Catalyst-Filtered Chemoresistive Sensors. *Advanced Science*, **7**, 2001503 (2020).

[26] X. Y. Kou, N. Xie, F. Chen, T. S. Wang, L. L. Guo, C. Wang, Q. J. Wang, J. Ma, Y. F. Sun, H. Zhang and G. Y. Lu, Superior acetone gas sensor based on electrospun SnO_2 nanofibers by Rh doping. *Sensors and Actuators B-Chemical*, **256**, 861-869 (2018).

[27] Y. J. Jeong, W. T. Koo, J. S. Jang, D. H. Kim, H. J. Cho and I. D. Kim, Chitosan-templated Pt nanocatalyst loaded mesoporous SnO_2 nanofibers: a superior chemiresistor toward acetone molecules. *Nanoscale*, **10**, 13713-13721 (2018).

[28] Q. A. Drmosh, Y. A. Al Wajih, I. O. Alade, A. K. Mohamedkhair, M. Qamar, A. S. Hakeem and Z. H. Yamani, Engineering the depletion layer of Au-modified ZnO/Ag core-shell films for high-performance acetone gas sensing. *Sensors and Actuators B-Chemical*, **338**, 129851 (2021).

[29] R. Jaisutti, M. Lee, J. Kim, S. Choi, T. J. Ha, J. Kim, H. Kim, S. K. Park and Y. H. Kim, Ultrasensitive Room-Temperature Operable Gas Sensors Using p-Type Na:ZnO Nanoflowers for Diabetes Detection. *Acs Applied Materials & Interfaces*, **9**, 8796-8804 (2017).

[30] F. D. Qu, Y. Yuan, R. Guarecuco and M. H. Yang, Low Working-Temperature Acetone Vapor Sensor Based on Zinc Nitride and Oxide Hybrid Composites. *Small*, **12**, 3128-3133 (2016).

[31] Z. R. Zhang, Y. X. Wu, H. Y. Du, Y. H. Sun, S. P. Sun, S. K. Xu, L. Y. Cong and P. C. Sun, Acetone sensing mechanism of Ar/O_2 plasma modified indium oxide electrospun fibers: A combined DFT and experimental study. *Journal of Alloys and Compounds*, **895**, 162017 (2022).

[32] T. I. Nasution, I. Nainggolan, S. D. Hutagalung, K. R. Ahmad and Z. A. Ahmad, The sensing mechanism and detection of low concentration acetone using chitosan-based sensors. *Sensors and Actuators B-Chemical*, **177**, 522-528 (2013).

[33] M. J. Ahmed, B. H. Hameed and E. H. Hummadi, Review on recent progress in chitosan/chitin-carbonaceous material composites for the adsorption of water pollutants. *Carbohydrate Polymers*, **247**, 116690 (2020).

[34] P. Feng, Y. Luo, C. Ke, H. Qiu, W. Wang, Y. Zhu, R. Hou, L. Xu and S. Wu, Chitosan-Based Functional Materials for Skin Wound Repair: Mechanisms and Applications. *Frontiers in Bioengineering and Biotechnology*, **9**, 650598 (2021).

[35] L. Wang, J. A. Jackman, J. H. Park, E.-L. Tan and N.-J. Cho, A flexible, ultra-sensitive chemical sensor with 3D biomimetic templating for diabetes-related acetone detection. *Journal of Materials Chemistry B*, **5**, 4019-4024 (2017).

[36] W. Lindinger, A. Hansel and A. Jordan, Proton-transfer-reaction mass spectrometry (PTR-MS): on-line monitoring of volatile organic compounds at pptv levels. *Chemical Society Reviews*, **27**, 347-354 (1998).

[37] Mirzaei, S. G. Leonardi and G. Neri, Detection of hazardous volatile organic compounds (VOCs) by metal oxide nanostructures-based gas sensors: A review. *Ceramics International*, **42**, 15119-15141 (2016).

[38] Gylienė, E. Servienė, I. Vepštaitė, R. Binkienė, M. Baranauskas and J. Lukša, Correlation between the sorption of dissolved oxygen onto chitosan and its antimicrobial activity against Esherichia coli. *Carbohydrate Polymers*, **131**, 218-223 (2015).

[39] Z. J. Li, H. Li, Z. L. Wu, M. K. Wang, J. T. Luo, H. D. Torun, P. A. Hu, C. Yang, M. Grundmann, X. T. Liu and Y. Q. Fu, Advances in designs and mechanisms of semiconducting metal oxide nanostructures for high-precision gas sensors operated at room temperature. *Materials Horizons*, **6**, 470-506 (2019).

[40] F. Zheng, L. Zhang, Y. Y. Li, Q. C. Liu, Z. J. Li and H. C. Yao, Bimetallic AuPd Alloy Nanoparticles Decorated on Macroporous WO_3 Supports for Selective Detection of Acetone. *Acs Applied Nano Materials*, **4**, 2713-2720 (2021).

[41] V. Saasa, M. Beukes, Y. Lemmer and B. Mwakikunga, Blood Ketone Bodies and Breath Acetone Analysis and Their Correlations in Type 2 Diabetes Mellitus. *Diagnostics*, **9**, 224 (2019).

[42] C. Anderson, S. G. Mattar, F. L. Greenway and R. J. Lindquist, Measuring ketone bodies for the monitoring of pathologic and therapeutic ketosis. *Obesity Science & Practice*, **7**, 646-656 (2021).

[43] M. Ahmadipour, A. L. Pang, M. R. Ardani, S. Y. Pung, P. C. Ooi, A. A. Hamzah, M. Wee, M. Haniff, C. F. Dee, E. Mahmoudi, A. Arsad, M. Z. Ahmad, U. Pal, K. M. Chahrour and S. A. Haddadi, Detection of breath acetone by semiconductor metal oxide nanostructures-based gas sensors: A review. *Materials Science in Semiconductor Processing*, **149**, 106897 (2022).

[44] Paleczek and A. Rydosz, Review of the algorithms used in exhaled breath analysis for the detection of diabetes. *Journal of Breath Research*, **16**, 026003 (2022).

[45] Dixit, S. Fardindoost, A. Ravishankara, N. Tasnim and M. Hoorfar, Exhaled Breath Analysis for Diabetes Diagnosis and Monitoring: Relevance, Challenges and Possibilities. *Biosensors-Basel*, **11**, 476 (2021).

[46] Langmuir, THE ADSORPTION OF GASES ON PLANE SURFACES OF GLASS, MICA AND PLATINUM. *Journal of the American Chemical Society*, **40**, 1361-1403 (1918).

[47] Rosenstock and E. Ferrannini, Euglycemic Diabetic Ketoacidosis: A Predictable, Detectable, and Preventable Safety Concern With SGLT2 Inhibitors. *Diabetes Care*, **38**, 1638-1642 (2015).

[48] S. Jang, S. J. Choi, S. J. Kim, M. Hakim and I. D. Kim, Rational Design of Highly Porous SnO_2 Nanotubes Functionalized with Biomimetic Nanocatalysts for Direct Observation of Simulated Diabetes. *Advanced Functional Materials*, **26**, 4740-4748 (2016).

[49] S. Freddi, A. V. Emelianov, Bobrinetskiy, II, G. Drera, S. Pagliara, D. S. Kopylova, M. Chiesa, G. Santini, N. Mores, U. Moscato, A. G. Nasibulin, P. Montuschi and L. Sangaletti, Development of a Sensing Array for Human Breath Analysis Based on SWCNT Layers Functionalized with Semiconductor Organic Molecules. *Advanced Healthcare Materials*, **9**, 2000377 (2020).

[50] T. Jolliffe and J. Cadima, Principal component analysis: a review and recent developments. *Philos Trans A Math Phys Eng Sci*, **374**, 20150202 (2016).

Chapter 7. Flexible multiplex InP nanowire sensor arrays for wearable device applications

For personalised health care, there is a growing demand for the development of flexible and wearable sensors due to their minimally invasive nature, ability to seamlessly integrate with routine health monitoring and provide patient-centric healthcare to reduce hospitalisation rates.[1] Moreover, to improve the efficacy of the devices, it highly desirable develop multifunctional device that can simultaneously monitor human vital signs, such as heart rate, body temperature, biomarkers from breath and sweat, and air pollutant in surrounding environment.[2-3]

To further explore the application of InP nanowire (NW), in this chapter, we demonstrated a muti-functional multipixel InP NW array based wearable device with the capability of gas sensing and vital signal detection for healthcare and environmental monitoring applications. An innovative flexible NW device fabrication optimisation was developed by assembling and transferring the vertical NW array to the flexible substrate. Our results indicate that InP NW arrays are promising material platform for the development of wearable and multipixel sensor devices for the next generation personalised healthcare devices.

7.1 Introduction

A sensor array is normally constructed by integrating multiple sensors with different functionalities onto a common platform.[1-3] For example, a multiplexed gas sensing array using mono- and bimetallic composites (Pd/Au/Ni) decorated Si channel transistors

can simultaneously detect H_2S, H_2, and NO_2 at room temperature.[4] Amorphous metal $Fe_{33}Zr_{67}$ was fabricated for multi-functional sensor array that enables pressure detection, owing to its high mechanical properties; temperature detection owing to its small negative temperature coefficient; and light detection as the metal electrode of a photo-thin film transistor based on In–Zn–O (IZO).[5]

To further achieve multiplexing wearable array sensors, many low dimensional/nanomaterials such as nanowire/nanofibril structures with intrinsic flexible/stretchable properties against mechanical bending or stretching have been investigated. For instance, single-walled carbon nanotubes (SWCNT) and metal oxide NWs have been used for multiple gas sensing capability with high strain tolerance;[6-7] reduced graphene oxide (RGO) and conductive polymers NWs have been applied for temperature or pressure array sensor with mapping capability[8-9]. However, many of the wearable devices based on these materials exhibited an inferior sensitivity or constrained to single sensing function,[8] limiting their applications.[10] Another key challenge of the multi-functional sensors is realising sensing signal decoupling from different sensing elements and stimulus on a mutual sensing interface, especially considering the complex and fluctuated operation environment of the wearable device. This is crucial to the accuracy of sensor arrays. [10-14]

Recently, thin film InP has been fabricated into flexible device by the epitaxial lift-off methods as solar cells and NO_2 sensing with a sub-ppb level sensitivity.[15-18] Due to their one-dimensional feature, NWs have the natural advantage for flexible devices. Various flexible NW devices, such as NW LEDs [19], photodetectors,[20] and solar cell[21] have been demonstrated. However so far flexible InP NW gas sensors have not been reported. In previous chapters we have shown InP NW based NO_2 and acetone

sensors.[22-23] On the other hand, wurtzite (WZ) InP NWs have been studied as an emerging piezoelectric material for electromechanical sensors based on their piezoelectric and mechanical properties,[24-25] which can be utilised for heart rate (pulse) measurement. Moreover, the temperature-dependent electrical properties of InP indicates its suitability as a thermistor for temperature monitoring.[26] Based on above, in this chapter, a multipixel InP NW array based flexible device have been fabricated. A signal decoupling strategy was designed and implemented through the NW sensor array fabrication processes, leading to the successful demonstration of body pulse rate and temperature measurements as well as high performance NO_2 and acetone sensing, showing great potential for health and environmental monitoring.

7.2 Signal decoupling strategy for multipixel InP NW sensor array

In a multiplexed sensing system, the mutual interferences of sensor arrays rising from the shared interface can lead to signal processing issues and compromise the reliability/accuracy of the system, in responding to a specific stimulus among concurrent signals.[27] In this work, we designed a new pathway for fabrication of a multifunctional (pressure, temperature, and gases) wearable sensor array with the capability of decoupling different types of stimulus, as shown in Figure 7-1. According to previous research, variation of InP NW geometries including diameter, pitch and length can lead to changes of their properties including the Young's modulus, piezoelectrical coefficient and gas sensitivity.[21, 24] Therefore, fabrication of multipixel NW arrays with different geometries could allow us to tailor their sensing behaviour to different chemical and physical stimulus, achieving multimode sensing capability. Apart from NW geometry, electrode materials and surface-functionalisation also play important roles for

multifunctional sensing. These form our signal decoupling strategy for multifunctional sensing:

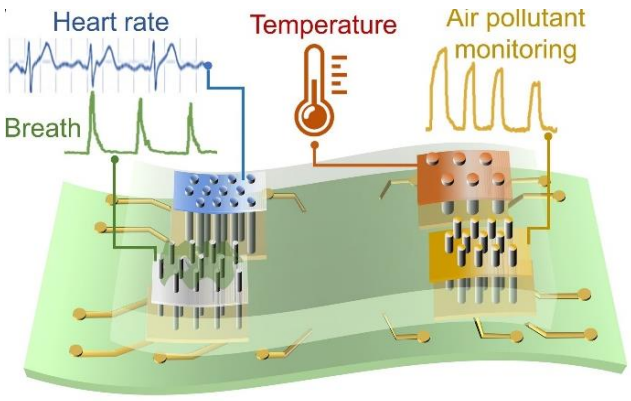

Figure 7-1. Schematic of multifunctional sensor for different sensing applications based on varied geometry design.

- For chemiresistive gas sensors, a larger surface area (thinner NWs) is favoured for analyte adsorption and thus high sensitivity. Increasing the NW length has a synergistic effect. As illustrated in Figure 7-2, substrate patterning with small hole diameters is designed for NO_2 and acetone sensing arrays to allow the SA-MOCVD growth of long and thin NWs for high gas sensitivity. In addition to NW diameter, metal contact and surface-functionalisation are also important components for gas sensor design[3], and is an effective strategy to achieve for gas discrimination.
- On the contrary, the gas sensitivity will be eliminated if the NWs are embedded in the planarization layer such as PMMA (Figure 7-2c, d). However, the device is still capable of sensing physical parameters such as pressure and temperature, through the piezoelectrical and thermal effect. The pressure sensitivity of the InP NW device based on the piezoelectrical effect is strongly correlated the NW thickness and aspect ratio according to their Young's modulus characterisation.[21, 24] Thinner NWs have a larger aspect ratio and deformation under the same pressure, leading to a higher pressure sensitivity (Figure 7-2d). Conversely, the strain effect can be minimised by

using of NWs with small aspect ratio, which is only suitable for temperature sensing with much suppressed pressure sensitivity.

Based on above the schematical design concept of our multipixel NW array sensor is presented in Figure 7-4d, consisting of four sensor elements: 1) NO_2 gas sensor pixels formed by NWs with design diameters of 60, 80, 160 and 200 nm; 2) acetone gas sensor pixels formed with the same NW design diameter of 60, 80, 160 and 200 and surface functionalised by a chitosan layer according to Chapter 6; 3) a pressure sensor pixel fabricated with NWs of ~60 nm and embedded in PMMA planarization layer; and 4) a temperature sensor pixel, fabricated with NWs with a much larger diameter of ~200nm. As will be shown later, by fabricating multiple NW arrays with different diameter design for the gas sensor, a principal component analysis (PCA) method can be applied to further enhance its analyte discrimination ability.

The NW arrays with different geometries can be realised by selective area metal-organic chemical vapor deposition (SA-MOVPE) growth based on different substrate pattern designs. After NW growth, PMMA planarization is performed, which uniformly covers the whole area of the multipixel sensor device. As the four NW arrays are of different lengths, different exposure lengths are obtained (corresponding to their diameter designs) after an ICP etching process, from the largest to smallest for the acetone sensor pixel, the NO_2 sensor pixel, and the temperature pixel. During the ICP process, the pressure sensor pixel was protected such that the NWs are fully embedded in the PMMA. Then, the other sensing pixels were covered to allow a short ICP etching of the pressure sensor pixel to expose the NW tip for subsequent contact formation.

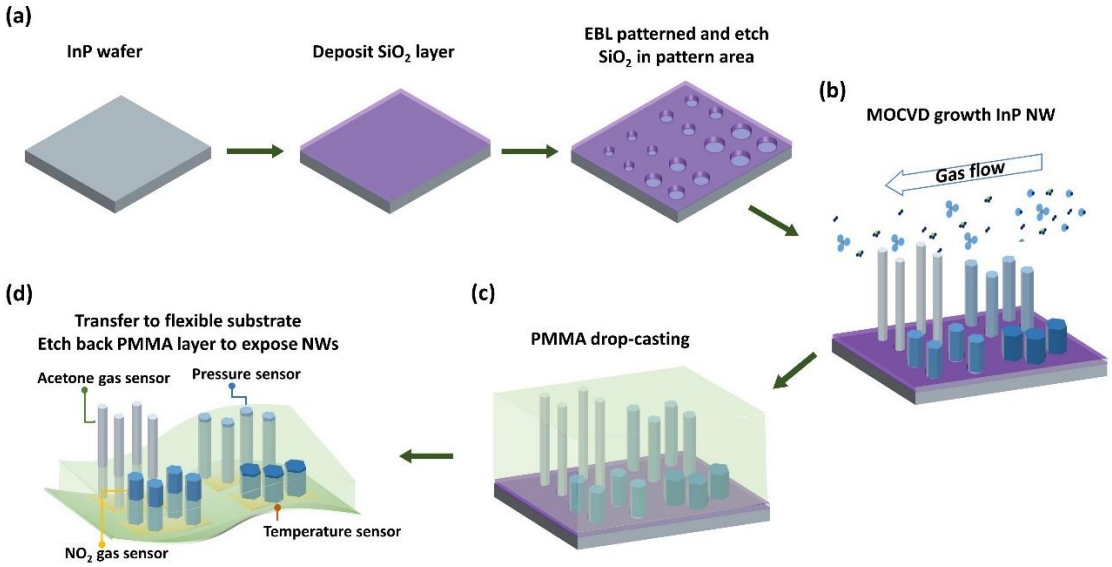

Figure 7-2. Schematics of SA-MOVPE growth process for different diameter NW arrays and the corresponding fabrication strategy for flexible device fabrication.

7.3 Experimental

7.3.1 SA-MOVPE growth of NW sensor array

In this chapter, undoped InP (i-InP) NWs with WZ structure were grown by SA-MOVPE, following the process described in Chapter 5.2.[28] The WZ crystal structure allows a precise diameter and length control of InP NWs due to its axial-dominating growth process as discussed in Chapter 2.[29-30] The substrate pattern for the NW growth is designed with hexagonal dots array in 4 × 4 sensor pixels (pixel sizing 100 × 100 μm), with the same dot interspacing of 600 nm and different diameter of 40, 60, 80, 100 nm, respectively by electron beam lithography (EBL) as shown in Figure 7-3.[31] The NW arrays in each row (labelled as 1, 2, 3, 4) are identical, whereas those in each column (labelled as column a, b, c, d) have gradually decreasing diameter.

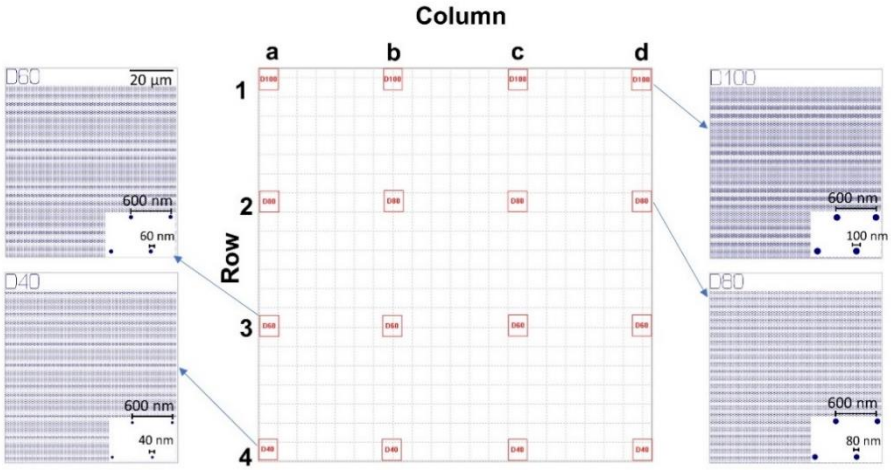

Figure 7-3. The designed pattern generated by Raith 150 software for the EBL patterning of the SA-MOVPE NW growth substrate with the same pattern diameter of 40, 60, 80, 100 nm, labelled as D40, D60, D80 and D100 for each row of the NW array respectively.

Figure 7-4a shows the scanning electron microscope (SEM) images of the as-grown NWs, with a slightly enlarged diameter of ~60, 80, 160 and 200 nm from the original pattern design due to a minor radial direction growth during the SAE-MOVPE process, corresponding to row 4, 3, 2, 1, respectively. Figure 7-4b reveals a linear correlation between the NW length and patterned diameter. As the NW diameter increases from 60 nm to 200 nm, the NW length decreased from ~6.8 to ~1.6 μm (Figure 7-4c), due to the consistent precursor supply as mentioned earlier.[32]

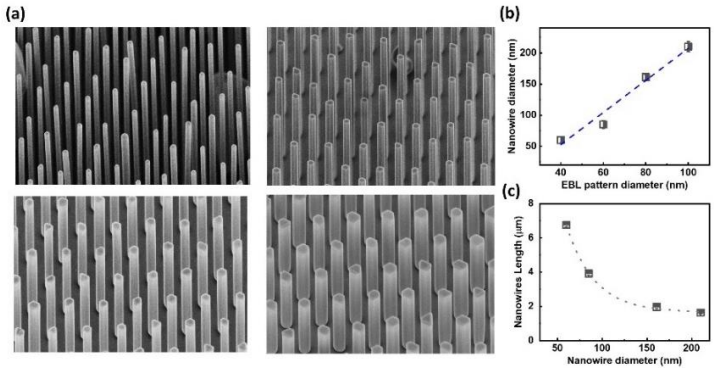

Figure 7-4. (a) SEM images of as-grown NW arrays based on the pattern designs plotted in Figure 7-3. (b) The diameter correlations between the pattern design and obtained NWs. (c) Correlation of the NW diameter and length.

7.3.2 Flexible sensor array fabrication

The as-grown NW sensor arrays were subsequently fabricated into a flexible device, following the process illustrated in Figure 7-5. First a layer of PMMA (946 A8) resist was drop-casted onto the sample to planarize the NW arrays at a thickness of ~ 5 μm.[15, 33-34] This layer (together with the embedded NW arrays) was peeled off from the InP substrate by soaking the sample in a 5% KOH aqueous solution, and was then transferred to a Au-coated flexible silicone substrate, as shown in Figure 7-5b, c.[35] After a careful controlled ICP etching of the PMMA layer, the top segment of NW can be uniformly exposed (see Figure 7-5d).[36-37] The tilt-angle metal deposition was then applied to form the top-contact of the NWs, with a thin layer (< 100 nm) of Au or Pt deposited on NW for electrical measurement. Pt was deposited on column a, b by cover the pixels in column c, d with Aluminium foil during the deposition; while Au was deposited on column c, d, with column a, b being covered. Finally, the Pt-electrode InP NW arrays were drop-casted with a chitosan functionalisation layer acetone sensing.

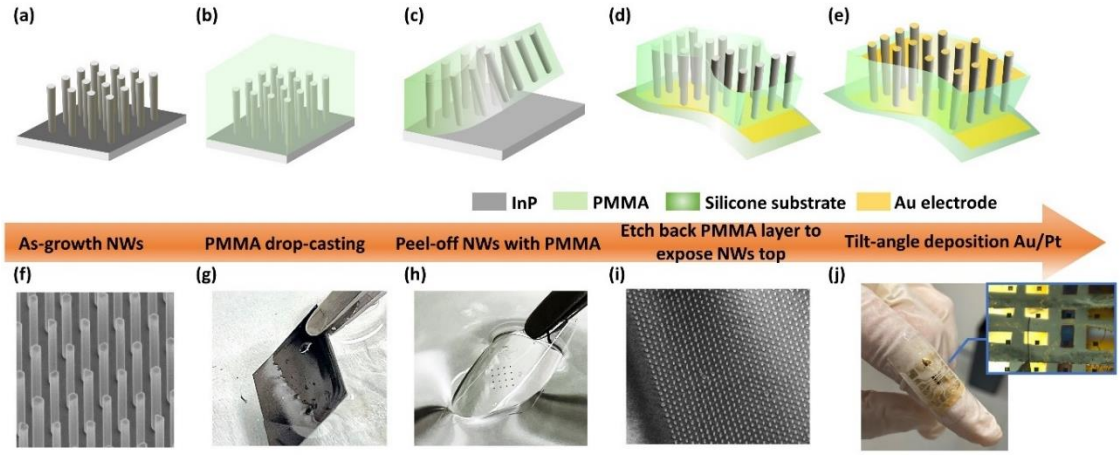

Figure 7-5. (a-e) Schematics of the InP NW flexible NW sensor fabrication process. (f-j) The corresponding SEM images and photographs of the fabrication process corresponding to (a-e).

After each fabrication steps, the SEM images of sensor arrays were taken. As shown in Figure 7-6, as designed, the morphologies of the four pixels are different. For convenience, the various pixels in the array sensor are named by their functionality and NW diameter as following:

- Column a: for acetone sensing and the pixels are labelled as Acet-D60-A, Acet-D80-A, Acet-D160-A, Acet-D200-A.
- Column b and d: for NO_2 sensing and the pixels are labelled as NO_2-D60-B, NO_2-D80-B, NO_2-D160-B, NO_2-D200-B, NO_2-D60-D, NO_2-D80-D, NO_2-D160-D, NO_2-D200-D.
- Column c: for pressure sensing and the pixels are labelled as Press-D60-C.
- Column c: for temperature sensing and the pixels are labelled as: Temp-D200-C.

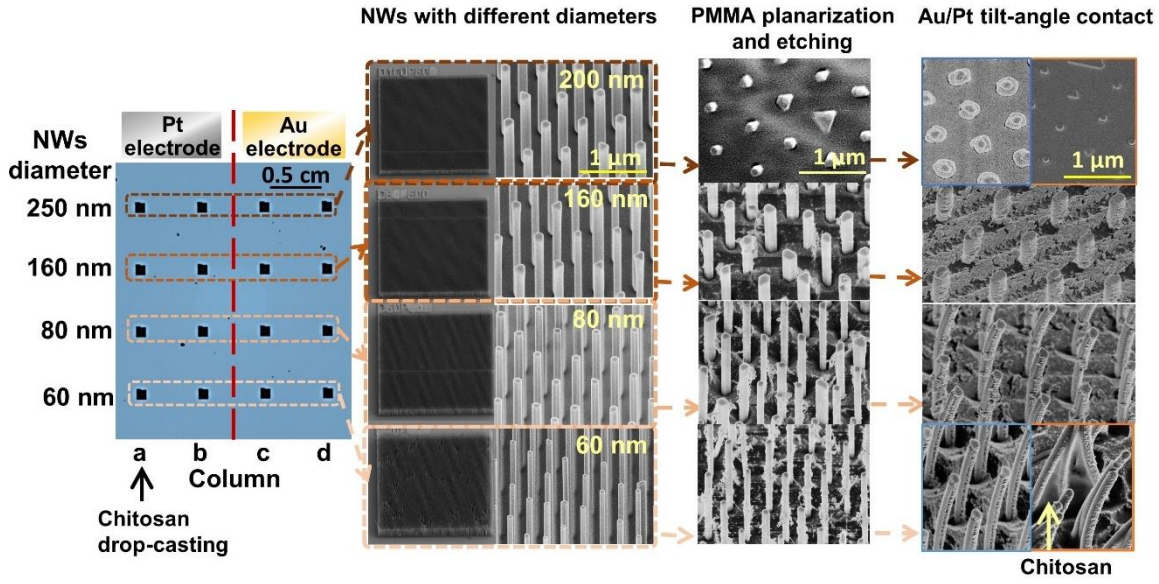

Figure 7-6. The morphology characterisation of the multiplex sensor array during fabrication process. (a) Schematic of the 4×4-pixel array sensor with NWs of different diameters and top electrode contact metals. (b-d) The SEM images corresponding to as-grown NWs (b), after PMMA planarization and (c), after metal contact deposition (d).

7.4. Multipixel sensor array characterisation

7.4.1 Flexibility characterisation

To test the flexibility of the fabricated NW device, the current-voltage (I-V) curves of the array sensor were measured under different bending conditions and multiple bending cycles, as shown in Figure 7-7. For all the array pixels, the measured I-V curves exhibit a negligible degradation (< 5%) even under a small bending radius (~2 mm) and after 100 times bending cycles regardless of the NW thickness metal and contact, indicating high stability and robustness. The one-dimensional vertical NW configuration contributed to this flexibility, as their electrical property is barely affected by the horizonal strain and the PMMA planarization also provides a mechanical support for these NWs.

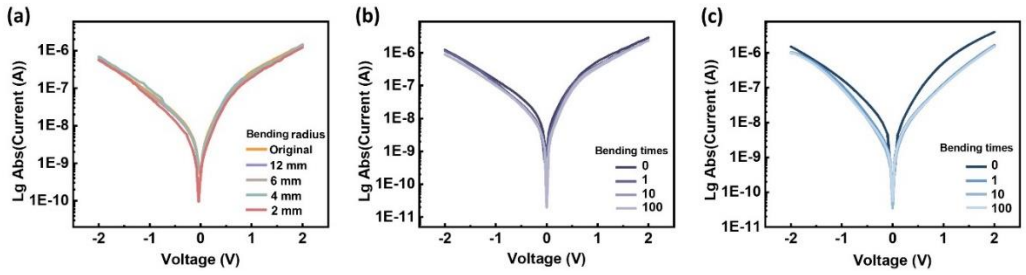

Figure 7-7. Flexibility characterisation by I-V curve measurements after (a) bending radius of ~2-12 mm for the D60 NW array; and (b, c) 0 - 100 times bending cycles at a bending radius of 4 mm for the D 60 and D200 arrays, respectively.

7.4.2 Pressure sensor array characterisation

The piezoelectric effect is the ability of certain material to generate an electric charge, proportionally in response to the mechanical stress or pressure applied on it. Conversely this electric charge can be collected for measuring the pressure, to form a pressure sensor.[38] To characterise the pressure sensitivity of the NW array, the transient current of pixel Press-D60-C measured under a range of pressures provided from a nanoindenter (Hysitron TI 950 TriboIndenter). Nanoindenter is an instrument used for precisely

measuring the mechanical properties of materials at the nanoscale by applying a controlled force to deform the surface of a material through an indenter tip.[39] For our pressure sensitivity measurements, a force ranging from 20 to 26 mN was applied from the indenter probe (tip size: diameter 100 µm, area ~ 0.785 μm^2). The tip size of this probe can be considered as the contact area and the pressure is calculated to be ~25.48 - 33.12 kPa. The measured pressure response is shown in Figure 7-8a. By linear fitting of the slope of pressure vs response curve,[15, 25] a sensitivity of -1.68 kPa^{-1} is obtained, which is defined as the resolution of the pressure sensor and attributed to the large aspect ratio of the InP NWs of ~ 1:100 (diameter: ~60 nm, length: ~ 6 µm).[23] Although this pressure sensitivity is less than the best reported value of the ZnO NWs, with a pressure sensitivity up to -6.8 kPa^{-1}, [40] it is comparable with other III-N NW based devices, such as GaN NWs, with a pressure sensitivity of 1.3 kPa^{-1}.[41] By further increasing the aspect ratio, it is expected that the pressure sensitivity of the InP NWs may be further improved.

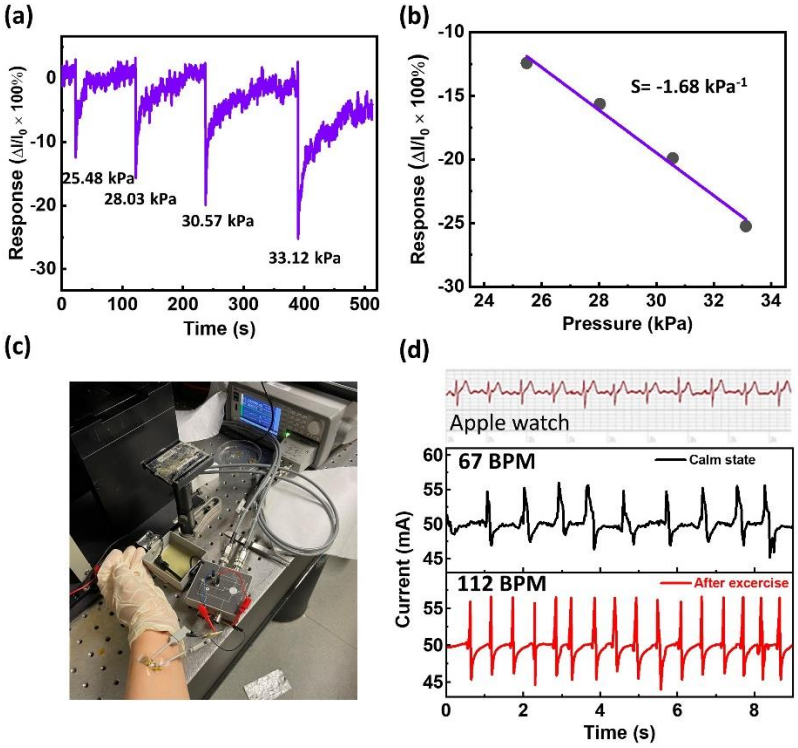

Figure 7-8. Characterisation of the pressure sensor pixel Press-D60-C. (a) The time-dependent pressure response. (b) Sensor response vs pressure plot, yielding a sensitivity of -1.68 kPa^{-1} in the

range of 25.48 - 33.12 kPa. (c) Picture of the pressure sensing measurement by placing wearable sensor on the radial artery of a human wrist. (d) Real-time transient pulse signal under the calm state and after exercise, and with a comparison with that measure by an Apple Watch.

Body pulse rate is one of the vital signs to assess the physical and mental state of a person.[42-43] Based on the pressure sensitivity characterisation, the Press-D60-C pixel was attached onto the wrist of a person as shown in Figure 7-8c. The pulse rate was measured under calm state and after intensive exercise. In Figure 7-8d, the pulse frequency shows a significant increase from 67 (calm state) to 112 BPM. The results measured under the calm state also shows an excellent consistency with the measurement by an Apple watch.

7.4.3 Temperature sensor array characterisation

Body temperature provides an insight into the physiological state of a person. An elevated body temperature is an indication of infection. A degraded body temperature signifies low blood flow due to circulatory shock. Therefore, body temperature is also a vital sign that requires to be monitored by temperature sensors with high accuracy, fast response, and long-term stability. Thermistor employed in this work is one of the most common device structures used for wearable temperature sensors whose resistance is temperature dependent.[44]

The pixel Temp-D200-C in the sensor array with short NWs that are fully immersed in PMMA (except for the tips that are contacted by the Au electrode) is applied to body temperature monitoring as mentioned in section 7.2. The fully covered surface and small aspect ratio (~1:6) of NWs in this pixel eliminate its sensitivity to other type of stimulus (strain, gas flow, etc.). Before the on-skin body temperature measurement, the

temperature sensitivity of the device as a thermistor was characterised. As shown in Figure 7-9a, the transient profiles of the current of Temp-D200-C were recorded (0.10 - 0.28 μA) at a bias voltage of 0.5 V, with the temperature variation in the body temperature ranging from 30.4 to 40.4 °C, controlled by the hotplate in the Linkam chamber used for the sensing measurement. The thermistor has a negative temperature coefficient (*NTC*) as the resistance decreases with temperature increasing, which is a common semiconductor property of InP in temperature range of 300 – 400 Kelvin.[45] The current and temperature exhibit a linear correlation measured with a temperature spacing of 0.2 °C which is adequate for body temperature monitoring as shown in the inset of Figure 7-9a.

The linear relationship greatly simplifies the post-measurement processing as it allows the direct conversion of measured current to temperature for practical applications. Body temperature varies with body parts.[46] Considering the NW sensor was placed at the wrist for pulse rate test, the body temperature was also conveniently collected at this position. Normally the wrist temperature is around 32 °C at room temperature (25 °C),[47] much lower than the core body temperature (37 °C). In Figure 7-9b, the results measured from Temp-D200-C shows that the average body temperature is 32.25 ± 0.31 °C on wrist with a stabilising time of ~ 5 s. An operating soldering iron was used to change the epidermal temperature by carefully approaching it to the sensor array on wrist with a distance of ~5 cm (inset of Figure 7-9b). The measured temperature increased to 35.81 ± 0.63 °C immediately with the soldering iron approaching (distance to wrist: ~5 cm) and decrease to ~ 32.9 °C after removing it, confirming the fast response and good sensitivity of the Temp-D200-C pixel. To examine the accuracy and reliability of this device, a digital thermometer from Pharmacy Care was applied for the body temperature

measurement at the same position, indicating a temperature of 32.60 °C with a standard deviation of < 1.1%. from the result measured by Temp-D200-C.

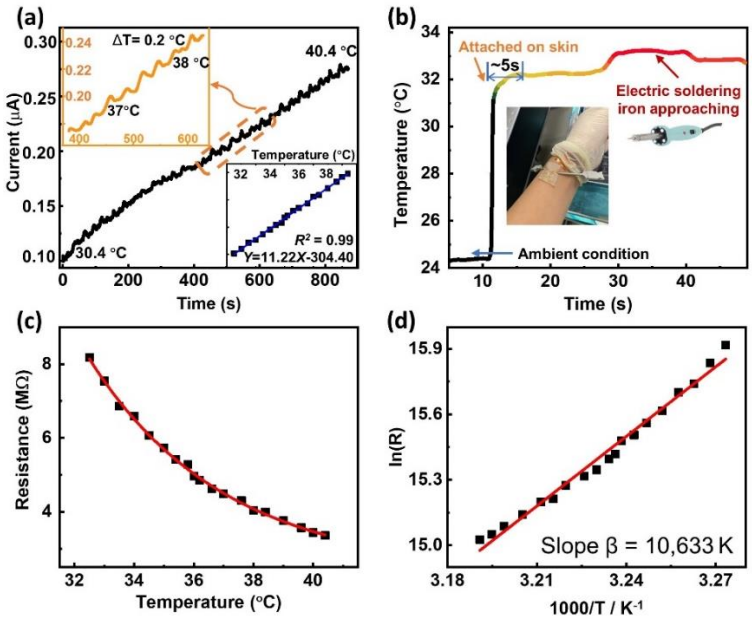

Figure 7-9. Characterisation of the temperature sensor pixel Temp-D200-C. (a) The current variation with the temperature in the range of 30.4 to 40.4 °C at a 0.2 °C interval measured by the array sensor element Temp-D200-C. Inset (orange colour): Enlarged plot in the temperature range of 36 - 38 °C. The temperature sensor testing intervals; Inset (black colour): The linear fitting of the temperature vs. current relationship. (b) Skin temperature monitored on the wrist. Inset: picture of the measurement. (c) Resistance variation with temperature. (d) Dependence of ln(R) on 1000/T showing a linear relationship.

The sensitivity of Temp-D200-C as a thermistor is further quantified by the temperature coefficient of resistance (*TCR*) and a beta (β) value.[46] Both of them are usually closely related to the properties of materials, and are commonly used to evaluate the accuracy of the thermistor for ensuring reliable temperature measurements. *TCR* is calculated from the following equation[48]:

$$TCR = \frac{1}{R_t}\frac{dR_t}{dT} = -\frac{\beta}{T^2}(\%K^{-1}) \quad (1)$$

where R_t is the resistance at temperature T, and β is the material constant for the thermistor, extracted from the general equation governing a thermistor as below:

$$R_t = R_0\, exp\, \beta(\frac{1}{T} - \frac{1}{T_0}) \quad (2)$$

where, R_0 is the resistance at a reference temperature T_0. And this equation can be rewritten as:

$$\ln R_t = \ln R_0\, exp\, \beta(\frac{1}{T} - \frac{1}{T_0}) \quad (3)$$

where β represents the slope of the ln(R_t) versus 1/T plot, with the units of Kelvin (K), while TCR represents the percentage change of resistance per Kelvin ($\%K^{-1}$).[49-50]

The R_t vs T relationship of the sensor array Temp-D200-C is plotted in Figure 7-9c showing a non-linear correlation as indicated by equation (2). A linear relationship between ln (R_t) and 1/T is established from equation (3),[48] as shown in Figure 7-9d, where the straight line is the linear fitting result for measured data (square dots). The extracted β and TCR are 10633 K and 11.81%K^{-1}, respectively. Bulk InP device has a TCR of ~ 8.35 $\%K^{-1}$ and β of ~ 7520 K,[51] indicating that the NW morphology improves the thermistor sensitivity, which could be resulted from their different crystal structures (ZB vs WZ).

7.4.4 Multi-gas sensor array characterisation

The gas sensing measurements were all performed with a bias voltage of 0.5 V and under illumination by a solar simulator (@AM1.5), with the exposure of different gases (NO_2, CO_2, acetone, ethanol, methanol, and propane). For applications of the wearable array sensor, the gases of interest are NO_2 and acetone, since NO_2 is known as one of the major pollutants, and acetone is a biomarker of ketone level in human body. As aforementioned, our InP NWs have already achieved a high sensitivity to NO_2, while with further surface

functionalisation of chitosan, they exhibit excellent acetone sensitivity, which has been studied in Chapter 4 and 6, respectively.[52-54] Here, these two gas sensing functions were integrated on the same sensor chip as separate pixel of NO_2 and acetone sensors and their sensing performance is presented in Figure 7-10.

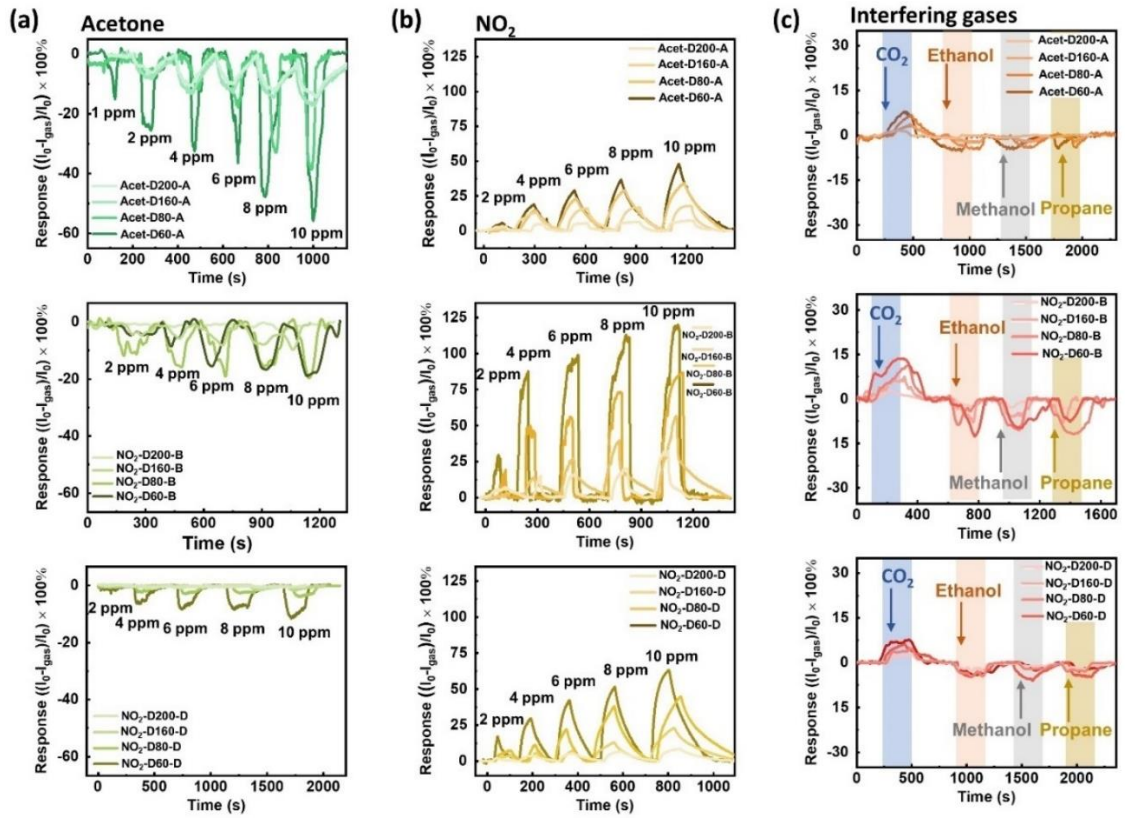

Figure 7-10. Time-dependent gas sensing response of the gas sensor pixels in the array sensor to (a) acetone, (b) NO_2 in the concentration range of 1 - 10 ppm and (c) interfering gases including ethanol, methanol, and propane at a concentration of 10 ppm and CO_2 of 10 %.

As expected, the bare InP NW pixels in column b (NO_2-D60-B, NO_2-D80-B, NO_2-D160-B, NO_2-D200-B), d (NO_2-D60-D, NO_2-D80-D, NO_2-D160-D, NO_2-D200-D) show a much lower sensitivity to acetone than chitosan functionalised pixels in column a (Acet-D60-A, Acet-D80-A, Acet-D160-A, Acet-D200-A), while exhibit a higher response to NO_2 (Figure 7-10a, b). Both acetone and NO_2 sensing measurements show that smaller NW diameter and longer NW length enhance the surface interaction, contributing to the

higher sensing response value and concentration dependence. The sensing results of the interfering gases which commonly exists in atmosphere and breath are shown in Figure 7-10c and these responses are much smaller than those from NO_2 and acetone, consistent with the results shown in Chapter 4 and 6.[22, 55]

Figure 7-11a summarises the gas sensing measurement results from all gas sensor pixels. Sensor pixels with Pt electrodes (column b) demonstrated a higher response to NO_2 than those with Au electrode (column d). This phenomenon could arise from the Schottky contact formed by Pt which dramatically deplete charge carrier concentration in the InP NWs, reducing the baseline of the sensing signal, leading to the increased sensing response.[56] The minor NO_2 response of Acet-D60-A and Acet-D80-A may attribute to the ununiform coverage of the chitosan on the NWs surface due to the drop-casting process on the flexible sensor pixels.

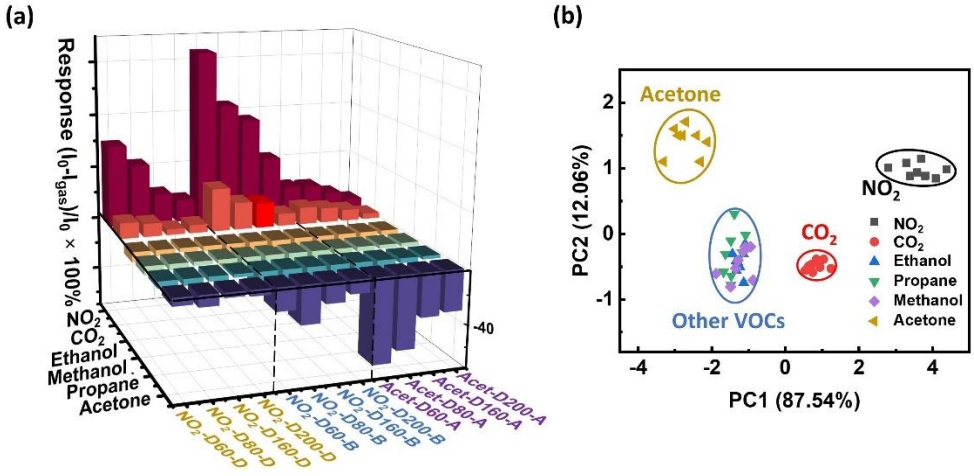

Figure 7-11. Sensor array response patterns to the six different gases (a). (b) PCA plot of the sensor responses from (a).

Due to the complexity and multivariate of the array gas sensor results, the PCA was applied to facilitate the data analysis.[57] PCA is the most common approach extracting the sensor response for the multivariate dimensional analysis to develop a relationship

between the different variables and condense them to two or three main dimensions.[58] The PCA-analysis of the gases (NO_2, Acetone, CO_2, etc) was performed by Principal Components Analysis online (labriata.github.io) to calculate the principal components (PC1, PC2) and the data points in each clusters are corresponding to the number of data we fed into this program. Through this dimensionality reduction process, our gas sensor array results can be simplified to extract critical information.[3] As shown in Figure 7-11b, by performing the PCA, our sensor array is not only able of distinguishing NO_2 and acetone with a distinct sensitivity, but also CO_2 which only shows a non-specific response to both NO_2 and acetone, confirming the effectiveness of our array sensor gases discrimination strategy as discussed in section 7.2. The physical and chemical diversities of the sensor array composed by NW geometry, contact metals and surface-functionalisation create a significant variance of sensing performance across the different pixels, leading to a multi-gases analysing capability.[58] Moreover, the gas sensing response from the pixels for temperature and pressure detection was also measured. The results in Figure 7-12 shows that the gas flow causes a negligible response to pixels Press-D60-C and Temp-D200-C, indicating successful signal decoupling of our sensor array design.

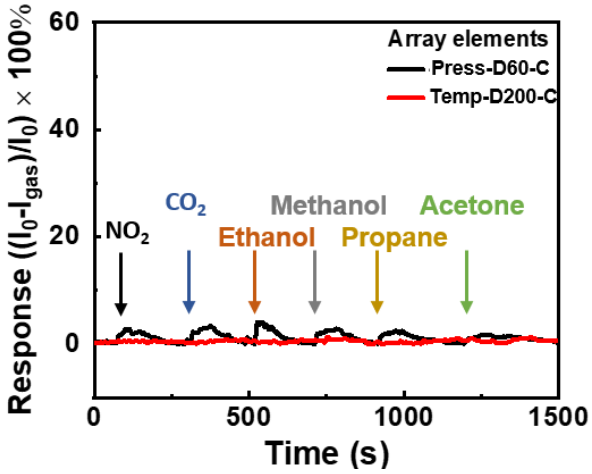

Figure 7-12. Chemical stability of temperature and pressure sensor pixels Press-D60-C and Temp-D200-C exposed to different multiple gases (CO_2: 10%, other gases: 10 ppm).

In future studies, the number of array pixels may be scaled-up to realise the temperature and pressure mapping to improve reliability of this sensor for real-time health and exercise monitoring. To decrease the equipment/fabrication costs, instead of bottom-up NW growth, the alternative top-down etching approach could also be considered for the NW sensor array fabrication for industrial mass production. Enhancing the chemical diversity by applying different surface-functionalisation materials could lead to the detection of other important health related biomarkers presented in human breath and sweat, for non-invasive health monitoring and diagnostic etc.

7.5 Summary

In this chapter, multipixel wearable InP NW array sensor has been demonstrated, based on an effective sensor signal decoupling strategy and newly developed flexible device fabrication process. Through the design of NW arrays with different geometry, metal contact, and further application of NW surface-functionalisation layer and PCA method, the multifunctional NW array sensor achieves excellent performance for room temperature NO_2, acetone, and CO_2 gas sensing, as well as body temperature and pulse rate monitoring with negligible response to chemical stimulus, showing great promise for personalised health and environmental monitoring applications. Our work provides a new material platform and pathway for the development of next-generation wearable devices for human-machine/ambience interfaces and smart healthcare setups.

References

[1] Y. Khan, A. E. Ostfeld, C. M. Lochner, A. Pierre and A. C. Arias, Monitoring of Vital Signs with Flexible and Wearable Medical Devices. *Advanced Materials*, **28**, 4373-4395 (2016).

[2] G. J. Ko, S. D. Han, J. K. Kim, J. Zhu, W. B. Han, J. Chung, S. M. Yang, H. Y. Cheng, D. H. Kim, C. Y. Kang and S. W. Hwang, Biodegradable, flexible silicon nanomembrane-based NOx gas sensor system with record-high performance for transient environmental monitors and medical implants. *Npg Asia Materials*, **12**, 71 (2020).

[3] R. J. Rath, S. Farajikhah, F. Oveissi, F. Dehghani and S. Naficy, Chemiresistive Sensor Arrays for Gas/Volatile Organic Compounds Monitoring: A Review. *Advanced Engineering Materials*, **25**, 2200830 (2023).

[4] H. M. Fahad, H. Shiraki, M. Amani, C. Zhang, V. S. Hebbar, W. Gao, H. Ota, M. Hettick, D. Kiriya, Y.-Z. Chen, Y.-L. Chueh and A. Javey, Room temperature multiplexed gas sensing using chemical-sensitive 3.5-nm-thin silicon transistors. *Science Advances*, **3**, e1602557 (2017).

[5] M. Jung, E. Lee, D. Kim, K. Kim, C. Yun, H. Lee, H. Kim, K. Rhie and S. Jeon, Amorphous FeZr metal for multi-functional sensor in electronic skin. *npj Flexible Electronics*, **3**, 8 (2019).

[6] C. F. Hua, Y. Y. Shang, Y. Wang, J. Xu, Y. J. Zhang, X. J. Li and A. Y. Cao, A flexible gas sensor based on single-walled carbon nanotube-Fe_2O_3 composite film. *Applied Surface Science*, **405**, 405-411 (2017).

[7] X. Y. Xue, T. T. Zhao, X. M. Tian, L. Yuan, Z. G. Wang, T. K. Li and J. H. Zhang, Flexible Dual-Parameter Sensor Array without Coupling Based on Amorphous Indium Gallium Zinc Oxide Thin Film Transistors. *Advanced Materials Technologies*, **7**, 2100849 (2022).

[8] T. M. Perfecto, C. A. Zito, T. Mazon and D. P. Volanti, Flexible room-temperature volatile organic compound sensors based on reduced graphene oxide-WO_3 center dot 0.33H(2)O nano-needles. *Journal of Materials Chemistry C*, **6**, 2822-2829 (2018).

[9] Z. Y. Zhu, C. C. Liu, F. X. Jiang, J. Liu, G. Q. Liu, X. M. Ma, P. P. Liu, R. Huang, J. K. Xu and L. Wang, Flexible fiber-shaped hydrogen gas sensor via coupling palladium with conductive polymer gel fiber. *Journal of Hazardous Materials*, **411**, 125008 (2021).

[10] W. Jeong, J. Song, J. Bae, K. R. Nandanapalli and S. Lee, Breathable Nanomesh Humidity Sensor for Real-Time Skin Humidity Monitoring. *Acs Applied Materials & Interfaces*, **11**, 44758-44763 (2019).

[11] H. L. Tai, S. Wang, Z. H. Duan and Y. D. Jiang, Evolution of breath analysis based on humidity and gas sensors: Potential and challenges. *Sensors and Actuators B-Chemical*, **318**, 128104 (2020).

[12] D. Wilson, Noninvasive Early Disease Diagnosis by Electronic-Nose and Related VOC-Detection Devices. *Biosensors-Basel*, **10**, 73 (2020).

[13] H. Chi, L. J. Ze, X. M. Zhou and F. K. Wang, GO film on flexible substrate: An approach to wearable colorimetric humidity sensor. *Dyes and Pigments*, **185**, 108916 (2021).

[14] J. Bandodkar, I. Jeerapan and J. Wang, Wearable Chemical Sensors: Present Challenges and Future Prospects. *Acs Sensors*, **1**, 464-482 (2016).

[15] Y. Y. Peng, M. L. Que, H. E. Lee, R. R. Bao, X. D. Wang, J. F. Lu, Z. Q. Yuan, X. Y. Li, J. Tao, J. L. Sun, J. Y. Zhai, K. J. Lee and C. F. Pan, Achieving high-resolution pressure mapping via flexible GaN/ZnO nanowire LEDs array by piezo-phototronic effect. *Nano Energy*, **58**, 633-640 (2019).

[16] T. Koskinen, V. Khayrudinov, F. Emadi, H. Jiang, T. Haggren, H. Lipsanen and I. Tittonen, Thermoelectric Characteristics of InAs Nanowire Networks Directly Grown on Flexible Plastic Substrates. *Acs Applied Energy Materials*, **4**, 14727-14734 (2021).

[17] J. Q. Zhang, T. Sun, Y. Chen, L. P. Liu, H. Q. Zhao, C. C. Zhang, X. C. Meng, D. K. Wang, Z. Y. Hu, H. Zhang, B. Li, S. C. Niu, Z. W. Han, L. Q. Ren and Q. Lin, Nanowires in Flexible Sensors: Structure is Becoming a Key in Controlling the Sensing Performance. *Advanced Materials Technologies*, **7**, 2200163 (2022).

[18] S. Wei, T. Haggren, Z. Li, H. H. Tan, C. Jagadish, A. Tricoli and L. Fu, Ultrasensitive Indium Phosphide Nanomembrane Wearable Gas Sensors. *Energy & Environmental Materials*, e12763 (2024).

[19] N. Gagrani, K. Vora, L. Fu, C. Jagadish and H. H. Tan, Flexible InP–ZnO nanowire heterojunction light emitting diodes. *Nanoscale Horizons*, **7**, 446-454 (2022).

[20] K. Sekar, R. Doineau, S. Mayarambakam, B. Schmaltz and G. Poulin-Vittrant, Control of ZnO nanowires growth in flexible perovskite solar cells: A mini-review. *Heliyon*, **10**, e24706 (2024).

[21] S. Wei, Z. Li, A. John, B. I. Karawdeniya, Z. Li, F. Zhang, K. Vora, H. H. Tan, C. Jagadish, K. Murugappan, A. Tricoli and L. Fu, Semiconductor Nanowire Arrays for High-Performance Miniaturized Chemical Sensing. *Advanced Functional Materials*, **32**, 2107596 (2022).

[22] S. Wei, Z. Li, K. Murugappan, Z. Li, M. Lysevych, K. Vora, H. H. Tan, C. Jagadish, B. I. Karawdeniya, C. J. Nolan, A. Tricoli and L. Fu, Nanowire Array Breath Acetone Sensor for Diabetes Monitoring. *Advanced Science*, **11**, 2309481.

[23] Y. Calahorra, X. Guan, N. N. Halder, M. Smith, S. Cohen, D. Ritter, J. Penuelas and S. Kar-Narayan, Exploring piezoelectric properties of III-V nanowires using piezo-response force microscopy. *Semiconductor Science and Technology*, **32**, 074006 (2017).

[24] M. Dunaevskiy, P. Geydt, E. Lahderanta, P. Alekseev, T. Haggren, J. P. Kakko, H. Jiang and H. Lipsanen, Young's Modulus of Wurtzite and Zinc Blende InP Nanowires. *Nano Letters*, **17**, 3441-3446 (2017).

[25] Y. Calahorra and S. Kar-Narayan, Piezoelectricity in non-nitride III-V nanowires: Challenges and opportunities. *Journal of Materials Research*, **33**, 611-624 (2018).

[26] M. Zhou, Y. Zhao, W. Yang, J. Zhang, M. Jiang, Y. Wu, Z. Xu and S. Lu, Detached Vertical (Al,Ga)N Nanowires to Realize the Flexible Ultraviolet Photodetector with High Ultraviolet/Visible Reject Ratio and Detectivity. *Energy Technology*, **10**, 2200885 (2022).

[27] Q. Gao, D. Saxena, F. Wang, L. Fu, S. Mokkapati, Y. A. Guo, L. Li, J. Wong-Leung, P. Caroff, H. H. Tan and C. Jagadish, Selective-Area Epitaxy of Pure Wurtzite InP Nanowires: High Quantum Efficiency and Room-Temperature Lasing. *Nano Letters*, **14**, 5206-5211 (2014).

[28] P. D. Dapkus, C. Y. Chi, S. J. Choi, H. J. Chu, M. Dreiske, R. Li, Y. Lin, Y. Nakajima, D. Ren, R. Stevenson, M. Yao, T. W. Yeh and H. Zhao, Selective area epitaxy by metalorganic chemical vapor deposition– a tool for photonic and novel nanostructure integration. *Progress in Quantum Electronics*, **75**, 100304 (2021).

[29] L. Xu, L. Wang and Q. Huang, Growth process modeling of semiconductor nanowires for scale-up of nanomanufacturing: A review. *IIE Transactions*, **47**, 274-284 (2015).

[30] J. Wong‐Leung, I. Yang, Z. Li, S. K. Karuturi, L. Fu, H. H. Tan and C. Jagadish, Engineering III–V semiconductor nanowires for device applications. *Advanced Materials*, **32**, 1904359 (2020).

[31] R. Al-Abri, H. Choi and P. Parkinson, Measuring, controlling and exploiting heterogeneity in optoelectronic nanowires. *Journal of Physics: Photonics*, **3**, 022004 (2021).

[32] F. Ge, S. Y. Wei, Z. Liu, G. H. Wang, X. H. Wang, G. B. Zhang, H. B. Lu, K. Cho and L. Z. Qiu, Tailoring Structure and Field-Effect Characteristics of Ultrathin Conjugated Polymer Films via Phase Separation. *Acs Applied Materials & Interfaces*, **10**, 9602-9611 (2018).

[33] S. Y. Wei, F. S. Tian, F. Ge, X. H. Wang, G. B. Zhang, H. B. Lu, J. Yin, Z. Q. Wu and L. Z. Qiu, Helical Nanofibrils of Block Copolymer for High-Performance Ammonia Sensors. *Acs Applied Materials & Interfaces*, **10**, 22504-22512 (2018).

[34] J. L. Wang, M. Hassan, J. W. Liu and S. H. Yu, Nanowire assemblies for flexible electronic devices: recent advances and perspectives. *Advanced Materials*, **30**, 1803430 (2018).

[35] L. Talazac, F. Barbarin, C. Varenne, L. Mazet, S. Pellier and C. Soulier, Gas sensing properties of pseudo-Schottky diodes on p-type indium phosphide substrates - Application to O_3 and NO_2 monitoring in urban ambient air. *Sensors and Actuators B-Chemical*, **83**, 149-159 (2002).

[36] K. Wierzbowska, B. Adamowicz, L. Mazet, J. Brunet, A. Pauly, L. Bideux, C. Varenne, B. Laure and J. P. Germain, High-sensitivity NO_2 sensor based on n-type InP epitaxial layers. *Optica Applicata*, **35**, 655-662 (2005).

[37] N. Sezer and M. Koc, A comprehensive review on the state-of-the-art of piezoelectric energy harvesting. *Nano Energy*, **80**, 105567 (2021).

[38] X. Sun, L. Li, Y. Guo, H. Zhao, S. Zhang, Y. Yu, D. Wu, H. Liu, M. Yu, D. Shi, Z. Liu, M. Zhou, L. Ren and L. Fu, Influences of organic component on mechanical property of cortical bone with different water content by nanoindentation. *AIP Advances*, **8**, 035003 (2018).

[39] M. Ha, S. Lim, J. Park, D.-S. Um, Y. Lee and H. Ko, Bioinspired Interlocked and Hierarchical Design of ZnO Nanowire Arrays for Static and Dynamic Pressure-Sensitive Electronic Skins. *Advanced Functional Materials*, **25**, 2841-2849 (2015).

[40] C. Chen, Q. Yu, S. Liu and Y. Qin, Piezotronic Transistors Based on GaN Wafer for Highly Sensitive Pressure Sensing with High Linearity and High Stability. *Acs Nano*, **18**, 13607-13617 (2024).

[41] Y. G. Wang, M. Y. Chao, P. B. Wan and L. Q. Zhang, A wearable breathable pressure sensor from metal-organic framework derived nanocomposites for highly sensitive broad-range healthcare monitoring. *Nano Energy*, **70**, 104560 (2020).

[42] X. L. Chen, J. Y. Shao, N. L. An, X. M. Li, H. M. Tian, C. Xu and Y. C. Ding, Self-powered flexible pressure sensors with vertically well-aligned piezoelectric nanowire arrays for monitoring vital signs. *Journal of Materials Chemistry C*, **3**, 11806-11814 (2015).

[43] C. C. Huang, Z. K. Kao and Y. C. Liao, Flexible Miniaturized Nickel Oxide Thermistor Arrays via Inkjet Printing Technology. *Acs Applied Materials & Interfaces*, **5**, 12954-12959 (2013).

[44] G. Farkas, in *Theory and Practice of Thermal Transient Testing of Electronic Components*, (Eds: M. Rencz, G. Farkas and A. Poppe), Springer International Publishing, Cham **2022**, p. 139-169.

[45] Y. Su, C. S. Ma, J. Chen, H. P. Wu, W. X. Luo, Y. M. Peng, Z. B. Luo, L. Li, Y. S. Tan, O. M. Omisore, Z. F. Zhu, L. Wang and H. Li, Printable, Highly Sensitive Flexible Temperature Sensors for Human Body Temperature Monitoring: A Review. *Nanoscale Research Letters*, **15**, 200 (2020).

[46] T. Q. Trung, T. M. L. Dang, S. Ramasundaram, P. T. Toi, S. Y. Park and N. E. Lee, A Stretchable Strain-Insensitive Temperature Sensor Based on Free-Standing Elastomeric Composite Fibers for On-Body Monitoring of Skin Temperature. *Acs Applied Materials & Interfaces*, **11**, 2317-2327 (2019).

[47] C. Yan, J. Wang and P. S. Lee, Stretchable Graphene Thermistor with Tunable Thermal Index. *Acs Nano*, **9**, 2130-2137 (2015).

[48] Y.-F. Lin, C.-H. Chang, T.-C. Hung, W.-B. Jian, K. Tsukagoshi, Y.-H. Wu, l. Chang, Z. Liu and J. Fang, Nanocontact Disorder in Nanoelectronics for Modulation of Light and Gas Sensitivities. *Scientific reports*, **5**, 13035 (2015).

[49] Alyabyeva, L.N., Zhukova, E.S., Belkin, M.A. *et al.* Dielectric properties of semi-insulating Fe-doped InP in the terahertz spectral region. *Scientific Reports*, **7**, 7360 (2017).

[50] J. Betko and K. Merínský, On the Temperature Dependence of the Intrinsic Concentration in Semi-Insulating InP Determined from Galvanomagnetic Measurements. *physica status solidi (a)*, **135**, K67-K70 (1993).

[51] Y. J. Su, T. N. Yang, X. Zhao, Z. X. Cai, G. R. Chen, M. L. Yao, K. L. Chen, M. Bick, J. J. Wang, S. D. Li, G. Z. Xie, H. L. Tai, X. S. Du, Y. D. Jiang and J. Chen, A wireless energy transmission enabled wearable active acetone biosensor for non-invasive prediabetes diagnosis. *Nano Energy*, **74**, (2020).

[52] P. H. Zhu, S. S. Li, X. Y. Jiang, Q. Wang, F. Q. Fan, M. Yan, Y. Zhang, P. N. Zhao and J. H. Yu, Noninvasive and Wearable Respiration Sensor Based on Organic Semiconductor Film with Strong Electron Affinity. *Analytical Chemistry*, **91**, 10320-10327 (2019).

[53] X. W. Chen, T. Wang, Y. T. Han, W. Lv, B. L. Li, C. Su, M. Zeng, J. H. Yang, N. T. Hu, Y. J. Su and Z. Yang, Wearable NO_2 sensing and wireless application based on ZnS nanoparticles/nitrogen-doped reduced graphene oxide. *Sensors and Actuators B-Chemical*, **345**, (2021).

[54] S. Y. Wei, Z. Li, A. John, B. I. Karawdeniya, Z. Y. Li, F. L. Zhang, K. Vora, H. H. Tan, C. Jagadish, K. Murugappan, A. Tricoli and L. Fu, Semiconductor Nanowire Arrays for High-Performance Miniaturized Chemical Sensing. *Advanced Functional Materials*, **32**, 210756 (2022).

[55] K. J. Albert, N. S. Lewis, C. L. Schauer, G. A. Sotzing, S. E. Stitzel, T. P. Vaid and D. R. Walt, Cross-reactive chemical sensor arrays. *Chemical Reviews*, **100**, 2595-2626 (2000).

[56] M. A. H. Khan, B. Thomson, R. Debnath, A. Motayed and M. V. Rao, Nanowire-Based Sensor Array for Detection of Cross-Sensitive Gases Using PCA and Machine Learning Algorithms. *Ieee Sensors Journal*, **20**, 6020-6028 (2020).

[57] T. Itoh, T. Akamatsu, A. Tsuruta and W. Shin, Selective Detection of Target Volatile Organic Compounds in Contaminated Humid Air Using a Sensor Array with Principal Component Analysis. *Sensors*, **17**, 1662 (2017).

[58] Z. Y. Wu, Z. X. Jiang, P. Y. Song, P. E. Tian, L. G. Hu, R. Liu, Z. L. Fang, J. Y. Kong and T. Y. Zhang, Nanowire-Seeded Growth of Single-Crystalline (010) -Ga_2O_3 Nanosheets with High Field-Effect Electron Mobility and On/Off Current Ratio. *Small*, **15**, 1900580 (2019).

Chapter 8. Conclusions and Future work

8.1 Conclusions

This thesis aims to develop high-performance gas sensor based on InP nanowire (NW) arrays. Sensing performance has been optimised at various levels, encompassing InP NW thickness, density, doping concentration, electrical structure, and surface functionalisation.

Chapters 1 to 3 present the research motivation, applications, and background for the development of gas sensors, particularly semiconductor gas sensors (SGSs). The importances of nanomaterials, in particular InP NWs, for SGS applications are discussed. Additionally, experimental techniques employed in this thesis are introduced, such as top-down etching and bottom-up SAE-MOVPE growth of InP NWs, device fabrication, and gas sensing properties characterisations.

Chapter 4 investigated and optimised the top-down etching conditions to achieve highly tailorable and well-ordered NWs array for NO_2 sensor applications. An innovative sensor configuration was demonstrated through tilt-angle deposition method, enabling partial contacting of vertical NWs for gas sensing. Results from NO_2 sensing measurements revealed a significant enhancement in sensitivity with decreased NWs diameter and increased NWs density. Electrical simulation and the Langmuir-isotherm kinetic theory were applied to explain the diameter and density effect on NO_2 sensitivity. This sensor achieved a 10-ppb level sensitivity, fast response speed (response time < 50s), high selectivity, humidity tolerance, and long-term stability at room temperature.

Chapter 5 showcases a self-powered NO_2 sensor based on p-n junction InP NWs by bottom-up approach. Guided by numerical simulation, NO_2 sensitivity can be enhanced by exposing the i-segment of the NWs, and i-n NWs is expected to outperform i-p NWs. An exposure window structure was developed to expose the junction region while preventing short-circuiting of the junction from the metal top contact on NWs. The self-powered gas sensing performance was characterised, achieving ppb-level sensitivity and a 0.49 ppb limit of detection. Moreover, the sensing response demonstrated fidelity to decreasing light intensity, even down to 5% of standard 1 sun illumination. Based on these superior properties, this self-powered device was applied to measure NO_2 concentrations from a vehicle exhaust in an outdoor environment, showing consistent results with those measured from a commercial sensor.

Chapter 6 explores the pathway for transitioning the sensitivity of InP NWs from NO_2 to acetone. This involves reducing the NW diameter, using Pt as the contact metal, and surface-functionalisation with chitosan. Through these modifications, InP NW arrays with high sensitivity and selectivity to acetone (compared to interruption gases, and potentially small volatile ketones (2-butanone)) have been achieved. The InP NW array acetone sensor also exhibited a wide dynamic range (0.4 ppb - 110,000 ppm) and humidity tolerance at room temperature. Sensing mechanism was studied by electrical simulation and control experiments. This acetone sensor was further integrated into a user-friendly portable apparatus, the Ketowhistle, as a prototype point-of-care breath testing tool successfully testing simulated exhaled breath.

Chapter 7 combines the research in Chapters 4-6 and further explores the physical sensing properties of InP NWs to demonstrate a multifunctional wearable array device. A signal decoupling strategy is developed, incorporating NW arrays with different geometries

achieved through substrate patterning design, MOVPE growth and wearable device fabrication steps, to enhance the detection accuracy under an interrupting environment. A new fabrication method was developed for the vertical assembling and transferring of the NWs array to a flexible substrate, to achieve different functionality from each array element for body temperature, heart rate, NO_2 and acetone sensing with high sensitivity. These results suggest that InP NW array is a new and promising material platform for development of next generation multiplex wearable sensors.

8.2 Future work

In this thesis, we have successfully realised InP NW array based gas sensors for both oxidising and reducing gases detection, featuring high sensitivity, selectivity, fast response and self-powered operation at room-temperature. Based on the understandings from our studies, three new research directions could be carried out in future work to broaden the capability and functionality of NW array based gas sensors: 1) exploration of new III-V NW materials; 2) design of radial junction NW structures (PV) gas sensing; 3) modification of surface-functionalisation layer; 4) incorporation NW array devices with microfluidic system for biosensor applications.

8.2.1 Exploration of new III-V NW materials

The change of NW array material could change or enhance the sensitivity to large subset of gases and broaden the detectable analytes.[1] In the future, different III-V semiconductor NWs can be synthesized and optimised to achieve high sensitivity for different types of gas molecules. Through NW transferring, the NW with different chemical composition (e.g. InAsP, InAsSb, AlGaAs …) can be assembled onto the same substrate, with different gas sensing functionalities in each pixel, as schematically shown

in Figure 8-1, to achieve highly integrated multipixel gas sensor array with wide chemical diversity.

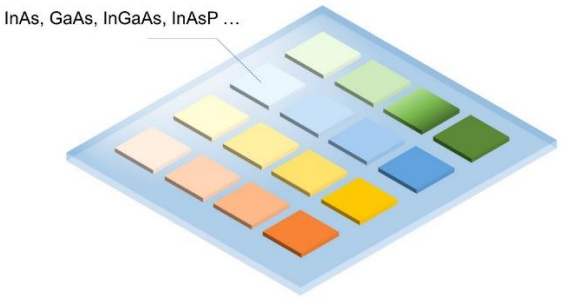

Figure 8-1. The schematic of the conceptual sensor array based on different NW arrays and assembled by the NW transfer process

8.2.2 Design of the radial p-n junction based PV gas sensors

To improve the device performance and functionalities of the self-powered devices as mentioned in Chapter 5, the axial p-i-n junction based NW structure an be further optimised by reducing the n-segment length and increased the i-segment length to further push the sensitivity. However as shown in Chapter 5, the fabrication process for the axial junction based PV gas sensor is quite complicated. Therefore, apart from the axial p-n junction, it may be worthwhile to investigate the radial-junction p-n NW structure, which could not only provide a larger junction region but also simplify the device fabrication process, as schematically shown in Figure 8-2.[2]

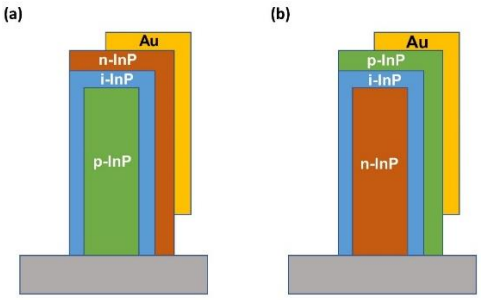

Figure 8-2. The Schematics of the conceptual radial junction self-powered InP NWs gas sensor. (a) n-shell/p-core and (b) p-shell/n-core. The i-region could be exposed by wet etching method to remove the shell layer.

8.2.3 Modification of surface-functionalisation layer

From the sensing mechanism study in Chapter 6, the acetone sensing mechanism is strongly related to the chitosan surface-functionalisation. Further fine tune of the molecular weight of chitosan and its degree of acetylation might lead to even better performance.[3] Chitosan layer thickness could also play a role in acetone sensitivity. Therefore, alternative deposition methods (to drop casting) that provide a better control of the layer thickness should also be explored.[4] Moreover, other functional layers with amine functional group could be investigated to explore for enhanced sensitivity and specificity for acetone sensing, whose potential candidates are listed in Figure 8-3. The molecule structure of chitosan can be further explored to improve gas adsorption. The chitosan used in this work was unmodified, and the research showed that the modification of chitosan could enhance its surface area and O_2 absorption, which is critical for producing oxygen ionic species in the acetone sensing mechanism to further enhanced the acetone sensitivity.[5]

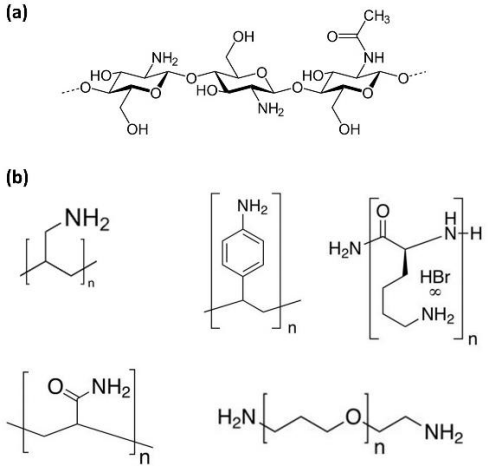

Figure 8-3. The chemical structure of chitosan and other polymers with -NH_2 functional group (a) including in Poly(allylamine), Poly(4-aminostyrene), Poly(l-lysine hydrobromide), Polyacrylamide, Poly(ethylene glycol) bis (2-aminoethyl) (b).

Furthermore, a range of new surface-functionalisation layers can be designed and applied to InP NW arrays to achieve its sensitivity other types of gases, in addition to NO_2 and acetone. For example, ammonia is a waste product that the kidneys usually filter out. Elevated levels of ammonia in the body can indicate kidney dysfunction or other health issues.[6] The sensing technology for ammonia in the context of renal disease could also be based on chemiresistive gas sensors.[7] To realise the ammonia sensitivity with the InP NWs gas sensor, surface-functionalisation is critical considering their reductive property. In the past, several types of materials have been found to have high ammonia affinity that could be considered as potential surface functionalisation layers for developing InP NW array based ammonia sensors, including organic ligands or polymers such as polyaniline and polypyrrole,[8] low dimensional materials such as graphene, carbon nanotube,[9] or immobilise biological recognition elements like enzymes or antibodies.[10]

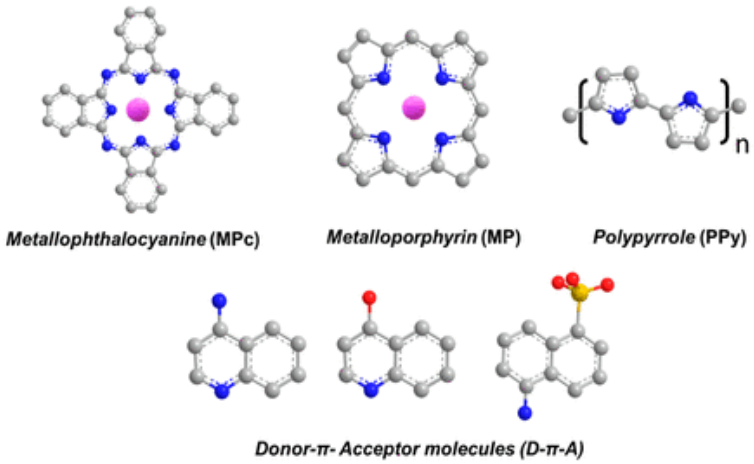

Figure 8-4. The chemical structure of organic ligands that have a high affinity for ammonia.

8.2.4 Incorporation of NW array devices with microfluidic system for biosensor applications

Microfluidic systems offer precise control and manipulation of small volumes of fluids, enabling the development of highly sensitive and portable devices for biosensing

applications.[11] A biosensor system is normally composed of microfluidic chip channels, pumping, sensor and transducer, on-chip processing, power supply, etc. Single InP NWs have already been study as the biomolecule sensing materials showing ultrasensitive detection of a Chagas disease biomarkers from Richard Janissen et. al.[12] In future, our InP NWs array sensor can also be integrated with a microfluidic system for biosensor investigations.

Finally, apart from the development of new gas sensors, the knowledge and understanding obtained in this thesis work can be extended to further integration of the gas sensors with Internet of things, wearable personal health monitoring systems, and even spacecrafts. The development of many other NW-based devices could also be further investigated for inspiring new research directions and potential applications, such as pressure sensors, and biosensors with the microfluidic system for medical studies, etc.

References

[1] S.-J. Choi and I.-D. Kim, Recent Developments in 2D Nanomaterials for Chemiresistive-Type Gas Sensors. *Electronic Materials Letters*, **14**, 221-260 (2018).

[2] S. Wang, X. Yan, X. Zhang, J. Li and X. Ren, Axially connected nanowire core-shell p-n junctions: a composite structure for high-efficiency solar cells. *Nanoscale Research Letters*, **10**, 22 (2015).

[3] M. J. Ahmed, B. H. Hameed and E. H. Hummadi, Review on recent progress in chitosan/chitin-carbonaceous material composites for the adsorption of water pollutants. *Carbohydrate Polymers*, **247**, 116690 (2020).

[4] Gylienė, E. Servienė, I. Vepštaitė, R. Binkienė, M. Baranauskas and J. Lukša, Correlation between the sorption of dissolved oxygen onto chitosan and its antimicrobial activity against Esherichia coli. *Carbohydrate Polymers*, **131**, 218-223 (2015).

[5] T. I. Nasution, I. Nainggolan, S. D. Hutagalung, K. R. Ahmad and Z. A. Ahmad, The sensing mechanism and detection of low concentration acetone using chitosan-based sensors. *Sensors and Actuators B-Chemical*, **177**, 522-528 (2013).

[6] P. P. Ricci and O. J. Gregory, Sensors for the detection of ammonia as a potential biomarker for health screening. *Scientific Reports*, **11**, 7185 (2021).

[7] D. Kwak, Y. Lei and R. Maric, Ammonia gas sensors: A comprehensive review. *Talanta*, **204**, 713-730 (2019).

[8] R. Kumar, A. Kumar, R. Singh, R. Kashyap, R. Kumar, D. Kumar and M. Kumar, Selective room temperature ammonia gas detection using 2-amino pyridine functionalized graphene oxide. *Materials Science in Semiconductor Processing*, **110**, 104920 (2020).

[9] E. R. Waclawik, J. Chang, A. Ponzoni, I. Concina, D. Zappa, E. Comini, N. Motta, G. Faglia and G. Sberveglieri, Functionalised zinc oxide nanowire gas sensors: Enhanced NO_2 gas sensor response by chemical modification of nanowire surfaces. *Beilstein journal of nanotechnology*, **3**, 368-377 (2012).

[10] K. Deshmukh, T. Kovářík and S. K. Khadheer Pasha, State of the art recent progress in two dimensional MXenes based gas sensors and biosensors: A comprehensive review. *Coordination chemistry reviews*, **424**, 213514 (2020).

[11] K.-K. Liu, R.-G. Wu, Y.-J. Chuang, H. S. Khoo, S.-H. Huang and F.-G. Tseng, Microfluidic systems for biosensing. *Sensors*, **10**, 6623-6661 (2010).

[12] Z. Fattahi and M. Hasanzadeh, Nanotechnology-assisted microfluidic systems for chemical sensing, biosensing, and bioanalysis. *TrAC Trends in Analytical Chemistry*, **152**, 116637 (2022).